

**Electromechanical design and development of the Virginia  
Tech Roller Rig testing facility for wheel-rail contact  
mechanics and dynamics**

Milad Hosseinipour

Dissertation submitted to the faculty of the  
Virginia Polytechnic Institute and State University  
in partial fulfillment of the requirements for the degree of

Doctor of Philosophy  
In  
Mechanical Engineering

Mehdi Ahmadian, Chair

Dong S. Ha

Brian Vick

Saeid Taheri

Reza Mirzaeifar

August 1, 2016

Blacksburg, VA

Keywords: railway, roller rig, electromechanical system, mechanical design,  
electrical design, train testing facility, wheel-rail contact, vehicle dynamics, motion  
control, encoder, hardware-in-the-loop operation

© Milad Hosseinipour, 2016

# **Electromechanical design and development of the Virginia Tech Roller Rig testing facility for wheel-rail contact mechanics and dynamics**

Milad Hosseinipour

## **Abstract**

The electromechanical design and development of a sophisticated roller rig testing facility at the Railway Technologies Laboratory (RTL) of Virginia Polytechnic and State University (VT) is presented. The VT Roller Rig is intended for studying the complex dynamics and mechanics at the wheel-rail interface of railway vehicles in a controlled laboratory environment. Such measurements require excellent powering and driving architecture, high-performance motion control, accurate measurements, and relatively noise-free data acquisition systems. It is critical to accurately control the relative dynamics and positioning of rotating bodies to emulate field conditions. To measure the contact forces and moments, special care must be taken to ensure any noise, such as mechanical vibration, electrical crosstalk, and electromagnetic interference (EMI) are kept to a minimum. This document describes the steps towards design and development of all electromechanical subsystems of the VT Roller Rig, including the powertrain, power electronics, motion control systems, sensors, data acquisition units, safety and monitoring circuits, and general practices followed for satisfying the local and international codes of practice.

The VT Roller Rig is comprised of a wheel and a roller in a vertical configuration that simulate the single-wheel/rail interaction in one-fourth scale. The roller is five times larger than the scaled wheel to keep the contact patch distortion that is inevitable with a roller rig to a minimum. This setup is driven by two independent AC servo motors that control the velocity of the wheel and roller using state-of-the-art motion control technologies. Six linear actuators allow for adjusting the simulated load, wheel angle of attack, rail cant, and lateral position of the wheel on the rail. All motion controls are performed using digital servo drives, manufactured by Kollmorgen, VA, USA.

A number of sensors measure the contact patch parameters including force, torque, displacement, rotation, speed, acceleration, and contact patch geometry. A unified communication protocol between the actuators and sensors minimizes data conversion time, which allows for servo update rates of up to 48kHz. This provides an unmatched bandwidth for performing various dynamics, vibrations, and transient tests, as well as static steady-state conditions.

The VT Roller Rig has been debugged and commissioned successfully. The hardware and software components are tested both individually and within the system. The VT Roller Rig can control the creepage within 0.3RPM of the commanded value, while actively controlling the relative position of the rotating bodies with an unprecedented level of accuracy, no more than 16nm of the target location. The contact force measurement dynamometers can dynamically capture the contact forces to within 13.6N accuracy, for up to 10kN. The instantaneous torque in each driveline can be measured with better than 6.1Nm resolution. The VT Roller Rig Motion Programming Interface (MPI) is highly flexible for both programmers and non-programmers. All common motion control algorithms in the servo motion industry have been successfully implemented on the Rig. The VT Roller Rig MPI accepts third party motion algorithms in C, C++, and any .Net language. It successfully communicates with other design and analytics software such as Matlab, Simulink, and LabVIEW for performing custom-designed routines. It also provides the infrastructure for linking the Rig's hardware with commercial multibody dynamics software such as Simpack, NUCARS, and Vampire, which is a milestone for hardware-in-the-loop testing of railroad systems.

# **Electromechanical design and development of the Virginia Tech Roller Rig testing facility for wheel-rail contact mechanics and dynamics**

Milad Hosseinipour

## **Executive Summary**

The VT Roller Rig is comprised of a wheel and a roller in a vertical configuration that simulate the single-wheel/rail interaction in one-fourth scale. The roller is five times larger than the scaled wheel, to keep the contact patch distortion that is inevitable with such setup to a minimum. This setup is driven by two independent AC servo motors that control the velocity of the wheel and the roller using state-of-the-art motion control technologies. Six linear actuators allow for adjusting the simulated load, wheel angle of attack, rail cant, and lateral position of the wheel on the rail.



**Figure 0.1. The mechanical setup of the VT Roller Rig. Arrows indicate the adjustable degrees of freedom.**

A number of sensors measure the contact patch parameters including, but not limited to force, torque, displacement, rotation, speed, acceleration, and contact patch geometry. A unified communication protocol between the actuators and sensors minimizes the data conversion time, which allows for servo update rates up to 48kHz. This provides an unmatched bandwidth for

performing vibration analyses that are accounted as contributors to wear, noise, and ride discomfort [1]. A high-speed vision system, incorporated into the Rig, can capture the instantaneous geometry of the contact patch and synchronize it with other measurements for post processing purposes. As shown in Figure 0.1, the Rig's configuration accommodates the addition of third-body layers at the wheel/rail interface for studying the effect of surface conditioning elements and friction modifiers.

A TN-S power system equipped with an isolating transformer and passive power filters delivers clean and highly balanced 3-phase power to the motion control drives of the Rig. A customary Faraday Cage for the control tower (Figure 0.2) ensures maximum signal-to-noise ratio and EMI shielding. The efforts towards proper grounding, shielding, and safety of the Rig satisfy the EMC and IEC codes.

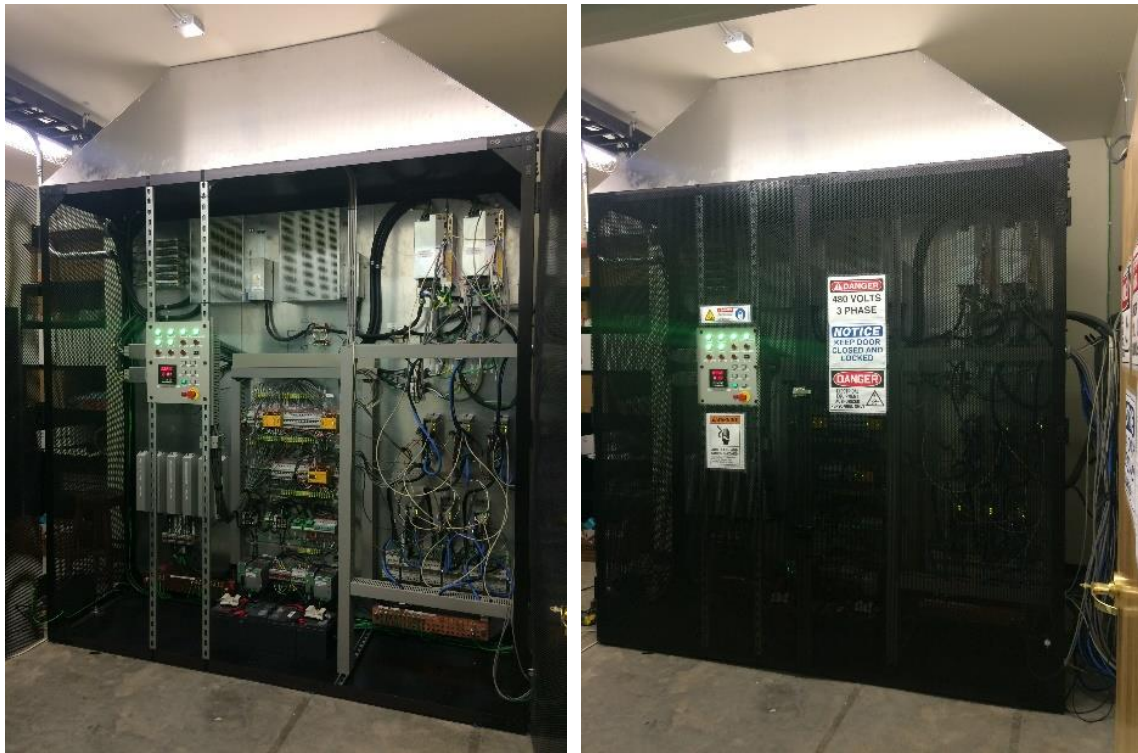


**Figure 0.2. The control tower of the VT Roller Rig that includes all adjustable speed drives, power devices, safety and monitoring systems, and unified user interface.**

Extensive instrumentation and motion control systems for the Rig, along with multiple layers of safety circuits, allow for investigating phenomena such as derailment and flanging. The flexible motion programming interface of the Rig is compatible with the majority of existing rail vehicle dynamics models for performing hardware-in-the-loop (HIL) operation. The immediate benefits from HIL are advanced train control algorithms and better traction/braking procedures. Further details about the design and components of the Rig can be found in [2] and [3].

To my mother and my wife.

# Acknowledgments

There are a few people that come to one's life for a limited time, but fill it for a lifetime. For me, Prof. Mehdi Ahmadian is one of those few. His lessons, words of wisdom and professional advice have changed my life forever. This project would have never made it to the end, without his confidence in me and continual support. He has had a great influence on me, both as an individual and a researcher, and my sincere regards will always be upon him.

I would also like to thank my committee members for their time, directions and advice. This project would not have advanced so quickly if it was not for their willingness to pass on their knowledge.

A very special thank you is due to the Federal Railroad Administration for providing the required funding for this research. In particular, I would like to thank Mr. Ali Tajaddini for his great support and insightful discussions throughout the project.

Many seasoned and knowledgeable engineers devoted their precious time to help me during the process of design, development, and fabrication of the VT Roller Rig. I would like to extend my sincere gratitude to the following people in particular:

- Michael Craft, Principal Engineer – Track Geometry at AMTRAK Engineering
- Steve Gerus, President at Bell Electric of Blacksburg, Inc.
- John Boyland, VP Engineering R&D at Kollmorgen Corporation
- Steve Reese, Director of Business Development at Kollmorgen Corporation
- Hurley Gill, Senior Applications/System Engineer at Kollmorgen Corporation
- Bill West, Global Application Engineering Director at Kollmorgen Corporation
- Lee Stephens, Senior Motion Control Engineer at Kollmorgen Corporation
- Richard (Rick) Armstrong Jr., Director & Engineering Consultant at Armstrong Tech.
- Wayne Coleman, Client Services Supervisor at Dresser-Rand Synchrony
- Bernie Diehl, Technical Support Engineer at Pilz Automation Safety
- Clinton 'Sam' Hommel, Product Engineer at Phoenix Contact
- Jeff Conner, Automation Engineer at Commonwealth Controls Corporation
- Jim Parker, Sales Engineer at Omron Electronics
- James R. Connor, Product Engineer at Aavid Thermalloy

The VT Roller Rig became viable only through valuable discussions with my colleagues and friends at CVeSS. I would like to thank all members of CVeSS family for their support and friendship. They have been a strong support behind this project. I appreciate Sajjad Z. Meymand's efforts towards development of the Rig's mechanical setup. Dr. Andrew Peterson's help have far exceeded his role as the research scientist and lab manager at CVeSS.

I would like to thank my family for their patience, assistance, and support throughout my life. Finally, but most importantly, I wish to thank my beloved best friend and wife, Farzaneh S. Tabataba, for her unconditional love and support while I spent days and nights working on this project. She took every step of this journey with me not only as my wife but also as an expert computer scientist who devoted many hours of her time to develop novel solutions to very complex problems. I am eternally grateful for having her in my life.

Milad Hosseinipour  
August 2016  
Blacksburg, VA

# Contents

Contents.....	viii
List of Figures .....	xiv
List of Tables.....	xxv
Chapter 1. Introduction .....	1
1.1 Motivation .....	1
1.2 Objectives .....	2
1.3 Approach .....	3
1.4 Contributions .....	3
1.5 Outline .....	4
Chapter 2. Background.....	6
2.1 History .....	6
2.1.1 Full-Scale Rigs .....	6
2.1.2 Scaled Rigs .....	8
2.2 Virginia Tech Roller Rig .....	11
2.3 Virginia Tech Roller Rig Configuration.....	14
2.3.1 Mechanical Components of the VT Roller Rig .....	14
Chapter 3. Powertrain.....	19
3.1 Vibration Analysis of Independent and Differential Drivelines.....	20
3.1.1 Axial Forces in Tripod Constant Velocity Joints .....	22
3.1.2 Outcome and Discussion .....	25
3.2 Non-chaotic Behavior of Independent Drivelines .....	26
3.2.1 Vibration Compensator for Unbalanced Rotation of the Wheel and/or Roller .....	28
3.2.2 Outcome and Discussion .....	34

3.3	Electromechanical Modeling of the VT Roller Rig.....	34
3.3.1	Equivalent Model of the Electrical System .....	34
3.3.2	Equivalent Model of the Mechanical system .....	39
3.3.3	Outcome and Discussion .....	44
Chapter 4.	Electromechanical Systems .....	46
4.1	Power Architecture .....	46
4.1.1	Mains Network .....	46
4.1.2	Isolating Transformer .....	49
4.1.3	Power Filtering .....	52
4.1.4	DC Power .....	54
4.1.5	DC-Bus .....	56
4.2	Grounding.....	57
4.2.1	Star Ground Topology .....	57
4.2.2	Shield Grounding.....	59
4.2.3	Additional Measures.....	61
4.3	Power Measurements.....	62
4.4	Noise Attenuation.....	74
4.4.1	Material Selection.....	80
4.4.2	Models .....	81
4.4.3	Simulations .....	83
4.4.4	Implementation and Experimental Results.....	92
4.5	Transformer Base Structure.....	96
4.6	Thermal Management.....	105
4.6.1	Solution I: HVAC Unit Only .....	108
4.6.2	Solution II: Roof Fan Only.....	109
4.6.3	Solution III: Finned Plate and Roof Fan.....	110
4.6.4	Solution IV: Liquid Cold Plates plus HVAC unit .....	112

4.6.5	Solution V: Liquid Cold Plates plus Roof Fan .....	115
4.6.6	Outcome and Discussion .....	116
Chapter 5.	Safety and Monitoring .....	124
5.1	Safe-Torque-OFF (STO) Safety Circuit .....	128
5.2	Hardware Enable Safety Circuit .....	129
5.3	Ready-to-Operate (RTO) Safety Function .....	131
5.4	Logic ON-OFF .....	132
5.5	Dynamic Braking.....	133
5.5.1	Regenerative Dynamic Braking.....	134
5.5.2	Motor-Short Dynamic Braking.....	135
5.6	Holding Brake .....	138
5.7	Emergency Stop.....	140
Chapter 6.	Commissioned Capabilities of the Virginia Tech Roller Rig .....	144
6.1	Novel Motion Control and Data Acquisition Architecture: Fast, Low-Noise, High-Performance, and Plug-n-Play.....	144
6.1.1	Motion Controller .....	153
6.1.2	Data Acquisition Units .....	154
6.1.3	Network Update Rate .....	158
6.2	Flexible Motion Programming Interface (MPI) .....	161
6.2.1	High-Level Motion Programming Interfaces .....	164
6.2.2	Packet Timing.....	169
6.3	Precise Independent Velocity Control.....	170
6.3.1	Roller Rig Demand Modes.....	171
6.3.2	Servo Tuning .....	175
6.3.3	D-Rate .....	189
6.3.4	Electronic Gearing / Master-Slave configuration.....	189
6.4	Precise Wheel-Rail Positioning.....	193

6.4.1	Scaling PID Parameters for Different Controller Update Rates .....	201
6.5	Accurate Measurement of Contact Forces and Moments.....	201
6.6	Accurate Torque Measurement .....	211
6.7	Unified Operating User Interface for Non-Electrically Certified Personnel .....	217
6.8	Hardware-In-The-Loop Testing Infrastructure.....	221
Chapter 7.	Identification and Modeling of the Quantization Error in Encoder Equivalent Output	225
7.1	Description of the Related Art.....	226
7.2	Background .....	228
7.3	Motivation .....	230
7.4	Other Errors in Encoder-Based Measurements .....	232
7.4.1	Sampling Error .....	232
7.4.2	Rounding Error.....	234
7.4.3	Data Transmission Error.....	235
7.4.4	Hardware Error.....	236
7.5	Quantization Error in Encoder Equivalent Output .....	237
7.5.1	ADC Sampling .....	238
7.5.2	Interpolation .....	240
7.5.3	Encoder Equivalent Output .....	244
7.6	Deterministic Estimator for Quantization Error .....	245
7.7	Experimental Noise Identification.....	247
7.8	Validating the Quantization Error Estimator.....	250
7.9	Conclusions .....	253
Chapter 8.	Component Selection.....	255
8.1	Rotational Servo-Motors .....	255
8.1.1	Four Quadrant Operation.....	257
8.1.2	S772 Digital Servo-Amplifier .....	259

8.2	Linear Positioning Servo-Systems .....	260
8.2.1	Motor Inductance.....	262
8.2.2	AKD Digital Servo-Amplifiers .....	264
8.3	Isolating Transformer .....	265
8.4	3-Phase Power Filters.....	267
8.5	DC Power System.....	268
8.5.1	Power Supply.....	268
8.5.2	Electronic Switchover Unit .....	269
8.5.3	Power Storage Unit.....	271
8.6	Relays .....	271
8.6.1	Logic ON-OFF Circuit .....	271
8.6.2	Emergency Stop Circuit .....	272
8.6.3	STO Circuit .....	273
8.6.4	Motor-Short Dynamic Braking Circuit.....	276
8.6.5	RTO Circuit.....	277
8.6.6	Hardware-Enable Circuit.....	277
8.7	Regenerative Resistors .....	280
8.8	Motor-Short Resistors .....	281
8.9	Contactors.....	283
8.10	Fuses and Circuit Breakers .....	283
Chapter 9.	Realizable Tests with the Virginia Tech Roller Rig.....	285
9.1	Precise Measurement of Creep-Creepage Curves .....	285
9.2	Accurate Measurement of Contact Geometry .....	286
9.3	Precise Evaluation of Third Body Layers.....	286
9.4	Dynamic Creepage Analysis .....	286
9.5	Wheel-rail Vibration Analysis.....	287
9.6	Wheel-Rail Wear Analysis .....	287

9.7	Derailment Mechanics.....	288
9.8	Hardware-in-the-loop (HIL) Operation.....	288
	References .....	290
	Appendices .....	305
A.	S772 Servo-Amplifier Diagrams .....	305
A.1	Block Diagram.....	305
A.2	Connector Assignment .....	306
A.3	Connection Diagram.....	307
B.	AKD-B00607 Servo-Amplifier Diagrams.....	308
B.1	Connector Assignment .....	308
B.2	Connection Diagram.....	309

# List of Figures

Figure 0.1. The mechanical setup of the VT Roller Rig. Arrows indicate the adjustable degrees of freedom.....	iii
Figure 0.2. The control tower of the VT Roller Rig that includes all adjustable speed drives, power devices, safety and monitoring systems, and unified user interface.....	iv
Figure 2.1. The final design of the VT Roller Rig. Arrows indicate the adjustable degrees of freedom.....	13
Figure 2.2. Final frame of the VT Roller Rig at machine shop.....	17
Figure 2.3. Lateral view of the VT Roller Rig showing motors, drivelines, roller and wheel. ....	17
Figure 3.1. Differential driveline requires compliant joints to allow for relative motion between the two wheels.....	20
Figure 3.2. Independent drivelines require controlling two servo motors to provide the desired creep profile. ....	21
Figure 3.3. Main components of a tripod joint.....	23
Figure 3.4. Net generated axial force in a tripod CV joint rotating at 350rpm and transmitting 450Nm load. ....	24
Figure 3.5. Net generated axial force in a tripod CV joint under 10Nm load, while the motor accelerates linearly. ....	24
Figure 3.6. Displacement of the shaft end due to net axial force generated in a tripod CV joint with ramp speed.....	25
Figure 3.7. Front and rear dynamometers for measuring the contact loads. ....	27
Figure 3.8. Mass-spring-damper model of the wheel/roller interaction. ....	29
Figure 3.9. Qualitative x and y responses of the wheel.....	31
Figure 3.10. Force phase plane as wheel rotates at the first natural frequency and roller rotates at the second natural frequency. ....	31
Figure 3.11. Force phase plane as both wheel and roller rotate at the 0.5×first natural frequency. ....	32
Figure 3.12. Force time history as wheel rotates at 5×first natural frequency and roller rotates at 5×second natural frequency.....	33

Figure 3.13. Force time history as wheel rotates at $0.1 \times$ first natural frequency and roller rotates at $0.1 \times$ second natural frequency.....	33
Figure 3.14. Arrangement of rectifier, braking chopper, and inverter inside the drive.....	35
Figure 3.15. Comparison between desired and actual electromagnetic torques.....	37
Figure 3.16. DC bus voltage and current.....	38
Figure 3.17. Output resistance current of the three-phase inverter (top) and stator current (bottom). .....	39
Figure 3.18. Speed profile of the motor under constant load and rotor inertia only.....	39
Figure 3.19. Schematic of wheel and roller drivelines.....	40
Figure 3.20. Frequency response of uncoupled wheel (top) and roller (bottom) drivelines.....	43
Figure 3.21. Frequency response of the coupled drivelines.....	44
Figure 4.1. TN-C System.....	47
Figure 4.2. TN-CS System.....	47
Figure 4.3. TN-S System.....	48
Figure 4.4. AEP specifications for 600A to 800A service upgrade (reprinted with permission, courtesy of AEP) [75].....	49
Figure 4.5. Application of an isolating transformer (courtesy of Kollmorgen) [73].....	52
Figure 4.6. Schaffner FN 258-100-35 filter and its block diagram (courtesy of Schaffner) [79]..	54
Figure 4.7. Uninterruptible auxiliary DC power system of the VT Roller Rig.....	55
Figure 4.8. Parallel connection of DC power systems for redundancy (courtesy of Phoenix Contact) [80].	56
Figure 4.9. DC-Bus link topology. The actual DC-Bus link is marked in red.....	57
Figure 4.10. Correct star ground connection (left) versus incorrect daisy chain ground (right, courtesy of Kollmorgen) [81].....	58
Figure 4.11. Earth resistance testing.....	59
Figure 4.12. Coupled noise source due to connection between ground earth and neutral line.....	61
Figure 4.13. The Faraday Cage (top) for the control tower (bottom) of the VT Roller Rig.....	62
Figure 4.14. Configuration of Fluke 437 Series II power analyzer for measuring the VT Roller Rig power distribution system.....	63
Figure 4.15. Volts/Amps/Hertz measurement of the distribution system.....	63
Figure 4.16. L1N Vrms phase-to-neutral during an hour of continuous experiment. The crest factor was 1.435.....	65
Figure 4.17. L2N Vrms phase-to-neutral during an hour of continuous experiment. The crest factor was 1.435.....	65

Figure 4.18. L3N Vrms phase-to-neutral during an hour of continuous experiment. The crest factor was 1.445.....	65
Figure 4.19. LNG Vrms during an hour of continuous experiment. ....	66
Figure 4.20. The frequency and voltage unbalance during an hour of experiment. ....	66
Figure 4.21. L1 Arms current during an hour of continuous experiment. The crest factor was 5. ....	66
Figure 4.22. L2 Arms current during an hour of continuous experiment. The crest factor was 4.5. ....	67
Figure 4.23. L3 Arms current during an hour of continuous experiment. The crest factor was 5.25. ....	67
Figure 4.24. Neutral Arms current during an hour of continuous experiment. ....	67
Figure 4.25. The frequency and current unbalance during an hour of experiment. Measurements were performed right before the drives' input.....	68
Figure 4.26. The phasor plot of the VT Rolle Rig power distribution system. Measurements were performed right before the drives' input. ....	68
Figure 4.27. The scope waveform plot of the VT Rolle Rig power distribution system.....	69
Figure 4.28. Voltage harmonics of the VT Roller Rig power distribution system during a normal test. Measurements were performed right before the drives' input. ....	70
Figure 4.29. Current harmonics of the VT Roller Rig power distribution system during a normal test. Measurements were performed right before the drives' input. ....	70
Figure 4.30. The frequency and current unbalance before the filters during an hour of experiment. The working conditions of the system are the same as Figure 4.25.....	71
Figure 4.31. The phasor plot of the VT Rolle Rig power distribution network. Measurements were performed before the passive filters. The working conditions of the system are the same as Figure 4.26.....	72
Figure 4.32. Voltage harmonics before the passive filters during a normal test. The working conditions of the system are the same as Figure 4.28. ....	72
Figure 4.33. Current harmonics before the passive filters during a normal test. The working conditions of the system are the same as Figure 4.29. ....	72
Figure 4.34. The power factor and $\cos \phi$ for the VT Roller Rig during an hour of normal test....	74
Figure 4.35 Permanent magnet AC synchronous motors for each degree of freedom of the Rig. ....	77
Figure 4.36. Eight digital servo drives run the VT Roller Rig testing facility. The drives are part of the control tower that is responsible for motion control and safety of the system. ....	78
Figure 4.37. The mechanical setup of the VT Roller Rig is located right across a hollow wall from the control tower, which includes all ASD's, power devices, and safety systems. ....	79

Figure 4.38. The Simplified 2D model of the electromagnetic source and perforated shield. ....	82
Figure 4.39. Mesh quality of the physical model in COMSOL Multiphysics. ....	84
Figure 4.40. a) Electric displacement field norm (D), and b) magnetic field density norm (B) at 100kHz without any EMI shielding. ....	85
Figure 4.41. Magnetic field density norm (B) at 100kHz with a) full aluminum shield, and b) perforated aluminum shield. ....	86
Figure 4.42. Electric displacement field norm (D) with full Aluminum shield at different frequencies along a line in the middle of the 2D domain. a) full shield and b) perforated shield. ....	87
Figure 4.43. $SM_{dB}$ of different materials at different frequencies. Shields are perforated in all cases. ....	89
Figure 4.44. $\Delta SM_{dB}$ of the various materials at different frequencies. Perforated shields are the same in all cases. ....	89
Figure 4.45. $SM_{dB}$ of copper, steel, aluminum, and PVC at different frequencies. Shields are perforated in all cases. ....	90
Figure 4.46. Effect of thickness on $SM_{dB}$ of steel at different frequencies. All shields are perforated. ....	91
Figure 4.47. The Faraday Cage for the VT Roller Rig control tower. ....	93
Figure 4.48. The loop antenna test setup. ....	94
Figure 4.49. Measurements inside the cabinet. Left figure is the time signal, and right figure is the FFT using Hanning window. ....	95
Figure 4.50. Measurements at a location adjacent to cabinet when the door is closed. Left figure is the time signal, and right figure is the FFT using Hanning window. ....	95
Figure 4.51. Measurements at a location at 4ft away from the cabinet when the door is closed. Left figure is the time signal, and right figure is the FFT using Hanning window. ....	96
Figure 4.52. Initial design of the isolating transformer structure: cantilevered structure with cable support against workshop I-beams (left), asymmetric statically indeterminate structure (right). .	98
Figure 4.53. Symmetric statically indeterminate structure for holding the isolating transformer. ....	99
Figure 4.54. Loading and boundary conditions for the finite element analyses of the isolating transformer structure. ....	100
Figure 4.55. Quality of mesh used for performing the finite element analysis. ....	100
Figure 4.56. Stress distribution in the isolating transformer base structure. ....	101
Figure 4.57. Displacement distribution in the isolating transformer base structure. ....	101
Figure 4.58. Strain distribution in the isolating transformer base structure. ....	102
Figure 4.59. First buckling mode of the isolating transformer base structure. ....	103

Figure 4.60. Second buckling mode of the isolating transformer base structure.....	103
Figure 4.61. Third buckling mode of the isolating transformer base structure. ....	104
Figure 4.62. Fourth buckling mode of the isolating transformer base structure.....	104
Figure 4.63. Most heat dissipative components of the VT Roller Rig. ....	106
Figure 4.64. Size of the room and materials used for modeling the heat dissipative components. .....	107
Figure 4.65. Extended surfaces on the back of S772 servo amplifiers.....	108
Figure 4.66. Heat transfer mechanisms for solution I. ....	109
Figure 4.67. Heat transfer mechanisms for solution II. ....	110
Figure 4.68. Fins on the back of mounting plate. ....	111
Figure 4.69. Heat transfer mechanisms for solution III.....	111
Figure 4.70. AavFin liquid cold plate (courtesy of Aavid Thermalloy) [117]. ....	113
Figure 4.71. Effect of flow rate, pressure drop and thermal contact resistance on the performance of AavFin liquid cold plates (courtesy of Aavid Thermalloy) [117].....	113
Figure 4.72. Proposed design for cooling the control panel down using liquid cold plates. ....	114
Figure 4.73. Heat transfer mechanisms for case IV. ....	115
Figure 4.74. Heat transfer mechanisms for case V.....	116
Figure 4.75. Temperature distribution for case I. Colors show the temperature and streamlines represent the temperature gradients.....	117
Figure 4.76. Temperature distribution for case II. Colors show the temperature and streamlines represent the temperature gradients.....	118
Figure 4.77. Temperature distribution for case III. Colors show the temperature and streamlines represent the temperature gradients.....	118
Figure 4.78. Temperature distribution for case IV. Colors show the temperature and streamlines represent the temperature gradients.....	119
Figure 4.79. Temperature distribution for case V. Colors show the temperature and streamlines represent the temperature gradients.....	119
Figure 4.80. Isotemperature surfaces for $T=308.15^{\circ}\text{K}$ ( $35^{\circ}\text{C}$ ) and above in case I. Arrows represent the temperature gradient. ....	120
Figure 4.81. Isotemperature surface for $T= 308.15^{\circ}\text{K}$ ( $35^{\circ}\text{C}$ ) and above in case II. Arrows represent the temperature gradient.....	121
Figure 4.82. Isotemperature surface for $T= 308.15^{\circ}\text{K}$ ( $35^{\circ}\text{C}$ ) and above in case V. Arrows represent the temperature gradient.....	122
Figure 5.1. Wiring example for stop Category 0 (courtesy of Kollmorgen) [73]. ....	125

Figure 5.2. Wiring example for stop Category 1 (courtesy of Kollmorgen) [73].	125
Figure 5.3. Wiring example for stop Category 2 (courtesy of Kollmorgen) [73].	126
Figure 5.4. Comparison between stop categories.	127
Figure 5.5. Dual-channel SIL CL2/PLd Cat3 STO control circuit for eight axes.	129
Figure 5.6. Hardware Enable control circuit for eight axes.	130
Figure 5.7. RTO intermittent circuit.	131
Figure 5.8. Logic ON-OFF and Emergency Stop circuits for the VT Roller Rig.	133
Figure 5.9. Regenerative Dynamic Braking circuit.	135
Figure 5.10. Typical connection for 3-phase PM motor for dynamic braking.	136
Figure 5.11. Motor-Short Dynamic Braking circuit.	138
Figure 5.12. Special sequence for switching off the output stage of the servo amplifier with the Holding Brake signal [73].	140
Figure 6.1. Node-to-node signaling in the Virginia Tech Roller Rig is full duplex.	146
Figure 6.2. An illustration of motor axis mapping concept.	147
Figure 6.3. Gantry axes of the VT Roller Rig (left: vertical, right: cant).	147
Figure 6.4. Gantry motion control scheme using two encoders.	149
Figure 6.5. Common motion control network topologies.	150
Figure 6.6. The Virginia Tech Roller Rig's control, power, and data acquisition architecture.	152
Figure 6.7. QMP-SynqNet-GB-PCIE-RJ motion controller.	153
Figure 6.8. Cable shield grounding at local nodes to prevent ground loop in the VT Roller Rig control loop (courtesy of Kollmorgen) [127].	154
Figure 6.9. SQIO communication through SPI serial busses. A digital module (DIN32DOUT32) and an analog module (ADC4DAC4) are cascaded to the SQID.	156
Figure 6.10. Current configuration of each data acquisition node on the VT Roller Rig SynqNet network.	157
Figure 6.11. The relation between background, foreground, and transmit times.	161
Figure 6.12. An example of the Roller Rig controller timing.	161
Figure 6.13. Objects used in the VT Roller Rig Motion Programming Interface.	164
Figure 6.14. MechaWare Simulink Plugin.	165
Figure 6.15. An overview of Roller Rig Motion Console user interface.	166
Figure 6.16. An overview of the Roller Rig Motion Scope user interface (data for lateral axis).	167
Figure 6.17. A snap-shot from the Roller Rig Bode Tool user interface (plant frequency response).	169
Figure 6.18. MechaWare schematic of PID servo algorithm in Torque Mode.	172

Figure 6.19. MechaWare schematic of PIV servo algorithm in Torque Mode. ....	173
Figure 6.20. MechaWare schematic of the position compensator in PIV servo algorithm. ....	173
Figure 6.21. MechaWare schematic of the velocity compensator in PIV servo algorithm. ....	174
Figure 6.22. MechaWare schematic of PID servo algorithm in Velocity Mode. ....	175
Figure 6.23. A snap-shot of Bode Tool ready for FFT measurement.....	177
Figure 6.24. Selecting the reference point for the Bode Tool Auto-tuner (plant frequency response). The simulated and measured open-loop responses are identical. ....	178
Figure 6.25. An example of acceptable Auto-tuning results using the Lead/Lag method. ....	179
Figure 6.26. Simulated and measured stabilities using PID (compare with Figure 6.25). ....	180
Figure 6.27. Simulated and measured stability in Nyquist plot.....	181
Figure 6.28. Multiple gain and phase margin in the bode plot. ....	182
Figure 6.29. Flowchart of PIV velocity fine tuning. ....	184
Figure 6.30. Instantaneous velocity error of the wheel axis at $91.553rpm$ .....	186
Figure 6.31. Instantaneous velocity error of the roller axis at $51.090rpm$ .....	187
Figure 6.32. Velocity control accuracy of the VT Roller Rig for the wheel axis at $91.553rpm$ with 90% probability band: $0.206rpm$ . ....	188
Figure 6.33. Velocity control accuracy of the VT Roller Rig for the roller axis at $51.090rpm$ with 90% probability band: $0.104rpm$ . ....	188
Figure 6.34. VT Roller Rig electronic-gearing architecture (the same holds for AKD-B00607). .....	191
Figure 6.35. VT Roller Rig electronic-gearing architecture with adjustable gear ratio (the same holds for AKD-B00607).....	192
Figure 6.36. Trapezoidal motion profile.....	193
Figure 6.37. S-Curve motion profile. ....	193
Figure 6.38. PID servo tuning with step behavior. ....	195
Figure 6.39. Positioning accuracy of the VT Roller Rig in a $20mm$ lateral motion at $22.52mm/s$ : $66.350\mu m$ error in motion, $5.398nm$ error at steady state.....	197
Figure 6.40. Positioning accuracy of the VT Roller Rig in a $20mm$ vertical motion at $19.3mm/s$ : $3.579\mu m$ error in motion, $8.567nm$ error at steady state.....	198
Figure 6.41. Positioning accuracy of the VT Roller Rig in a $20mm$ cant motion at $19.15mm/s$ : $17.79\mu m$ error in motion, $16.07nm$ error at steady state.....	199
Figure 6.42. Positioning accuracy of the VT Roller Rig in a $20mm$ AoA motion at $17.2mm/s$ : $21.14\mu m$ error in motion, $10.17nm$ error at steady state.....	200
Figure 6.43. Contact creep forces are reacted by the positioning system.....	202

Figure 6.44: The path for the contact forces to the ground includes two routes: one through the wheel bearings, and the other one through the motor mounting plate (force shunt). ..... 203

Figure 6.45: Top view of the Rig showing wheel and motor dynamometers installed under the wheel driveline. .... 203

Figure 6.46. Contact force measurement dynamometers consist of four triaxial sensors preloaded between two plates (left: motor, right: wheel)..... 204

Figure 6.47. Arrangement of loadcells in each dynamometer (courtesy of Kistler Holding AG) [102]. ..... 204

Figure 6.48. Accumulative baseline error of both dynamometers in X direction with no motion and wheel drive disabled ( $\sum F_x^{motor\ dyno} + \sum F_x^{wheel\ dyno}$ ). ..... 207

Figure 6.49. Accumulative baseline error of both dynamometers in X direction at *91.553rpm* ( $\sum F_x^{motor\ dyno} + \sum F_x^{wheel\ dyno}$ ). ..... 207

Figure 6.50. Force measurement accuracy of both dynamometers in X direction at *91.553rpm with 90% probability band* ( $\sum F_x^{motor\ dyno} + \sum F_x^{wheel\ dyno}$ ): *13.59N*. ..... 208

Figure 6.51. Accumulative baseline error of both dynamometers in Y direction with no motion and wheel drive disabled ( $\sum F_y^{motor\ dyno} + \sum F_y^{wheel\ dyno}$ ). ..... 208

Figure 6.52. Accumulative baseline error of both dynamometers in Y direction at *91.553rpm* ( $\sum F_y^{motor\ dyno} + \sum F_y^{wheel\ dyno}$ ). ..... 209

Figure 6.53. Force measurement accuracy of both dynamometers in Y direction at *91.553rpm with 90% probability band* ( $\sum F_y^{motor\ dyno} + \sum F_y^{wheel\ dyno}$ ): *11.48N*. ..... 209

Figure 6.54. Accumulative baseline error of both dynamometers in Z direction with no motion and wheel drive disabled ( $\sum F_z^{motor\ dyno} + \sum F_z^{wheel\ dyno}$ ). ..... 210

Figure 6.55. Accumulative baseline error of both dynamometers in Z direction at *91.553rpm* ( $\sum F_z^{motor\ dyno} + \sum F_z^{wheel\ dyno}$ ). ..... 210

Figure 6.56. Force measurement accuracy of both dynamometers in Z direction at *91.553rpm with 90% probability band* ( $\sum F_z^{motor\ dyno} + \sum F_z^{wheel\ dyno}$ ): *10.57N*..... 211

Figure 6.57. KiTorq measuring system comprising a KiTorq measuring flange and a KiTorq stator evaluation unit. Each torque flange is connected to the shaft via a torsion-proof multi-disk coupling [145,146]. ..... 212

Figure 6.58. Permissible shaft misalignments in the wheel and roller drivelines (courtesy of Kistler Holding AG) [146]. ..... 213

Figure 6.59. An example of torque measurements in the wheel axis of the VT Roller Rig (no motion and drive disabled). ..... 214

Figure 6.60. An example of torque measurements in the roller axis of the VT Roller Rig (no motion and drive disabled). .....	215
Figure 6.61. Wheel torque measurement in the VT Roller Rig at 91.553rpm constant speed. ...	215
Figure 6.62. Torque measurement accuracy of the VT Roller Rig for the wheel axis at 91.553rpm with 90% probability band: 4.94Nm. ....	216
Figure 6.63. Roller torque measurement in the VT Roller Rig at 91.553rpm constant speed. ....	216
Figure 6.64. Torque measurement accuracy of the VT Roller Rig for the roller axis at 51.090rpm with 90% probability band: 6.10Nm. ....	217
Figure 6.65. The control tower of the Rig includes S772 drives, AKD drives, regenerative and dynamic brake resistors, safety/control circuits, etc. All the components are placed inside a Faraday cage and are controlled through operator interface panel. ....	218
Figure 6.66. CAD model of the VT Roller Rig control cabinet. ....	220
Figure 6.67. Rear view of the VT Roller Rig control cabinet. ....	221
Figure 7.1. Typical incremental encoder disk (left) and absolute encoder disk (right, courtesy of Kollmorgen) [155]. ....	228
Figure 7.2. An example of how the high-frequency noise manifests itself in position and velocity data. ....	231
Figure 7.3. The effect of LPR on the resolution of encoders. ....	233
Figure 7.4. The effect CPQ on the resolution of encoders. ....	233
Figure 7.5. Difference between accuracy and resolution (courtesy of Kollmorgen) [156]. ....	234
Figure 7.6. Phase error with +0.1% offset in both signals A and B (courtesy of Texas Instruments) [167]. ....	235
Figure 7.7. Phase error with $(90 + 0.36^\circ)$ phase shift between signals A and B (courtesy of Texas Instruments) [167]. ....	235
Figure 7.8. Typical signal distortion due to cable capacitance (courtesy of Kollmorgen) [156].	236
Figure 7.9. Phase shift of $A_{TTL}$ to A due to hysteresis (courtesy of Texas Instruments) [169]. ...	236
Figure 7.10. Simplified diagram of encoder circuit in a digital drive ( $\times$ and $\div$ denote resolution change). ....	239
Figure 7.11. Absolute sine encoder connected to Kollmorgen S772 drive with EnDat 2.1 (courtesy of Kollmorgen) [73]. ....	242
Figure 7.12. Position DFT from 20s of rotation at a constant speed using ServoStar drive. The encoder type, motion profile, and user update rate are the same for Figure 7.12 and Figure 7.13. The receiving electronics, interpolation methods, and interpolation factors are different between Kollmorgen ServoStar and AKD drives. ....	247

Figure 7.13. Position DFT from 20s of rotation at a constant speed using AKD drive. The encoder type, motion profile, and user update rate are the same for Figure 10 and Figure 11. The receiving electronics, interpolation methods, and interpolation factors are different between Kollmorgen ServoStar and AKD drives. ....	248
Figure 7.14. Captured position at 2kHz update rate shows a peak 500Hz. The receiving electronics, encoder, and speed are the same between Figure 7.13, Figure 7.14, and Figure 7.15. ....	248
Figure 7.15. Captured position at 16kHz update rate shows multiple harmonics of 1500Hz. The receiving electronics, encoder, and speed are the same between Figure 7.13, Figure 7.14, and Figure 7.15.....	249
Figure 7.16. The noise is highly dependent on the speed of the shaft. Compare the speed and frequencies of this figure with those of Figure 7.15.....	249
Figure 7.17. Simulated encoder equivalent output for AKD drives with 16kHz user update rate when the shaft rotates perfectly at 457.76rpm. Compare this figure with Figure 7.15. ....	251
Figure 7.18. Simulated encoder equivalent output for AKD drives with 16kHz user update rate when the shaft perfectly rotates at 457.19rpm. Compare this figure with Figure 7.16. ....	252
Figure 7.19. Aliased encoder equivalent output for AKD drives with 4kHz user update rate. Compare this figure with Figure 7.13.....	253
Figure 7.20. Aliased encoder equivalent output for AKD drives with 2kHz user update rate. Compare this figure with Figure 7.14.....	253
Figure 8.1. Section cut of the AKM84T 3-phase permanent magnet AC synchronous motor (courtesy of Kollmorgen) [68].....	256
Figure 8.2. Four quadrant diagram for a servo system. ....	258
Figure 8.3. A typical motion profile and its relationship to motor torque in a frictionless servo system. ....	258
Figure 8.4. S772 servo amplifier for driving AMK84T AC servo motors (courtesy of Kollmorgen) [73]. ....	260
Figure 8.5. Cross-section of an EC4 linear positioning servo system with parallel motor mounting (courtesy of Kollmorgen) [180].....	261
Figure 8.6. Two hall-effect limit switches protect each EC4 linear actuator of the VT Roller Rig against jam conditions (courtesy of Kollmorgen) [180].....	262
Figure 8.7. Wiring diagram of PSN Hall-effect sensor to the servo amplifier (courtesy of Kollmorgen) [180].....	262
Figure 8.8. AKD-B00607 servo amplifier driving EC4 linear actuators (courtesy of Kollmorgen) [181]. ....	265

Figure 8.9. HPS Sentinel isolating transformer.....	266
Figure 8.10. Schaffner FN 258-100-35 filter and its block diagram (courtesy of Schaffner) [79]. .....	267
Figure 8.11. Typical filter attenuation of Schaffner FN 258 filters (courtesy of Schaffner) [79]. .....	268
Figure 8.12. Quint-PS/ 3AC/24DC/40 power supply and its block diagram (courtesy of Phoenix Contact) [182].....	269
Figure 8.13. Connection of Quint-PS/ 3AC/24DC/40 power supply to different mains networks (courtesy of Phoenix Contact) [182]. ....	269
Figure 8.14. Quint-UPS/ 24DC/24DC/40 and its block diagram (courtesy of Phoenix Contact) [80]. .....	270
Figure 8.15. UPS-BAT/VRLA/24DC/38AH power storage unit and its block diagram (courtesy of Phoenix Contact) [80]. ....	271
Figure 8.16. PR2-R 4PDT relay and its block diagram for the Logic ON-OFF circuit (courtesy of Phoenix Contact) [183].....	272
Figure 8.17. Connection of PNOZ S4 relay (left) and S11 contact expansion module (right) for emergency stop circuit (courtesy of Pilz Automation Safety) [184,185]. ....	273
Figure 8.18. Block diagrams of PNOZ S4 relay (left) and PNOZ S11 expansion module (right, courtesy of Pilz Automation Safety) [184,185].....	273
Figure 8.19. Configuration of PNOZ mm0.1p relay (center), S11 and S7.1 contact expansion modules for STO circuit (courtesy of Pilz Automation Safety) [186].....	274
Figure 8.20. Block diagrams of PNOZ mm0.1p relay (top), PNOZ S11 expansion module (left), and PNOZ S7.1 expansion module (right, courtesy of Pilz Automation Safety) [185–187]. ....	275
Figure 8.21. Block diagram and adjustable switches of the PNOZ S5 relay for Motor-Short Dynamic Braking circuit (courtesy of Pilz Automation Safety) [188].....	276
Figure 8.22. Block diagram and front view of the PNOZ S3 relay for the RTO circuit (courtesy of Pilz Automation Safety) [189].....	277
Figure 8.23. Time behavior of PNOZ S3, S4, and S5 solid-state safety relays (courtesy of Pilz Automation Safety) [184,188,189].....	279
Figure 8.24. BAS(U) 6000-10 Kollmorgen regenerative resistor. ....	281
Figure 8.25. Surface temperature of the regenerative resistors relative to continuous dissipation (courtesy of Kollmorgen) [190].....	281
Figure 8.26. Single CJT800 resistor. Each S772 servo amplifier requires a set of three. ....	282

# List of Tables

Table 3.1. Estimated constants for the rectifier, DC bus, braking chopper, and inverter used in SimPowerSystems model. ....	37
Table 3.2. Constants used in the three-phase sinusoidal model of the electrical system [68]. ....	38
Table 3.3. Performance specifications of gearhead. ....	41
Table 3.4. Material and geometric properties of the shafts. ....	42
Table 4.1. Minimum estimated power, voltage, and load requirement of the VT Roller Rig. ....	48
Table 4.2. Specifications for the VT Roller Rig isolating transformer. ....	51
Table 4.3. Technical data of 3-phase Schaffner FN 258-100-35 filters [79]. ....	53
Table 4.4. A summary of harmonics sequences. ....	70
Table 4.5. Electrical specifications of S772 and AKD digital servo drives [73,108]. ....	77
Table 4.6. Material properties of aluminum (Al), copper (Cu), Iron (Fe), carbon steel, and PVC. ....	81
Table 4.7. Material properties of air. ....	83
Table 4.8. Skin depth for some common materials [116]. ....	91
Table 4.9. Load factors for the first four buckling modes of the isolating transformer base structure. ....	102
Table 4.10. Results of the 5 case studies. ....	117
Table 5.1. Function of safety circuits in the VT Roller Rig. ....	127
Table 5.2. Possible servo amplifier status between STO and HW-Enable. ....	130
Table 5.3. Internal faults that cause the RTO contact to open. ....	132
Table 5.4. Iterative calculations for sizing motor-short dynamic braking resistors. ....	137
Table 6.1. SPI rate of different data acquisition modules. ....	156
Table 6.2. SPI delays for the VT Roller Rig data acquisition units depending on the SPI load. ....	157
Table 6.3. Update rate of digital servo drives used in the Virginia Tech Roller Rig. ....	159
Table 6.4. Network latency for each update rate. ....	159
Table 6.5. Comparison between common servo tuning methods [138]. ....	176

Table 6.6. A comparison between phase and gain margin versus stability measurement. ....	183
Table 6.7. Stability of the VT Roller Rig Axes. ....	183
Table 6.8. Velocity control accuracy of the VT Roller Rig after servo tuning. ....	185
Table 6.9. External encoders for providing input in electronic gearing. ....	190
Table 6.10. Comparison between Trapezoidal and S-Curve motion parameters. ....	194
Table 6.11. Positioning accuracy of the VT Roller Rig after servo tuning. ....	196
Table 6.12. Compensations for PID parameters at different controller update rates. ....	201
Table 6.13. Maximum estimated creep forces at the contact patch. ....	202
Table 6.14. Technical specification of piezoelectric triaxial loadcells [102]. ....	205
Table 6.15. Force measurement accuracy of the VT Roller Rig in three directions. ....	206
Table 6.16. Measurement specification of the Roller Rig torque measuring system (Including a KiTorq-4550A measuring unit and a KiTorq-4542A evaluation unit) [103,145]. ....	212
Table 6.17. Permitted misalignments in the wheel and roller multi-disk couplings. ....	213
Table 6.18. Torque measurement accuracy of the VT Roller Rig for the wheel and roller axes. ....	214
Table 7.1. Dedicated Serial Interfaces. ....	230
Table 7.2. Analysis of Phase Error Examples [167]. ....	235
Table 8.1. Technical data of AKM84T 3-phase permanent magnet AC synchronous motor [68]. .....	257
Table 8.2. Technical data of S772 digital servo amplifier [73]. ....	259
Table 8.3. Technical data of AKD-B00607 servo amplifier [181]. ....	264
Table 8.4. Technical data of HPS Sentinel isolating transformer. ....	266
Table 8.5. Technical data of 3-phase Schaffner FN 258-100-35 filters [79]. ....	267
Table 8.6. Technical data of Quint-PS/ 3AC/24DC/40 power supply [182]. ....	269
Table 8.7. Technical data of Quint-UPS/ 24DC/24DC/40 switchover unit [80]. ....	270
Table 8.8. Keywords used for describing the time behavior of the solid-state safety relays. ....	280
Table 8.9. Technical data of CJT800 dynamic resistors [191]. ....	282
Table 8.10. Technical data of LC1D40ABD 3PST-NO contactor [192]. ....	283
Table 8.11. VT Roller Rig fuses and circuit breakers. ....	284

# Chapter 1. Introduction

## 1.1 Motivation

A review of current roller rigs [4] indicated that many desired functional requirements for studying contact mechanics are not available. Benefiting from the state-of-the-art technologies available in motion control, instrumentation, data acquisition, system integration, and safety, it is possible to bring a new level of accuracy, consistency, and flexibility to the field of railway vehicle dynamics and contact mechanics. Piezo-electronics, micro-electromechanical systems, laser/LIDAR sensors, thermal IR cameras, and ultrafast vision systems have introduced revolutionary different sensory systems that could pave the way towards better measuring the phenomena that occur between a railcar's wheel and rail. Recent breakthroughs in ultrahigh-clock microprocessors, combined with unified communication protocols between sensors, data acquisition systems, software suites, and servo controllers allow for implementing a new generation of hardware-in-the-loop operations that supersede all previous efforts in accuracy, data volume, and analogy to real working conditions.

Modules for data acquisition, transfer, and storage have never been this efficient and smart. Data mining, neural network algorithms, and pattern recognition methods are readily available to process hundreds of channels of synchronized data at tens of kilohertz to find unforeseen patterns and trends. Image processing tools allow for incorporation of high-speed cameras to visually inspect the experiments at the wheel-rail contact with magnifications that have never been this high. These tools can extract tremendously valuable information from the images taken from the contact patch. Actual shape and size of the contact patch at each working condition is only one of the many features that such system can provide.

Only one of the major railroads spends more than \$2B on the maintenance of wheels and tracks every year. Railroads are investing significant funds on studying the effect of friction modifiers, non-destructive structural health monitoring systems, and online track-wheel fault detections to reduce the cost of maintenance. A fully equipped test rig that can afford all required tests in a consistent and repeatable manner can have significant contributions to the optimization of railway

designs and solutions. As a result, Virginia Tech's Railway Technologies Laboratory (RTL) embarked on a mission to develop a state-of-the-art testing facility that incorporates the cutting edge technologies to allow for experimental testing at the wheel-rail contact interface for railway applications.

The design goals for the VT Roller Rig are:

- Precise control of the relative position and velocity of the wheel and rail
- Real time adjustment of wheel-roller configuration including angle of attack, cant angle, lateral displacement, and vertical loading
- Accurate measurement of the contact forces, moments, driveline torques, and accelerations
- High bandwidth for measurements and data collection
- Repeatable measurements with maximum signal to noise ratio
- Compatible with commercial multi-body dynamics modeling tools and vehicle performance simulators for performing hardware-in-the-loop operations
- Provisions for measuring contact geometry, synchronized with force, torque, moments, displacement, acceleration, and position measurements

### 1.2 Objectives

This research was conducted at the Center for Vehicle Systems and Safety of Virginia Tech in accordance with the guidelines set by the Federal Railway Administration. The aim of this project was to design and development of a unique testing facility for studying railway dynamics and contact mechanics. This complex project was achieved through satisfying all of the following objectives:

- Electromechanical design and development of a state-of-the-art testing facility from scratch that can provide the infrastructure for a broad range of accurate measurements of the wheel-rail contact mechanics and dynamics
- Commissioning the Rig and performing a series of contact mechanics and dynamics experiments
- Developing a flexible motion programming interface that is compatible with common programming languages, analytics software, and commercial multi-body dynamics simulators
- Ensuring precision and repeatability of the measurements by taking possible undesired vibrations and noise coupling mechanisms into account

- Ensuring maximum safety for the users and machinery, while keeping the costs within the available budget and conforming to the international and local standards
- Providing the means for performing hardware-in-the-loop operations

### 1.3 Approach

The general approach to satisfying the goals of the project involved the following tasks:

- Identify the system requirements, design objectives, and available resources
- Perform required analyses, modeling, and calculations for understanding the differences between possible solutions
- Design and develop the electromechanical components of the Rig
- Ensure satisfaction of engineering and safety requirements through design reviews with experts in automation, system integration, and motion control
- Optimize the designs for including the unique features of the Rig such as hardware-in-the-loop operation, contact geometry measurement, and flexible motion programming interface
- Select the most cost effective options for the available components, suppliers, and contractors
- Perform individual evaluations for assuring the quality of implemented/fabricated subsystems
- Integrate the sub-systems into the final VT Roller Rig system
- Evaluate the performance of the designed sub-systems when integrated with other mechanical components
- Characterize the entire Rig through experimental testing
- Commission the Rig and start gathering data
- Analyze the experimental data for quantifying the system performance

### 1.4 Contributions

The VT Roller Rig can have significant contributions to both academic and industrial aspects of railroad engineering. The major contributions thus far are:

- Development of a state-of-the-art testing facility for evaluating contact mechanics and dynamics experiments

- Providing the following unique features to the railway researchers:
  - Accurate control of wheel-rail creepage
  - The electromechanical test setup for measuring the contact forces and moments with an unprecedented level of accuracy
  - Dynamic adjustment of wheel-rail configurations for simulating possible working conditions
  - Ultra-high servo update rates for performing hardware-in-the-loop operations
  - Flexible motion programming interface for interacting with existing vehicle performance models
  - Real-time measurement of contact geometry using vision processing systems
  - Synchronized measurements of force, moment, torque, displacement, velocity, acceleration, and contact geometry
- Providing the means for experimental evaluation of the influence of various conditions, such as wheel-rail configuration, third-body layers, and worn wheel-rail, on the wheel-rail contact mechanics

### 1.5 Outline

This document is divided into 11 chapters. Chapter 1 discusses the motivation and objectives of this project. It also provides an overview of the approach towards fulfilling the research goals.

Chapter 2 provides a background and literature review on the past and existing roller rigs. It also introduces the VT Roller Rig and its capabilities. More details about the configuration of the Rig is also provided.

Chapter 3 discusses the details of various vibration analyses and electromechanical modeling that have been performed for optimizing the powertrain design and contact measurements of the Rig. These analyses provided a better understanding of the system multi-body dynamics, in particular as the mechanical and electrical components interact with each other.

In Chapter 4, the design of power architecture for driving the Rig is described. Mains network, power filtering and isolation, as well as DC power system, comprise this chapter. Electromagnetic interference, grounding, thermal management, and development of required structures are also inherent to the interdisciplinary design of the power system for the VT Roller Rig.

Multiple layers of safety circuits and monitoring systems ensure safety for the users and machinery against 200A hot lines at 480VAC, and large inertia rotating at 350rpm. Chapter 5 thoroughly

explains the circuitry, responsibilities, and communications of these systems. This chapter is an essential resource for future users of the Rig.

Chapter 6 reports the commissioned capabilities of the VT Roller Rig. This chapter covers various deliverables including high bandwidth motion control, velocity control for creepage regulation, wheel-rail relative positioning for emulating field conditions, measuring contact forces and moments, driveline torque measurements, and flexible motion programming interface.

Chapter 7 presents an invention related to the discovery of a new type of error in digital drives that control the position of a motor after processing the data from a feedback device. In one embodiment, this invention provides the methods for identifying quantization error in encoder equivalent output generated by the control drive. In another aspect, this innovation allows for estimating the noise harmonics in the encoder equivalent output. In this chapter, a method is provided for adjusting the accuracy of estimations at the expense of computational load to adapt the estimator for filtering the output in the drives. This invention provides the means for adapting, learning, or adjusting the existing filtering techniques while the drive is operating. This is only possible using the train data generated by the proposed deterministic noise estimator for de-noising the drive output

Chapter 8 summarizes the fundamentals of component selection for various systems of the Rig. A thorough understanding of the limitations, block diagrams, wirings, and behavior for each element is essential before making any modification to the systems described in previous chapters.

Various tests are realizable with the delivered VT Roller Rig. Few of these fields of research are summarized in Chapter 9. References, and Appendices provide some additional useful resources.

## Chapter 2. Background

The controlled laboratory environment allows for better understanding the wheel/rail dynamics in various working conditions. Roller rigs are essential laboratory equipment for performing accurate and repeatable studies in different aspects of railway vehicle systems [5,6]. Some have been used to validate the existing theories in railway vehicle dynamics [7], while others focused on improving rail vehicle performance in a variety of applications, including but not limited to traction, braking, derailling, and turning [7–10]. Development of first roller rigs dates back to early 20<sup>th</sup> century, for testing locomotive systems in a laboratory environment [11]. Since then, roller rigs have been playing a vital role in replicating and studying wheel-rail dynamics. Various full-scale [12–14] and scaled rigs have been developed to perform repeatable tests in a controlled manner, using various sensors and data acquisition systems that often cannot withstand the harsh environments in the field. The following section provides a brief review of the most well-known roller rigs, followed by the introduction of the VT Roller Rig and its capabilities.

### 2.1 History

#### 2.1.1 Full-Scale Rigs

One of the most well-known roller rigs was developed at the Railway Technical Research Institute, Japan in 1957. This two-axle roller was used for simulating track irregularities, vibrations<sup>1</sup>, hunting, derailment, and regenerative braking [5,7]. A 500kW DC motor ran each axle at up to 500km/h under 200kN maximum axle load. The rig could accommodate 1000 to 1676mm gauge,  $\pm 30$ mm lateral displacement, and  $\pm 12$ mm vertical displacement. The rig was in operation for more than 3 decades and made a significant contribution to the development of Shinkansen bolsterless high-speed bogies [7,15].

The German Federal Minister of Research and Technology developed a four-axle roller rig in 1977 for performing a broad range of studies including stability, ride comfort, failure analysis, and

---

<sup>1</sup> The rig was renovated in 1989 for vibration studies.

actively controlled bogies. Two DC motors drove the four axles such that left and right rollers turned at the same speed, therefore, the rig was only suitable for straight track experiments. The rig was equipped with various hydraulic actuators for simulating track irregularities under 100kN at up to 500 km/h speed. A significant accomplishment of this rig compared with its predecessors was capturing up to 120 data channels with its data acquisition unit that allowed for measuring and monitoring many more parameters simultaneously [16,17].

In 1978, a four-axle roller rig facility was developed at the Transportation Technology Center, Inc. (TTCI), USA for testing locomotives traction efforts, as well as vehicle dynamics of passenger cars, and non-powered vehicles [18]. It was equipped with four 600hp drivetrains that could run the axles at the maximum speed of 230km/h. The rig could accommodate tangent track simulations, but did not allow for lateral or vertical irregularities or curving experiments [19,20].

During 1980's, The National Research Council, Canada developed a two-axle roller rig for optimizing bogie designs and wear tests. A main motor was responsible for rotating both left and right rollers, while a differential motor would adjust the gear ratio of a differential gear system to allow for differential speeds between the rollers. Therefore, the rig was capable of simulating curving conditions. It was also equipped with constant velocity couplers that allowed for canting the rollers [21–23]. The design of this rig evolved into a single-axle rig for studying wheel-rail wear tests, the effect of contaminations such as water and grease on brakes and bearings, and general contact mechanics. This rig could provide up to 350kN vertical load on the wheels rotating at up to 135km/h. It could simulate the application of partial, normal or emergency brakes, while third-body layer materials were added to the wheel-rail contact [24,25].

In 1992, The Ansaldo Transport Research Center in Naples, Italy, developed a four-axle roller rig for studying traction effort of locomotives during transient states. The rig could accommodate up to 300km/h speed of 1.4 to 3.5m bogies, with maximum traction force of 100kN [18]. The rig did not allow for speed differentials between the two rollers, therefore, it could only simulated straight track conditions. Driving motors were connected to the drivelines directly, without any intermittent speed reducer, and that allowed for controlling the speed of the drivelines directly through the motors.

One of the first prominent efforts towards developing full-scale rigs was in 1995 that led to the development of a four-axle<sup>2</sup> roller rig at the State Key Laboratory of Traction Power in Southwest Jiaotong University, China. It was mainly used for conducting basic research on hunting stability,

---

<sup>2</sup> Further extended to six axles

braking, traction, derailment mechanism, and vibration analysis. The rig was capable of running two rollers at adjustable speeds up to 450km/h. Each axle was driven by a DC motor, double-articulated universal joints, and four cone gearboxes, while a differential gearbox set the speed differential between them during curving [18]. Therefore, the rig was capable of simulating straight and curved track with a minimum curve radius of 200m. The rig was equipped with hydraulic actuators that could adjust the vertical, lateral, yaw, and cant angle (max 7°) of each roller set. Results of studies performed with this rig on different contact surface conditions, as well as creep curves at different longitudinal velocities and axle loads are available in the literature [14,26,27].

In the 2000's, the Voestalpine Schienen GmbH, Austria introduced a single-wheel roller rig for studying rail wear and rolling contact fatigue (RCF). This rig is a departure from the previous full-scale rigs since it uses a short straight piece of track as the rail instead of a roller. As the wheel rotates, hydraulic cylinders move the rail back and forth at a maximum speed of 0.5m/s. The rig is equipped with other actuators for applying the vertical and lateral loads to the wheel-rail contact, as well as adjusting the cant and angle-of-attack parameters for simulating curving. Contact forces are measured indirectly from the pressures within the hydraulic cylinders [13].

### 2.1.2 Scaled Rigs

During the 1950's, The Railway Research Institute in Japan developed two of the first scaled roller rigs. These 1/5<sup>th</sup> and 1/10<sup>th</sup> scale rigs were primarily designed to improve the rail vehicle suspensions [7]. Contemporary to that, C&O-B&O railroad developed a 1/10<sup>th</sup> scale roller rig in the United States for studying lightweight railcars [25]. Those efforts were evolved into a more precisely designed 1/5<sup>th</sup> scale rig in the 1970's at the Princeton University.

During 1980's, The National Research Council, Canada developed a single-axle 1/8<sup>th</sup> scale roller rig for performing various wheel-rail wear studies. The rig was constituted of two top discs representing the wheels, and two bottom discs representing the rollers. The bottom discs were driven by 20hp adjustable speed motors. The wheelset bearing assembly would allow for vertical, lateral and rail cant movements, while its rigid movable support could adjust the yaw motion. The flexure pivot arms and load cells in the support assembly measured the longitudinal forces and two load cells in the rail disc cantilever support assemblies measured the lateral and vertical loads [28,29].

In about the same time, the Institut National de Recherche sur les Transports et leur Sécurité (INRETS)<sup>3</sup>, developed a roller rig that is mostly known due to its large diameter of rollers (13m) with UIC60 rail profiles. That size roller allowed for performing tests at up to 250km/h equivalent full-scale speed. It also made the wheel-roller contact condition closer to those on tangent tracks. A 1/4<sup>th</sup> scale bogie was used for performing the tests. The rig was equipped with pneumatic actuators for adjusting the vertical load on the wheels. The rig was used for performing various tests, from which calculation of Kalker's coefficients is one of the most important ones [30].

The German Oberpfaffenhofen, currently a major site of the German Aerospace Center, developed a two-axle 1/5<sup>th</sup> scale roller rig in 1984. The rig was developed based on the dual disc on disc concept. A DC motor drove the axles at up to 1100rpm (full-scale equivalent speed of 75km/h) via toothed belts. The left and right 360mm diameter rollers were connected to each other with a rigid shaft. This rig was primarily used for improving bogie and wheel designs, software models, and limit cycle behaviors [6,31].

In 1992, the Manchester Metropolitan University developed a two-axle 1/5<sup>th</sup> scale rig for optimizing suspension designs as well as single wheels and performing wheel-rail wear studies. A DC motor was used to drive the rollers at full-scale equivalent speed of 400km/h via belt and pulleys. The left and right rollers are connected to each other with splined and hooked joint shafts. Hydraulic actuators allowed for actively controlling the lateral movement of the rollers as well as their yaw motion [32,33].

The Czech Technical University, Czech Republic, developed a two-axle 2/7<sup>th</sup> scale roller rig in 1990's for measuring contact forces and testing active steering mechanisms for wheelsets. A 5.5kW asynchronous motor was used to drive the 0.5m diameter rollers at up to 700rpm (the equivalent of 230km/h full-scale speed). A differential gearbox between the left and right rollers was used to actively control the speed differential between the two rollers for simulating curving conditions. A secondary servo drive system was responsible for controlling the yaw motion of the wheelsets. A slew of 16 strain gauges on the rollers was used for measuring the contact forces [34–36].

The Sheffield University, England, developed a single-wheel roller rig in 1995 for conducting various fatigue, wear, and third-body layer (water, oil, soil, etc.) experiments. Creep analyses have also been performed using this test setup. However, it only provided longitudinal creepage. A 7.5kW AC induction motor rotated the roller at up to 1600rpm, independent of the wheel. A secondary motor adjusted the speed of the wheel according to the desired creepage profile. A

---

<sup>3</sup> Former French national institute for transport and safety research

hydraulic actuator below the pivoted bearing of the roller driveline, provided up to 29kN vertical load to the wheel-rail contact. The rig was equipped with an Eddy current probe for scanning the wheels for cracks. This rig did not allow for any cant or yaw adjustments [37–39].

In early 2000's Politecnico di Torino in Italy introduced a two-axle 1/5<sup>th</sup> scale roller rig for studying wheel-rail wear and dynamic analysis of railcars. Two permanent magnet AC servo motors drive the left and right rollers independently. Therefore, the Rig is capable of simulating the conditions during curving. It is equipped with mechanisms for adding third-body layer materials at the wheel-rail contact. A slew of sensors including load cells, accelerometers, torque sensors, encoders, and laser displacement sensors capture the experiments [40–42].

Contemporary to the efforts in Italy, National Traffic Safety & Environment Laboratory, Japan, developed a single-axis 1/5<sup>th</sup> roller rig for studying creep forces between wheel and roller in various configurations. Two AC induction motors are used to drive the left and right 0.86m-rollers independently with a high degree of precision (0.03rpm). Motors can provide up to 700Nm for rotating the rollers at a maximum speed of 312.5rpm [43].

In about the same period, Jiaotong University in China developed a two-axle 1/4<sup>th</sup> scale roller rig for performing various tribological studies such as wheel-rail wear, fatigue, and corrugation. On each axle, one electric motor rotates the left and right rollers, while another electric motor rotates the wheels independent of the first one. The rig is equipped with hydraulic actuators for applying normal loads [44,45].

In 2003, Research Centre of Firenze Osmannoro in Italy introduced its modern two-axle 1/4<sup>th</sup> scale<sup>4</sup> roller rig for conducting hardware-in-the-loop operations to test various onboard safety systems such as traction/stability control, wheel slide protection, and automatic train protection. Two electric motors drive the 0.5m rollers at up to 200km/h equivalent full-scale speed. The rig is equipped with two auxiliary motors for testing bogies with independent wheels [26,46–48].

The Seoul National University of Science and Technology, Korea, developed a two-axle 1/5<sup>th</sup> scale roller rig in 2011 for studying derailment. A 3.7kW AC motor rotates the 0.45m diameter rollers at up to 1150rpm. The motor shaft is connected to the rollers with belts and pulleys, which allows for incorporation of other actuators for adjusting the cant angle, angle-of-attack, and wheelbase. This rig is being used for investigating stability and wheel-rail dynamics experiments [49,50].

---

<sup>4</sup> The same institute developed a full-scale version of the same rig too.

The review of current roller rigs [4] indicates that many desired functional requirements for studying contact mechanics are not available. Benefiting from the state-of-the-art technologies available in servo motion, instrumentation, data acquisition, systems integration, motion monitoring and safety, it is possible to bring a new level of accuracy, consistency, and flexibility to the field of wheel-rail contact mechanics and dynamic. Recent breakthroughs in ultra high clock microprocessors, combined with unified communication protocols between sensors, data acquisition systems, software suites, and servo controllers allow for implementing a new generation of hardware-in-the-loop operations that supersede all previous efforts in accuracy, data volume, and analogy to the real working conditions. Piezo-electronics, micro-electromechanically systems, laser/LIDAR sensors, thermal IR cameras, and ultrafast vision systems have introduced revolutionary different sensory systems that could pave the way towards a better understanding of the wheel-rail dynamics and contact mechanics. Systems for data acquisition, transfer, and storage have never been this efficient and smart. Data mining, neural network algorithms, and pattern recognition methods are readily available to process big data taken from data acquisition systems to handle hundreds of channels of data at tens of kilohertz, and find unforeseen patterns and trends. Image processing tools allow for incorporation of high-speed cameras to visually inspect the experiments at the wheel-rail contact with magnifications that have never been this high. These highly efficient tools can extract tremendously valuable information from the images taken from the contact patch. Actual shape and size of the contact patch at each working condition is only one of the many features that such system provides.

Only one of the major railroads spends more than \$2B annually on the maintenance of wheels and tracks. Now that major railroads are investing significant funds on the effect of friction modifiers, non-destructive structural health monitoring systems, and online track-wheel fault detection, no instrument can better contribute to the optimization of upcoming novel designs and solutions more than a fully-equipped test rig that can afford all required tests in a consistent, repeatable manner. As a result, the Virginia Tech's Railway Technologies Laboratory (RTL) embarked on a mission to develop a state-of-the-art testing facility that incorporates the cutting edge technologies to allow for experimental testing at the wheel-rail contact interface for railway applications.

### 2.2 Virginia Tech Roller Rig

A scaled vertical roller rig is developed at the Virginia Tech's Railway Technology Lab (RTL). The VT Roller Rig is aimed to shed more light on the wheel/rail contact mechanics with an unprecedented level of accuracy. The rig is comprised of a wheel and a roller that simulate the

single-wheel/rail interaction. The test rig is one-fourth scale, surrounded by control and sensory systems [51]. In a vertical configuration, the scaled wheel with AAR-1B profile and 8” diameter, is placed on a roller that has the scaled profile of US136 rail. The roller that simulates the rail is five times (40”) the wheel. The scaling factor and roller/wheel diameter ratio are selected such that the Rig remains within the available budget, and also any distortion at the contact patch is minimized [51].

The rig is equipped with two independent, direct drivelines that provide the required power to drive the wheel and roller as well as precisely control the differential speed at the contact (creepage). Each driveline is driven by an independent AC servo motor. The rolling rail is powered to rotate the wheel up to a specified speed, where steady state testing is performed. Based on the 1/4<sup>th</sup> scaling factor, the design speed for the VT Roller Rig is 10mph, which corresponds to 330.8rpm for the wheel and 73.5rpm for the roller. Using a 5:1 gear ratio for the wheel and 28:1 gear ratio for the roller, the maximum motor speed is found to be 2058RPM.

Also, the VT Roller Rig is equipped with positioning mechanisms to replicate real working conditions in railway vehicles. Six linear actuators allow for adjusting the simulated load, the angle of attack, rail cant, and lateral displacement at the wheel-rail interface using state-of-the-art motion control technologies.

The controlled laboratory environment will provide a successful path for accurately measuring creepage, and creep forces in various conditions. This is essential for better understanding the fundamental wheel-rail contact mechanics and dynamics, and provide more accurate parameters for rail dynamics modeling. A slew of sensors measure the contact parameters including, but not limited to:

- Force
- Torque
- Moment
- Displacement
- Angular rotation
- Speed
- Acceleration
- Contact patch geometry

Incorporated into each driveline, a torque sensor measures the instantaneous shaft torque and speeds. Two dynamometers are configured to measure the contact forces and moments accurately.

One is mounted in line with the contact patch plane, and the other one is mounted under the powertrain to account for any potential force shunt through the motor housing structure. These dynamometers outperform off-the-shelf wheel force transducers that are common in tire applications.

A unified communication protocol between the sensors, data acquisition systems, and actuators minimizes data conversion time, which allows for servo update rates up to 48kHz. This provides an unmatched bandwidth for performing vibration analyses that are accounted as contributors to wear, noise, and RCF [1]. As shown in Figure 2.1, the Rig configuration accommodates the addition of third-body layers at the wheel/rail interface for studying the effects of surface conditioning elements. Extensive instrumentation and motion control systems of the Rig, along with multi-layer safety systems, allow for investigating phenomena such as derailment and flanging. Flexible motion programming interface of the Rig is compatible with the majority of commercial rail vehicle dynamic simulators for performing hardware-in-the-loop operations. The immediate benefits from HIL are advanced train control algorithms and better traction/braking procedures. Further details about the design and components of the Rig can be found in [2] and [3].

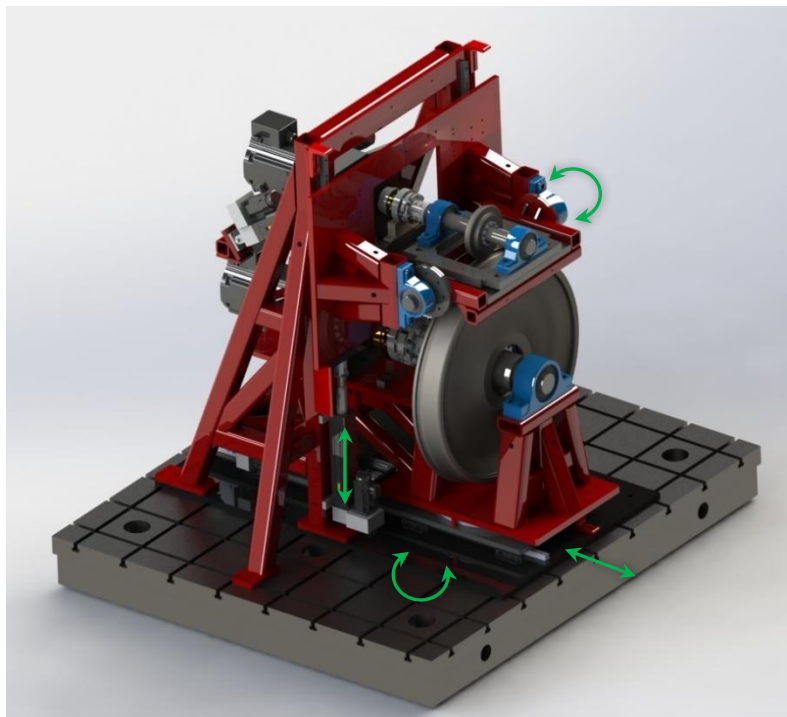


**Figure 2.1. The final design of the VT Roller Rig. Arrows indicate the adjustable degrees of freedom.**

## 2.3 Virginia Tech Roller Rig Configuration

As Figure 2.1 shows, the main mechanical components of the test rig are:

- Scaled wheel and roller
- Drivelines that include shafts, bearings, couplers, and torque sensors for connecting motors to the wheel and roller
- Positioning mechanisms for adjusting the relative position of the wheel and roller with high degree of precision
- The load frame that all components are attached to it
- A base plate for providing rigid flat basement for the frame

Electromechanical subsystems of the Rig include:

- Two AC servo motors for driving the wheel and roller
- Power electronics that include mains power network, power isolation and filtering, DC power, and DC bus
- Grounding and shielding mechanisms for minimizing electromagnetic noise coupling
- Thermal management systems for maintaining the temperature of the power electronics below standard/manufacturer regulations
- Safety and monitoring circuits that include Safe-Torque-Off, Hardware Enable, Ready-to-Operate, Logic ON-OFF, Emergency Stop, Dynamic Braking, and Holding Brake (static)
- Instrumentation, motion control and sensory systems including command and feedback network, data acquisition systems, electronic gearing, motion programming interface, and control tower
- Unified user interface that allows full control of the system while isolating the user from hot lines, significant kinetic energy, and radiations

Details about the mechanical hardware development are available in [52]. A brief description of these components is provided below. The rest of this document provides the detailed discussions on design, optimization, development, and fabrication of the electromechanical subsystems.

### 2.3.1 Mechanical Components of the VT Roller Rig

One of the most important design goals of the VT Roller Rig is accurately controlling the differential speed between the wheel and the roller (creepage). Two independent direct drivelines rotate the wheel and roller with accurately controllable motions. Each driveline is driven by a

permanent magnet AC synchronous 3-phase servo motor. To deliver the motor torques to the wheel and roller, two planetary gearboxes are directly face-mounted on the motors. The gearheads are bolted to a mounting bracket, and a jack-screw anti-vibration mechanism takes the weight of each cantilevered motor and gearhead assembly. The output of these heavy-duty and low-backlash gearboxes are rotating flanges that are directly connected to torque sensor flanges. Details about these servo motors can be found in Section 8.1 of this document.

Each torque sensor consists of a rotor and a stator unit. The rotor captures the torques using strain gauges at 35kS/s sampling rate. The stator unit supplies power to the rotor and amplifies the generated signals. It also has integrated circuitry for measuring the speed. More extensive discussion on the driveline configuration of the VT Roller Rig is available in Section 3.1 of this document.

Two shafts made of 1045 carbon steel connect the torque sensor couplings to the rotating bodies, through spherical bearings. Two spherical roller bearings hold the rotating shaft in each driveline (4-inch roller shaft and 3-inch wheel shaft). Two heavy-duty keyless bushings are used to secure the wheels on the shafts. Keyless bushings allow for simple installation, as well as easily replacing the wheel and roller due to wear or for testing other head profiles.

A unique command and feedback network allows for controlling the motions of wheel and roller dependently or independently in velocity and torque modes. Extensive discussion on these power/motion control circuits is available in Sections 6.1 and 6.2 of this document.

The VT Roller Rig is capable of adjusting the wheel-rail relative position in real time. Linear actuators provide the actuation forces for the positioning mechanisms. Details about these actuators can be found in Section 8.2 of this document.

The angle between the plane of the wheel and the track plane (roller plane in the case of VT Roller Rig) is known as the angle-of-attack (AoA). AoA is a major factor in the interaction between wheel and rail, as it determines the lateral and spin creepage. There are various theories on the AoA-based derailment, wear, and noise available in the literature. Testing these theories requires a rigid adjustable setup covering a broad range of AoA values [53–55]. A cross roller ring underneath the roller bearing posts provides accurate rotation around the vertical axis that the center of contact patch and center of the cross roller ring. It takes all radial, axial, and moment loads and makes the AoA adjustments possible with the least amount of actuation force. The actuation force is provided with a linear actuator that is secured to the bottom plate of the cross roller ring.

The distance between the plane of wheel and plane of rail as they are in parallel with each other is called lateral distance. Due to conicity of the wheels, lateral displacement of a wheelset on the track changes the effective turning wheel radii on both sides and therefore causes a speed difference between the left and right wheels. As a result, lateral displacements play a vital role in the dynamic stability of wheelsets on the track. Underneath the cross roller ring of the VT Roller Rig, two linear guides allow for relative motion between the bottom plate of the cross roller ring and a 1-inch thick plate underneath the entire rig. They take the vertical and longitudinal contact forces and provide a low friction lateral motion. One linear actuator provides the actuation force for moving the cross roller bottom plate on the 1-inch bottom plate.

The difference between the elevation of left and right rails is called superelevation. Superelevation causes an inclination in a moving wheelset from the vertical line on the rail. This angle is often referred to as cant angle and plays a major role in the dynamic stability of the railcar around a curve. The VT Roller Rig is equipped with a simple mechanism for accommodating cant angle adjustments. A cradle holds the wheel and its entire driveline while being supported on two aligned shafts on the sides that share their central axes with the contact patch. Rotation of this cradle around the shaft axes changes the cant angle between the wheel and roller. Therefore, cant angle adjustment is possible through moving the wheel and its entire driveline. The cradle is made of  $3 \times 3 \times 3/8$ " steel tubing to provide enough rigidity for holding the wheel driveline. Two linear actuators on the sides of the sides of the cradle actively control the cant angle of the VT Roller Rig.

The vertical positioning mechanism allows for adjusting the vertical load on the wheel and roller. Similar to the lateral positioning mechanism, two linear guides are mounted on a 1-inch thick steel plate in front of the load frame. The wheel cradle is supported on this plate. Therefore, the motion of the plate changes the vertical distance between the wheel and roller. Two linear actuators provide the required force for moving the front panel and its attached components vertically.

The load frame of the Rig takes all the contact forces with minimum deflection while accommodating for the powertrains and positioning mechanisms. It is made of  $4 \times 4 \times 3/8$ " low-carbon steel tubing in a triangular form. Low-carbon tubing provides the highest rigidity to mass ratio while maintaining the cost of material within the acceptable range. The triangular structure ensures the required rigidity of the load frame without adding to the footprint of the Rig or limiting the access to rig components. Finite element analyses on the load frame showed that maximum deflection of the frame under designed working loads would not exceed the permissible numbers for the linear guides and bearings. Moreover, FEM modal analyses confirmed that first natural frequency of the load frame is 95 Hz in side bending mode, which is well above the frequencies of

interest in railway dynamics and contact mechanics tests [3]. Figure 2.2 shows the final fabricated frame of the VT Roller Rig.



**Figure 2.2. Final frame of the VT Roller Rig at machine shop.**

A cast-iron T-slotted base plate, filled with non-shrinking grout, provides a rigid flat basement for the frame and the lateral linear guides underneath the roller structure with a top surface flatness accuracy of  $\pm 0.03\text{mm}$ . It takes all the loadings and isolates the Rig from surrounding vibrations and mechanical noises. The load frame and linear guide plates are secured to the base plate via T-slots. The base plate is anchored to the 6-inch floor of the CVeSS facility via ten 1.5-inch anchors.

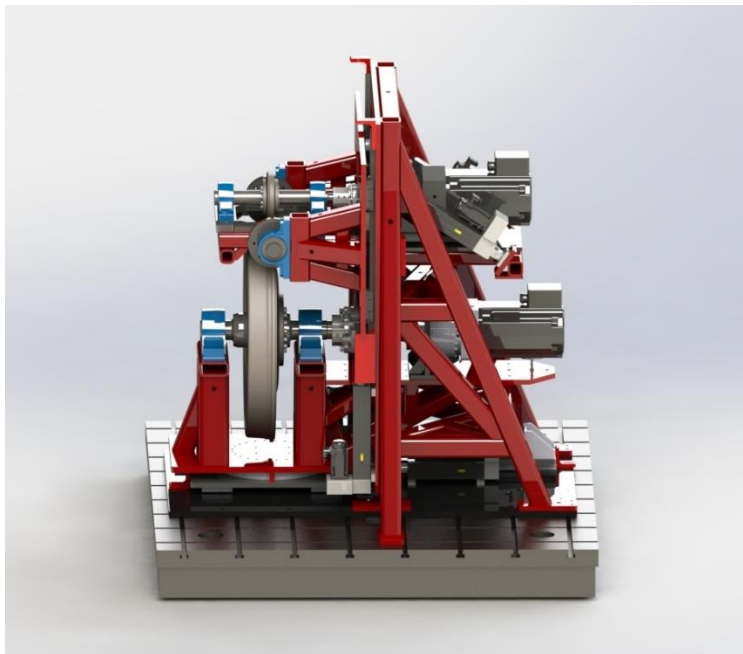


**Figure 2.3. Lateral view of the VT Roller Rig showing motors, drivelines, roller and wheel.**

The electrical inductances, resistances, and back EMF of the motors determine the relationship between the electrical currents supplied to the motors from the power supplies and the torque and velocity that the motors apply to the wheel and roller. The dynamics of the rotating bodies to the motor torque is affected by their rotational inertia, damping, and frictional losses. The rotation of each motor is dictated by the driving voltage and contact forces at the interface between the wheel and roller (contact patch). Conversely, the contact patch forces and moments are directly affected by the internal dynamics of the AC servo motors and drivelines, particularly during acceleration and deceleration. Therefore, a thorough understanding of the internal dynamics of the motors, as well as the drivelines, is vital for assuring the accuracy of measurements. An important step in the design and development of the powertrains is understanding the dynamics of the motors and drivelines, in particular as they interface with other subsystems. On the other hand, it is essential to make sure that the measurements are only due to the particular subject of study and not any intermittent source of disturbance. Sections 3.1 and 3.2 provide two vibration analyses towards designing the powertrain of the Roller Rig and compensating for undesired vibrations due to unbalanced rotations.

Another essential step in designing and developing the mechanical test setup is understanding the dynamics of the motors and drivelines, in particular as they interface with other subsystems. Of most importance is any resonance or jitter that may be caused by the internal, electromagnetic dynamics of the AC motor, rotor, stator, bearings, and other components. Section 3.3 provides a detailed dynamic model of the electromechanical system and other elements that it interacts with. The model includes the internal dynamics of the two AC motors that are used for driving the wheel and roller, as well as the compliance of other components such as the drivelines and couplers. Appropriate consideration is given to providing an accurate mathematical model for the motors, and other critical elements. The mathematical model is implemented in Simulink for numerical modeling. A parametric study of the effect of electrical and mechanical components is carried out to find the damped natural frequencies of the test rig. The results of the study are presented and analyzed in detail.

A sophisticated powering, monitoring, and motion control architecture is configured to drive all the components actively. It integrates multiple sub-systems such as power distribution, safety, motion control, and data acquisition. It provides a unified command and feedback network between all the components with high update rate. The design and features of these systems are discussed in Chapter 4, Chapter 5, Chapter 6, and Chapter 8.

## Chapter 3. Powertrain

This chapter provides two vibration analyses on the VT Roller Rig. Rotation of each disk is dominated by internal dynamics of the motors, gearheads, couplers, and flexible shafts. As a result, dynamics of each component has a direct effect on the relative speed of the wheel and the roller at the contact patch. On the other hand, it is essential to make sure that the measurements are only caused by the particular subject of study and not any intermittent source of disturbance such as unbalanced rotation. This study aims to analyze the effect of incorporating compliant joints in the drivelines, as well as unbalanced dynamics in the disks. Appropriate consideration is given to providing an accurate mathematical model of each phenomenon. The mathematical models are implemented in Simulink for numerical modeling. A model of the axial force generated in a tripod joint is then studied within the scope of this application. Two parametric studies will elaborate possible issues with incorporating a constant velocity joint in the driveline. A four degree of freedom mass-spring-damper model of the wheel and roller will be developed to study the possibility of designing a vibration compensator for unbalanced rotations. Results of this study are presented for different working conditions. The results of these studies indicate that incorporation of constant velocity joints in sensitive instruments like the VT Roller Rig leads to inevitable axial vibrations that affect both driver and driven sides. This chapter also provides a tool for filtering the undesired vibrations from the contact measurements due to unbalanced rotation or other sources of the same nature.

An essential step for the successful design and development of the test rig is modeling the motors and the roller/wheel drivelines. The third section of this chapter provides the details of an electromechanical model of the Rig components for studying the overall behavior of the coupled drivelines. The model includes the electromagnetic dynamics of the AC motors, the compliance, and damping of the drivelines, the inertial properties of the motors, shafts, couplers, and the rotating wheels, in a multi-domain (electrical, magnetic, and mechanical) lumped-parameter model. The model is used to determine the damped natural frequencies of the coupled system. In this section, appropriate consideration is given to providing an accurate mathematical model of each component.

Numerical case studies using this model indicate that the compliances of the driveline mechanics are the most critical element in maintaining a prescribed speed at the driven wheel, and also controlling the relative creep between the wheel and the simulated (round) rail.

### 3.1 Vibration Analysis of Independent and Differential Drivelines

This section has been published and presented in part at the 2015 Joint Rail Conference, San Jose, CA [56].

As discussed in [3], two approaches are available in designing the powertrain for producing slip between the two rotating bodies. In the first approach, a differential driveline that works based on a differential gearbox can be designed such that one motor drives both wheels and creep is controlled by adjusting the differential gear ratio of the gearbox. As shown in Figure 3.1, the energy of the driven wheel is transferred back into the driveline, which minimizes the required rated power for running the system (8.5hp). On the other hand, only one precisely controllable motor is needed to control the creepage.

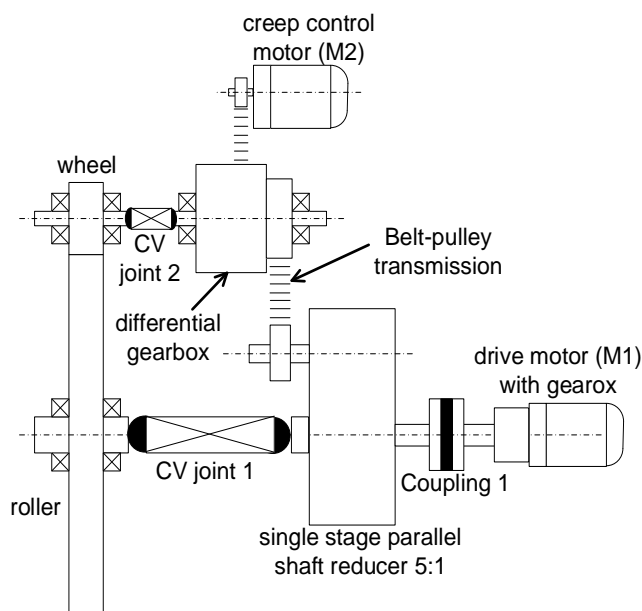


**Figure 3.1. Differential driveline requires compliant joints to allow for relative motion between the two wheels.**

In the second approach, wheel and roller are mounted directly on two independent motors as per Figure 3.2, without any gearbox or mechanical speed adjustment. Using servo drives, it is possible to run the two motors off a common DC-bus in digital master-slave mode (electronic gearing) to control the creepage. This approach requires two sets of precisely controllable digital servo motors, servo drives, and their associated electrical components for running the system. This increases the

required rated power to 25hp for each motor (50hp total), and also adds to the overall cost of the system.

Another major difference between the two designs is that the differential concept requires flexible power transmission through compliant connections. Since the two rotating bodies can change their relative position (AoA, cant, lateral), compliant joints should allow for relative displacement and rotation between the input and output shafts. To provide the exact speed profile for each wheel, these joints should maintain an absolute 1:1 speed ratio between the driver and the driven sides, without any lead or lag.

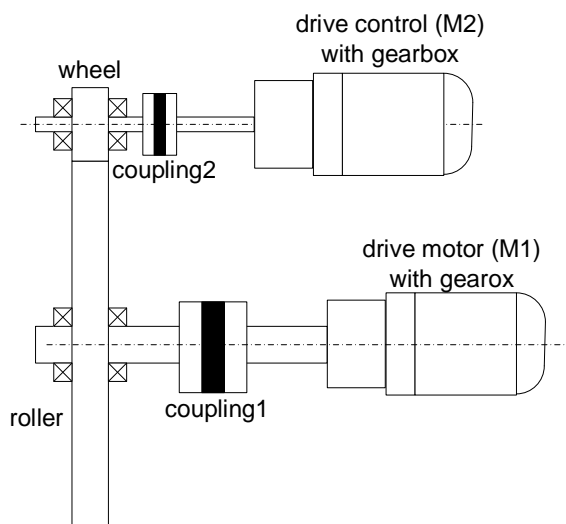


**Figure 3.2. Independent drivelines require controlling two servo motors to provide the desired creep profile.**

Constant velocity (CV) joints are one of the most common types of compliant joints that meet the criteria mentioned above. They are extensively used in automobile drive shafts, especially in front-wheel vehicles [57]. They are also popular in wheelsets of rail vehicles as part of length-adjustable shafts [58]. They play a major role in every active steering mechanism [59]. Although the motor manufacturer application engineers agreed on the simplicity of creepage control with the differential driveline, they expressed a general concern regarding low positioning accuracy of servo motors when placed in line with flexible joints. They had witnessed unreliable positioning characteristics in such mechanisms, with speed and load dependent behavior. To make an educated decision, a vibration analysis on this problem is necessary. Results of this analysis can be beneficial to similar applications in the railway and automotive industries.

### 3.1.1 Axial Forces in Tripod Constant Velocity Joints

Studies on constant velocity joints and similar types of flexible transmission joints are not so abundant in the literature. Due to the inherent limitation on disclosing proprietary product information, few experimental measurements and dynamic models are available to the researchers. These joints are capable of transmitting the torque and rotational motion from one shaft to another when their axes are inclined. The inclination angle (or bending angle) may be constant or variable during the operation. Incorporation of these joints into the driveline provides easier torque transmission. However, they also add to the overall torsional compliance of the driveline. Different types of CV joints such as Rzeppa, Thompson, and tripod are available in the market. Compared to other CV joints, a tripod joint does not provide as much inclination angle but is more efficient and lower in cost. This makes them the most common type of CV joints in power transmission applications.

Watanabe et al. [60] proposed a kinematics and dynamics model for tripod constant velocity joints. Baron [61] showed that shudder motion, consisting of low-frequency vibrations, originates from axial force components generated by a tripod plunging joint. Serveto et al. [62] presented a model for predicting the axial force generated by tripod joints of automotive drive shafts. Results of the latter work are further developed here to get a better understanding of how tripod constant velocity joints can decrease the performance of highly accurate systems, such servo motors.

A tripod joint consists of three spherical or cylindrical rollers at the end of a tripod spider attached to the output shaft (Figure 3.3). The tripod spider sits in a tulip with three matching ramps parallel to the input shaft and attached to it. During a joint revolution, the roller has a rectilinear trajectory along the ramp. Mariot et al. [63] showed that the Columb friction between ramps and rollers causes a so-called *shudder* motion. Serveto et al. [62] proposed a model and experimentally validated that for predicting the axial force generated by a tripod joint of an automotive drive shaft. The axial force along the tulip shaft can be obtained as:

$$F = \sum_{i=1}^3 F_i = \sum_{i=1}^3 \frac{T_0}{3r} \mu_t \sin(\chi_i) \text{sign}(v_{ramp_i}^{roller}) \quad (1)$$

where  $i$  is the roller index,  $T_0$  is the transmitted torque,  $r$  is the tulip radius, and  $\mu_t$  is the roller-ramp friction coefficient.  $\chi_i$  is the roller yaw angle given as the solution to the following trigonometric equation:

$$\chi_i = \arccos\left(1 - \frac{\delta^2}{2} \cos^2 \phi_i\right), \quad i = 1, 2, 3 \quad (2)$$

$\delta$  is the angle between the input and output shafts, and  $\phi_i$  is the ramp  $i$  input angle.  $\phi_i$  is related to input shaft angle,  $\phi$ , by the following equation:

$$\phi_i = \phi + (i - 1) \frac{2\pi}{3}, \quad i = 1, 2, 3 \quad (3)$$

Back to equation 1,  $V_{ramp_i}^{roller}$  is the kinematic twist at roller  $i$ 's contact point. Its value is defined as:

$$V_{ramp_i}^{roller} = I_i \sin(\chi_i), \quad i = 1, 2, 3 \quad (4)$$

in which  $I_i$  is the velocity of the rectilinear movement of the roller along the ramp. It is related to the input shaft velocity,  $\dot{\phi}$ , and input shaft angle as below:

$$I_i = -r_i \dot{\phi} \sin \delta \sin \phi_i, \quad i = 1, 2, 3 \quad (5)$$

In equation 5,  $\dot{\phi}$  is related to the rotor angle,  $\omega_r$ . The rotor angle is determined by the dynamics of the gearhead and the AC servo motors running the Rig. Extensive discussion on electromechanical modeling of the Rig is available in [2]. The  $r_i$  coefficient is also a function of  $\phi_i$  and tulip radius:

$$r_i = r + e(1 + 2 \cos(2\phi_i)), \quad i = 1, 2, 3 \quad (6)$$

$e$  is the offset between tripod center and tulip shaft, projected in the tripod plane and is not usually zero. It may change between  $0.0019r$  and  $0.0321r$  [62].

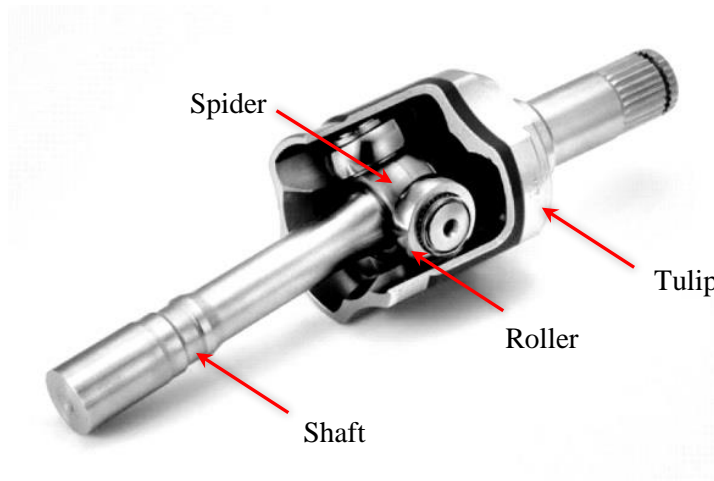


Figure 3.3. Main components of a tripod joint.

To study the generated forces in a regular operation, two case studies are done below. First, assuming that the input shaft is rotating at a constant speed, the motor provides enough torque to rotate the output shaft of the tripod CV joint and the load it is carrying. Second, assuming a constant load on the output shaft, the motor (input shaft) speeds up linearly. Generated axial forces in each case are shown in Figure 3.4 and Figure 3.5. In both cases  $\mu_g = 0.04$  and  $r = 0.025m$ . For the first case, 4 different  $\delta$  values are studied, while  $\delta = 15^\circ$  for the second case.

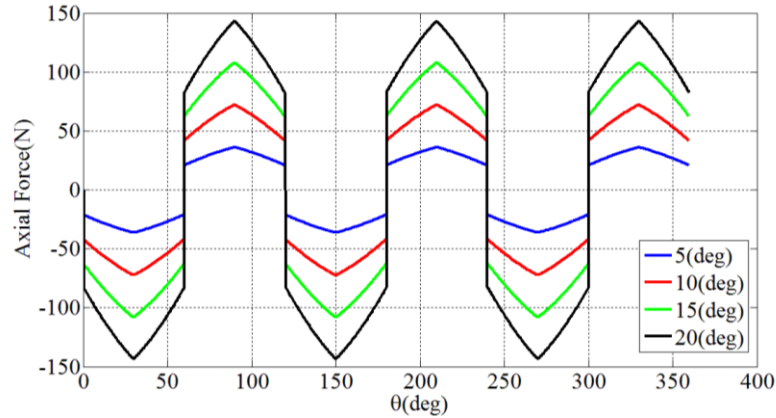


Figure 3.4. Net generated axial force in a tripod CV joint rotating at 350rpm and transmitting 450Nm load.

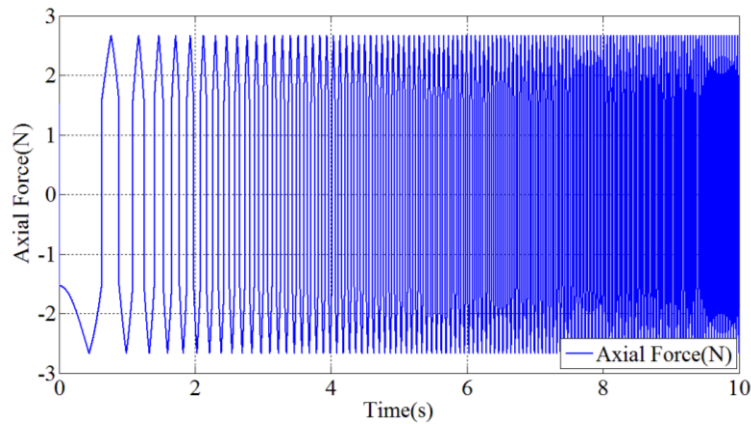
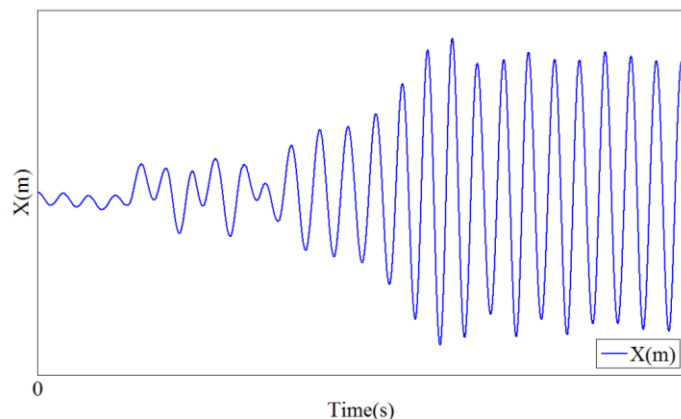


Figure 3.5. Net generated axial force in a tripod CV joint under 10Nm load, while the motor accelerates linearly.

For the constant speed case, the net generated axial force has harmonic behavior with a considerable amplitude. This force can be seen by both gearhead-motor (driver) and shaft-disk (driven) sides. It is clear that any undamped vibration in the rotor leads to unstable rotor position within the stator. This changes the back EMF of the motor and affects the overall performance of the servo controller.

Relying on the motor’s front bearing may alleviate this issue, but the second case study shows that it cannot be the ultimate solution. As shown in Figure 3.5, the frequency of the net generated axial force changes linearly with speed, very much similar to a chirp signal. Although it does not sweep

the full  $\pm F_{max}$  region as a sine wave does, but nonetheless, it can lead to resonance in components with relatively low natural frequencies. To better elaborate this issue, the resulting force from constant torque case is applied to an axial model of the flexible shaft developed in [2], using an 8-segment lumped model in clamped-free boundary condition. Figure 3.6 provides a qualitative representation of damped response of the shaft, when speed is increased until resonance occurs.



**Figure 3.6. Displacement of the shaft end due to net axial force generated in a tripod CV joint with ramp speed.**

Figure 3.4, Figure 3.5, and Figure 3.6 show that the CV joints will generate a reciprocating axial force from pure shaft torque. The amplitude of this force is a function of torque ( $T_0$ ), bending angle ( $\delta$ ), and geometry of the tulip ( $r, e$ ). The frequency of this force has direct relationship with the speed of rotation ( $\dot{\phi}$ ). Since speed of both rotating bodies may be variable during a test, the frequency could possibly match the natural frequency of neighboring components and lead to resonance. Even if properly designed, the vibrating force exerts a high magnitude noise on the rotor that can affect the performance of the servo motors. This force will also be captured by the front and rear dynamometers, and require further data processing for filtering it out, similar to the case of unbalanced rotation.

### 3.1.2 Outcome and Discussion

Incorporation of tripod joints into a driveline could have three major adverse effects on the performance of the servo motor. First, the frequency of the net generated axial force is a function of speed. As the speeds of the rotating bodies are variable during a test, the frequency could match the natural frequency of neighboring components. Even if properly designed, the vibrating force exerts a high magnitude noise on the rotor that can affect the performance of the motor. Second, it is a well-known fact that there is an inevitable backlash with constant velocity joints [64]. This leads to a delay in torque transmission when the direction of rotation is reversed. Finally, contrary to the name of these joints, there might be a deviation in output angle from the input angle that

affects the one-to-one speed ratio between the input and output shafts. For a tripod CV joint, this deviation is given by:

$$\phi - \theta = \theta_0 \sin 3\phi \quad (7)$$

where  $\theta$  is the output angle and  $\theta_0$  is experimentally measured for each bending angle [62].

In addition to the above, the generated axial force will get superposed to the contact forces, measured by the front and rear dynamometers. This will have a negative effect on the accuracy of the measurements, and requires further data processing. Overall, these results provide enough reasons to select the direct driveline concept as the powertrain of the VT Roller Rig.

Using constant velocity joints is tempting from a design standpoint since they make the design of transmission driveline less costly and more straightforward. However, application engineers do not suggest incorporation of such joints into highly accurate instruments. Results of the kinetics analysis of these joints for the VT Roller Rig were presented here as a reference for similar applications. A mathematical model of the net generated axial force in a tripod CV joint was developed based on a previously available model. Considering two cases of constant and ramp speed, it was seen that the harmonic behavior of these forces could easily excite adjacent components. In the latter case, the net generated force had a chirp-like behavior with a speed-dependent frequency that could lead to resonance.

### 3.2 Non-chaotic Behavior of Independent Drivelines

This section has been published and presented in part at the 2015 Joint Rail Conference, San Jose, CA [56].

Although much effort is put towards making the Rig both simple and rigid, precautionary considerations should be taken into account for removing undesirable noise from the contact measurements. Besides isolation, disturbance rejection and accommodation techniques in control applications may be helpful for post-processing the data. Tools such as predictors, filters, and smoothers are fairly well developed for passive data processing. However, there is always a risk of losing part of the valuable information with these techniques. Active noise cancellation for the sensors is another option that is more involved and depends on the nature of each experiment. Another point of interest in this study is to evaluate the possibility of developing a vibration compensator for deterministic disturbances caused by unbalanced rotation of the wheel, roller, or both wheel and roller. All rotating bodies are machined with tight tolerances to minimize this effect.

However, unbalanced rotation may originate from non-homogeneity of a worn disk, air gap variation in any motor, winding short, or stator weakness. Due to the high sensitivity of the load cells (7.8pC/N) [3], unbalanced rotation can generate large enough forces to be captured by the load cells. As shown in Figure 3.7, the wheel and driveline connected to it are carried by two dynamometers. Each dynamometer has four similar triaxial load cells, sandwiched between the top and bottom plates. These dynamometers will see any force generated by unbalanced rotation of the rotating bodies. Often harmonic in nature, such forces will be superposed to the sensor readings that represent the actual subject of study. In other words, such disturbances can have frequencies equal to the desirable test frequency; therefore, passive filtering will not be possible. A more intelligent signal processing approach is required for analyzing the contact measurements. Unlike disturbances from coupled noise mechanisms, such as EMI or RFI, it is possible to study such undesirable dynamics and subtract them from the sensor outputs without the risk of data loss. This will also provide a tool for predicting damaging vibrations that may damage the sensors or lead to out-of-bound noise in the measurements.

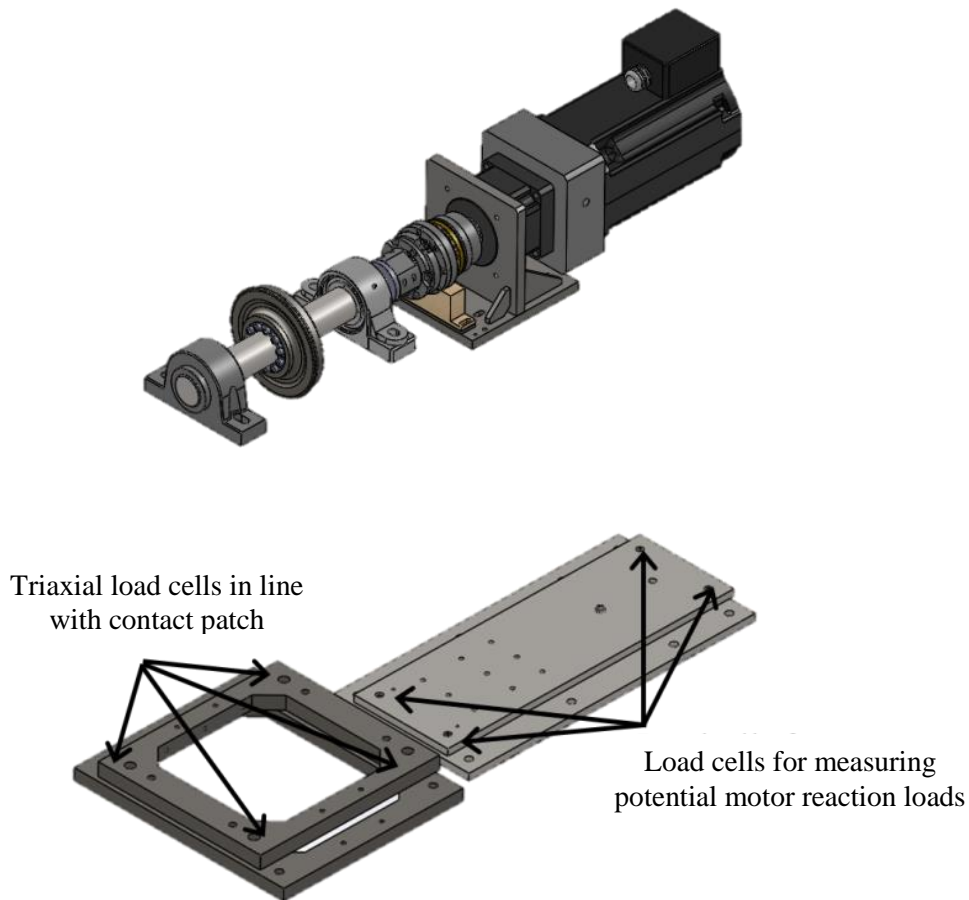


Figure 3.7. Front and rear dynamometers for measuring the contact loads.

### 3.2.1 Vibration Compensator for Unbalanced Rotation of the Wheel and/or Roller

Unbalanced rotation of the wheel and/or roller causes vertical and longitudinal vibrations. As mentioned earlier, unbalanced rotation can be originated from non-homogeneity of a disk, air gap variation in the motor, winding short, or stator weakness. One of the dynamometers shown in Figure 3.7 measures the motor reaction forces, and the other one supports the wheel cradle in-line with the contact patch. Contact forces and moments are further calculated from both dynamometer readings [3]. Load cells have been selected based on their sensitivity to detect any dynamic load change, even though small, and reflect it in the dynamometer outputs. Therefore, any vibration, generated on either the wheel or the motor side, will affect the contact measurements. The main purpose of this section is to develop a means for compensating deterministic noises in the sensors due to the unbalanced rotation. Using a simplified wheel-roller model as shown in Figure 3.8, it is possible to solve for the coupled unbalanced rotations.  $c$  and  $k$  denote damping coefficient and stiffness of each disk.  $m$  is the disk mass without unbalanced mass.  $k_{e,x}$  and  $k_{e,y}$  are compression springs that represent the elastic stiffness of the wheel and roller in  $x$  and  $y$  directions.

The reference frame in Figure 3.8 is oriented such that  $x$  is in the vertical and  $y$  is in the longitudinal direction. Due to similarity of the solutions in both directions, only vertical equations are presented here. However, results will cover both directions. The common convention in engineering vibration is used throughout the following equations. Scalars are written in regular lowercase, matrices in bold uppercase, and vectors in regular uppercase.

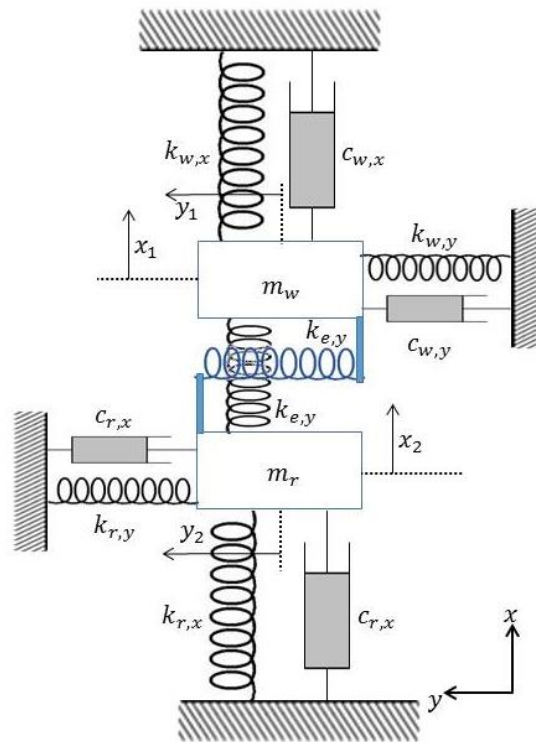


Figure 3.8. Mass-spring-damper model of the wheel/roller interaction.

The vertical equation of motion of the system can be formulated in matrix format as given in equation 8.  $m_w$  and  $m_r$  are the mass of the wheel and the roller, respectively.  $c_{w,x}$  and  $c_{r,x}$  denote the internal damping of the wheel and roller in the  $x$  direction.

$$\mathbf{M}\ddot{\mathbf{X}}(t) + \mathbf{C}\dot{\mathbf{X}}(t) + \mathbf{K}\mathbf{X}(t) = \mathbf{B}\mathbf{F}(t),$$

$$\mathbf{M} = \begin{bmatrix} m_w & 0 \\ 0 & m_r \end{bmatrix}$$

$$\mathbf{C} = \begin{bmatrix} c_{w,x} & 0 \\ 0 & c_{r,x} \end{bmatrix}$$

$$\mathbf{K} = \begin{bmatrix} k_{w,x} + k_{e,x} & -k_{e,x} \\ -k_{e,x} & k_{r,x} + k_{e,x} \end{bmatrix}$$

(8)

$$\mathbf{B} = \mathbf{I}_2$$

$$\mathbf{X} = \begin{bmatrix} x_1 \\ x_2 \end{bmatrix}$$

where  $\mathbf{M}$ ,  $\mathbf{C}$  and  $\mathbf{K}$  are the mass, damping and stiffness matrices. Defining the Cholesky decomposition of mass matrix as  $\mathbf{L}$ , one can write:

$$\mathbf{L}^{-1} = \mathbf{M}^{-\frac{1}{2}} = \begin{bmatrix} 1 & 0 \\ \sqrt{m_w} & 1 \\ 0 & \sqrt{m_r} \end{bmatrix} \quad (9)$$

From that, the normalized stiffness matrix can be found as:

$$\tilde{\mathbf{K}} = \mathbf{L}^{-1}\mathbf{K}\mathbf{L}^{-1} \quad (10)$$

The modal coordinate system,  $R(t)$ , is defined as:

$$R(t) = \mathbf{P}^T \mathbf{L} \quad (11)$$

in which  $\mathbf{P}$  is the matrix of normalized eigenvalues of  $\tilde{\mathbf{K}}$ . Substituting  $R(t)$  in equation 8, and multiplying it by  $\mathbf{P}^T$ , one gets the modal equations as:

$$\mathbf{I}\ddot{R}(t) + \mathbf{P}^T\tilde{\mathbf{C}}\mathbf{P}\dot{R}(t) + \mathbf{\Lambda}R(t) = \mathbf{P}^T\mathbf{L}^{-1}\mathbf{B}F(t) \quad (12)$$

where  $\tilde{\mathbf{C}} = \mathbf{L}^{-1}\mathbf{C}\mathbf{L}^{-1}$  and  $\mathbf{\Lambda}$  is the diagonal matrix of natural frequencies squared. Whether  $\tilde{\mathbf{C}}$  decouples the left hand side or not, depends on the validity of the following equation:

$$\mathbf{C}\mathbf{M}^{-1}\mathbf{K} = \mathbf{K}\mathbf{M}^{-1}\mathbf{C} \quad (13)$$

If equation 13 is valid, then  $\mathbf{Z} = \mathbf{P}^T\tilde{\mathbf{C}}\mathbf{P}$  will decouple the equations. In that case,  $\mathbf{Z}$  will be the diagonal matrix of  $2\zeta_n\omega_n$  where  $\zeta_n$  is the damping ratio and  $\omega_n$  is the natural frequency ( $n = 1,2$ ). If equation 13 does not hold for all  $t$ , then equation 12 should be numerically solved. In either case, it is possible to solve the equations, however, assuming the validity of equation 13 allows moving forward with the analytical solution. One could construct  $F(t)$  as below and solve for the decoupled  $R(t)$ . If  $m_{w,u}$  and  $m_{r,u}$  are unbalanced masses on the wheel and roller drivelines, then:

$$F(t) = \begin{bmatrix} F_w(t) \\ F_r(t) \end{bmatrix} = \begin{bmatrix} m_{w,u}(\omega_w)^2 \sin \omega_w t \\ m_{r,u}(\omega_r)^2 \sin \omega_r t \end{bmatrix} \quad (14)$$

Equations 8-14 hold for the  $y$  direction too, with only one difference in the forcing matrix such that the sinusoidal terms in the wheel and roller equations should be substituted by cosine. Since the accumulated values of the damping and stiffness coefficients should be experimentally determined, the results provided here are intended to provide qualitative understanding of the system. In order to get a better intuition of how the solutions would look like, one could plot the  $x$  and  $y$  responses

of the wheel as the wheel rotates at the first natural frequency and the roller rotates at the second natural frequency. Although this is a rare condition in practice, it represents an interesting worst-case scenario and also helps to further extend the analysis. Figure 3.9 shows the  $x$  and  $y$  responses of the wheel, by solving equation 12 for both coordinates.

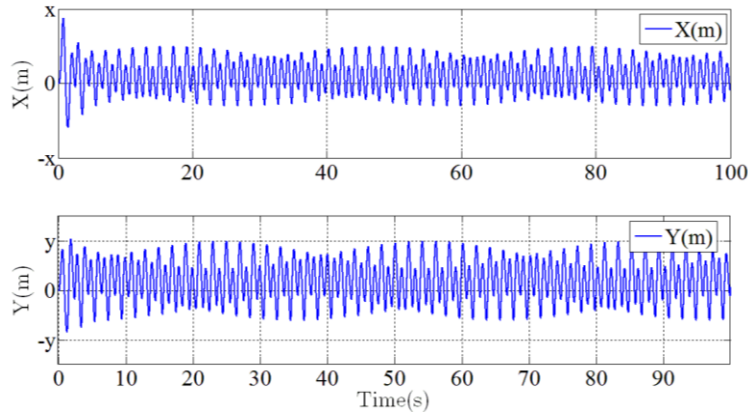


Figure 3.9. Qualitative  $x$  and  $y$  responses of the wheel.

Load cells hold the wheel in place to measure the creep forces at the contact patch. In the case of unbalanced rotation of the wheel and/or roller, the following forces will be superposed to the sensor readings:

$$\begin{aligned} \hat{F}_x &= k_{w,x}x_1 + c_{w,x}\dot{x}_1 \\ \hat{F}_y &= k_{w,y}y_1 + c_{w,y}\dot{y}_1 \end{aligned} \tag{15}$$

From equation 15, one could plot the force phase plane to better show the transmitted forces at the transient and steady state conditions. Figure 3.10 shows the  $(x, y)$  view of a 3D  $(\hat{F}_x, \hat{F}_y, t)$  plot.

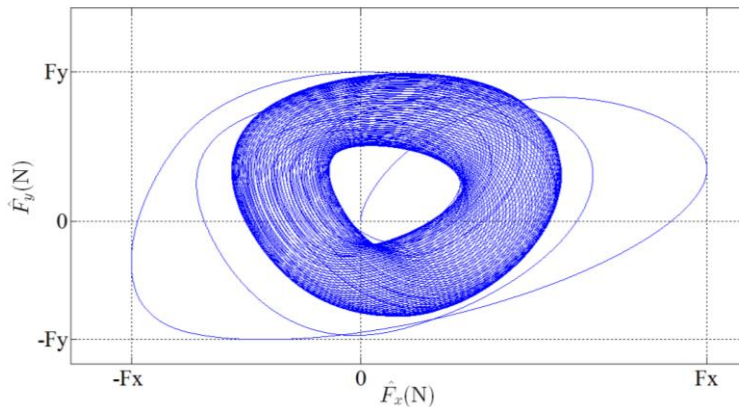
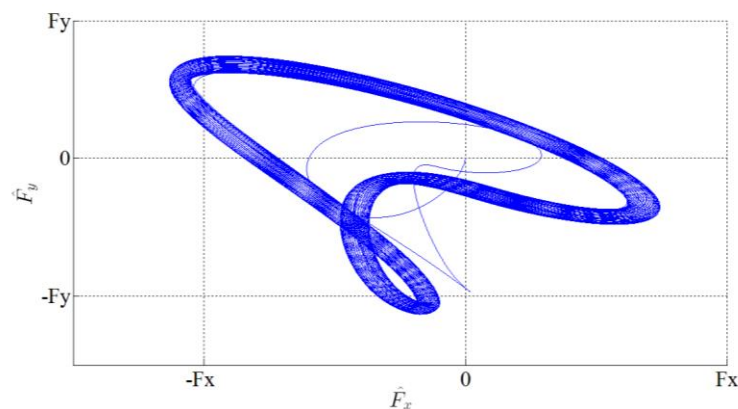


Figure 3.10. Force phase plane as wheel rotates at the first natural frequency and roller rotates at the second natural frequency.

Figure 3.11 is another possible case in which both wheel and roller rotate at  $0.5 \times$  first natural frequency.



**Figure 3.11. Force phase plane as both wheel and roller rotate at the  $0.5 \times$  first natural frequency.**

Considering the periodic set of numerical trajectories towards which the system tends to evolve, one could conclude that the system behaves like an attractor as time approaches infinity. Force responses that get close to this attractor in the two-dimensional space  $(x, y)$ , remain close to it even if slightly disturbed. In this specific problem, the system limits to an isolated periodic orbit (limit cycle) or stays within a finite vicinity of it. Further case studies showed that responses do not exhibit sensitive dependence on the initial conditions, as is the subject of chaotic systems. To which attractor the responses limit to, strongly depends on the wheel and roller rotational frequencies.

Two other cases are reported below to show the dependency of the attractor on either of the rotation frequencies. First, it is assumed that the wheel rotates at  $5 \times$  first natural frequency, while the roller rotates at  $5 \times$  second natural frequency. In the other case, the wheel rotates at  $0.1 \times$  first natural frequency, and the roller rotates at  $0.1 \times$  second natural frequency. Similar to what was mentioned earlier for Figure 3.9, Figure 3.10, and Figure 3.11, results could be presented for any set of wheel/roller frequencies. The reason for choosing similar multiplication factors for the speeds of rotation in the following cases is that the speeds of wheel and roller will often be related to each other by a factor for generating a constant creep profile. The following circumstances present a few of the many possible situations that could happen. In both cases, the system tends towards a limit cycle.

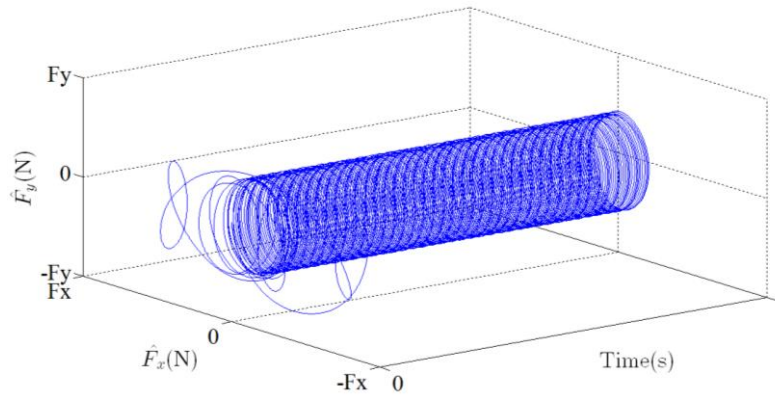


**Figure 3.12. Force time history as wheel rotates at  $5\times$ first natural frequency and roller rotates at  $5\times$ second natural frequency.**

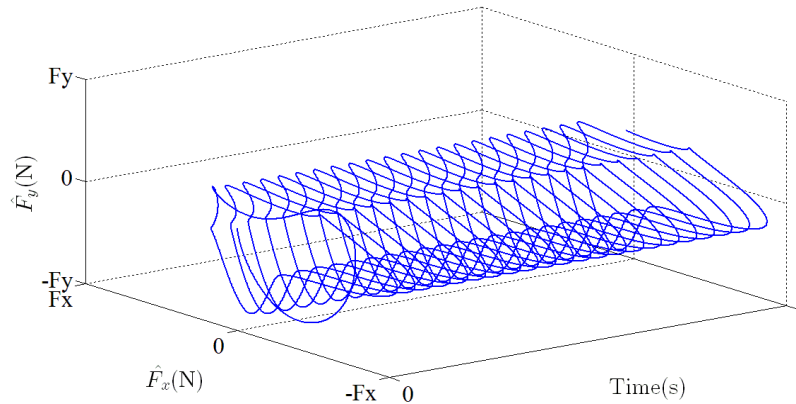


**Figure 3.13. Force time history as wheel rotates at  $0.1\times$ first natural frequency and roller rotates at  $0.1\times$ second natural frequency.**

Based on the Poincaré-Bendixson theorem, if a strange attractor exists in this two-dimensional system, then it could be enclosed by a closed subset in the phase space that converges to a limit cycle [65]. Considering the nonchaotic behavior of the system, it is possible to map the phase plane of the forces versus frequency to find the limit cycle. A signal processor could then compensate for undesired vibrations due to unbalanced rotations by removing the mapped forces from the sensor readings.

Knowing that a repetition is happening is not enough evidence for proving the existence of a limit cycle. Instead of proving the existence of limit cycles, it is often possible to check the non-existence of limit cycles. In autonomous systems, theories like Bendixson's criterion or critical points [65] could be helpful in checking the non-existence of limit cycles. In non-autonomous systems such as equation 8, however, the proof is much more involved, and computational tools are often used to search for the limit cycles [66].

### 3.2.2 Outcome and Discussion

The possibility of developing a vibration compensator for deterministic disturbances caused by unbalanced rotation of the wheel and/or roller was then studied. Using a 4 DOF simplified wheel-roller model, it was possible to solve for the coupled unbalanced rotations. These results can be used to compensate for any unbalanced rotation in the disks. For doing so, it is required to run the wheel and roller separately and measure the base forces. Finding an equivalent  $m_{ue}$  for each case, it would be possible to resolve the effect of these unbalanced rotations from the sensor readings; hence increasing the accuracy of the contact patch measurements.

As mentioned during the development of the solution for unbalanced rotation, equation 13 is a critical check for the possibility of decoupling the equations. Fortunately, the values on the main diagonal of the damping matrix are time invariant functions of material properties.

The model developed and presented here should be used along with measurements and experimental data to accurately model the dynamics at the contact patch. The point loaded contact model used here does not take all mechanics into account. However, authors believe that this simple model is able to simulate, different working conditions. On the other hand, development of the contact model is beyond the scope of this study and the discussion provided here is intended to be used as a stepping-stone for future research.

### 3.3 Electromechanical Modeling of the VT Roller Rig

This section has been published and presented in part at the 2014 Joint Rail Conference, Colorado Springs, CO [2].

#### 3.3.1 Equivalent Model of the Electrical System

Two independent three-phase permanent magnet servo motors drive the wheel and roller. Each motor is controlled by a digital servo drive that controls stator currents, rotor speed, and position. Each motor and drive, along with the three-phase AC power supply comprise the electrical system responsible for accurately following the desired speed profile against time varying load. The three-phase rectifier, braking chopper, three-phase inverter, field oriented controller (FOC), and speed controller are the main parts of the drive. The permanent magnet synchronous machine (PMSM) and the position sensor are the main parts inside the motor housing. An optional mechanical brake may also be added. The PMSM has permanent magnets mounted on the surface of the rotor, with a uniform air gap and no saliency.

Unfortunately, due to restrictions and limitations of proprietary products, it is not possible to get access to the actual models of commercialized motors. On the other hand, it is vital for any HIL operation to have a relatively accurate model of every component included in the loop. Fortunately, most of the models for the above-mentioned components are available in SimPowerSystems library of MATLAB. Therefore, it is possible to tune an equivalent model for the electrical system using this toolbox. While the performance of the simulated and actual systems match in both transient and steady state conditions, it is possible to use the model as an accurate prediction of the behavior of the real system.

The rectifier, braking chopper, and inverter form an AC/DC/AC converter that feeds the PMSM. Figure 3.14 shows the arrangement of the rectifier, the braking chopper, and the inverter. Both inverter and rectifier can be simulated by naturally commutated (or line-commutated) power electronic devices such as diodes, or forced commutated devices such as MOSFET or IGBT. The braking chopper contains a DC bus capacitor and a dynamic brake, which absorbs the kinetic energy of the motor during deceleration. By using the DC bus in parallel with the rectifier, the PMSM would only operate in the motoring mode and not in regeneration. A resistor in series with the chopper is placed parallel to the DC bus to prevent its voltage from increasing during deceleration. This dynamic brake along with a diode bridge three-phase rectifier and a pulse width modulated IGBT-diode three-phase inverter will sufficiently prevent numerical oscillation when the system is discretized.

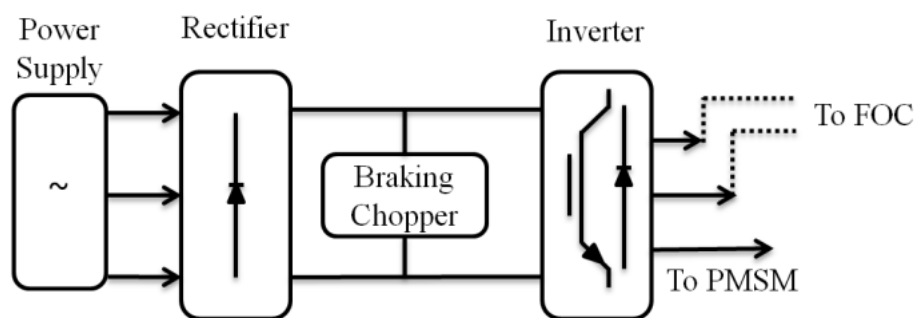


Figure 3.14. Arrangement of rectifier, braking chopper, and inverter inside the drive.

Since the motor is intended to follow a reference speed profile, the controller can be approximated by a PI regulator. The regulator sets the desired electromagnetic torque, which is input to the FOC. A rate limiter bounds the rate of change of the input speed based on motor acceleration and deceleration slew rate ( $r_s$ ). Moreover, the electromagnetic torque cannot be greater than motor peak torque ( $T_p$ ). The slew rate  $r_s$  can be easily found by dividing the peak torque by the combined inertia of the rotor and load. Another limiting factor is the maximum mechanical speed of the rotor,

$N_{max}$ , which is provided by the motor manufacturer. After calculating the electrical angle from the mechanical rotor angle, the FOC calculates the three motor line currents. Finally, a bang-bang three-phase current controller feeds the inverter by these reference currents.

All power electronic models are implemented in discrete time domain with a simulation time step of  $T_s$ , in order to simulate a digital controller. In a digital controller, different sampling times can be used for speed controller and FOC. However, they should be integer multiples of the simulation time step.

Three-phase sinusoidal model of an electrical system is given as [67]:

$$\begin{aligned} \frac{d}{dt} i_d &= \frac{1}{L_d} v_d - \frac{R}{L_d} i_d + \frac{L_q}{L_d} p \omega_r i_q \\ \frac{d}{dt} i_q &= \frac{1}{L_q} v_q - \frac{R}{L_d} i_q - \frac{L_d}{L_q} p \omega_r i_d - \frac{\lambda p \omega_r}{L_q} \\ T_e &= \frac{3}{2} p [\lambda i_q + (L_d - L_q) i_q i_d] \end{aligned} \quad (16)$$

where  $L_d$  and  $L_q$  are the q and d axis inductances,  $R$  is the resistance of the stator windings,  $i_q$  and  $i_d$  are the q and d axis currents,  $v_q$  and  $v_d$  are the q and d axis voltages,  $\omega_r$  is the angular velocity of the rotor,  $\lambda$  is the amplitude of the induced flux by the permanent magnets of the rotor in the stator phases,  $p$  is the number of pole pairs, and  $T_e$  is the provided electromagnetic torque. The mechanical load on the motor is related to the provided electromagnetic torque by the following equation:

$$\frac{d}{dt} \omega_r = \frac{1}{J} (T_e - T_f - C_f \omega_r - T_m) \quad (17)$$

where  $J$  is the total inertia of the rotor ( $J_r$ ), load ( $J_l$ ), and optional brake ( $J_m$ ). The term  $C_f$  is the total viscous friction coefficient of the rotor and load,  $T_m$  is the mechanical load, and  $T_f$  is the shaft static friction. Table 3.1 and Table 3.2 show the afore-mentioned constants for the VT Roller Rig. Assuming a round rotor with no air gap, there will be no variation in the phase inductances ( $L_q = L_d$ ).

**Table 3.1. Estimated constants for the rectifier, DC bus, braking chopper, and inverter used in SimPowerSystems model.**

Component	Constant	Value
Rectifier	Snubbers Resistance	$10^3(\Omega)$
	Snubbers Capacitance	$12 \times 10^{-8}(F)$
	Diodes Resistance	$0.001(\Omega)$
	Diodes Forward Voltage	$1.3(V)$
DC Bus	Capacitance	$1.2 \times 10^{-3}(F)$
Braking Chopper	Resistance	$6.7(\Omega)$
	Frequency	$4000(Hz)$
	Activation Voltage	$320(V)$
	Shutdown Voltage	$310(V)$
Inverter	resistance	$9.8 \times 10^{-4}(\Omega)$

To better show the performance of the equivalent model, the following case study is performed. Assuming no inertia other than the rotor,  $J_m$  and  $J_l$  are set equal to zero. A constant load  $T_m = 10Nm$  is applied to the rotor at  $t = 0$ . Speed is linearly increased from 0 to 150rpm at  $t = 0.5s$ , followed by another increment to 350rpm at  $t = 0.75s$ . Thereafter, it is desired for the motor to maintain a constant speed till  $t = 1.25s$ . Then, it should slow down to 150rpm at  $t = 1.5s$  and finally stop at  $t = 2s$ . The power is provided by a three-phase 480 V AC-60Hz power supply.

In Figure 3.15, the reference electromagnetic torque is compared with its actual value. Depending on the desired performance specifications, it is possible to change the P and I gains of the controller to decrease the error.

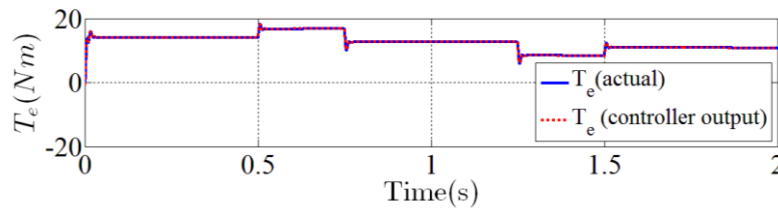


**Figure 3.15. Comparison between desired and actual electromagnetic torques.**

**Table 3.2. Constants used in the three-phase sinusoidal model of the electrical system [68].**

Constant	Value
$L_d$	2.5(mH)
$L_q$	2.5(mH)
$R$	0.058( $\Omega$ )
$\lambda$	0.19517(Wb)
$p$	5
$J_r$	495(kg.cm <sup>2</sup> )
$J_m$	5.53(kg.cm <sup>2</sup> )
$C_f$	0.00873(N.m.s)
$T_f$	2.34(N.m)
$T_p$	668(N.m)
$N_{max}$	3000(rpm)
$T_s$	2( $\mu$ s)

Figure 3.16 shows the DC bus current and voltage, fed into the three-phase inverter. As expected, the DC bus voltage remains almost constant after startup, while the current follows the speed profile with jumps corresponding to the electromagnetic torque.

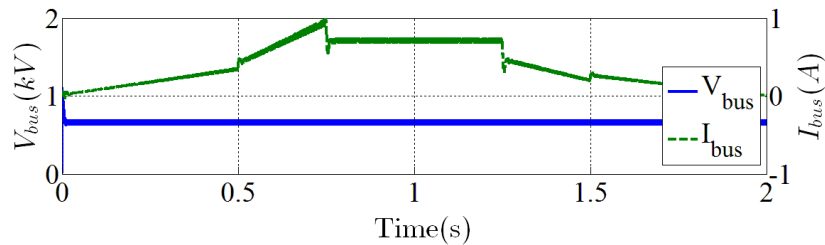


**Figure 3.16. DC bus voltage and current.**

Figure 3.17-top shows the sensitivity of the resistance output current of the three-phase inverter to speed change. An acceleration leads to an increase in the amplitude of this current, while deceleration decreases that. As is shown in Figure 3.17-bottom, stator current changes to provide the required electromagnetic torque.

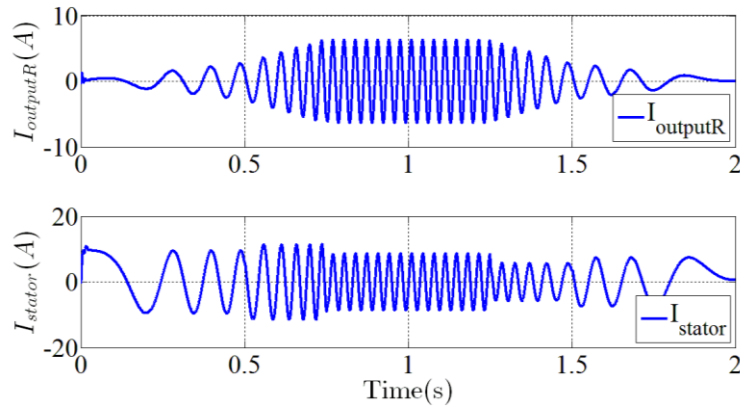


Figure 3.17. Output resistance current of the three-phase inverter (top) and stator current (bottom).

Figure 3.18 provides a means for evaluating the overall performance of the model by comparing the desired and actual speed profiles. The error increases, as the desired speed profile gets closer to a step function, i.e. at higher accelerations.

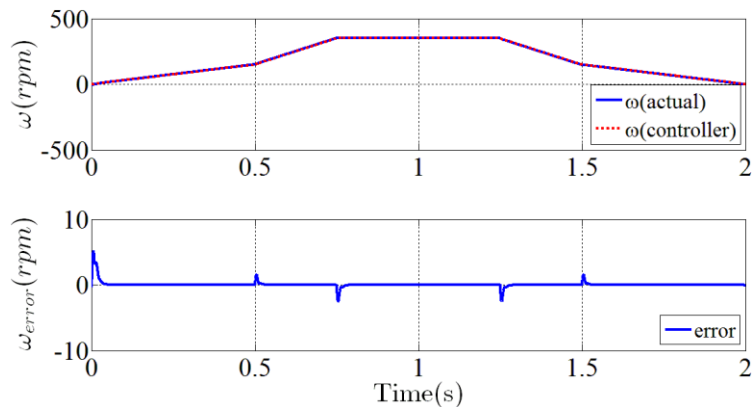


Figure 3.18. Speed profile of the motor under constant load and rotor inertia only.

The above case is only presented to show the accuracy of the model using available toolboxes as an approximation of the real electrical system. In practice, however, the load inertia is not zero, and the load torque will not be constant unless designed so. Load torque is an accumulated resistance of the wheel, roller, and their respective drivelines. It cannot be found unless precisely modeling each driveline and the wheel-rail interaction at the contact patch. The following section discusses this topic in details.

### 3.3.2 Equivalent Model of the Mechanical system

As Figure 3.19 shows schematically, both wheel and roller torque transmission drivelines consist of a gearhead and a flexible shaft. A contactless torque sensor is provided on each shaft to provide

an instantaneous measurement of the transmitted torque. Compared with shafts and gearheads, torque sensors are assumed to have negligible inertia, torsional stiffness, and damping.

Gearheads

Right after the rotor shaft, there is a gearhead with 5:1 ratio for the wheel and 28:1 ratio for the roller. In practice, the gearhead transfers the torque by an efficiency of  $0 < \eta \leq 1$ . It can be either constant or load dependent. Since the gearhead is supposed to run mostly at a relatively limited load range,  $\eta$  is assumed to be constant. Precision of the gearhead is dominated by the amount of backlash ( $b_g$ ). Although included in the model and reported here, the motor is not intended to operate in reversing motion. The effect of backlash is modeled by a delay in torque transmission from the gearhead to the output shaft, upon a sign change in angular velocity of the shaft. The values of these parameters for both gearheads are given in

‘w’ and ‘r’ superscripts denote wheel and roller, respectively.

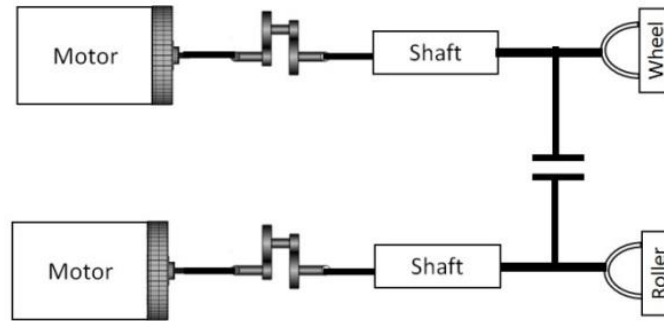


Figure 3.19. Schematic of wheel and roller drivelines.

$J_g$  is the mass moment of inertia reflected to the input shaft (including pinion assembly),  $k_g$  is the torsional stiffness of the gearhead and  $\mu_g$  brings the total viscous damping of the gearhead into the model.

In each gearhead, the transferred torque is reduced by Coulomb and viscous frictions. Viscous friction is only applied to the input shaft since it rotates at higher speed than the output one in both gearheads.

$$T_{v,g} = \mu_g \cdot \omega_r \tag{18}$$

$$T_{f,g} = g \cdot |T_e - T_{v,g}| \cdot (1 - \eta) \tag{19}$$

$$T_{out} = g \cdot T_e - T_{f,g} \tag{20}$$

$T_{v,g}$  is the viscous friction torque,  $T_{f,g}$  is the Coulomb friction torque,  $T_{out}$  is the transmitted torque and  $g$  is the gearhead ratio.  $T_e$  and  $\omega_r$  are found from equation 17.

**Table 3.3. Performance specifications of gearhead.**

Constant	Value
$\eta^w$	95%
$b_g^w$	4(arc – min)
$J_g^w$	20(kg.cm <sup>2</sup> )
$k_g^w$	150(Nm/arc – min)
$\mu_g^w$	0.015(Nms/rad)
$\eta^r$	90%
$b_g^r$	4(arc – min)
$J_g^r$	13.5(kg.cm <sup>2</sup> )
$k_g^r$	138(Nm/arc – min)
$\mu_g^r$	0.017(Nms/rad)

### Shaft Lumped Model

The shafts transmitting torque from the gearhead to the wheel or roller have a finite amount of torsional compliance. They should be modeled accordingly to study the effect of their compliances on the actual relative speed at the contact patch. A shaft, however, is a distributed parameter system and as found in any vibrations handbook, satisfies the following equation:

$$\frac{\partial^2 \theta(x, t)}{\partial t^2} = \left( \frac{G_s}{\rho_s} \right) \frac{\partial^2 \theta(x, t)}{\partial x^2} \quad (21)$$

where  $G_s$  and  $\rho_s$  are shear modulus and density of the shaft. Although solving equation 21 numerically is practical, it is not computationally efficient. Moreover, since a limited number of natural frequencies could be included in the final solution, there will be a certain level of approximation forced into the results. Another approach can include using an equivalent lumped model with finite number,  $N$ , of inertia-spring-damper elements in series with a final inertia at the end. The total inertia of the shaft is split into  $N + 1$  sub-inertias. Starting from the first sub-inertia, torsional spring-dampers connect the sub-inertias ending with the  $N + 1$  one. Damping here refers to internal material damping of the shaft that is related to the material properties and is defined by a damping ratio,  $c_s$ . For  $N = 1$ , this approach leads to the common one segment equivalent model

of a shaft  $[J_s^p, K_s, c_s]$ , where  $K_s = (J_s^p G_s)/L_s$  and  $J_s^p = (\pi D_s^2)/32$ .  $D_s$  is the shaft diameter,  $L_s$  is the shaft length,  $J_s^p$  is the polar moment of inertia and  $K_s$  is the lumped torsional stiffness. For more discussion on how to find these values for higher  $N$  see [69,70]. Larger  $N$  increases the accuracy, but reduces the speed. Using 16 segments, 0.1 percent error is reported for the first natural frequency [70].

Motor, gearhead, and shaft models connected in series, construct a drive system that runs the wheel or roller. Adding a constant inertia to each one of these systems gives an acceptable approximation of the two drivelines. Setting  $N = 16$  and using the constants given in Table 3.4, the first damped natural frequencies of the wheel and the roller drivelines are found to be 463.4Hz and 77.6Hz.  $J_r$  and  $J_w$  are the mass moments of inertia of the roller and the wheel, respectively. Figure 3.20 shows the uncoupled frequency response of the wheel and the roller drivelines.

**Table 3.4. Material and geometric properties of the shafts.**

Constant	Value
$L_s^w$	0.76(m)
$D_s^w$	0.08(m)
$\rho_s^w$	$7.85 \times 10^3(kg.m^3)$
$G_s^w$	78(GPa)
$c_s^w$	0.01
$L_s^r$	1.053(m)
$D_s^r$	0.091(m)
$\rho_s^r$	$7.85 \times 10^3(kg.m^3)$
$G_s^r$	78(GPa)
$c_s^r$	0.01
$J_r$	100.81(kg.m <sup>2</sup> )
$J_w$	0.06(kg.m <sup>2</sup> )

Changing any of the material or physical parameters in Table 3.3 and Table 3.4 affects the damped natural frequencies of the driveline. For instance, neglecting the mass moment of inertia of the roller gearhead increases the first damped natural frequency by up to 19%.

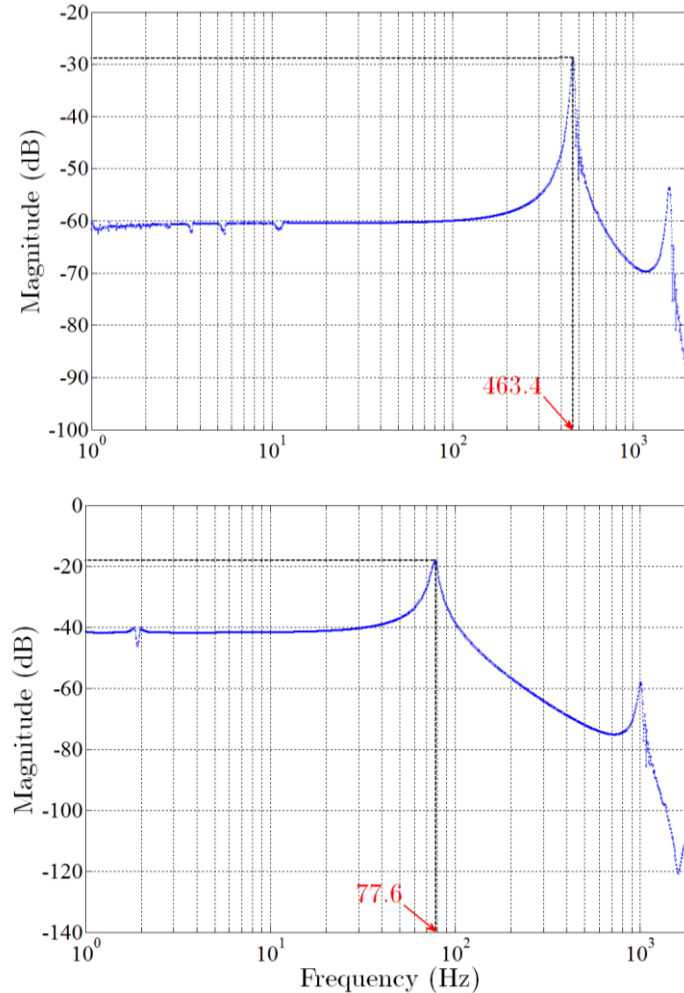
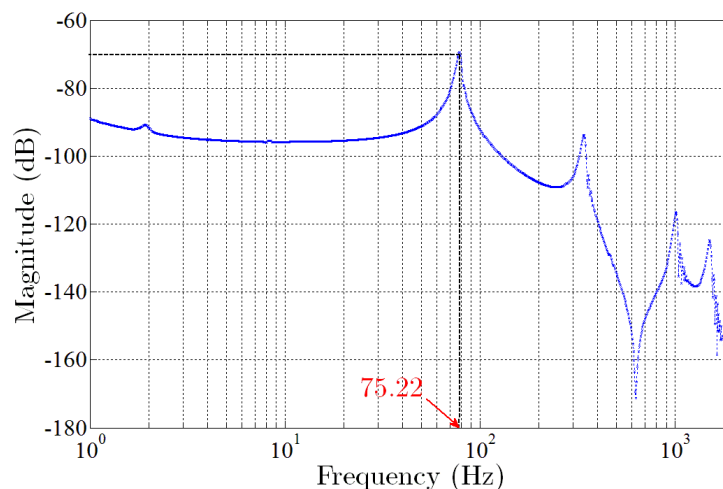


Figure 3.20. Frequency response of uncoupled wheel (top) and roller (bottom) drivelines.

The contact model between the wheel and the roller couples these two drive systems. For the sake of this study to move forward, a simplified loaded contact frictional model is used to couple the two systems. A discussion on the reasonability of this model is provided at the end of this section.

In this model, the wheel and roller have a relative creep if the friction force exceeds the static friction that is defined by the product of the coefficient of friction and normal force. Below that, the wheel and roller will rotate at the same speed in a “locked” state.  $\mu_s = 0.4$  and  $\mu_k = 0.3$  denote the dry static and kinetic friction coefficients for steel-steel contact. The normal force represents the wheel load. Considering the one-quarter-scale factor of the Rig, the design normal force is selected to be 12kN. By introducing the contact between the wheel and the roller, the drivelines will be coupled, and hence the boundary conditions will change. In order to find the first damped natural frequency, it is assumed that the contact model is in locked state. Figure 3.21 shows the

frequency response of the coupled drivelines. The first damped natural frequency of the coupled drivelines is found to be 75.22Hz.



**Figure 3.21. Frequency response of the coupled drivelines.**

### 3.3.3 Outcome and Discussion

Studying the mechanics at the contact patch has been the main motivation for the VT Roller Rig. An accurate model describing all forces is the best choice for coupling the two drive systems. However, the models developed and presented here should be used along with measurements and experimental data to accurately model those dynamics at the contact patch. The point loaded contact model used here does not take all mechanics into account. However, authors believe that this simple model is able to simulate, and not emulate, different working conditions in studying the possible vibrations in the motors and drivelines. On the other hand, development of the contact model is beyond the scope of this study and the discussion provided here is intended to be used as a stepping-stone for future research.

A scaled vertical roller rig is currently under development at VT Railway Technology Lab (RTL). This study summarized the electromechanical model of the Rig. The model consisted of motors, servo drives, gearheads, couplings, wheel, and roller. It was implemented in MATLAB using Simulink and SimPowerSystems toolboxes. The electrical system included permanent magnet synchronous motor, pulse width modulated IGBT-diode three-phase inverter, diode bridge three-phase rectifier, DC bus with dynamic brake, field oriented controller, and speed controller. Each driveline consisted of a gearhead, flexible shaft, and a rotating body. A simplified loaded contact frictional model coupled the two drivelines. Using the proposed model, damped natural frequencies of the drivelines were calculated for both independent and coupled conditions. The effects of

nonrealistic assumptions on the results were then evaluated, such as neglecting the mass moment of inertia of the gearhead.

## Chapter 4. Electromechanical Systems

### 4.1 Power Architecture

#### 4.1.1 Mains Network

ServoStar servo amplifiers are supplied from 3-phase symmetrically grounded (earthed) industrial supply networks. Permissible network types are TN and TT systems with grounded neutral point with no more than 42krms symmetrical amperes rated current at 480VAC<sup>+10%</sup> maximum [71]. In a TN system, the neutral line of the transformer supplying the power is earthed. Grounding is performed at this neutral point. TN Systems are subdivided into TN-C, TN-C-S, and TN-S according to the design of the protective conductor.

In TN-C systems, a PEN conductor acts as both protective earth (PE) and neutral line (N). Since the neutral line is a current carrying conductor when the three phases are unevenly loaded, a voltage differential is usually present between the housings of the equipment connected to a PEN conductor and the earth. This voltage difference is generated from the PEN conductor's resistance due to Ohm's law. If the PEN conductor is interrupted in a TN-C system, the full outer conductor voltage (i.e. up to 480V) will be applied to the device housings connected downstream of the interrupt point. This is due to the connection between the outer conductor and the PEN conductor within the instrument. IEC 60364 limits the smallest cross section of the PEN conductor to 10mm<sup>2</sup> copper and 16mm<sup>2</sup> aluminum, in order to minimize the risk of PEN interruption [72]. Figure 4.1 shows a TN-C system schematically.

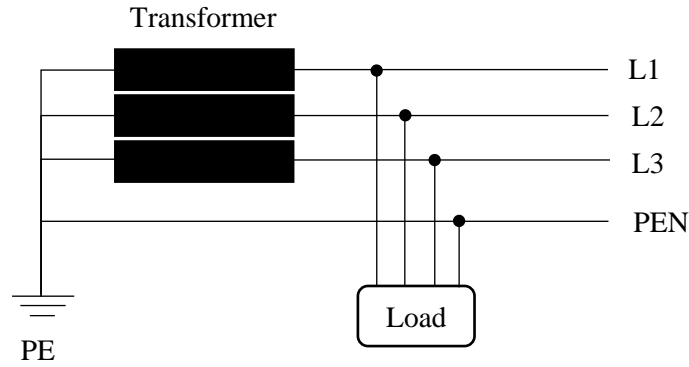


Figure 4.1. TN-C System.

A TN-CS system is similar to TN-C from a transformer point of view. Unlike TN-C, however, the PEN conductor is separated into PE and N at some point downstream of the point where the cross section of the PEN conductor is required to be above the minimum stipulated cross section. After that, the PE and N conductors are channeled separately and must not be combined with the rest of the network.

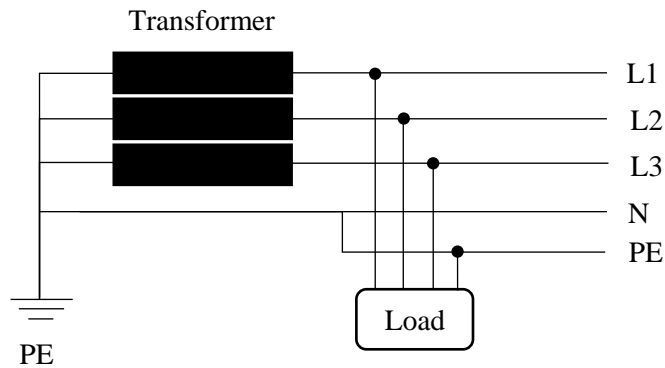


Figure 4.2. TN-CS System.

In a TN-S system, a separate neutral line and protective earth are channeled all the way from the transformer to the consumables. The problems caused by interruption of PEN conductor in TN-C and TN-CS systems do not occur in TN-S systems. Therefore, TN-S is safer than other TN systems. This method is predominantly used in the major industrial systems that are equipped with their transformer and are typically supplied with medium voltage.

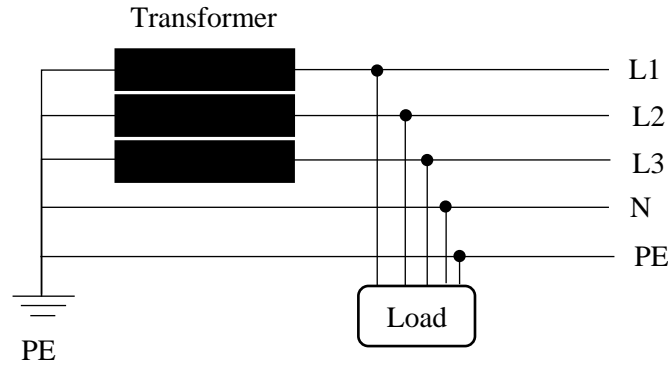


Figure 4.3. TN-S System.

Periodic over-voltages between phases (L1, L2, and L3) and the housing of the servo amplifier must not exceed 1000V crest [73]. By IEC 61800, voltage spikes less than 50µs between phases must not exceed 1000V. Moreover, voltage spikes less than 50µs between a phase and the housing must not exceed 2000V [74]. In the case of mains voltage unbalance more than 3%, a mains choke must be used. The actual measurements of the final power distribution system are given in Section 4.3 of this document. Table 4.1 summarizes the power, voltage, and current requirements for the VT Roller Rig.

Table 4.1. Minimum estimated power, voltage, and load requirement of the VT Roller Rig.

Equipment	Power (KVA)	Voltage (V)	Current (A)
ServoStar	2 × 50	3 × 208 to 480VAC 50 to 60Hz	2 × 60
AKD	6 × 4.49	3 × 240 to 480VAC 50 to 400Hz or DC	6 × 5.4
PSU	2 × 1.46	3 × 320 to 575VAC 45 to 65Hz	2 × 2.1
Other	10	3 × 240 to 480VAC 50 to 60Hz	40

American Electric Power Company (AEP) agreed to upgrade the existing 3-phase 480/277VAC service at the CVeSS facility from 600A to 800A. AEP engineers calculated that the additional electrical load could be added to the existing transformer and used a spare 4" PVC conduit to provide an additional 200kVA dedicated to the Roller Rig. To perform the upgrade, CVeSS was required to update the CT cabinet per AEP specifications [75]. CVeSS was also responsible for following the service meter and disconnect regulations provided on the AEP Service Guide [76].

CVeSS sought professional help from Bell Electric of Blacksburg Inc. to perform the required modifications for the service upgrade. Figure 4.4 shows the APCO specifications followed throughout the service upgrade.

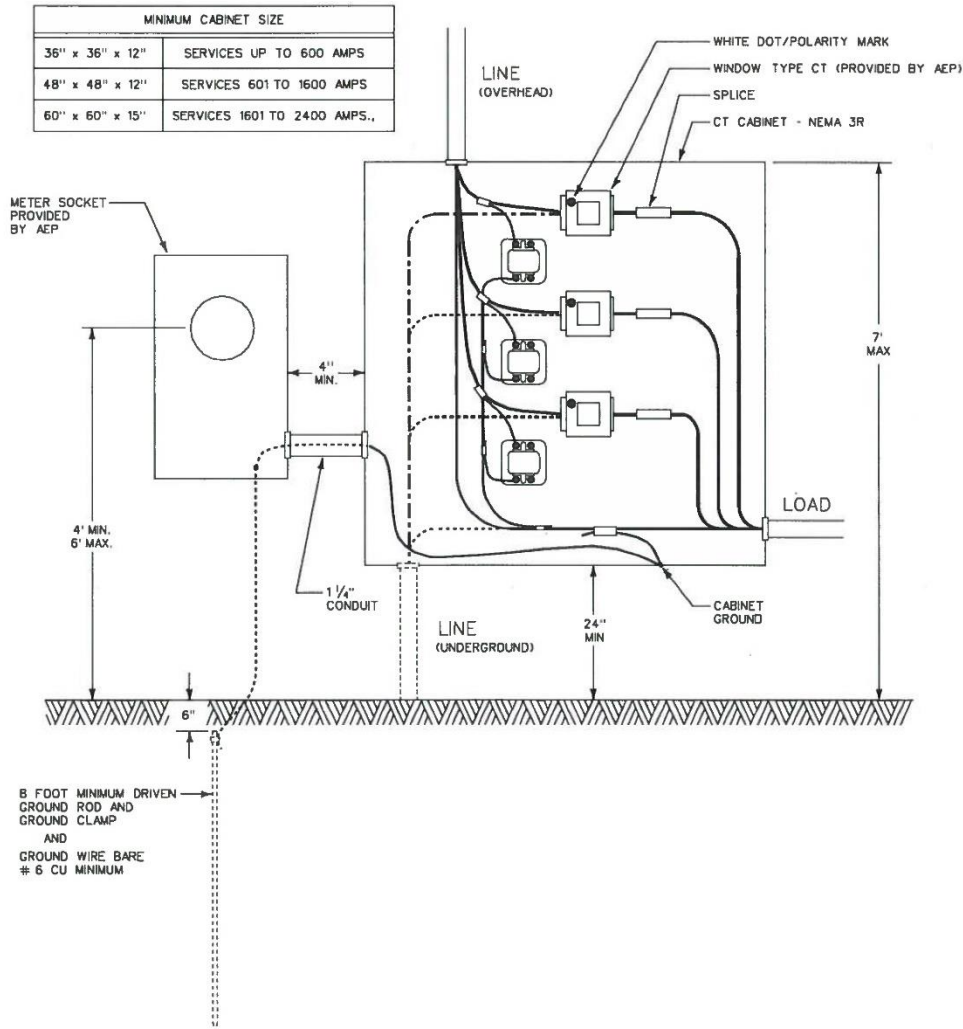


Figure 4.4. AEP specifications for 600A to 800A service upgrade (reprinted with permission, courtesy of AEP) [75].

#### 4.1.2 Isolating Transformer

Considering the high sensitivity of digital drives to the incoming power noise, proper isolation is required to eliminate the electrical noise coming in from the electrical service. Isolating transformers have been considered as a traditional solution for providing high isolation in electronic circuitry without adding too much size, weight, complexity, and cost to the system. They offer an effective means for meeting the requirements of domestic and international safety standards for electronic equipment. In the United States, such standards are set by the Occupational Safety and

Health Administration (OSHA), with product testing performed according to appointed laboratories, such as Underwriters Laboratories (UL). Throughout Europe, safety standards are established by the International Electrotechnical Commission (IEC), with testing performed by the laboratories of individual member nations, such as the Verband Deutscher Elektrotechniker (VDE) in Germany.

Considering possible future expansions in the VT Roller Rig, the load may incorporate linear power supplies, switched-mode power supplies (SMPS), or a combination of both. A single isolating transformer can help the system design meet all of the isolating requirements now and in the future. SMPSs convert AC voltage to DC directly in an off-line rectifier followed by a capacitive filter. The converted high voltage is switched at frequencies from kHz to MHz. MOSFETs are used to switch the voltage waveforms on and off. The output voltage of the SMPS is proportional to the pulse width of the switched or chopped waveform and duty cycle of the pulse wave.

By modulating the pulse width of the output waveform, the output voltage can be automatically adjusted. Pulse-width-modulated (PWM) voltage is applied to the motor terminals. During both rising and falling edges of the PWM voltages, the motor case tends to follow the voltage applied due to the capacitive coupling from the motor winding to the motor case. Current will flow in the ground wire of a grounded motor when the voltage rises and falls. These current pulses are short in duration and occur at the PWM frequency. Electrical noise due to these pulses can radiate if proper shielding techniques are not used. Shielded motor cables with the ground can prevent the radiated or capacitively coupled noise to other cables. Another effective technique is to use tightly bundled or twisted motor cables with ground. Detailed discussions on electromagnetic shielding and grounding are provided in Section 4.4.

When used with an SMPS, an isolating transformer can prevent higher-order harmonic signals from degrading the performance of consuming circuitry. This is especially important for microprocessors, which rely on harmonically rich, high-frequency clock signals for their timing. Improperly isolated, these harmonic signals can appear as interference to other functions in the system, even resulting in excessive output voltage ripple in the power supply.

Motor manufacturer recommends using an isolating transformer for 400V to 480V networks that are asymmetrically grounded or not grounded as shown in Figure 4.5 [73]. At the CVeSS facility, protection against indirect contact is vital, and the highest level of shock hazard protection is maintained. The ServoStar and AKD drives can be operated via a 3-phase isolating transformer with Wye-N secondary connection, 480Y/277 secondary voltage, Delta primary connection. The

latter requirement is due to the existing service available at the CVeSS. Moreover, CSA and UL approvals are required, and the transformer should comply with DOE/TP1 and C802.2 efficiency regulations.

The performance of an isolating transformer can be affected by temperature [77]. As a result, isolating transformers often add cooling requirements to the design. An effective way around this issue is using K-factor transformers instead of regular ones, wherever possible. K-factor transformers are designed to tolerate heating due to harmonics associated with non-linear loads [78]. Harmonics can indicate their presence in many ways: over-heating, device malfunctions, telephone interference, equipment vibration, and breakers tripping.

The HPS Sentinel energy efficient K-factor transformers (Hammond Power Solutions, Inc., WI, USA) are designed to tolerate heating due to harmonics associated with non-linear loads. These components have become a popular means of addressing overheating problems where drives, personal computers, electronic ballasts, telecommunication equipment and other similar power electronics are found in high concentration. For the purpose of the VT Roller Rig, a K20 transformer was selected. Table 4.2 summarizes the specifications of the equipment.

**Table 4.2. Specifications for the VT Roller Rig isolating transformer.**

Specification	Value
K-Factor	20
Rating	200kVA 3Phase
Primary Voltage	480D
Secondary Voltage	480Y/277VAC
Frequency	60Hz
Temperature Rise	150°C
Efficiency Regulation	DOE/TP1 and C802.2
Impedance	4% - 7%

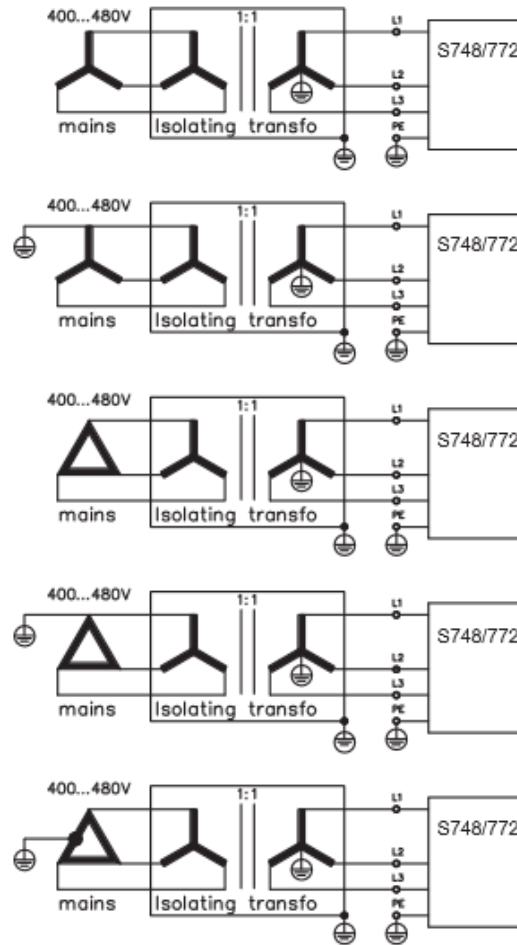


Figure 4.5. Application of an isolating transformer (courtesy of Kollmorgen) [73].

#### 4.1.3 Power Filtering

Since the ServoStar servo amplifiers are used in an industrial park and close to small industrial operations, then additional filter measures must be implemented. Moreover, these devices can cause high-frequency interferences in non-industrial environments. This requires measures for interference suppression like additional external EMC filters.

The filtering effect of the mains filters is only assured when the permissible power rating of the mains filters is not exceeded even on peak loading of the servo amplifiers. The maximum permissible power rating of the mains filter ( $P_{Fmax}$ ) is

$$P_{Fmax} = \sqrt{3}V_R \cdot I_{RF}, \tag{22}$$

where  $V_R$  and  $I_{RF}$  are the rated voltage and current of the filter. Maximum power consumption of the servo amplifier ( $P_{Smax}$ ) is

$$P_{Smax} = g\sqrt{3}V_R \sum_{i=1}^n I_{peakSi}, \quad (23)$$

where  $g$  is the coincidence factor( $\leq 1$ ),  $n$  is the number of axes on the filter, and  $I_{peakSi}$  is the peak current of each servo amplifier axis. For proper sizing the mains filters,  $P_{Fmax}$  should be bigger than  $P_{Smax}$ .

Based on the motor manufacturer recommendation, the rated current of the filter  $I_{RF}$  should be

$$I_{RF} > 2. \sum_{i=1}^n I_{RSi}, \quad (24)$$

and  $I_{RSi}$  is the rated current of the amplifiers on each axis. Assuming  $g = 1$  and single axis on each filter,  $P_{Smax}$  is found to be 66.51kVA (38.4kW). Schaffner’s 3-phase FN 258 filters have been known as the industry standard EMC solution for power drive systems. The FN 258-100-35 component well satisfies the requirements of the VT Roller Rig. Table 4.3 summarizes the technical data of this filter.

**Table 4.3. Technical data of 3-phase Schaffner FN 258-100-35 filters [79].**

Maximum continuous operating voltage	$3 \times 480/277VAC$
Operating frequency	$dc$ to 60Hz
Typical drive power rating	55kW
Rated current	100A at 50°C (110A at 40°C)
Overload capability	4 × rated current at switch on, 1.5 × rated current for 1 minute, once per hour
Leakage current	25.8mA
Power loss	51W

Figure 4.6 shows the 3-phase FN 258-100-35 filter and its block diagram. Typical filter attenuation of the FN 258 filters is also given in Figure 4.6.

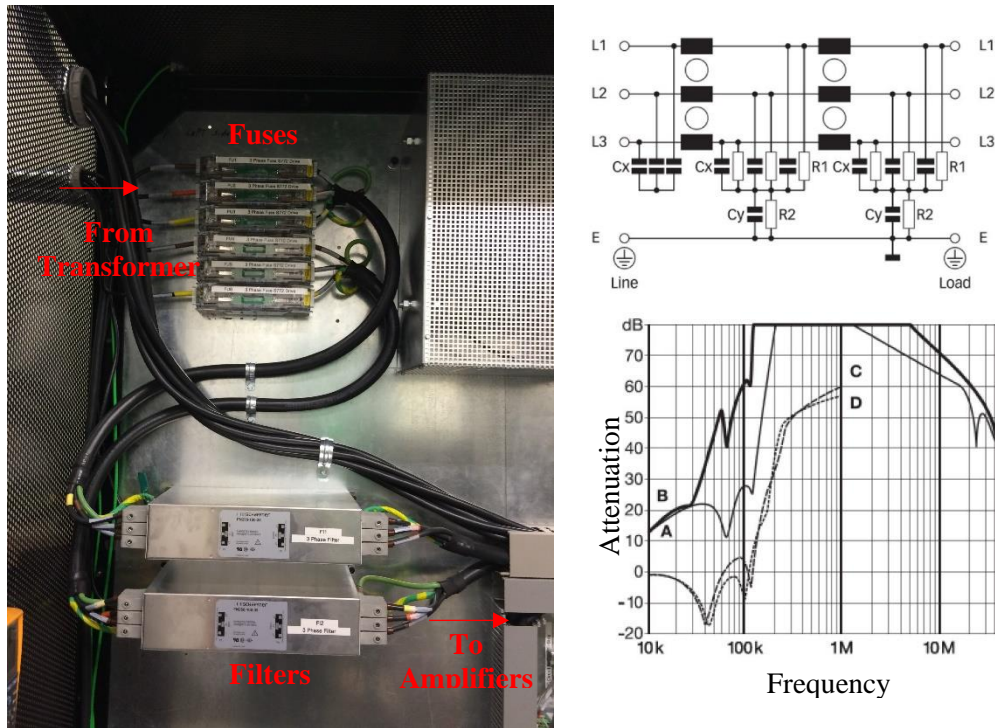


Figure 4.6. Schaffner FN 258-100-35 filter and its block diagram (courtesy of Schaffner) [79].

#### 4.1.4 DC Power

Multiple layers of safety and monitoring systems ensure maximum safety for the VT Roller Rig users and machinery. Extensive discussion of these systems is given in Chapter 5 of this document. Safe-Torque-Off (STO), Ready-to-Operate (RTO), Emergency Stop, Regenerative Dynamic Braking, Holding Brake, and Thermal Monitoring systems are the most critical safety systems that should remain ON regardless of the status of the Rig. Under no circumstances should the user be allowed to bypass these systems. Special procedures should be followed after killing the mains lines, before touching the servo amplifiers inside the control cabinet. Simple disconnection of mains switch is not sufficient. This group of safety systems should not be excluded, even if the Logic ON-OFF is deactivated.

An uninterruptible auxiliary power system feeds the circuitry mentioned above at 24VDC. It consists of two parallel DC power systems that each can provide up to 40A rated current (-25°C to 70°C), and up to 215A peak current for 12ms. An electronic switchover unit switches to battery operation without interruption so that loads continue to be consistently supplied. It also provides information regarding the charging state, remaining runtime, and service life of the rechargeable battery module at all times and thereby increases system availability. One power supply feeds the RTO, Regenerative Dynamic Braking, Holding Brake, and the logic circuitry of

servo amplifiers. The negative pole of this power supply is grounded, since the voltage should be 24VDC non-floating. The other system feeds the STO, Hardware Enable, Logic ON-OFF, emergency stop, and Motor-Short Dynamic Braking circuits.

Each DC power system consists of a Quint-PS 3Phase-480VAC to 24VDC power supply, a Quint-UPS 24VDC to 24VDC electronic switchover unit, and a 38Ah 24VDC battery (all from Phoenix Contact, Blomberg, Germany). The DC power system has a separate mains switch that is only manually switchable. It is isolated from the circuit breaker with shunt trip capability that feeds the servo amplifiers. Shielded AWG10 power lines of the DC power supplies are protected with 16A circuit breakers against surges. Figure 4.7 shows the DC Power system of the VT Roller Rig.

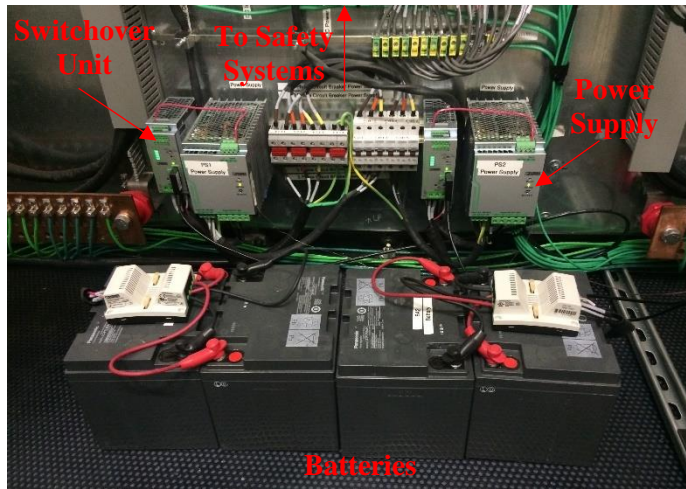
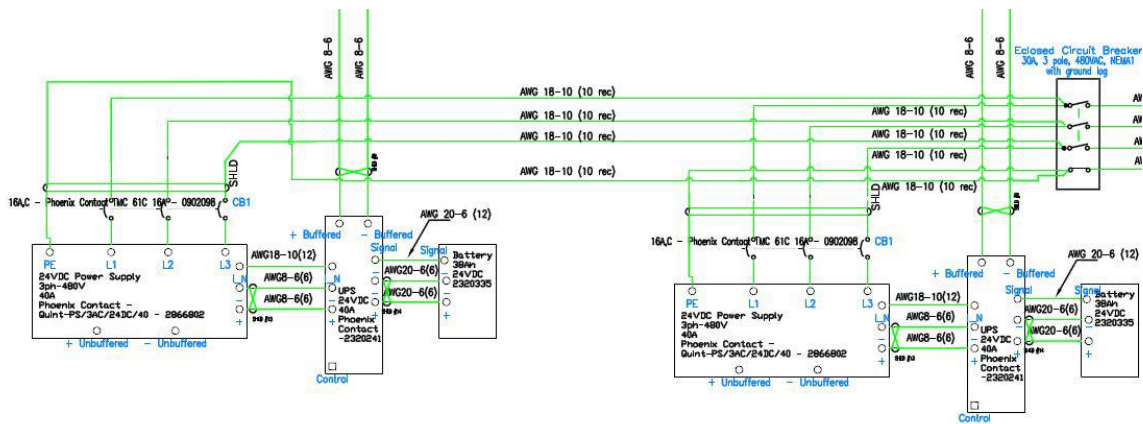


Figure 4.7. Uninterruptible auxiliary DC power system of the VT Roller Rig.

These two power systems run in parallel, but independently. In case higher operational safety is required, the systems could be interconnected in parallel for redundancy. If a fault occurs in one of the electronic switchover units, the second system automatically takes over the entire supply without interruption. With this configuration, each electronic switchover unit should be sized

properly so that it can handle the total current requirements (80A). Figure 4.8 is a schematic of the parallel connection of the two DC power systems for redundancy.

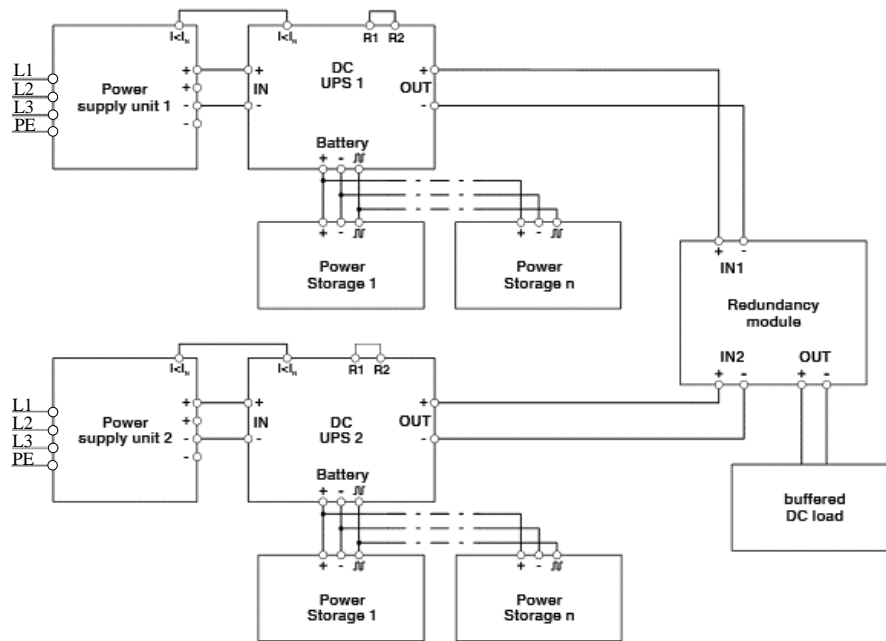


Figure 4.8. Parallel connection of DC power systems for redundancy (courtesy of Phoenix Contact) [80].

#### 4.1.5 DC-Bus

The regenerated power (due to braking or motor-generator operation mode) is divided between the two ServoStar servo amplifiers by connecting them through a common DC-Bus link circuit. Each ServoStar servo amplifier has a 900 $\mu$ F capacitor. The rated voltage of the AKM84T motors are at least as high as the DC bus link voltage divided by  $\sqrt{2}$  produced by the servo amplifier ( $U_{n \times Motor} \geq U_{DC} / \sqrt{2}$ ).

If one of the devices fails due to an internal short circuit, other devices can become damaged. Therefore, intermediate circuit fuses are required on the DC-Bus Link. If an internal short circuit occurs in one of the devices, only the intermediate fuses will be tripped, and the rest of the system continues uninterrupted. The sum of the rated currents for all of the servo amplifiers connected in parallel to a ServoStar must not exceed 96A. Figure 4.9 shows the DC-Bus link topology between the two ServoStar servo amplifiers.

If the under-voltage threshold is undershot in the DC bus link, the servo amplifier generates a fault, and it will not be ready to operate (not RTO see Section 5.3). Contacts of the servo amplifier may still be live, even after disconnecting the servo amplifier from the main supply. The manufacturer recommends waiting for at least eight minutes after disconnecting the servo amplifiers from the

mains supply before touching potentially live sections of the equipment or removing any connections. The DC bus link voltages should always be measured and components not handled until the voltage is below 40V.

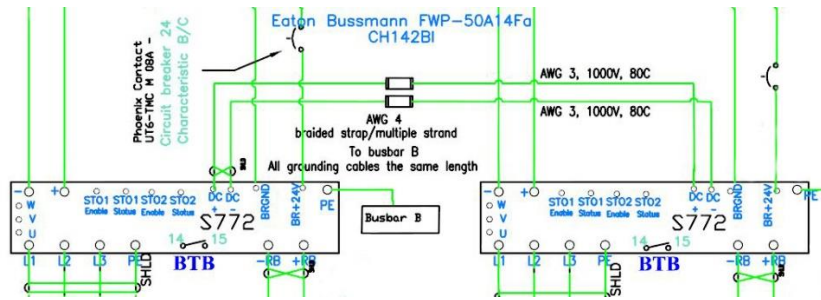


Figure 4.9. DC-Bus link topology. The actual DC-Bus link is marked in red.

## 4.2 Grounding

### 4.2.1 Star Ground Topology

All chassis ground, signal ground, or common points need to be tied together at a star connection internal to the equipment. A star connection is a single point ground. This star connection is then tied with a single conductor to an earth ground point [81]. The single conductor used in this technique is sized per the International Electrical Code (IEC) and should be low in inductance. Practicing this grounding technique will prevent ground loops and ensure properly grounded equipment against shock hazards. System grounding is essential for proper performance of the drive system. Figure 4.10 compares the correct and incorrect grounding topologies.

In addition to the safety grounding, a high-frequency ground must be provided that connects the back panel to the enclosure and, ultimately, to earth ground. The objective is to provide a highly low impedance path between the filters, drives, power supplies, and earth ground. This high-frequency ground is accomplished with the use of a flat braid or copper bus bar. It is important not to rely on a standard wire for the high-frequency ground. In general, a cable has an inductance of 8 nH-per-inch, regardless of diameter. At higher frequencies, this unwanted inductance between grounds equates to limited filter performance.

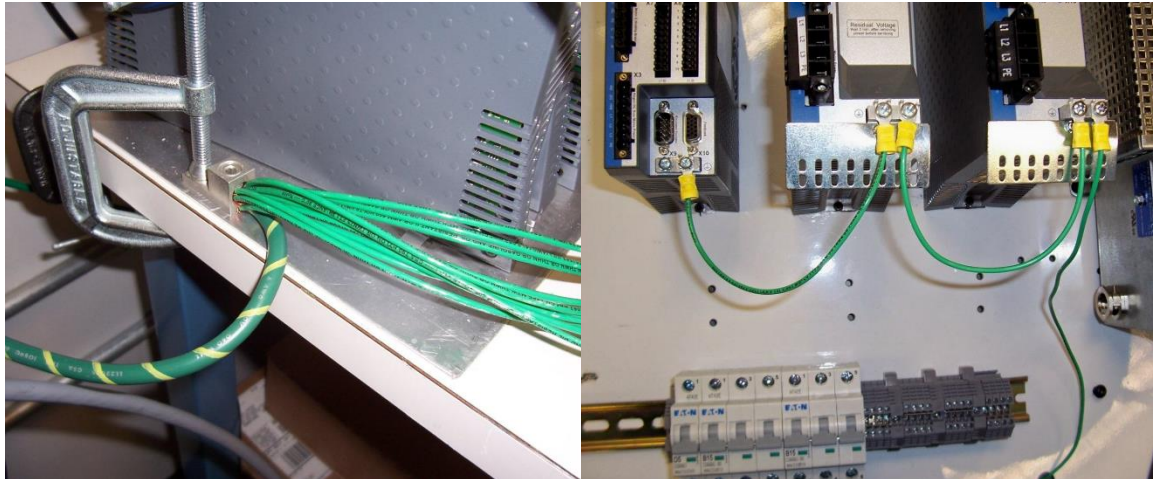


**Figure 4.10. Correct star ground connection (left) versus incorrect daisy chain ground (right, courtesy of Kollmorgen) [81].**

Two new 5/8"(D) by 8'(L) copper-clad steel rods were installed at the CVeSS facility for the Roller Rig. The procedure for installing the ground rods included:

- A 3-inch diameter hole was augured to a depth of X, 6 inches shorter than the length of the ground rod
- The ground rod was placed into the augured hole and driven 1 foot (if possible) into bottom of the hole
- Connections to ground rod using were made using ERICO CADWELD Exothermic connections (Pentair, Manchester, UK)
- Ground Enhancement Material (GEM) was premixed into a slurry form
- The appropriate amount of GEM was poured around the ground rod
- The area around the ground rod was tamped with a pole to ensure the GEM material completely fills the hole
- After 1 hour, the hole was filled with soil backfill
- The ground resistance was measured to ensure the ground rod had impedance less than  $20\Omega$

For measuring the ground resistance, an EXTECH Digital Earth Resistance Tester (FLIR Systems, Inc., MA, USA) was used. The test with one ground rod showed a  $32.7\Omega$  resistance. Therefore, a second ground rod was added at least one ground rod length away from the first rod. Stranded green THHN wire was used to connect the two ground rods. The second test showed  $19.5\Omega$  resistance for the two rods, which is less than the design goal for the VT Roller Rig.



Figure 4.11. Earth resistance testing.

#### 4.2.2 Shield Grounding

The rules for grounding the cable shield differ significantly from one system to another [82]. While some engineers believe in grounding the shield at one end to prevent ground loops [83], motor and power supply manufacturers have had repeated experiences where undesired noise was only eliminated through grounding both ends [84,85]. Some application notes specifically instruct the user not to terminate both ends of the shield to ground [86]. Meanwhile, others claim that if a cable's shield is grounded at one end only the opposing end of the shield is under-grounded, and it can represent a fire and shock hazard if the cable's shield becomes energized due to AC power system ground faults [87]. There is even a debate among those who agree with one end grounding on whether termination should be on the signal's source side or the receiver side.

The myth originates from the fact that low-frequency crosstalk is the sum of inductive and capacitive coupling contributions [88]. If the shield is grounded at one end, the shield voltage becomes zero, and the capacitive coupling will be ideally eliminated. Consequently, shielding a wire and grounding the shield at only one end will reduce the crosstalk only for high-impedance loads where capacitive coupling dominates inductive coupling before the addition of the shield. If inductive coupling dominates capacitive coupling before the addition of the shield, grounding the shield at only one end will not reduce the total crosstalk, and the shield will be ineffectual. In the case of low-impedance loads, a shield will reduce the total crosstalk by reducing the dominant

inductive coupling component only if it is grounded at both ends. This allows a current to flow back along the shield which provides a magnetic flux that cancels the magnetic flux from the generator circuit current.

From numerous discussions with experts in the field, and comparing textbooks with product instruction manuals, the final answer is that no single approach can fit all. The final approach for each system is a combination of source-side grounding, receiver-side grounding, and both-side grounding. To understand this statement, one should look at the frequency response and sensitivity. Tube receivers from 1960's had a combination of grounds at both ends. Audio sections of the same devices were grounded at one end. For the tuner section, the unwanted noise was the high frequency (above 108.1MHz in the US). In order to use both magnetic and capacitive coupling shields, grounds at both ends with no break in the shields were used. The audio section, however, was susceptible to 60Hz, which is a low frequency. It was also sensitive to ground differentials, therefore it had grounds at one end, the source side.

In today's circuitry, differential inputs are used to resolve the low-frequency noise caused by ground differentials. In cases where a single-ended signal with high gain is shielded, one may have to use an isolated ground. Primary shields may be used with internal shields grounded at one end, and secondary shields referenced at both ends for rejecting the high frequency. A good example of such signal in the VT Roller Rig is the force measurements from the dynamometer charge amplifiers. All measurements are single ended with a common ground. Provisions for grounding the shields at both ends assures maximum noise attenuation. The ultimate grounding solution remains to be verified through testing.

A common direct coupled noise source is when the ground that is being used for return or reference is not referenced to earth as expected. This is especially prevalent in a sensitive high-gain circuit like the VT Roller Rig. An important criterion in proper ground referencing in this system is separating the earth ground and neutral line in the power system. As shown in Figure 4.12, the earth ground and the neutral are at the same potential only at the main transformer in a power distribution network. Connecting the power return of the line to the ground instead of neutral would work, but it would likely put unintended noise on the ground line, negatively affecting all of the devices connected to it. The difference between the neutral line and earth ground is that neutral is a current carrying conductor while earth ground is a non-current carrying conductor by definition.

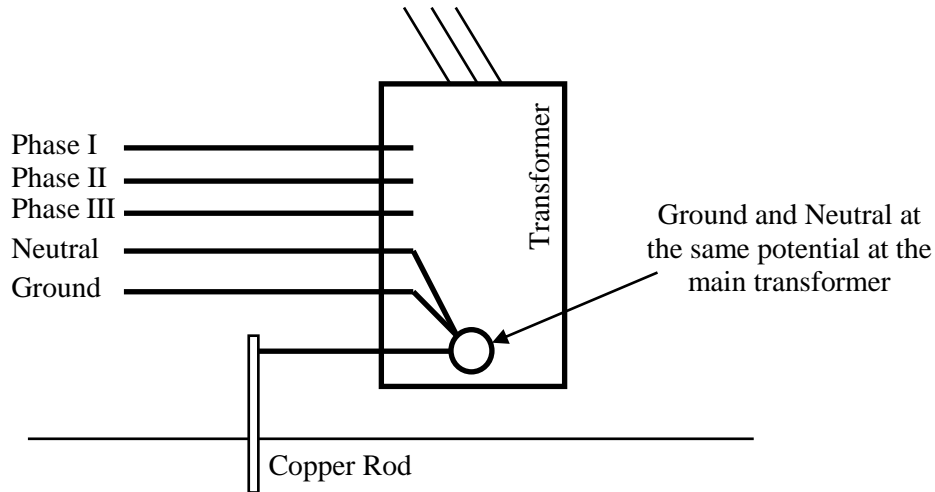


Figure 4.12. Coupled noise source due to connection between ground earth and neutral line.

#### 4.2.3 Additional Measures

To reduce the noise coupling possibilities, control and signal cables must be separated from power and motor wires. A distance of 20cm (8in.) is sufficient in most cases. These cables should also be shielded to reduce the effects of radiated interference. Where control cables cross power or motor wires, they should have an angle of 90 degrees to reduce the electromagnetic coupling effect.

The motor should be grounded close to the servo amplifier to obtain the lowest impedance to the current source. This reduces the noises in the machine grounds. The expense of this technique is an excessive amount of cable that complies with local electric codes. These cables are often expensive. Any unused wires should be terminated to ground to reduce the noise risks.

The eight servo drives shown in Figure 4.13 drive the eight permanent magnet AC servo motors of the Rig. These devices are manufactured according to certain EMC standards (i.e. IEC61000). Nevertheless, customary shielding is essential for preventing interference. VT engineers were warned by the motor and drive manufacturer that the digital servo drives will radiate high amplitude electromagnetic noise that sweeps the whole range of low frequency to 5MHz. Other sensitive motion control electronics, as well as all the sensory systems nearby, could be affected by this noise. Therefore, VT engineers paid particular attention to the task of designing a proper shielding for the PWM power electronics. The approach taken at the RTL to design a proper shield (Faraday Cage) for a slew of PWM controlled power electronics running the VT Roller Rig testing facility is reported in Section 4.4. Figure 4.13 shows the custom fabricated Faraday Cage for the VT Roller Rig. The Faraday Cage, cable shields, and motor housings are connected the isolated ground rod. Inside the Faraday Cage, all panels are bonded together using braided cables at paintless spots.



**Figure 4.13. The Faraday Cage (top) for the control tower (bottom) of the VT Roller Rig.**

### 4.3 Power Measurements

Various measurements are possible for checking the performance of a power distribution system. A Power Analyzer offers an extensive and powerful set of measurements including RMS values, phasor plot, event capture, scope waveform, and harmonics. Some give a general impression of power system performance, while others can be used to investigate specific details. This section provides an overview of the measurements performed on the VT Roller Rig power distribution

network. Figure 4.14 shows the configuration of Fluke 437 Series II power analyzer that was used for performing various measurements on the VT Roller Rig power distribution system.

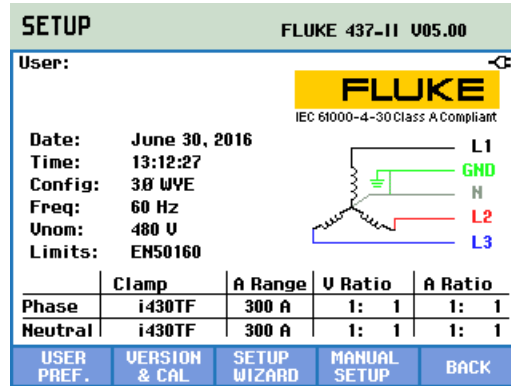


Figure 4.14. Configuration of Fluke 437 Series II power analyzer for measuring the VT Roller Rig power distribution system.

In a 3-phase power, phase voltages should be close to the nominal value. The RMS voltages should be measured neutral-to-line and line-to-line to check if power applied to the 3-phase motors is in balance. Voltage waveforms must be a sine wave that is smooth and free from distortion. Each phase voltage should not differ more than 1% from the average of the three. Current unbalance should not exceed 10% [89]. Voltage unbalance causes high unbalanced currents in stator windings resulting in overheating and reduced motor life. In the case of excessive unbalance, other measuring techniques should be used to further analyze the power system. The measurement shown in Figure 4.15 was taken during a normal test when both wheel and roller are rotating at a constant speed to maintain a constant creepage. After switching on each measurement, a settling time of about 10 seconds passed before the measurement started.

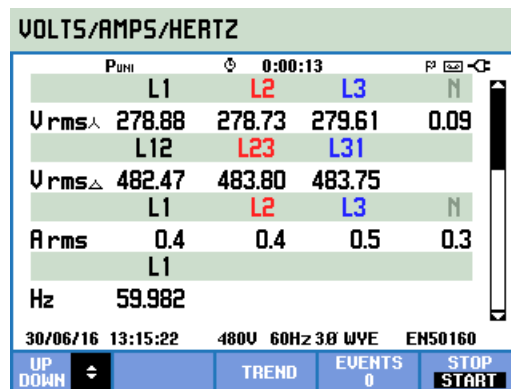


Figure 4.15. Volts/Amps/Hertz measurement of the distribution system.

Three most important events that should be monitored for a power quality analysis are Dips and Swells, Interruptions, and Rapid voltage changes. Dips (Sags) and Swells are fast deviations from the normal voltage. The magnitude may be ten up to hundreds of volts. The duration may vary from

a half cycle to a few seconds as defined in EN61000-4-30. During a dip, the voltage drops; during a swell the voltage rises. In three phase systems, a dip begins when the voltage on one or more phases drops below the dip threshold and ends when all phases are equal to or above the dip threshold plus hysteresis. The trigger conditions for dips and swells are threshold and hysteresis. Dips and swells are characterized by a duration, magnitude, and time of occurrence. The occurrence of Dips (Sags) and Swells may indicate a weak power distribution system. In such a system, the voltage will change considerably when a big motor, such as AKM84T, is switched on or off. This may cause lights to flicker or even show visible dimming. It may cause reset and loss of data in computer systems and process controllers. By monitoring the voltage and current trend at the power service entrance, it is possible to find out if the cause of the voltage dip is inside or outside the building. The cause is inside the building (downstream) when the voltage drops while current rises; it is outside (upstream) when both voltage and current drop.

During an Interruption, the voltage sinks well below its nominal value. In three phase systems, an interruption begins when the voltage on all phases are below the threshold and ends when one phase is equal to or above the interruption threshold plus hysteresis. The trigger conditions for interruptions are threshold and hysteresis. Interruptions are characterized by a duration, magnitude and time of occurrence.

Rapid voltage changes are quick transitions of the RMS voltage between two steady-states. Rapid voltage changes are captured based on steady voltage tolerance, steady time, minimum step detected, and minimum rate (%/s). When a voltage change crosses the dip or swell thresholds, it is considered a dip or swell and not a rapid voltage change. Over three one-hour continuous tests, the power analyzer did not capture any events. Measurements were recorded at every 0.1s. Figure 4.16 through Figure 4.19 show the bar graph of voltage for three phases and the neutral line. The frequency was pretty consistent throughout the tests, 59.98Hz. Figure 4.20 shows the frequency and voltage unbalance during an hour of the experiment. Similarly, Figure 4.21 through Figure 4.24 shows the bar graph of current for the three phases and the neutral line. Figure 4.25 shows the frequency, and current unbalance during an hour of the experiment. For all these figures, measurements were performed right before the drives' input, after the passive filters. The Vdc on the three phases and neutral were measured 0.04V, -0.02V, 0V, and 0.02V, respectively.

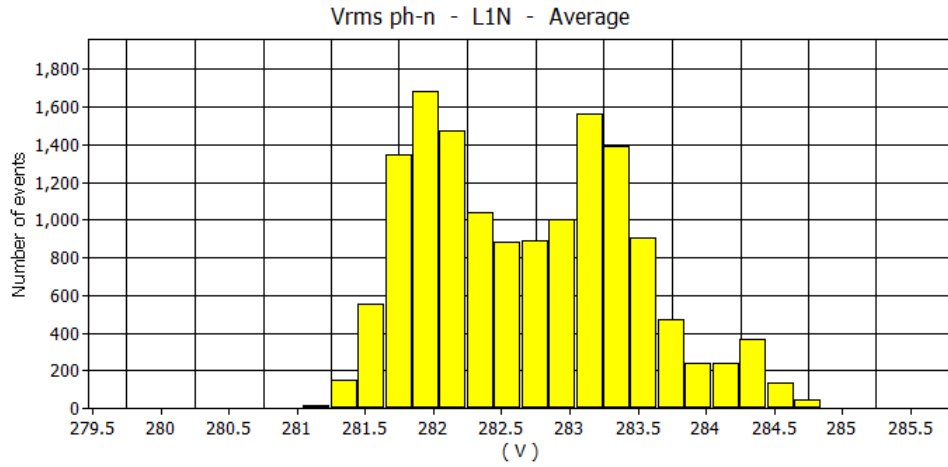


Figure 4.16. L1N Vrms phase-to-neutral during an hour of continuous experiment. The crest factor was 1.435.

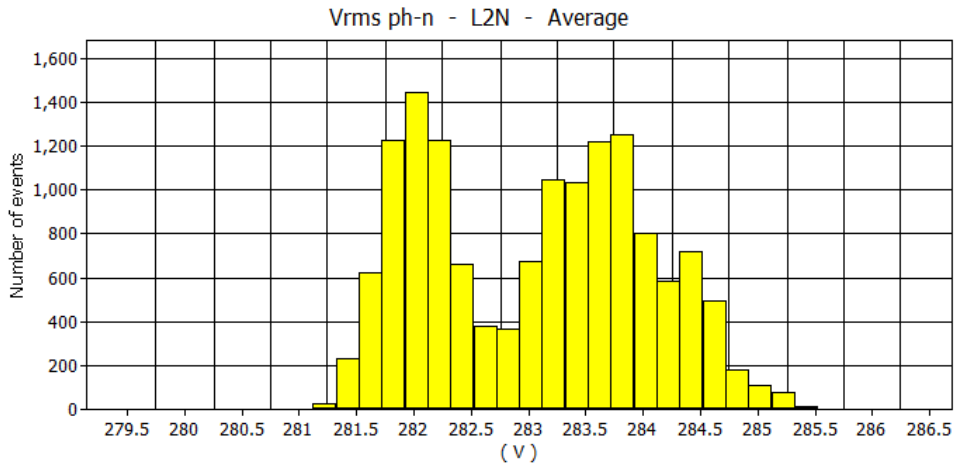


Figure 4.17. L2N Vrms phase-to-neutral during an hour of continuous experiment. The crest factor was 1.435.

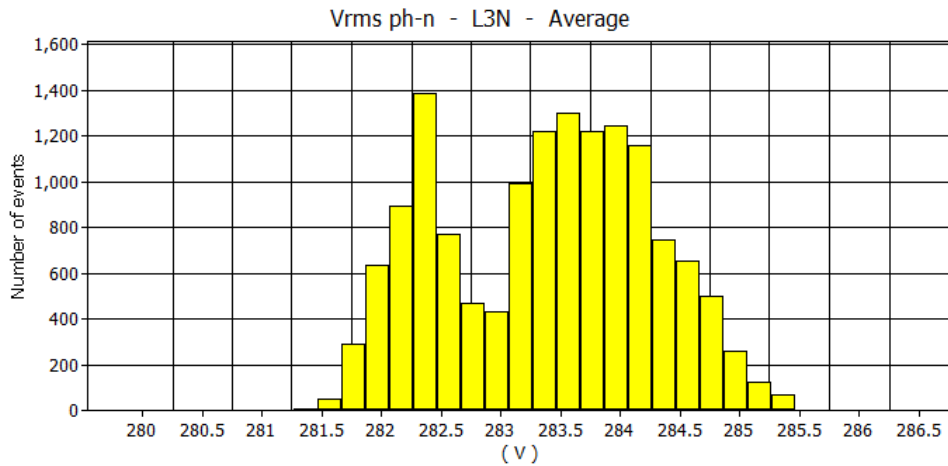


Figure 4.18. L3N Vrms phase-to-neutral during an hour of continuous experiment. The crest factor was 1.445.

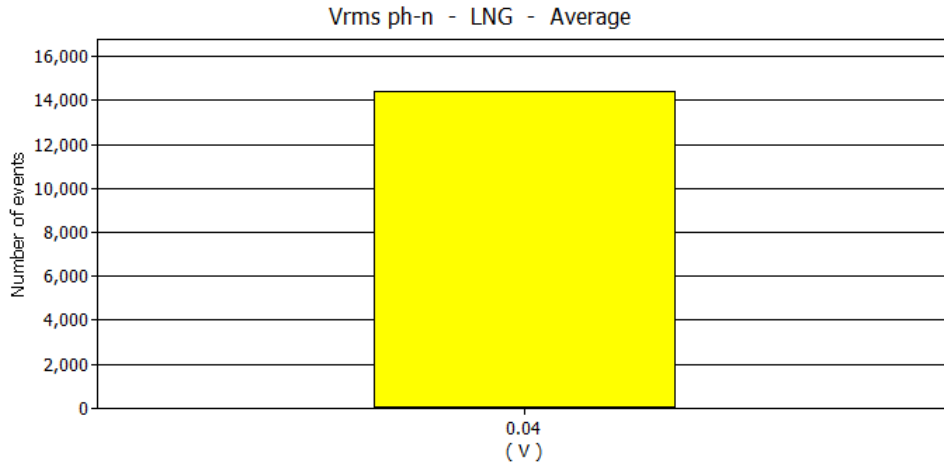


Figure 4.19. LNG Vrms during an hour of continuous experiment.

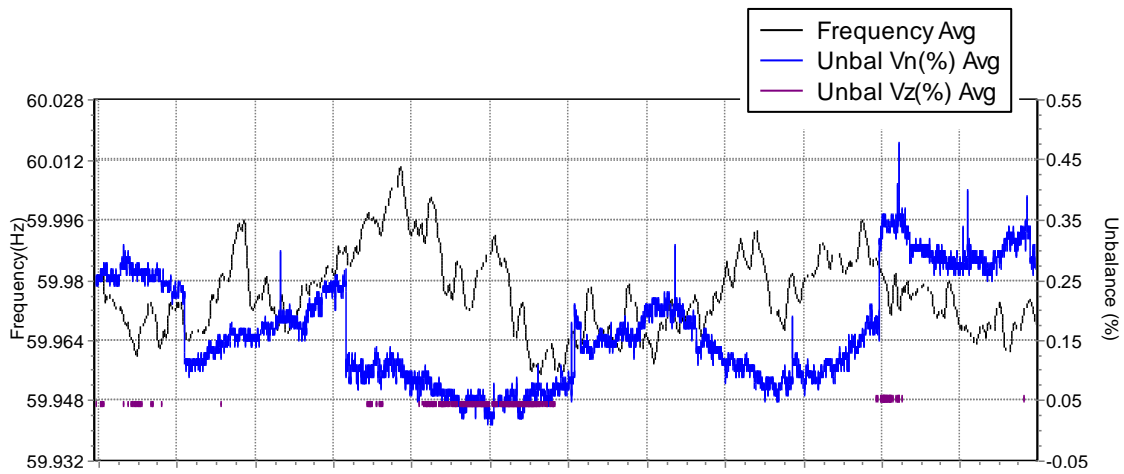


Figure 4.20. The frequency and voltage unbalance during an hour of experiment.

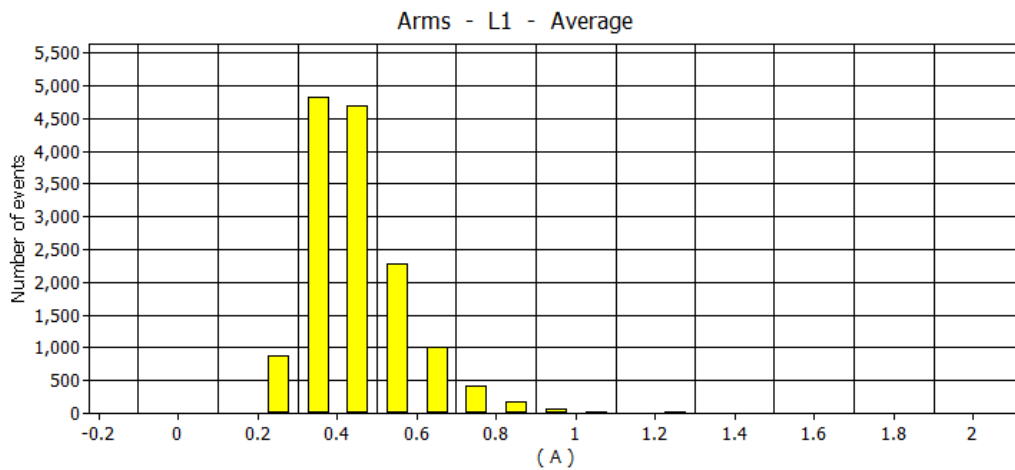


Figure 4.21. L1 Arms current during an hour of continuous experiment. The crest factor was 5.

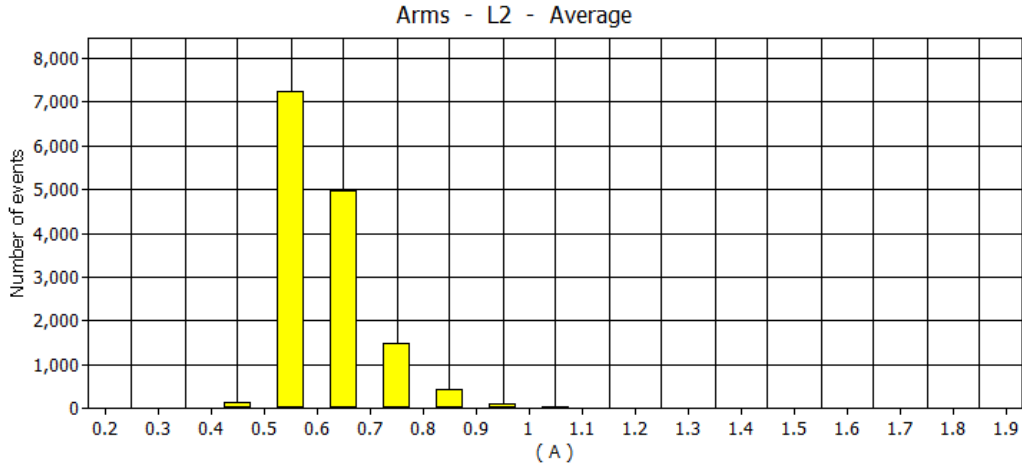


Figure 4.22. L2 Arms current during an hour of continuous experiment. The crest factor was 4.5.

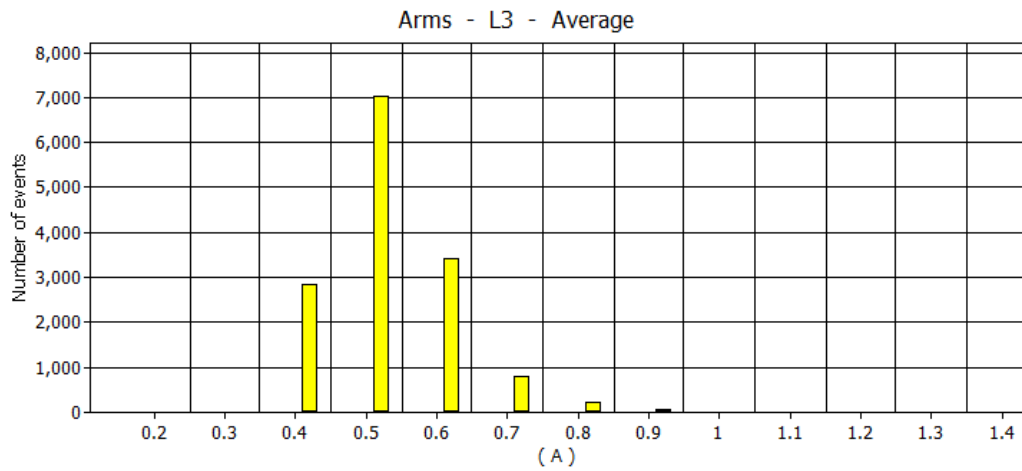


Figure 4.23. L3 Arms current during an hour of continuous experiment. The crest factor was 5.25.

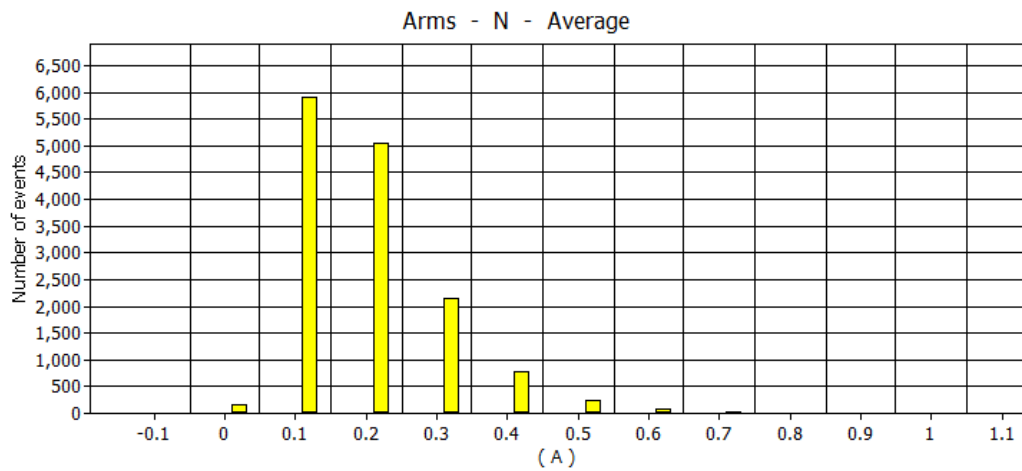


Figure 4.24. Neutral Arms current during an hour of continuous experiment.

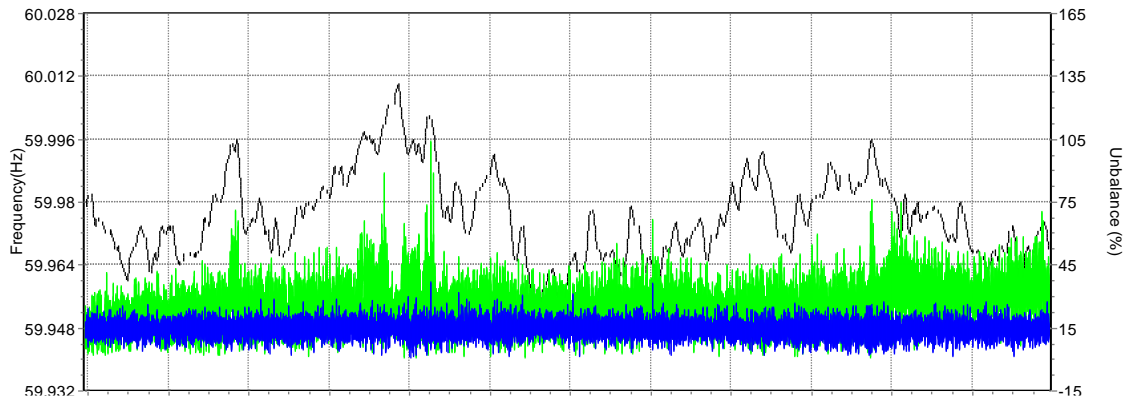


Figure 4.25. The frequency and current unbalance during an hour of experiment. Measurements were performed right before the drives' input.

The phasor plot in Figure 4.26 shows the phase relation between voltages and currents in a vector diagram. In the vector diagram the phase voltages and currents A (L1), B (L2), and C (L3) appear in sequence at equal distance (120 degrees). Current vectors should have the same direction as the voltage vector with usually less than 30-degree phase shift. The vector of reference channel A (L1) points to the positive horizontal direction. The A (L1) amplitude is also a reference for the measuring grid size. Additional numerical values are fundamental phase voltage and/or current, frequency, and phase angles. The screen header shows RMS voltage and/or current values.

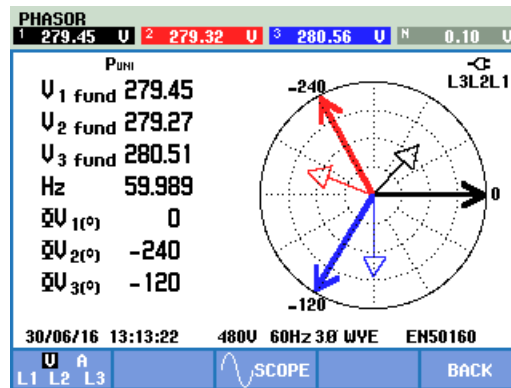


Figure 4.26. The phasor plot of the VT Rolle Rig power distribution system. Measurements were performed right before the drives' input.

The scope waveform plot shown in Figure 4.27 shows an oscilloscope-style display of voltage and/or current waveforms with a fast update rate. The screen header shows the related RMS voltage/current values. Four waveform periods are displayed. Channel A (L1) is the reference channel. The Crest Factor CF indicates the amount of distortion: a CF of 1.41 means no distortion and higher than 1.8 means high distortion. [89].

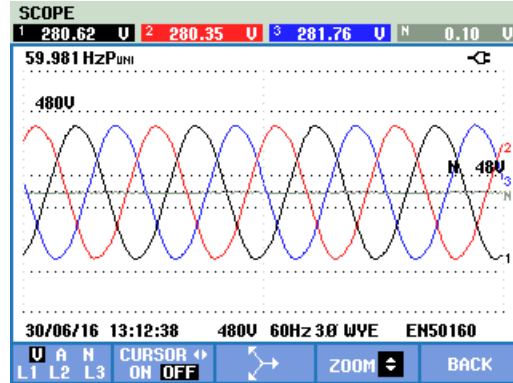


Figure 4.27. The scope waveform plot of the VT Rolle Rig power distribution system.

A waveform can be considered as a combination of various sine waves with different frequencies and magnitudes. The contribution of each of these components to the full signal is measured. Readings can be given as a percentage of the fundamental, as a percentage of all harmonics combined (RMS value), or as RMS value. Harmonics are often caused by non-linear loads such as switched mode power supplies, and adjustable speed motor drives. Harmonics can cause transformers, conductors, and motors to overheat.

The harmonics measurements can be viewed in a bar graph. The bar graph shows the percentage contribution of each of the components related to the full signal. A signal without distortion should show a 1<sup>st</sup> harmonic (the fundamental) at 100% while the others are at zero. In practice, this will not occur because there always is a certain amount of distortion resulting in higher harmonics. A pure sine wave becomes distorted when higher frequency components are added to it. The THD percentage represents distortion. Two other similar measurements are the percentage of the DC component and the K-factor. The K-factor is measured for current and power. It is a number that quantifies potential overload in transformers due to harmonic currents. Higher order harmonics influence the K-factor more than low order harmonics. K-factor is an indication that should match the selected transformer. Proper K-factor along with kVA are required for handling non-linear, harmonics-rich loads, such as that of S772 and AKD drives. When measuring harmonics with inter-harmonics off, harmonics group according to IEC61000-4-7 is used, and a 1.5s smoothing filter is applied.

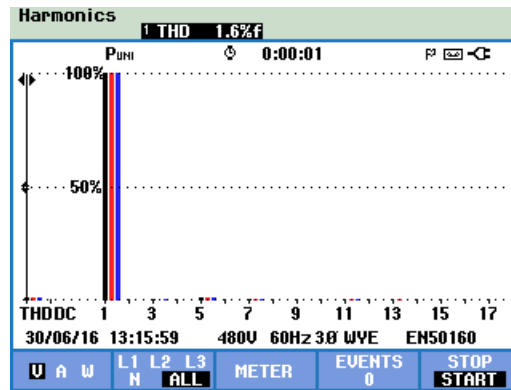


Figure 4.28. Voltage harmonics of the VT Roller Rig power distribution system during a normal test. Measurements were performed right before the drives’ input.

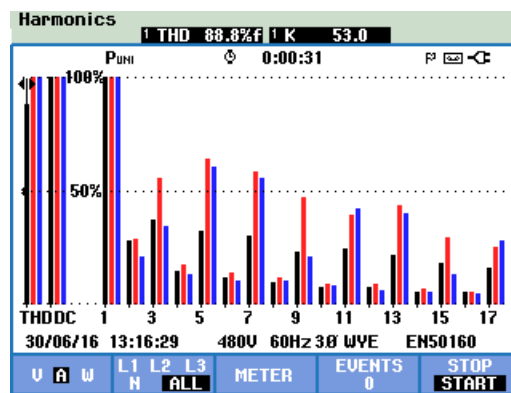


Figure 4.29. Current harmonics of the VT Roller Rig power distribution system during a normal test. Measurements were performed right before the drives’ input.

The harmonic number indicates the harmonic frequency: the first harmonic is the fundamental frequency (60 or 50Hz), the second harmonic is the component with two times the fundamental frequency (120 or 100Hz), and so on. The harmonics sequence can be positive (+), zero (0), or negative (-). The table below gives an overview.

Table 4.4. A summary of harmonics sequences.

Order	1 <sup>st</sup>	2 <sup>nd</sup>	3 <sup>rd</sup>	4 <sup>th</sup>	5 <sup>th</sup>	6 <sup>th</sup>	7 <sup>th</sup>	8 <sup>th</sup>	9 <sup>th</sup>	10 <sup>th</sup>	11 <sup>th</sup>	...
Frequency (Hz)	60	120	180	240	300	360	420	480	540	600	660	...
Sequence	+	-	0	+	-	0	+	-	0	+	-	...

The positive sequence component is the normal component such as present in balanced 3-phase systems. Positive sequence harmonics try to make a motor run faster than the fundamental. The negative sequence component results from unbalanced phase-to-phase currents and voltages. This component, for instance, causes a ‘braking’ effect in 3-phase motors: making the motor run slower

than the fundamental. In both cases, the motor loses torque and heats up. Harmonics can also cause transformers to overheat. Even harmonics disappear if waveforms are symmetrical, i.e. as equally positive and negative. Zero sequence current harmonics add in Neutral conductors. This can cause overheating of these conductors. Unbalance exceeding 2% is considered as too high [89].

Current distortion is to be expected in a system with non-linear loads like DC power supplies and variable frequency drives (VFD). When the current distortion starts to cause voltage distortion (THD) of more than 5%, this signals a potential problem.

The Schaffner FN-258 filters are known for reducing the line harmonics, in addition to improving operating conditions and voltage fluctuations. Figure 4.30 through Figure 4.33 show the effect of passive filters on the line side of the power distribution network. For all these figures, measurements were performed before the passive filters. Comparing Figure 4.25 and Figure 4.30 shows the significant effect of passive filters in lowering the current unbalances from 30% to around 8%. Comparing Figure 4.29 and Figure 4.33 reveals a significant drop in THD from 88.8% to 39.1% (15% to 5% for Az). This further leads to a reduction in the K-factor from 53 to 20.6, which is just equal to the K-factor of the selected isolating transformer (Table 4.2).

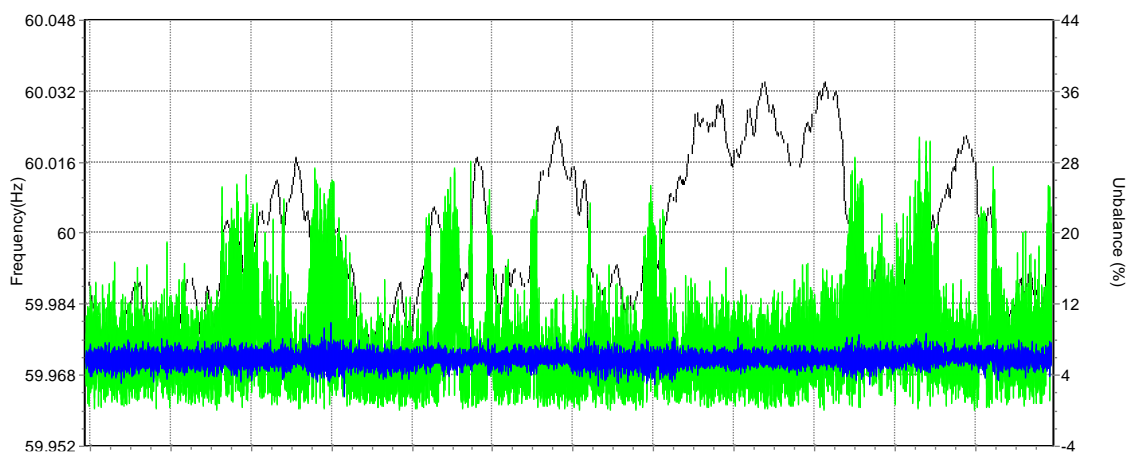


Figure 4.30. The frequency and current unbalance before the filters during an hour of experiment. The working conditions of the system are the same as Figure 4.25.

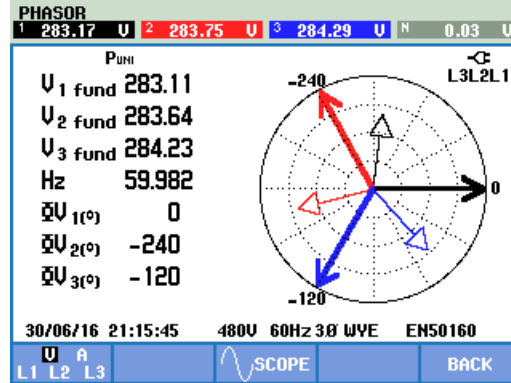


Figure 4.31. The phasor plot of the VT Rolle Rig power distribution network. Measurements were performed before the passive filters. The working conditions of the system are the same as Figure 4.26.

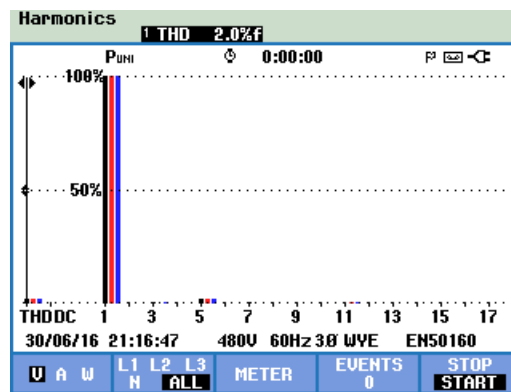


Figure 4.32. Voltage harmonics before the passive filters during a normal test. The working conditions of the system are the same as Figure 4.28.

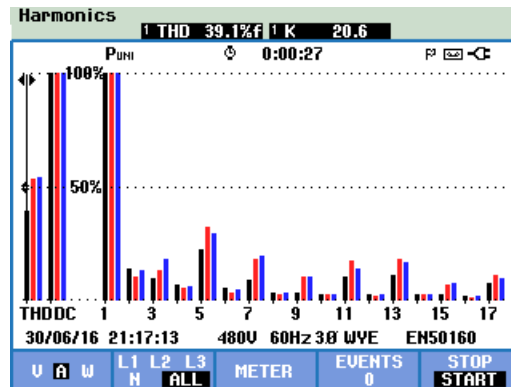


Figure 4.33. Current harmonics before the passive filters during a normal test. The working conditions of the system are the same as Figure 4.29.

Power measurements can be used to record apparent power (kVA) of a transformer over several hours to check if the transformer is overloaded. The following power and energy measurements are critical in a 3-phase power system:

- Real power (W, kW): measurement of the full spectrum as normally registered by energy usage meters.

- Apparent power (VA, kVA): the entire spectrum is used.
- Reactive power (var, kvar): the fundamental frequency is used.
- Harmonic power (VA or kVA Harm): non-fundamental frequency powers.
- Unbalance power (VA or kVA Unb.): unbalance part of the real power.
- Fundamental real power (W or kW fund): the fundamental frequency is used.
- Fundamental apparent power (VA, kVA fund): the fundamental frequency is used.
- $\cos \phi$  or DPF:  $\cos \phi$  is phase angle between fundamental voltage and current.

Energy measurements include:

- Active energy (Wh, kWh).
- Apparent energy (VAh, kVAh).
- Reactive energy (varh, kvarh).
- Forward energy (Wh, kWh forw.): energy consumed.
- Reverse energy (Wh, kWh rev): energy delivered.

Reactive power (var) is most often due to inductive loads such as motors, inductors, and transformers. Reactive powers (var) do not contribute to efficient energy transfer. They are not included in the real power (W, kW) measurement, but cause energy losses due to wire resistance. Additionally, utilities may charge additional cost when var readings are high because they need to provide apparent power (VA, kVA) that does not include both var and W. Unbalanced powers and harmonic power are included in Watt measurement of energy usage meters so that the user has to pay for it. However, these powers cannot be converted effectively into mechanical energy and are therefore considered a loss. Increasing the diameter of conductors reduces copper loss (Effective kW). If harmonics are present, consult a qualified engineer before installing capacitors. Nonlinear loads such as adjustable frequency motor drives cause non-sinusoidal load currents with harmonics. Harmonic currents increase the kvar and thereby decrease total power factor.

A power system is utilized in an optimal way if voltage and current are sinusoidal, in phase, and balanced. Any deviation from this will cause efficiency loss and thus a waste of energy. A low power factor is usually resulting from reactive devices such as transformers and motors. The ideal situation is a  $\cos \phi$  or DPF equal or close to 1. The PF in a power measurement can be interpolated as follows:

- PF = 0 to 1: not all supplied power is consumed, a certain amount of reactive power is present. Current leads (capacitive load) or lags (inductive load).

- PF = 1: the device consumes all supplied power. Voltage and current are in phase.
- PF = -1: device generates power. Current and voltage are in phase.
- PF = -1 to 0: device is generating power. Current leads or lags.

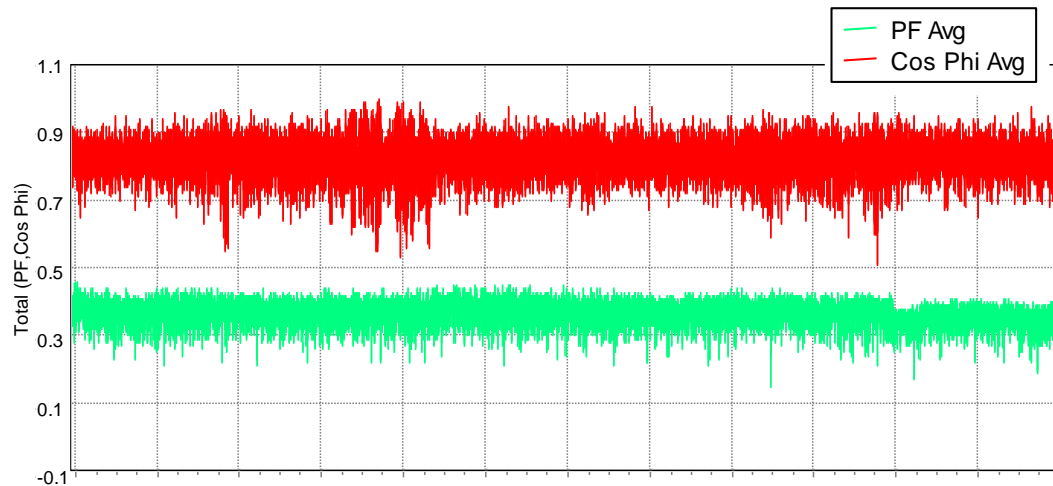


Figure 4.34. The power factor and  $\cos \phi$  for the VT Roller Rig during an hour of normal test.

The power factor can be improved by adding capacitors in parallel with the inductive load. Considering the current harmonics in the Rig's power system, a qualified engineer can add PF-correction capacitors to increase the PF.

In general, the most efficient way to troubleshoot electrical systems is to begin at the load and work towards the building's service entrance. Measurements are taken along the way to isolate faulty components or loads.

#### 4.4 Noise Attenuation

Energy transfer could happen through different coupling mechanisms between a noise source and a receptor (victim). The source and the victim can both be electronic hardware devices, and coupling mechanism can take one or a combination of the following forms: conductive, capacitive, magnetic (or inductive), and electromagnetic (or radiative). Electromagnetic coupling usually occurs when devices are separated from each other by a distance equal or greater than the wavelength of the emitted wave. Both source and victim act like an antenna that can transmit energy regardless of the intermittent material. In the real world, a system or subsystem can be simultaneously an emitter and a receptor.

Electromagnetic interference (EMI) can disrupt the operation of electronic devices in the vicinity of electromagnetic fields. Electromagnetic compatibility (EMC) studies the undesired generation,

propagation, and reception of energy through electromagnetic interference or radio frequency interference (RFI). It is achieved by reducing the emissivity of the source or susceptibility of the victim. This compatibility is accomplished using electronic filtering for the sources, and equipment shielding for the victims. References on the general principles of EMI are available [90–92], as well as methodologies for calculating radiated emissions [93].

The primary solution in the industry and testing facilities for efficient motion control remains an induction or AC synchronous motor fed by a pulse width modulated (PWM) adjustable speed drive (ASD) [94]. However, the switching nature of ASD converter circuits results in waveforms that contain not only the required fundamental components but also unwanted harmonic voltages. The waveforms are primarily associated with the steep-fronted PWM voltage pulses in the drives [95]. Although present with BJT's, the EMI contamination with IGBT's is often more severe due to their extremely low rise times (50 to 150ns) [96].

The frequency characteristics of the PWM output of modern drives have been established [97,98]. The low-order harmonic voltages are most likely to provoke unwanted torque response from the motor. The high-order harmonics can lead to acoustic noise, which can excite a mechanical resonance [99]. But most importantly, all harmonics can radiate and interfere with contiguous sub-systems [100]. The resulting EMI not only threatens the performance of the motion control system but corrupts other low-power measurement signals that can be the main outcome of the entire system. The EMI can influence the performance of motion control system through contaminating position feedback or corrupting the ground reference. Common mode chokes with shielded cables are proven to be effective in reducing or contain the dv/dt currents [101]. Proximate susceptible signals can be extremely sensitive such as electrostatic measurements of a piezoelectric load cell ( $\pm 30$  pC) [102], a strain gage torque measuring flange ( $\pm 10$ VDC) [103], or a photoelectric laser sensor (4-20A) [104]. On the other hand, the high power at the output stage of the drives, as well as broad spectrum of emitted frequency, make it difficult to reduce and contain the noise.

Certain factors increase the EMI risk. Higher drive AC line voltages lead to higher DC bus voltages (Table 4.5 line 5). Faster switching frequencies of converters/inverters increase the number of switch transitions and sum of total radiated energy (Table 4.5 line 6). The higher output switching dv/dt increases peak common-mode ground current (Table 4.5 line 7). Finally, assembling large quantities of drives in a concentrated area increases the potential to cause EMI with adjacent sensitive equipment [97]. Some or all of the above may be inevitable depending on the motion requirements.

This study, reports the approach taken at the Railway Technologies Laboratory (RTL) of Virginia Tech (VT) to design a proper shield for a slew of ASD's running the VT Roller Rig testing facility. The eight servo motors in Figure 4.35 are driven by eight servo drives in Figure 4.36. Table 4.5 summarizes the electrical specifications of S772 and AKD digital servo drives (Kollmorgen, Radford, VA) that are utilized in the VT Roller Rig. Both product series are the latest technologies offered globally. According to the manufacturer, these servo amplifiers have been tested by authorized laboratories to ensure their conformity with the EC EMC directive (2014/30/EC) [73]:

- IEC 61000-6-1 / 2 (Interference Immunity in Residential & Industrial Areas)
- IEC 61000-6-3 / 4 (Interference Generation in Residential & Industrial Areas)

These servo amplifiers meet the noise emission requirements to the C2 environmental category as per IEC 61800-3, granted that the motor cable is kept shorter than 10m. With a motor cable length of 10m or longer, the drives meet the requirements to the category C3. Increased motor cable length also may lead to overvoltages that exceed the motor safe level [105]. In fact, the installation can significantly affect the actual achieved emission level. Motor cable length and type, the grounding system, as well as the voltage supply system used, all influence the final result. C2 is considered the correct and most cost effective ASD solution for all environments [106]. There are drives on the market claiming to be C1 compliant [107]. Other manufacturers doubt that this is valid only for conducted emissions, and they do not necessarily comply with the limits for radiated emissions [106].

Depending on the surrounding equipment and number of drives, the ASD's can cause interference even if C2 certified and installed properly. This can require measures for interference suppression like additional shielding and external EMC filter, if possible. The manufacturer of the machine/plant is responsible for keeping the emissions within the required noise levels. The ASD output voltage transition times and typically conducted noise oscillation frequency in mostly concentrate in AM radio frequency band [97]. VT engineers were warned by the motor and drive manufacturer that the digital servo drives will emit high power electromagnetic noise that sweeps the whole range of low frequency to 5MHz. Therefore, VT engineers paid particular attention to the task of designing a proper shielding for the ASD's.

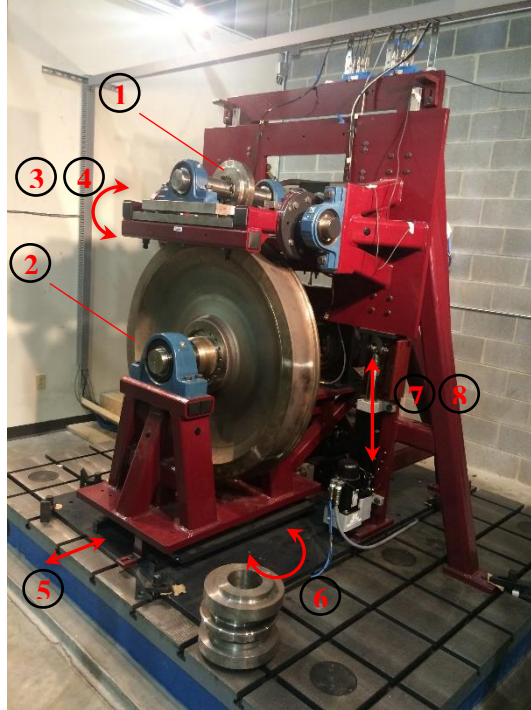


Figure 4.35 Permanent magnet AC synchronous motors for each degree of freedom of the Rig.

Table 4.5. Electrical specifications of S772 and AKD digital servo drives [73,108].

Electrical Data	S772	AKD
Rated supply voltage (L1, L2, L3)	3 × 480V, 50/60Hz	3 × 480V, 50/60Hz
Rated input power for continuous operation	50kVA	4.49kVA
Rated output current (rms value, ±3%)	72Arms	6Arms
Peak output current (for approx. 0.5s, ±3%)	140Arms	18Arms
Rated DC bus link voltage	290 – 675V	340 – 680V
Switching frequency of the output stage	8 or 16kHz	8kHz
Voltage rise speed dU/dt	4.8 $\frac{kV}{\mu s}$	7.2 $\frac{kV}{\mu s}$
Bandwidth of current controller	> 1.2 kHz	2.5 to 4 kHz



**Figure 4.36. Eight digital servo drives run the VT Roller Rig testing facility. The drives are part of the control tower that is responsible for motion control and safety of the system.**

Grounding and shielding are the two primary techniques for reducing the emission or diverting the electromagnetic noise away by providing an alternative low-impedance path [109]. Grounding is implemented in a star scheme to prevent any ground loop formation between the protected components. In practice, ground rods are tested to make sure that they provide the least impedance path for the noise. Shielding of cables is often implemented by surrounding them with an outer conductive layer that is grounded at one or both ends. A specially shaped conducting material can be used to form a shield against EMI by partially or entirely surrounding an EMI emitter, such as an electronic circuit. Typical materials used for electromagnetic shielding include metallic alloys in the form of sheet, screen, and foam [110].

Looking at Figure 4.36 and Table 4.5, reveals the essential task of protecting measurements of the VT Roller Rig against concentrated high-power emissions of ASD's. Moreover, proper shielding for these drives is limited by other system requirements including heat management, structural strength, cable routing, safety, cost, size, mobility, and aesthetics. Figure 4.37 shows the close distance between the VT Roller Rig mechanical setup and control tower, which includes all ASD's,

power devices, and safety systems. Various local and international codes of practice deal with the issue of electromagnetic radiation, particularly in residential environments (e.g. IEC 61000, UL 1283, ISO 11451, CISPR 11). An engineer can change many factors in his design to comply with the system requirements and the EMC directives. The result, however, may or may not provide enough protection for the sensitive instruments. Some of the objectives that the designer often has to deal with include the significance of the radiated noise, susceptibility of the nearby electronics, and the estimated shielding effectiveness of the shield. The first two parameters are often approximated from the data provided by manufacturers. The latter, however, requires calculation or simulation. The simulation environment allows for changing the design parameters to get the necessary shielding effectiveness while satisfying other constraints in the overall system.



**Figure 4.37. The mechanical setup of the VT Roller Rig is located right across a hollow wall from the control tower, which includes all ASD's, power devices, and safety systems.**

Different materials provide different shielding properties if used as an enclosure. Enclosures often have apertures for wiring and ventilation purposes. When thermal management is involved, the enclosure may have to be fully perforated. The skin effect changes with the frequency of radiation; therefore, the thickness of the shield is also a determining factor in the overall shielding effectiveness of the enclosure. On the other hand, when various equipment are installed in a cage, mobility, and structural rigidity can be very limiting. The effects of material, apertures, and thickness are evaluated in this study using finite element analysis on a simplified two-dimensional (2D) model. The shielding effectiveness is assessed as the proportion of electric or magnetic field intensity at the place of an observer in the presence and absence of the enclosure. Results show that

magnetic permeability and electrical conductivity are the most critical properties in choosing the proper shielding material. They affect the capability of the material in forming the flux lines to divert the electromagnetic field. They also change the sensitivity of the overall shield to openings and apertures. This paper also shows how skin effect can drastically reduce the performance of the same enclosure at lower frequencies. The shield is optimized through iterative simulations and fabricated with particular attention to grounding and gap sizes. After commissioning the VT Roller Rig, experimental tests are performed using a conventional loop antenna to measure the actual shielding effectiveness of the implemented cage, and the results are compared against expected simulated numbers.

#### 4.4.1 Material Selection

In some cases, EMI/RFI shielding is in the form of a spray. The spray is acrylic based and is applied to plastic electronic housings. Highly pure metals such as nickel, silver, and copper in the spray help to reduce or eliminate EMI and RFI [111]. EMI/RFI shielding agents are also available as paints and brush on coatings. RF shielding enclosures filter a range of frequencies for specific conditions. Copper is used for radio frequency (RF) shielding because it absorbs radio and magnetic waves. Properly designed and constructed copper RF shielding enclosures satisfy most RF shielding needs, from the computer and electrical switching rooms to hospital CAT-scan and MRI facilities. Aluminum, steel, and iron have also been used for shielding purposes whenever there is a cost or material limitation [112]. PVC is widely used in electrical conduits. EMI shielding effectiveness of PVC is also of interest. Table 4.6 shows the material properties of these materials that are pertinent to electromagnetic considerations.

In evaluating the performance of different materials for EMI shielding purposes, three material properties are the most important factors: electrical conductivity, relative permittivity, and relative electromagnetic permeability. Electrical conductivity measures the ability of material to conduct the electric field. It is often denoted by  $\sigma$  that is defined as the inverse of resistivity  $\rho$ . The permittivity of a material relates the electric flux density to the electric field. It is denoted by the symbol  $\epsilon$  and represents the resistance that is encountered when forming electric fields inside a medium. In an isotropic material, relative permittivity ( $\epsilon_r$ ) is usually given as a division of permittivity of the medium to that of free space  $\epsilon_0 = 8.85 \times 10^{-12} F/m$ . Relative permittivity is always greater than or equal to 1, which means that electric field is always reduced relative to what it would be in free space.

Electromagnetic permeability ( $\mu$ ) is a measure of how easily a magnetic field can pass through a material. It represents the orientation of bound magnetic particles within a material and relates the magnetic flux density ( $H$ ) to the magnetic field ( $B$ ) through  $B = \mu H$ . The permeability of vacuum is denoted by  $\mu_0$  and is equal to  $\mu_0 = 4\pi \times 10^{-7} H/m$ . The electromagnetic permeability of a medium is often denoted by its relative permeability  $\mu_r$  that is a measure of the permeability of a medium relative to that of vacuum. Paramagnetic and ferromagnetic materials have  $\mu_r$  greater than 1, while  $\mu_r$  is less than 1 for diamagnetic materials. When a paramagnetic or ferromagnetic material is inserted into a magnetic field, like inside a coil, it causes the lines of magnetic flux to concentrate. This increases the inductance of the coil compared with the same coil with an air core.

**Table 4.6. Material properties of aluminum (Al), copper (Cu), Iron (Fe), carbon steel, and PVC.**

Property	Name	Unit	Property Group	Al	Cu	Fe	Carbon Steel	PVC
Relative Permeability	$\mu_r$	1	Magnetic	1.000022	0.999994	5000*	100	1
Electrical Conductivity	$\sigma$	$\frac{S}{m}$	Electrical	$3.774e^7$	$5.998e^7$	$1.12e^7$	$4.032e^6$	$1e^{-16}$
Relative Permittivity	$\epsilon_r$	1	Electrical	1	1	1	1	3.18
Density	$\rho$	$\frac{kg}{m^3}$	Mechanical	2700	8700	7870	7850	1375
Young's Modulus	E	Pa	Mechanical	$70e^9$	$110e^9$	$200e^9$	$200e^9$	$3.38e^9$

\* Maximum Value

#### 4.4.2 Models

Field radiated from an electromagnetic source is represented by transversal waves (TE) that are described by the following Maxwell's equation in 2D [113]:

$$\nabla \times \mu_r^{-1}(\nabla \times E) - k_0^2 \left( \epsilon_r - \frac{j\sigma}{\omega\epsilon_0} \right) E = 0, \tag{25}$$

where E is the electric field intensity vector,  $\omega$  is the frequency, and  $k_0 = \omega\sqrt{\epsilon_0\mu_0}$ . The terms inside the second parentheses denote the complex permittivity of the environment.

Depending on the material, an enclosure between the source and emitter can diminish the strength of coupling between them. The effectiveness of this electromagnetic shield is expressed as the ratio of two values of the electromagnetic field at a particular location in presence and absence on the

shield. Electric shielding effectiveness  $SE_{dB}$  and magnetic shielding effectiveness  $SM_{dB}$  can be defined as [114]:

$$SE_{dB} = 20 \times \log\left(\frac{E_1}{E_2}\right), \quad (26)$$

or

$$SM_{dB} = 20 \times \log\left(\frac{H_1}{H_2}\right), \quad (27)$$

where E is the electric field and H is the magnetic field at a particular location. For an infinite conducting shield,  $SE_{dB}$  and  $SM_{dB}$  are equal and only depend on the frequency of the wave, conductivity, permeability, and thickness of the shield. For finite enclosures,  $SE_{dB}$  and  $SM_{dB}$  are different and depend on the location within the enclosure [114]. These two equations can be used as the tools for measuring the performance of a specific shield or compare the effectiveness of two shields in the same field. In this study, equation 27 is used for plotting the results and discussions.

For simulation purposes, the radiation source can be modeled as a magnetic boundary source  $H(x, y, z)$  with the frequency given by parameter  $\omega$ . The parametric solver of the finite element package accounts for the frequency by switching the direction of the magnetic field coordinates harmonically. Changing the magnetic field generates the moving electrical field that radiates throughout the physical domain. Due to symmetry in generation and propagation of the electromagnetic field in the above configuration, the domain can be reduced to 2D. Figure 4.38 shows the simplified 2D model used in finite element analysis. A cross section of the shield with apertures is shown in this figure. Openings are assumed to have the same dimensions and the longest dimension of the apertures to be in the plane of cross section shown in Figure 4.38.

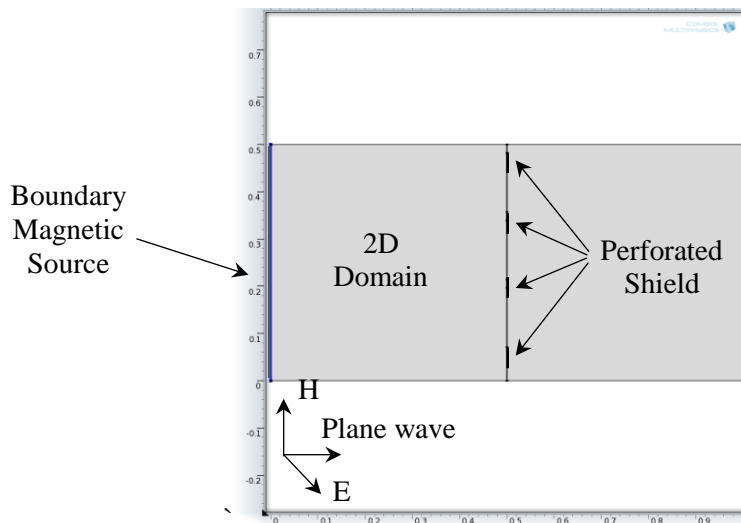


Figure 4.38. The Simplified 2D model of the electromagnetic source and perforated shield.

#### 4.4.3 Simulations

COMSOL Multiphysics has a set of solvers for PDE-based problems in the frequency domain. The geometry and configuration of Figure 4.38 are defined in COMSOL with 2D axisymmetric structure. Material properties of air are assigned to the 2D domain, as given in Table 4.7. The boundary magnetic source is assumed to have one component in y direction  $H_y = 10A/m$ . This forces the longest side of the apertures to be normal to the E-field, which is the worst case for shielding [114]. Since the ratio of electric or magnetic fields at the same location determines the shielding effectiveness, the intensity of the field at the boundary source will not affect the results. The 2D domain is 0.5m (h)×1m (w), and thickness of the shield is 1mm in the first set of simulations. The effect of thickness will be further evaluated in the second part of the paper.

Three apertures are shown in Figure 4.38 to create a perforated shield. Each opening is 0.125m(h), which is identical to removing 75% of the full shield. The size of openings in the sheet plate is enforced by the minimum ventilation required for keeping the high power electronics below maximum allowable temperature. Smaller openings cause less air intake, thus higher temperature within the enclosure.

**Table 4.7. Material properties of air.**

Property	Name	Value	Unit	Property Group
Relative Permeability	$\mu_r$	1	1	Magnetic
Electrical Conductivity	$\sigma$	0	$\frac{S}{m}$	Electrical
Relative Permittivity	$\epsilon_r$	1	1	Electrical
Density	$\rho$	1.275	$\frac{kg}{m^3}$	Mechanical

Figure 4.39 shows the mesh quality of the proposed 2D model. The minimum mesh quality is 0.8372 with a total number of 32892 triangular elements. To have enough degrees of freedom in evaluating the skin effect, fine mesh with a minimum quality of 0.8659 is used for the shield.

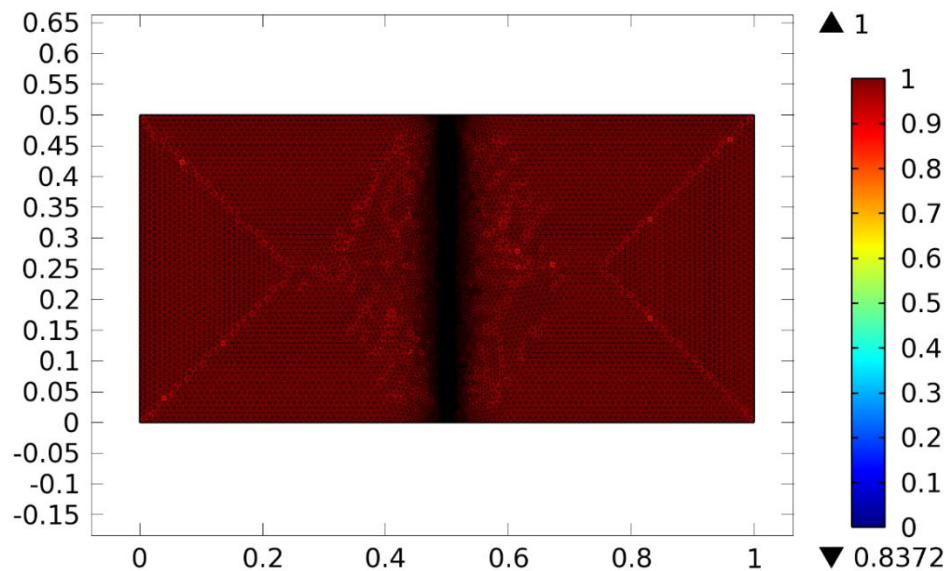


Figure 4.39. Mesh quality of the physical model in COMSOL Multiphysics.

COMSOL provides three different solvers for electromagnetic problems: MUMPS, PARDISO, and SPOLES. For fast simulations, it is suggested to use MUMPS and PARADISO. MUMPS is usually required for cluster computation while PARADISO is multi-core capable. Results given in this paper are found with MUMPS direct solver.

#### 4.4.3.1 $SM_{dB}$ of different materials

Figure 4.40 shows the electric displacement field norm (D) and magnetic field density norm (B) at  $\omega = 100\text{kHz}$  without any shield. Figure 4.41 shows B, when full and perforated aluminum shields are added to the model. As mentioned above, full shield means that there is no perforation or opening in the shield. Perforated shield means that three 0.125m openings are cut out of the shield for ventilation purposes.

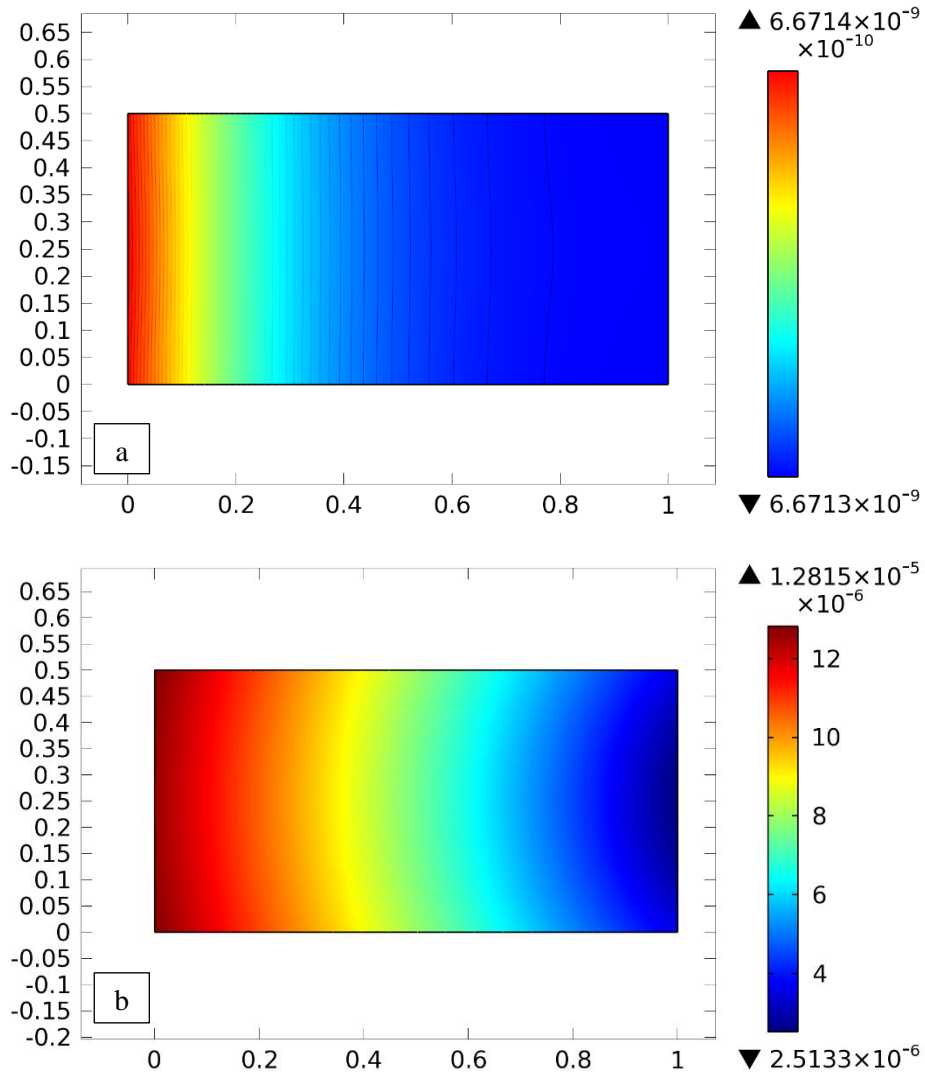


Figure 4.40. a) Electric displacement field norm (D), and b) magnetic field density norm (B) at 100kHz without any EMI shielding.

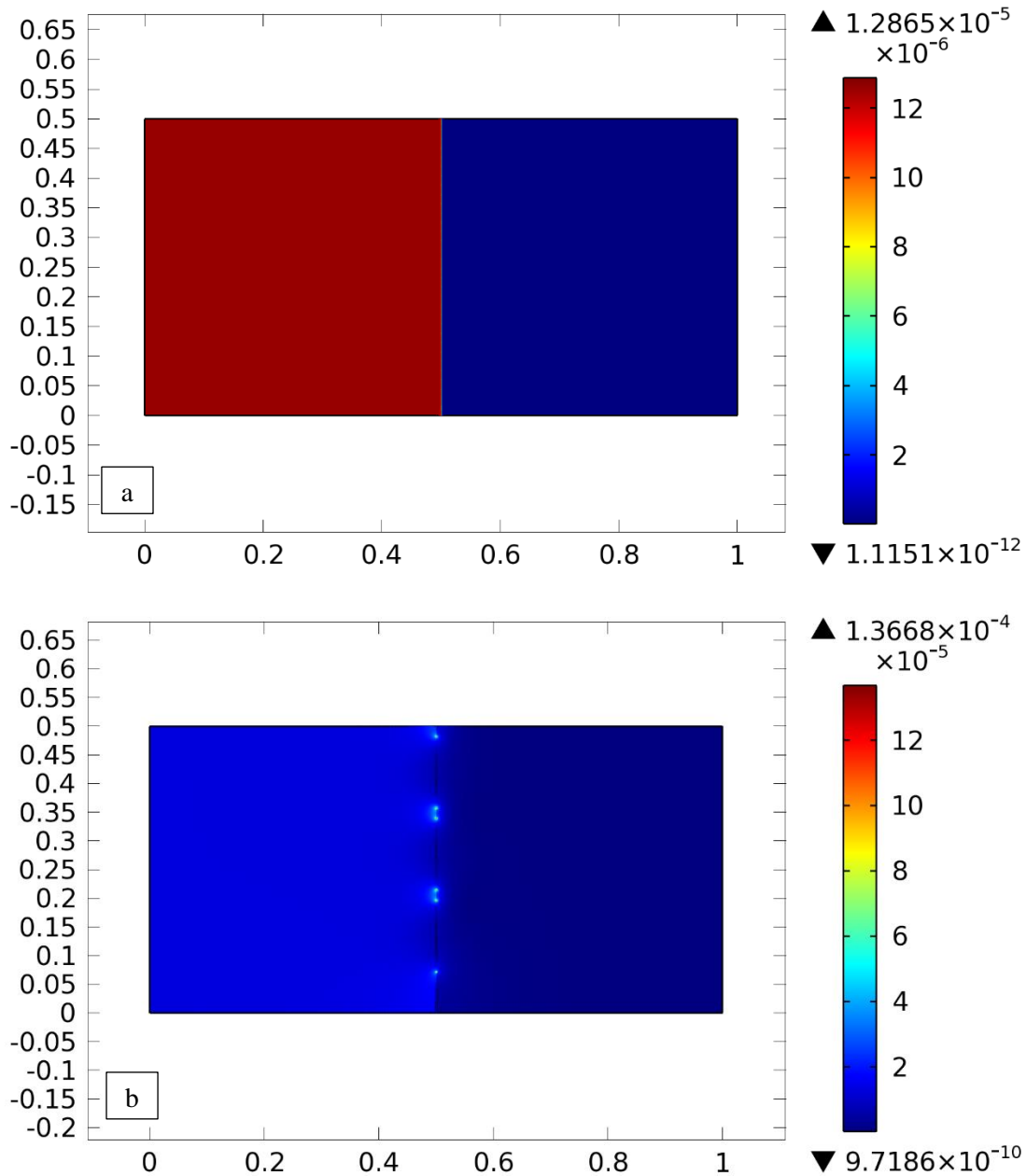
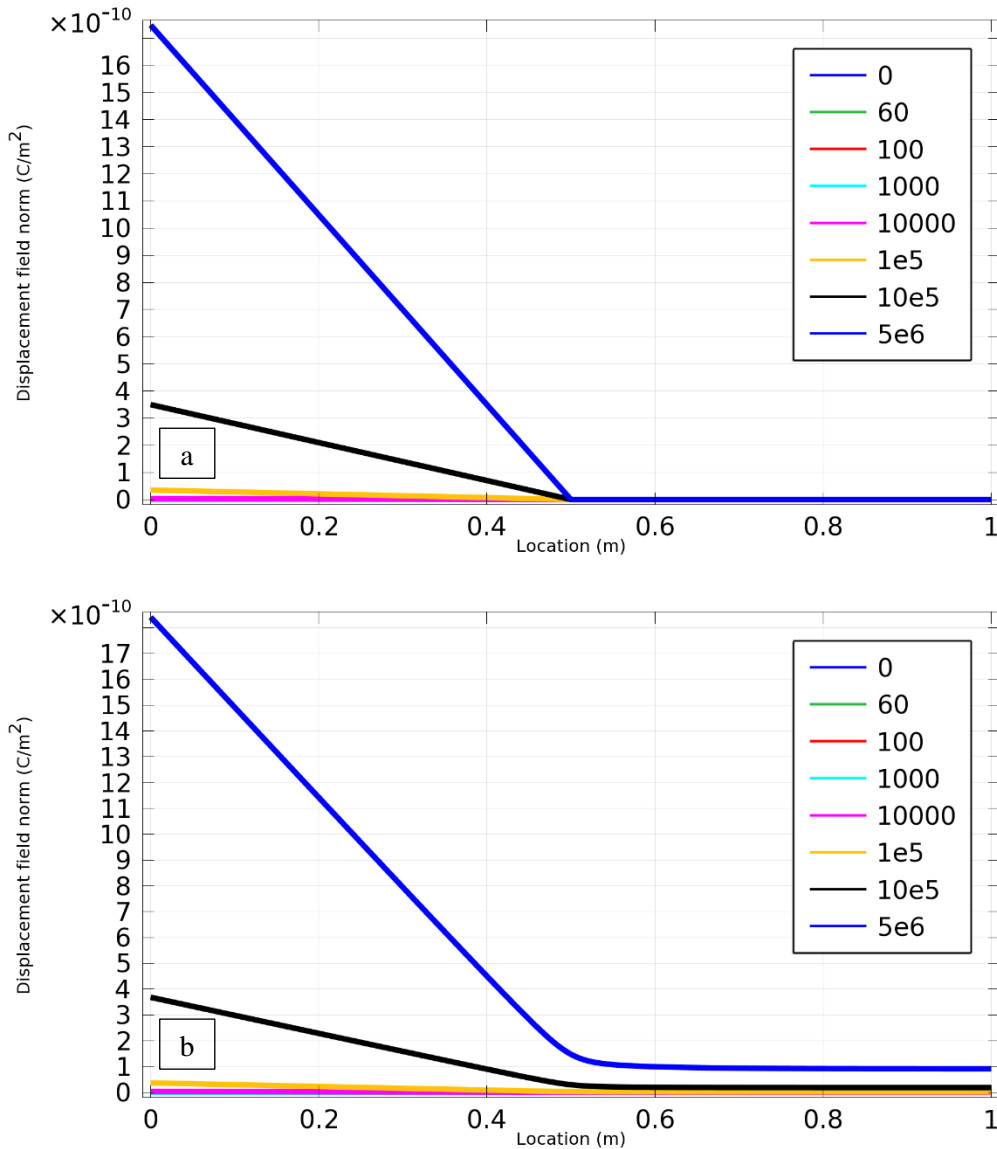


Figure 4.41. Magnetic field density norm (B) at 100kHz with a) full aluminum shield, and b) perforated aluminum shield.

The first major difference between Figure 4.40-b, Figure 4.41-a, and Figure 4.41-b is the significant decrease in the maximum field norm. In Figure 4.41-b, the value of magnetic field density norm at the shield is much higher than the rest of the domain, which causes the left-hand boundary values turn out blue. To better show the effect of shields, results are plotted along a horizontal line in the middle of the 2D domain. Figure 4.42 shows the electric displacement field norm plotted at  $f = [0, 60, 100, 1000, 10e^3, 100e^3, 1e^6, 5e^6]$ Hz with full (Figure 4.42-a) and perforated (Figure 4.42-b) aluminum shields.



**Figure 4.42. Electric displacement field norm (D) with full Aluminum shield at different frequencies along a line in the middle of the 2D domain. a) full shield and b) perforated shield.**

Results of simulations for full and perforated shields made of copper, aluminum, iron, and carbon steel are summarized in Figure 4.43 to better elaborate  $SM_{dB}$  of different materials at different frequencies. Using equation 27,  $SM_{dB}$  is found for  $f = [0, 60, 100, 1000, 10e^3, 100e^3, 1e^6, 5e^6]$  Hz at a point 1m away from the boundary source. Shield is perforated for all these cases with 0.125m openings. This size of the opening is smaller than the wavelength of all evaluated frequencies.

The shield is located 0.5m away from the boundary source. As shown in Figure 4.42, the field intensity is higher out of the enclosure when the shield is a perforated. An important factor in

choosing the proper material for shielding purposes is the sensitivity of the shielding effectiveness to the size of openings and apertures. To study the sensitivity of different materials to openings, equation 27 is modified as below:

$$\Delta SM_{dB} = 20 \times \log\left(\frac{M_p}{M_g}\right), \quad (28)$$

where  $M_f$  and  $M_g$  denote the full shield and perforated shield field intensities at a particular location.  $\Delta SM_{dB}$  represents the difference between the two cases:

$$\begin{aligned} \Delta SM_{dB} &= SM_{dB}^{full} - SM_{dB}^{perf} = 20 \times \left[ \log\left(\frac{M_f}{M_{no\ shield}}\right) - \log\left(\frac{M_p}{M_{no\ shield}}\right) \right] \\ &= 20 \times \log\left(\frac{M_p}{M_g}\right). \end{aligned} \quad (29)$$

Figure 4.44 shows the  $\Delta SM_{dB}$  for the respective cases of Figure 4.43 . The smaller the  $\Delta SM_{dB}$ , the less sensitive enclosure performance is to the aperture size. It is found that the shielding effectiveness is practically determined by the penetration of energy through the apertures in the enclosure rather than through the walls. Figure 4.44 provides a means for comparing the contribution of walls and apertures to the escaping field.

Figure 4.43 shows the dependency of the shielding effectiveness on the frequency of the electromagnetic wave. At frequencies equal to or greater than 100kHz these four materials provide almost the same attenuation. At low frequencies, however, copper and aluminum behave much better than steel or iron. At 60Hz, copper attenuates the electromagnetic field 20.99% better than steel, while the difference is about 9.64% at 5MHz.

As shown in Figure 4.44, steel has the least sensitivity to perforated shielding, especially at frequencies above 10kHz. This means that upon changing the size of openings,  $SM_{db}$  for steel would change less compared with other materials. Iron shows a different reaction to the gird shield; at low frequencies there is a small difference that tends to get bigger as the frequency increases. This could be attributed to the larger relative permeability (5000 times larger than copper) and smaller conductivity (70.3% less than copper) of iron. At low frequencies the electromagnetic shielding is more possible through attenuating magnetic field, therefore permeability plays a more important role in the performance of the material. At high frequencies however, electric field attenuation dominates the shieling effectiveness of the material. The overall behavior of the material depends on conductivity, permeability, and frequency.

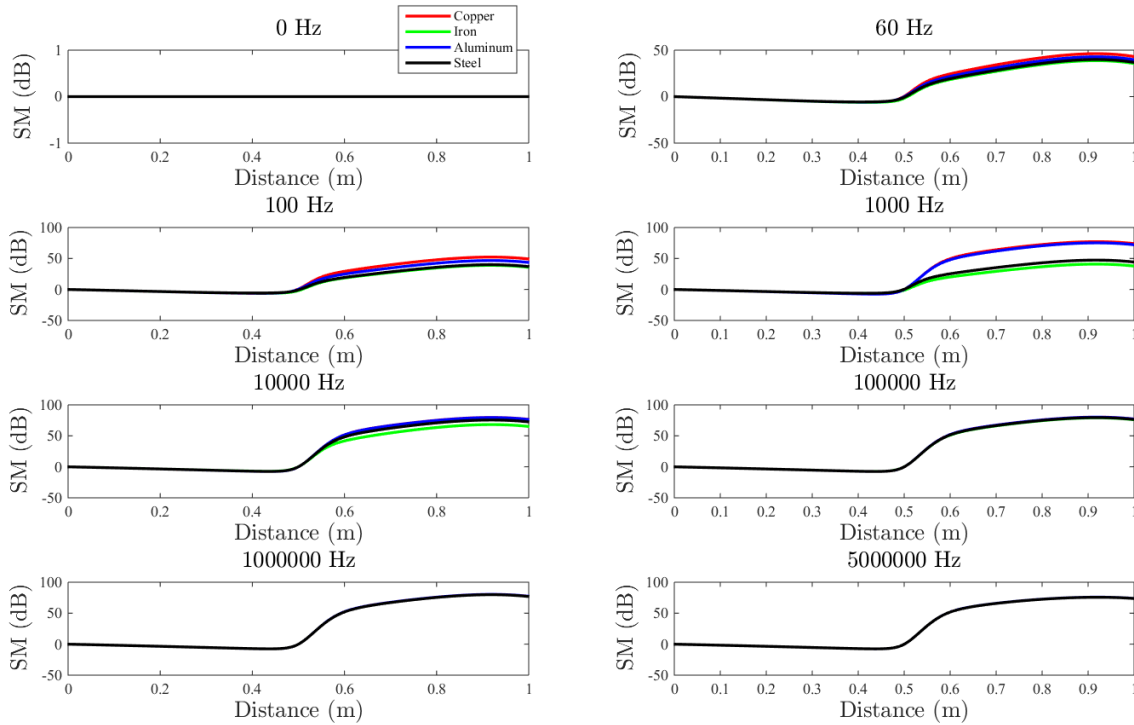


Figure 4.43.  $SM_{AB}$  of different materials at different frequencies. Shields are perforated in all cases.

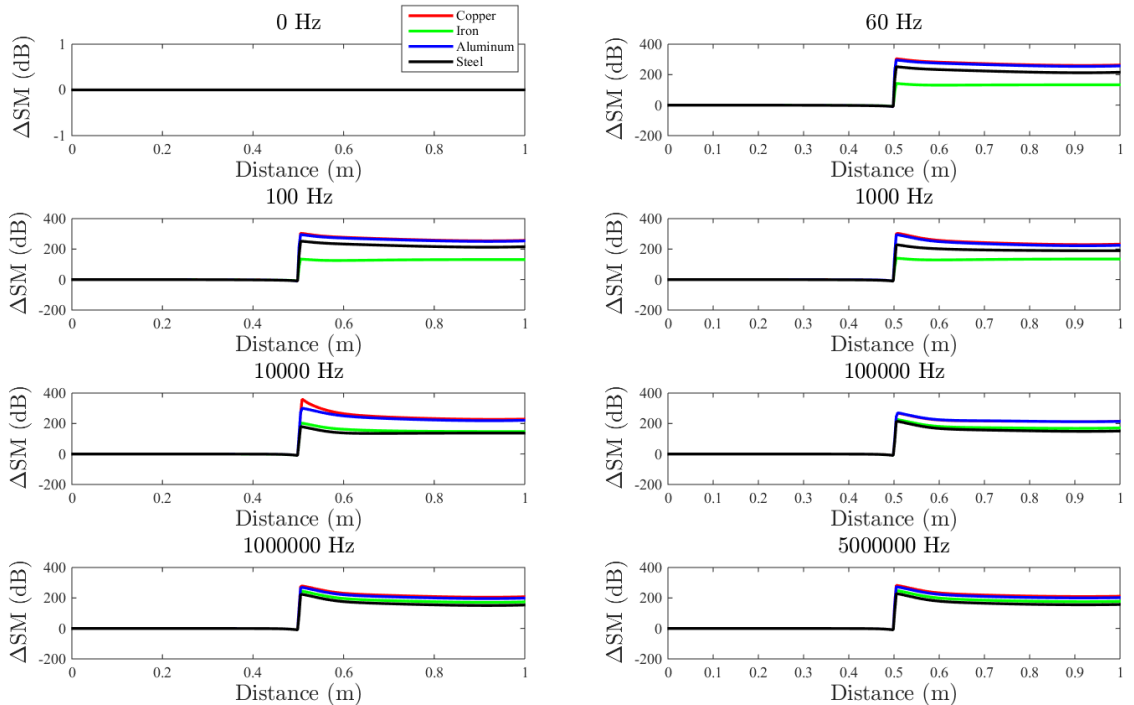
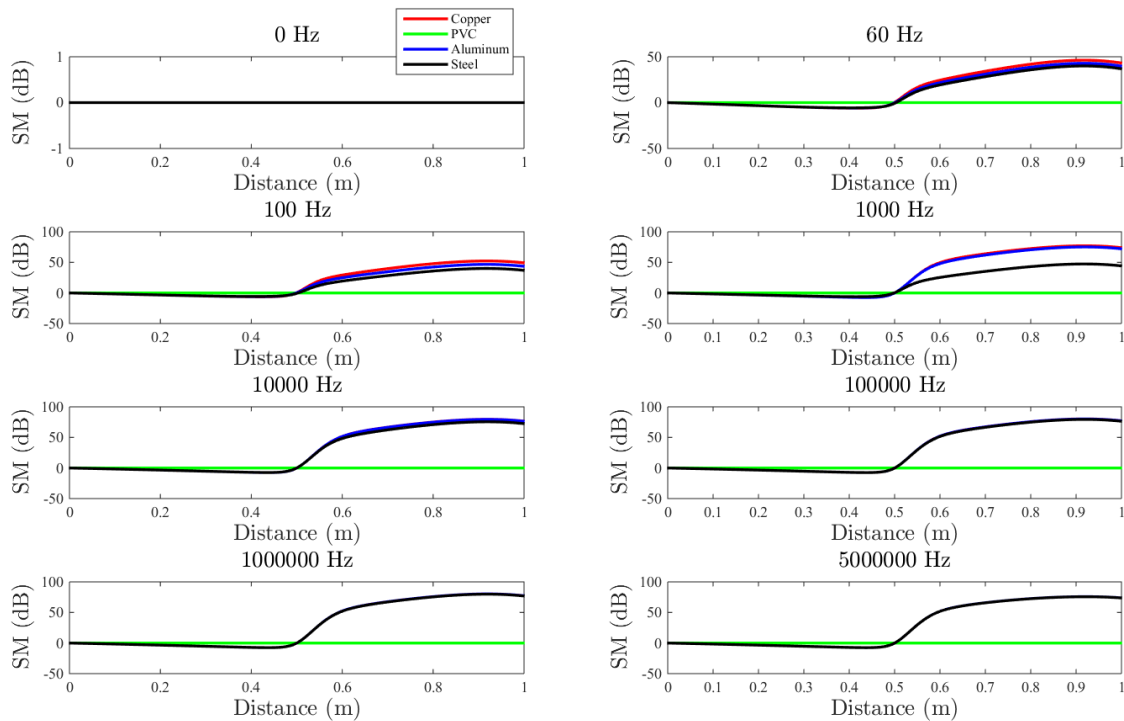


Figure 4.44.  $\Delta SM_{AB}$  of the various materials at different frequencies. Perforated shields are the same in all cases.

A time varying magnetic field is accompanied by a time-varying electric field that induces time-varying currents in the shield and a secondary time-varying magnetic field. From the Lenz's law,

the induced currents produce a magnetic field that opposes the external magnetic flux, so that the total flux reduces. The larger the conductivity, the larger the induced currents. Also, the larger the permeability, the more significant the flux reduction.

To provide a measurement of the shielding effectiveness of PVC in comparison with metals,  $SM_{dB}$  of steel, copper, aluminum, and PVC are plotted in Figure 4.45. The effectiveness of PVC is not zero but, it is much smaller than the other two materials considered in this comparative study. The maximum achievable attenuation with PVC with this configuration is less than 1dB at 5MHz. This low performance was expectable due to low permeability and conductivity of this material. The only major difference between electrical properties of PVC and air is relative permittivity (3.18 for PVC versus 1 for air), which does not show a significant effect on the results.



**Figure 4.45.**  $SM_{dB}$  of copper, steel, aluminum, and PVC at different frequencies. Shields are perforated in all cases.

#### 4.4.3.2 Effect of thickness on $SM_{dB}$ of steel

The skin effect is the tendency of a time-varying current to concentrate near the surface of a conductor. At high frequency, the current is restricted to a very thin layer near the conductor surface. Therefore, the shield could be coated with highly pure metals to increase the shielding effectiveness. The skin effect is much higher in ferromagnetic materials compared with diamagnetic materials [115]. Skin depth for some common materials is given in Table 4.8. To better

understand the effect of thickness on the shielding effectiveness of material at different frequencies, the geometry of Figure 4.38 is regenerated for shield thicknesses of 0.5mm to 3mm at every 0.5mm step. Results of those simulations are summarized in Figure 4.46.

**Table 4.8. Skin depth for some common materials [116].**

Material	60Hz	1kHz	10kHz	1MHz
Copper	8.61mm	2.1mm	0.652mm	67 $\mu$ m
Iron	0.275mm	67.2 $\mu$ m	21.27 $\mu$ m	2.127 $\mu$ m
Carbon Steel	3.24mm	0.793mm	0.250mm	25 $\mu$ m
Aluminum	10.59mm	2.59mm	0.82mm	82 $\mu$ m

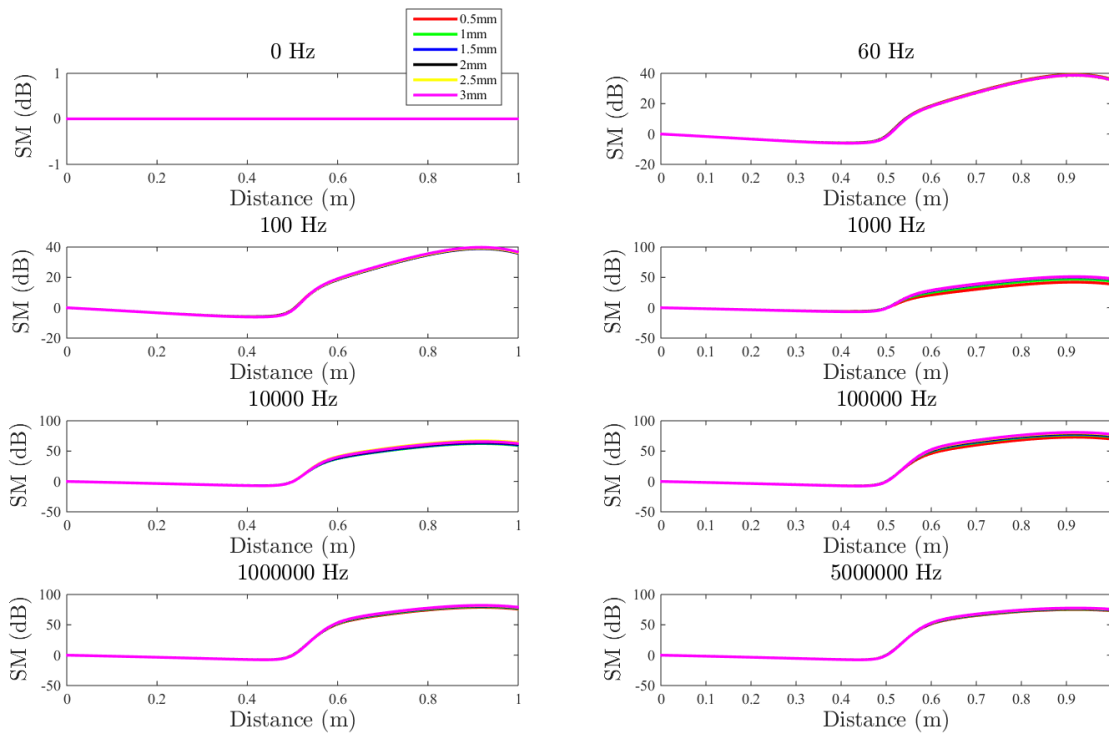


**Figure 4.46. Effect of thickness on  $SM_{dB}$  of steel at different frequencies. All shields are perforated.**

As the frequency increases, the skin effect decreases. Proper shielding is possible if the thickness of the shield is greater than the skin effect. In other words, the same material and thickness may perform well for high frequencies, but it will saturate at low frequencies. Results of 1000Hz in Figure 4.46 show 23.4% difference between 0.5mm and 3mm, while the difference is about 3.5% at 5MHz.

#### 4.4.4 Implementation and Experimental Results

##### 4.4.4.1 *The Electromagnetic Shield for the VT Roller Rig Control Tower*

Based on the findings in section 4.4.3.1, steel was selected for fabricating the enclosure. Although, steel provides the least effectiveness compared with copper, aluminum, and iron, the difference does not support the cost difference. Copper provides only 20% more attenuation at 60Hz and such difference drops below 10% at 5MHz. As mentioned earlier, steel shows the least amount of attenuation reduction caused by material removal. In other words, there will be less change in the behavior of steel due to further apertures for running cables or installing the user interface. For the same gauge sheet plate, the cost difference between the four aforementioned materials is significant. Surveying the market reveals that the availability of copper, aluminum, and iron perforated sheet metals at the desired thickness and perforated size is quite restricted.

Considering the results in section 4.4.3.2, 16GA sheet was selected for fabricating the enclosure (1.5 mm). This thickness is readily available in the market, and is in the middle of the spectrum shown in Figure 4.46. The closest conventional perforated structure that was available in the market was 1/4" circular holes staggered at 3/8". This is equivalent to 80% material removed, which is a little more than 75% material removal used in the simulations.

The electronics inside the cabinet weight more than 200lb without the cables. The back plate of the enclosure should bear the weight of all components without buckling. On the other hand, it should be bare conductive metal for grounding purposes. After structural FEA analysis galvanized 14GA sheet plate reinforced with 2 × 1 C-beams on the back was used as the back plate of the enclosure.

Particular attention was paid to the assembly of the cabinet such that the biggest gap between mating components remains smaller than 1/4". The enclosure was assembled using bolts and nuts. Figure 4.47 shows the final enclosure with the electronic equipment and cables installed. For securing the cabinet from tipping over, it was anchored to the ground with four Grade 5 steel stud anchor for concrete, 1/2" diameter.

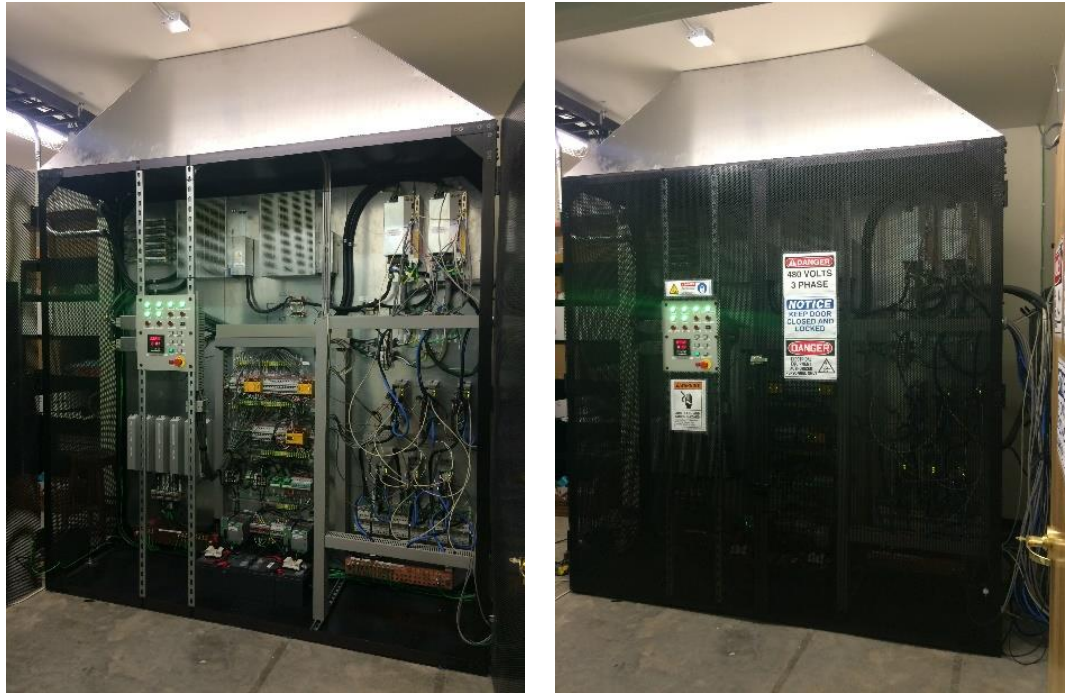


Figure 4.47. The Faraday Cage for the VT Roller Rig control tower.

#### 4.4.4.2 Test Setup

An experimental setup was used to measure the actual radiations from the power electronics inside the cage. The setup consisted of a loop antenna, a passive matching circuit, and a Tektronix TDS 2004B digital oscilloscope. The loop antenna was made by 50 rounds of copper wire around a circle with a 6.37cm radius. The measured resistance of the antenna was  $1\Omega$ . Due to the direct coupling of loop antenna to the magnetic field, unlike most other antenna types, the loop antenna is relatively insensitive to electric-field noise from nearby sources. Thus, by adjusting the pattern of the antenna on the target, it is possible to measure the radiation from target more correctly. The resistance load and probe of oscilloscope together constitute the matching circuit of the loop antenna. A  $100\Omega$  resistance was used as a front load for the antenna. The oscilloscope probes were set at  $\times 1$  magnification. Therefore, the probes do not affect the load on the loop antenna. Since the captured wave does not have a monotone nature, a 5MHz sinusoidal external trigger was used to show the standing wave on the screen of the oscilloscope. The external trigger wave was generated by a Tektronix AFG 3022B function generator. Figure 4.48 shows the experimental test setup.

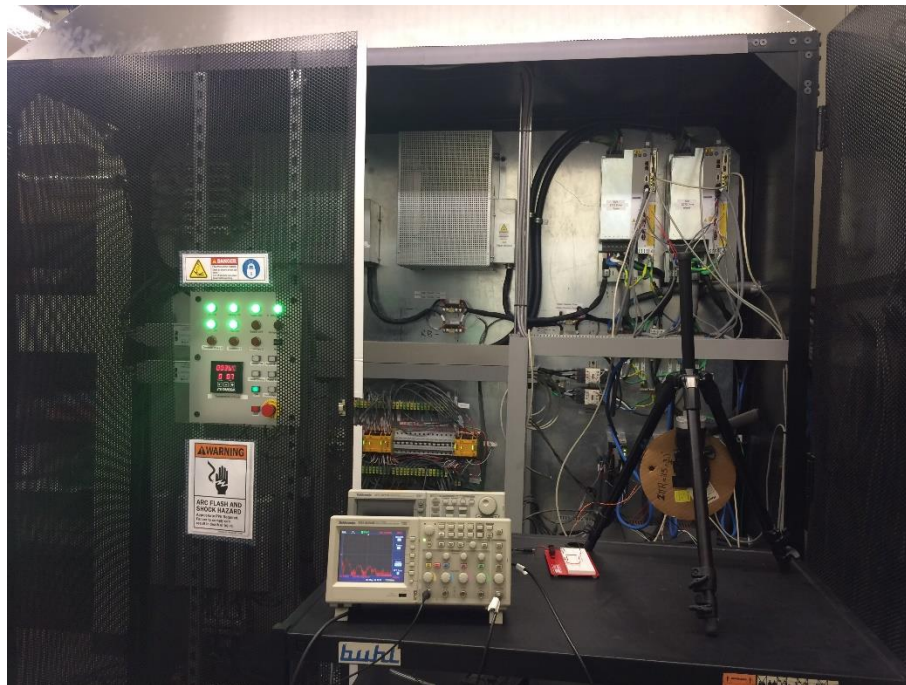


Figure 4.48. The loop antenna test setup.

#### 4.4.4.3 Results

Measurements were taken at three spots all along the same line and the same height, with different distances from the enclosure:

- Inside the cabinet with the doors open
- Outside the enclosure adjacent to the doors with the doors shut
- Outside the enclosure, 1m away from the doors with the doors shut

Measurements at the second and third spots, when the doors are open, show a negligible difference compared to spot number one. The minimal difference could be related to distance, but also, the stochastic nature of the signal. For the sake of future comparisons, the measurement at spot one is assumed to be valid for spots number two and three with the doors open.

As mentioned above the signal shows stochastic behavior, meaning that is slightly different between consecutive measurements. The data reported below are intended to represent the worst case scenario for the shield, i.e. minimum noise inside the cabinet, maximum noise outside the enclosure.

The first set of data given in Figure 4.49, shows the time and frequency of the signal inside the enclosure. As expected, the maximum power is transferred with low to 5MHz frequency, which agrees with the information provided by the manufacturer. The peak on the FFT plot occurs at

around 2.25MHz with 42dB amplitude. Repeating the measurements reveal that the peak can go as high as 48dB.

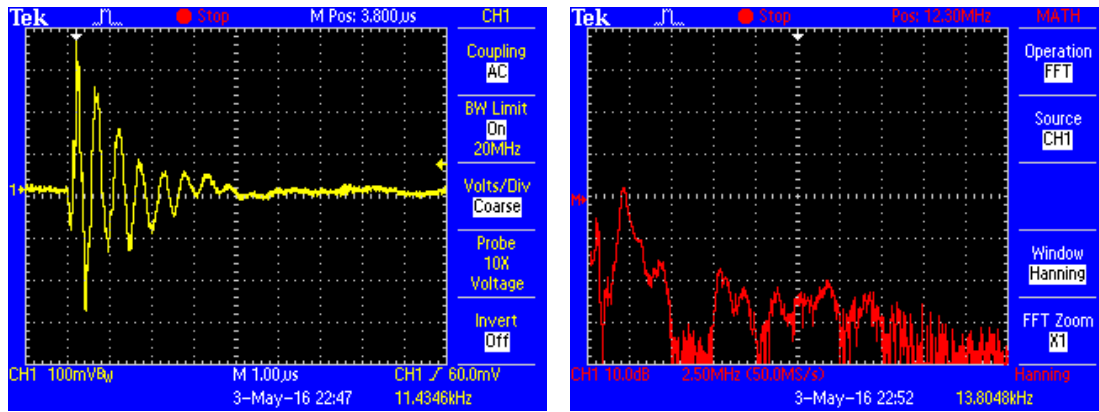


Figure 4.49. Measurements inside the cabinet. Left figure is the time signal, and right figure is the FFT using Hanning window.

The shape of the wave in the time domain cannot be illustrated by a closed form mathematical formula. However, it is similar to the Sinc function in the time domain ( $Sinc(x) = sin(x)/x$ ). As shown in Figure 4.49-right, the detected wave has two picks of power around 2.25MHz and 7.75MHz frequency with 2.5MHz bandwidth. The highest peak occurs around 2.25MHz, which is in agreement with the prediction from the manufacturer.

The second set of data given in Figure 4.50, shows the measurements right after the enclosure when the doors are shut. The FFT plot shows about 26dB attenuation compared with the doors open. Consecutive measurements show less than a 5dB change in the amplitude of the peak at 2.25MHz.

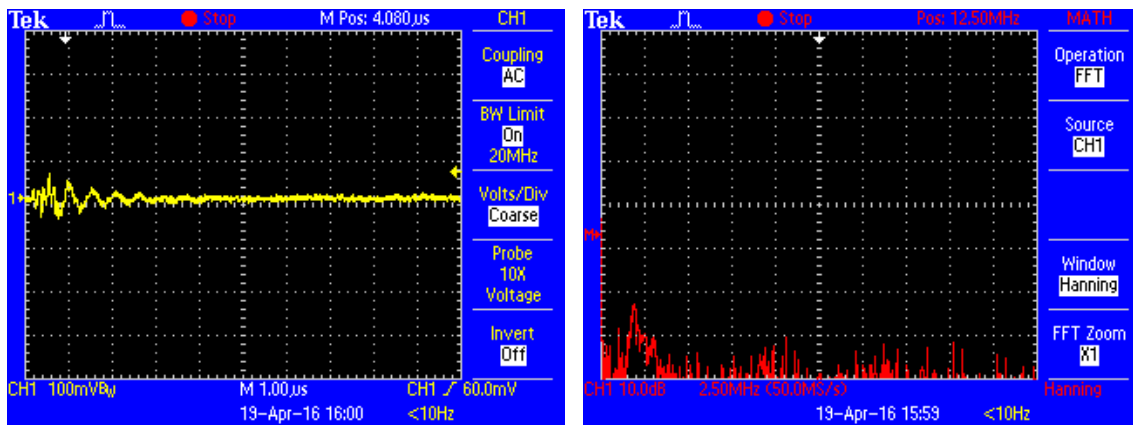
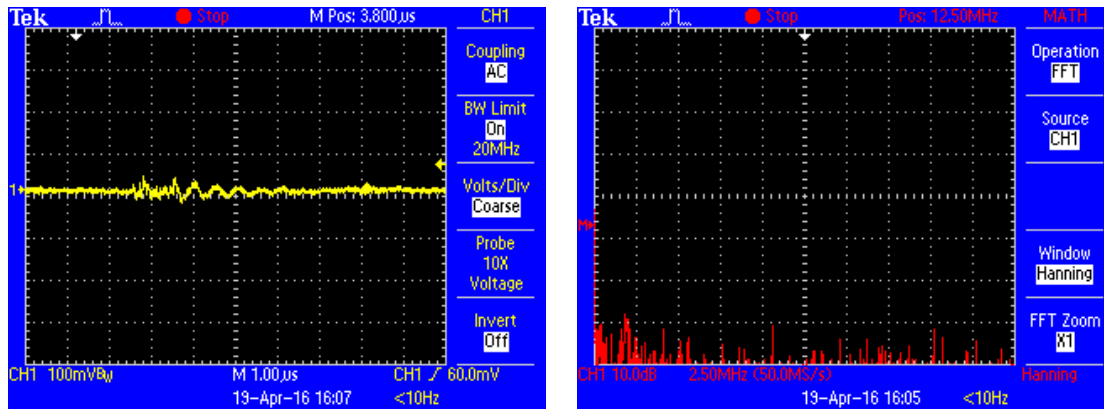


Figure 4.50. Measurements at a location adjacent to cabinet when the door is closed. Left figure is the time signal, and right figure is the FFT using Hanning window.

Finally, Figure 4.51 shows the measurements at 1m distance from the enclosure. Comparing it with Figure 4.49 reveals that the enclosure is successfully attenuating the whole DC to 25MHz. The

peak in the FFT plot is difficult to capture and is mostly between 0 to 10dB. The amplitude at 2.25MHz drops to 0 to 10dB, which is equivalent to 32 to 48dB shielding effectiveness.



**Figure 4.51.** Measurements at a location at 4ft away from the cabinet when the door is closed. Left figure is the time signal, and right figure is the FFT using Hanning window.

The rms value of the electromotive force at the output of a loop antenna is  $V_{\text{rms}} = 2\pi N A f B_{\text{rms}} \cos\theta$ , where  $N$  is the number of loops,  $A$  is the loop area,  $f$  is the frequency,  $B_{\text{rms}}$  is the rms value of magnetic induction, and  $\theta$  is the angle between the magnetic field lines and the loop normal. Between consecutive measurements, all parameters are the same with the exception of  $B_{\text{rms}}$ . Therefore, the ratio between two  $V$ 's are the same as the ratio between their corresponding  $B$ 's. This allows for putting the experimental and simulation results side-by-side. The maximum noise mitigation achieved with the cabinet is 48dB, while the peak in Figure 4.43 is about 72dB. Notice that the difference between the simulated peak at 1MHz and 5MHz is less than 5dB. The difference between the simulation and experimental results are justifiable, considering that the thickness and perforation size of the acquired steel sheet is the closest off-the-shelf product to the one used in simulations, however, not exactly the same. Also, the simulation does not take the 3D emission effects into account. Mechanisms such as reflection from other surfaces, and the orientation of loop normal with respect to magnetic field lines can reduce the measured voltages. Finally, the material properties used for steel in Table 4.6 are the average values, and may not reflect the exact numbers for the batch acquired.

#### 4.5 Transformer Base Structure

Description of the final selected isolating transformer for the VT Roller Rig is given in Section 8.3 of this document. The transformer can dissipate a significant amount of heat. As discussed in the next part of this chapter, heat management is already a big issue for the components inside the

electronics room. Therefore, mounting the transformer out of the electronics room is the only option.

The cable that connects the isolating transformer to the I-line panel is AWG 3/0 and not shielded. Since it is on the clean side of the power circuit, it is desirable to keep this cable as short as possible. The shorter length will minimize the electromagnetic noise coupling between this cable and nearby noise generating components.

Based on the data sheet provided by the manufacturer, the isolating transformer weighs 1350LB, and measures 51.5(h)×39.5(w),×34(d) in. Considering the location of the electronics room at CVeSS with respect to the door of the office area, it is not possible to install this component out of the electronics room, right next to the wall. It will block the pathway with less than 3-feet clearance on the sides, both of which are not permitted by Occupational Safety and Health Administration (OSHA).

These limitations leave only one option that guarantees all requirements. A structure is needed to be custom-designed and fabricated to lift the transformer up, out of the electronics room, and right next to the wall. The structure should both satisfy the OSHA safety regulations with a small footprint, such that it does not occupy too much space on the office pathway. Several designs and structures were considered. The possibility of using a cantilevered structure with cable support on the free end against one of the workshop I-beams was evaluated. Figure 4.52 shows the CAD model of this design. The finite element analysis showed acceptable results with the proposed design (safety factor of 3.9 with maximum cable tension of 243lbf). However, tying the structure to the building I-beams added various liability and safety issues to the problem. Therefore, the design was changed into an asymmetric statically indeterminate structure that placed the center of mass of the transformer on the vertical uprights Figure 4.52 shows the CAD model of this structure. The initial idea was to support the transformer tray with gussets on one side, and fix it against the roof of the electronics room from the other side. Finite element analysis shows that this structure can withstand the load of the transformer with a safety factor of 4.6.

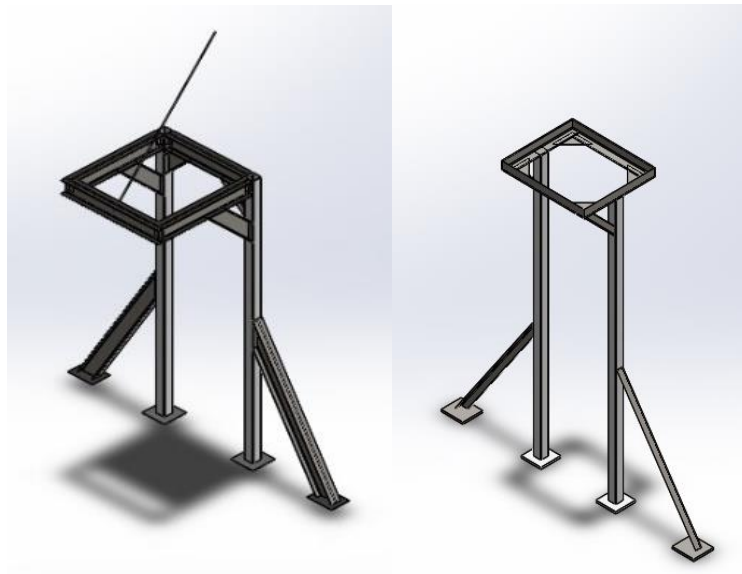


**Figure 4.52. Initial design of the isolating transformer structure: cantilevered structure with cable support against workshop I-beams (left), asymmetric statically indeterminate structure (right).**

The roof of the electronics room is rated for  $20\text{lb}/\text{ft}^2$ , which is greater than what this structure requires. However, if more support is required in future, this design will have limited room for expansion. Finally the design evolved into a symmetric statically indeterminate structure. Figure 4.53 shows the CAD model of the final structure design. This design places the center of mass of the transformer at the center of the structure tray, therefore, provide higher factor of safety with almost the same structural weight. It does not require any support from the building structure, which eliminates many liability and safety issues. It is also standing independent of the electronics room, which allows for getting more support from the roof of the electronics room in case more support is required in future.



**Figure 4.53. Symmetric statically indeterminate structure for holding the isolating transformer.**

The structure has two 145in upright made of  $4 \times 4 \times 0.25$ in A500HR steel tubings. Two 70in side arms made of the same size tubing support the structure laterally. The uprights and side arms are anchored to the floor via sixteen 1in bolts. The bolts are fastened to 0.75in thick A36HR steel plates that are welded to the tubings.

In order to fasten the transformer to the uprights, a tray is made of  $3 \times 5 \times 0.25$ in A36HR L brackets and a  $48(w) \times 37(d) \times 0.25(t)$ in A36HR steel plate. All components are welded together with at least 0.1875in weld bead. Eight 0.5in holes are fabricated on the tray that line up with those available on the bottom C-channels of the isolating transformer. This allows for easy installation of the transformer. The tray is gusseted against the uprights with four  $3 \times 3 \times 0.1875$ in A36HR L brackets. These L brackets are welded to the uprights, but bolted to the tray. The reason for bolting them to the tray is explained at the end of this section.

In order to evaluate the structural rigidity of the structure, static and buckling finite element analyses were performed using SolidWorks Simulations Package. Figure 4.54 shows the loading and boundary conditions for the analyses. It was assumed that the weight of the transformer is evenly distributed on the surface of the tray plane. Weldments between the components were included in the model based on the fact that a good welding can provide a rigid enough joint between the two components. The static analysis was performed using FFEPlus solver and high-quality solid mesh. Elements had 4 Jacobian points. The entire structure was meshed with 99767 elements and 194848 nodes, with 0.042825 intolerance. Figure 4.55 shows the quality of mesh used for performing the finite element analysis.

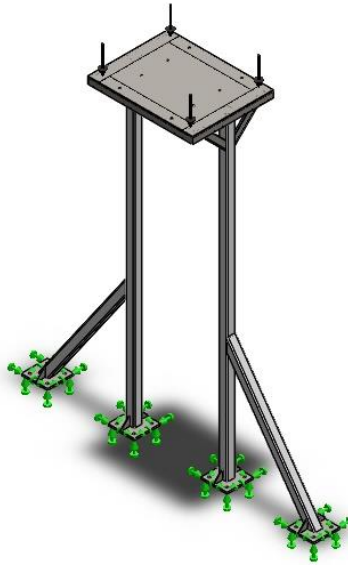


**Figure 4.54.** Loading and boundary conditions for the finite element analyses of the isolating transformer structure.

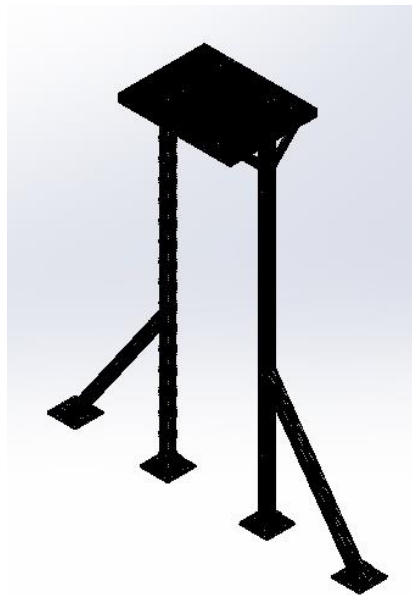


**Figure 4.55.** Quality of mesh used for performing the finite element analysis.

The next three figures show the results of the static finite element analysis. The maximum Von Mises stress is found to be 32.0MPa (Figure 4.56). This gives a safety factor of 9.84.

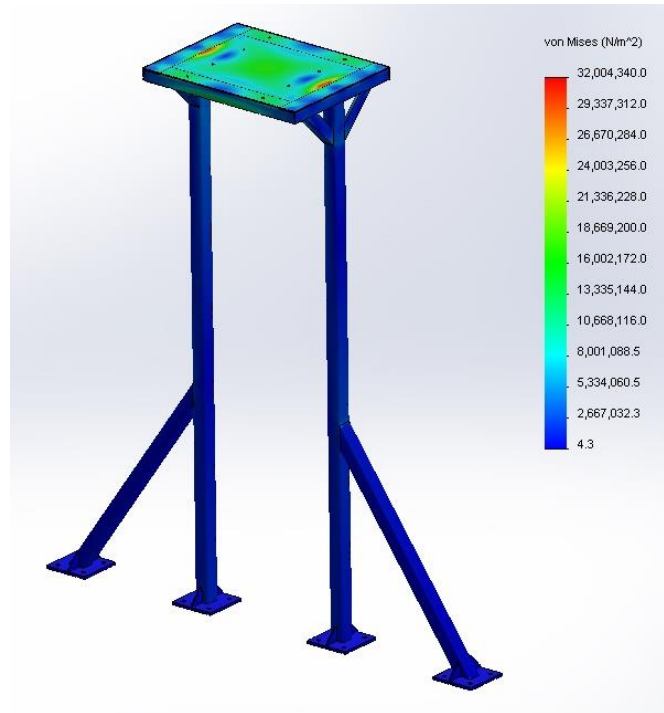


Figure 4.56. Stress distribution in the isolating transformer base structure.

The maximum displacement and strain in the structure due to the weight of the isolating transformer is found to be 1.38mm and  $8.5 \times 10^{-5}$ , respectively. The displacement and strain distributions are provided in Figure 4.57 and Figure 4.58.

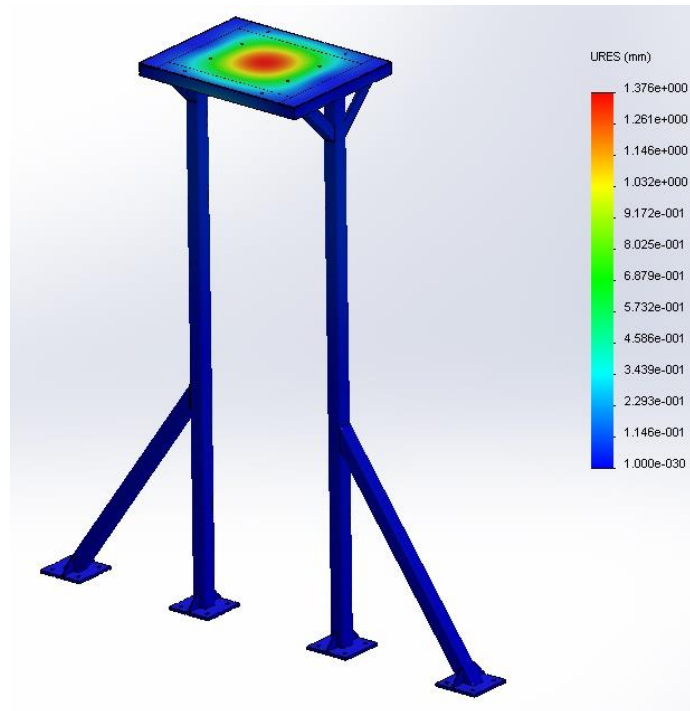


Figure 4.57. Displacement distribution in the isolating transformer base structure.

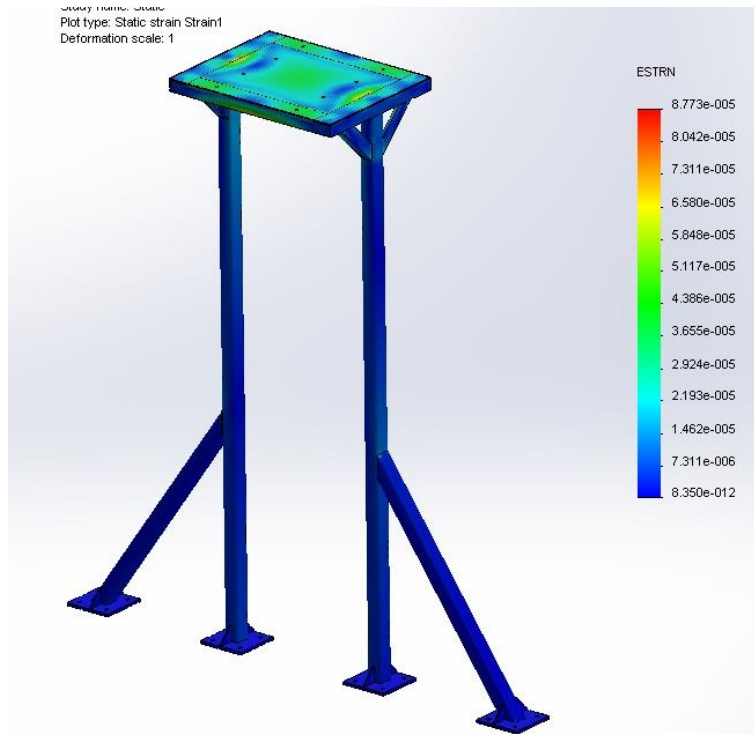


Figure 4.58. Strain distribution in the isolating transformer base structure.

In addition to the static analysis, a buckling analysis was performed to find the first four load factors for the structure. The simulation was done using FFEPlus solver and high-quality solid mesh and the elements had 4 Jacobian points. The entire structure was meshed with 65484 elements and 128903 nodes, with a tolerance of 0.0535313in. Figure 4.59 through Figure 4.62 show the first four buckling modes of the structure. Table 4.9 lists the four load factors.

Table 4.9. Load factors for the first four buckling modes of the isolating transformer base structure.

Mode Number	Load Factor
1	40.506
2	44.015
3	52.396
4	54.967

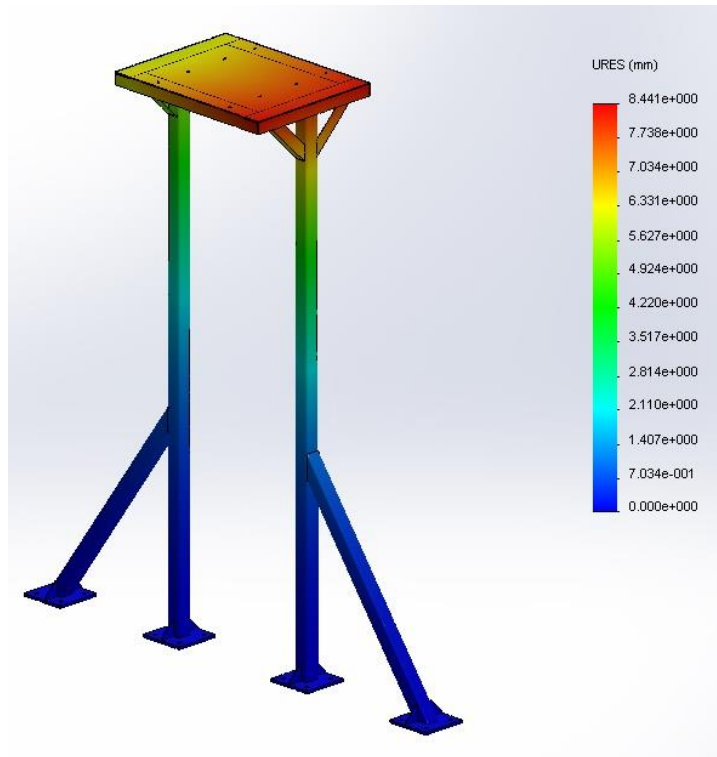


Figure 4.59. First buckling mode of the isolating transformer base structure.

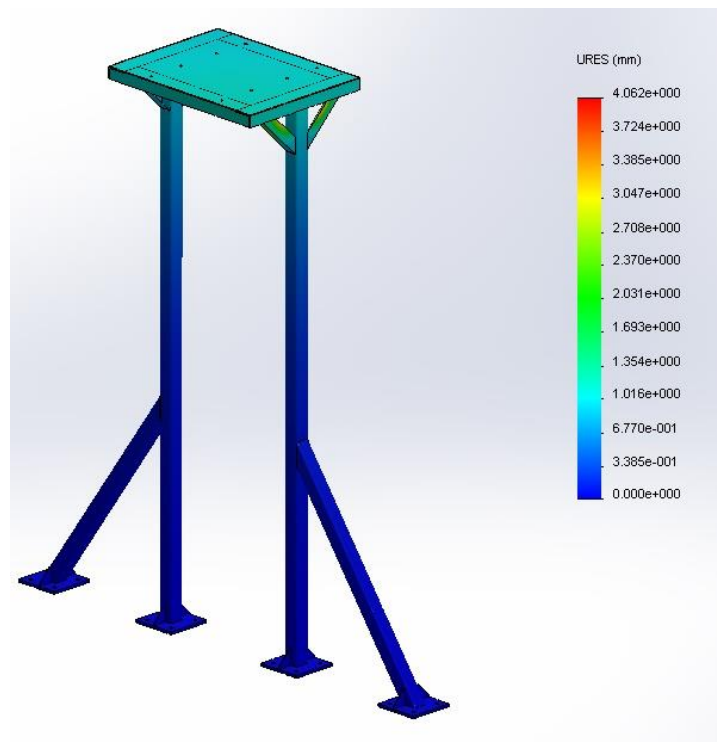


Figure 4.60. Second buckling mode of the isolating transformer base structure.

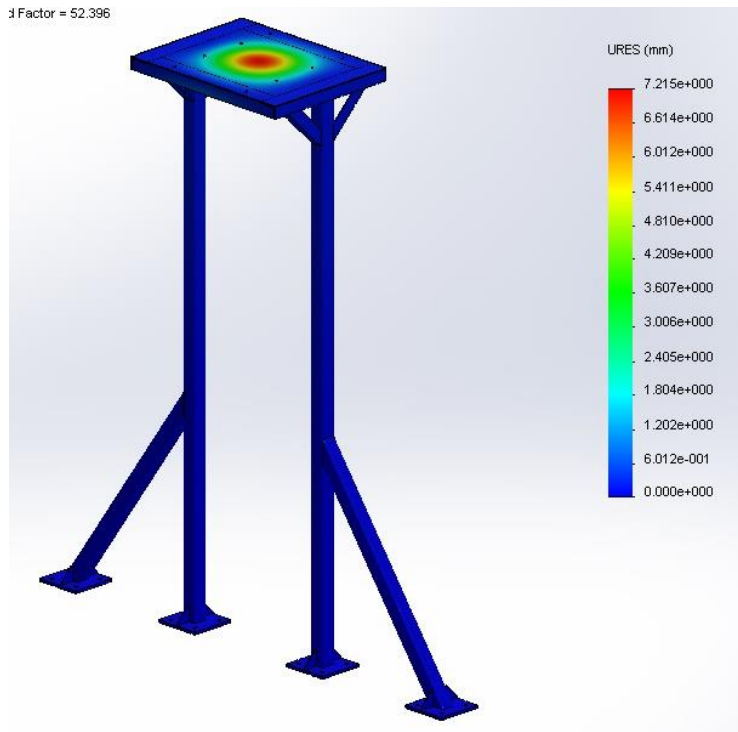


Figure 4.61. Third buckling mode of the isolating transformer base structure.

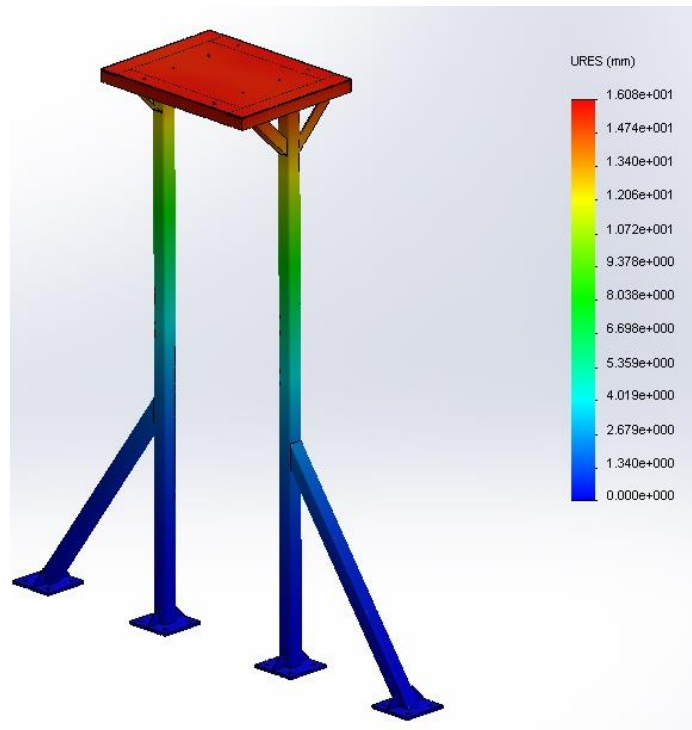


Figure 4.62. Fourth buckling mode of the isolating transformer base structure.

## 4.6 Thermal Management

Each electrically driven system has some power loss through heat loss. When power ranges go up to 150kVA, heat dissipation can lead to significant temperature rise in the environment. This increased temperature is both inconvenient for the users of the VT Roller Rig and also affects the performance of the components. Heat transfer analysis and computational fluid dynamics showed that this much heat dissipation can increase the temperature to above 140°C, not permissible by any of the component manufacturers. On the other hand spreading the components away from each other is not possible, first because the cable lengths are limited, and second due to the space limitation inside the electronics room. IEC has certain regulations for the minimum distance around the high voltage electrical equipment, and that limits the size of the control cabinet can be. This cabinet serves as a base for mounting auxiliary cooling systems and temperature monitoring apparatus for maintaining the environment temperature within the permissible range by the manufacturers.

This section discusses an extensive heat transfer analysis for choosing the proper cooling mechanism to dissipate the generated heat from the power electronics of the VT Roller Rig. Not every cooling system can transfer the heat fast enough to keep the surface temperatures below acceptable range. On the other hand, choosing a custom-designed cooling system can significantly increase the cost. In this chapter, realistic simulations of the working condition of five different cooling systems are provided:

- HVAC unit for the electronics room
- Roof fan for the electronics room
- Extended surfaces on the back of control cabinet with embedded fans
- Liquid cold plates on the back of control cabinet plus HVAC unit for the electronics room
- Liquid cold plates on the back of control cabinet plus roof fans for the electronics room

Through temperature distribution analysis, systems that achieve the desired temperature range are identified. From the isotherm surface analysis, the domain of effect of each system is visualized. The decision was then made through a cost-performance analysis. Figure 4.63 shows rated and estimated heat dissipation from the VT Roller Rig power electronics.

Although the numbers for the regenerative and motor-short resistors (on the left) are larger, they only occur for a few seconds, or in the case of regenerative resistors as millisecond pulses. The main continuously heat dissipative components of the VT Roller Rig are:

- S772 servo amplifiers
  - Quantity: 2
  - Weight: 13Kg
  - Dimensions: 0.505(h)×0.190(w)×0.285(d)m
- AKD-B00607 servo amplifiers
  - Quantity: 6
  - Weight: 2.9Kg
  - Dimensions: 0.290(h)×0.100(w)×0.225(d)m

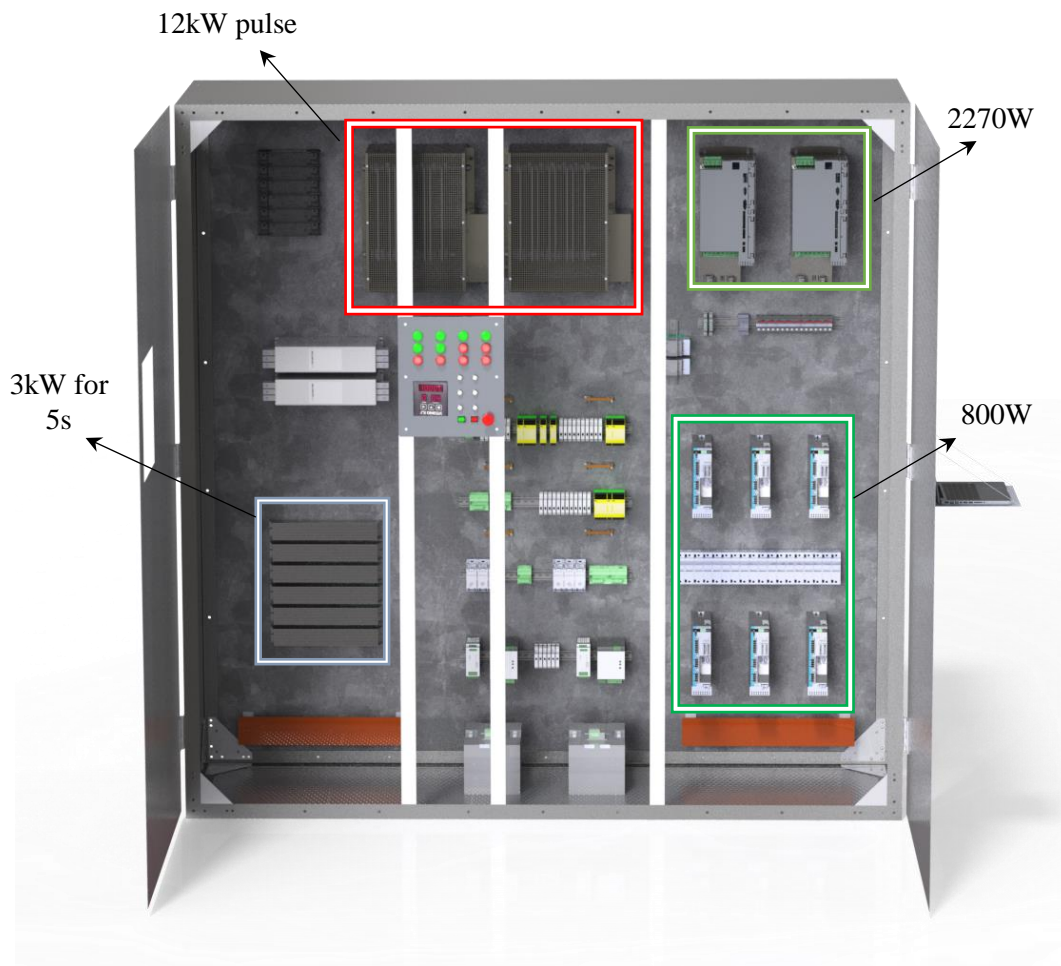


Figure 4.63. Most heat dissipative components of the VT Roller Rig.

A simulation model is set up using CAD models of the components in the electronics room. Actual dimensions of the electronics room and assumed material for each component are shown in Figure 4.64. Different cooling systems are modeled as boundary conditions on the back plate of the control panel that holds the S772 and AKD-B00607 servo amplifiers. Heat transfer analyses are performed in COMSOL Multiphysics software.

In all simulations, temperatures of room walls are assumed to be constant,  $T_{wall} = 303.15 K$ . Extended surfaces on the back of S772 drives are included in the CAD models to get a better representation of the actual cooling capacity of the drive fans. In all case studies, the effect of cooling fans is modeled by forced convection over the extended surfaces. Assuming a known air flow, one can calculate the air velocity as:

$$V = \frac{CFM \times 0.00047}{A} \quad (30)$$

where CFM is the cubic foot per minute air blow of the fan, 0.00047 is a conversion factor for CFM to cubic meter per second, and A is the area of the fan.

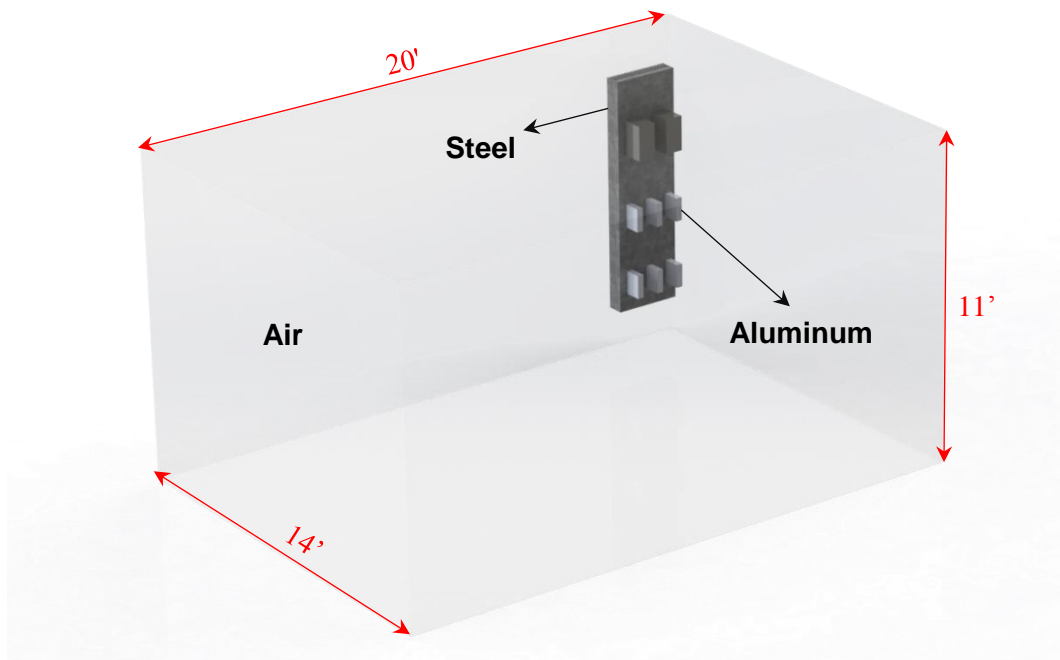


Figure 4.64. Size of the room and materials used for modeling the heat dissipative components.

The S772 servo amplifiers have three 100mm fans that cover the extended surfaces on the back of the unit. Figure 4.65 shows the CAD model of these extended surfaces. Substituting the respective values for a 62CFM Aavid PE Series fan, air velocity is found as:

$$D_{S772 fan} = 100mm \rightarrow A = 0.00785m^2$$

$$Ari Flow = 62CFM$$

$$V = \frac{62 \times 0.00047}{0.00785} = 3.76 \frac{m}{s} \quad (31)$$

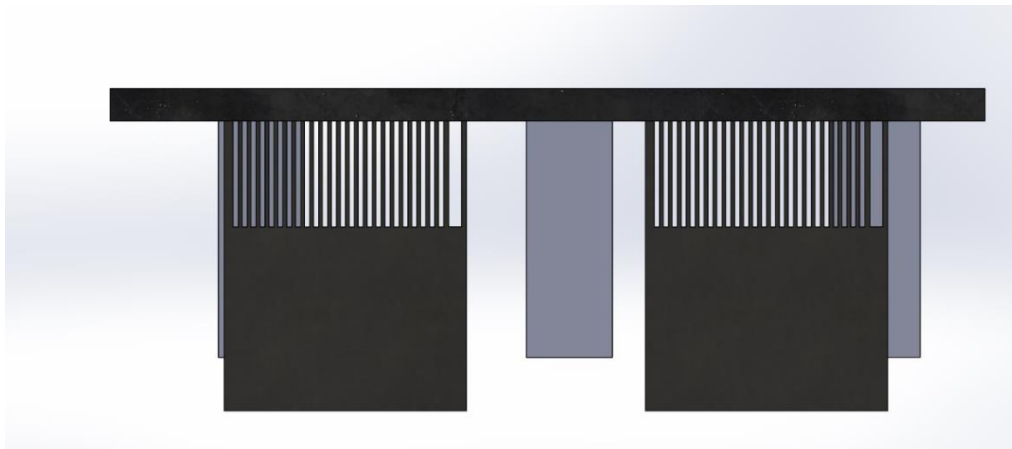
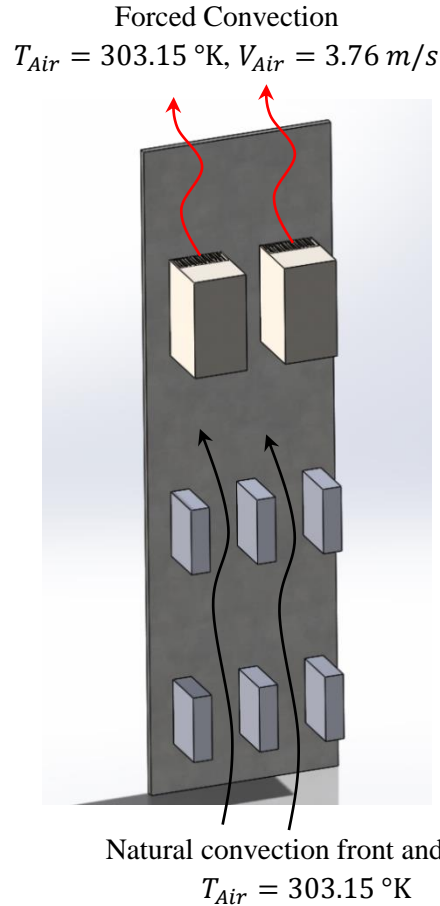


Figure 4.65. Extended surfaces on the back of S772 servo amplifiers.

#### 4.6.1 Solution I: HVAC Unit Only

An HVAC unit can be installed in the room to monitor the air temperature constantly. Choosing an HVAC system with large enough cooling capacity, and installing it such that vents point directly at the inputs of the servo amplifier fans, one can assume that the air temperature for forced convection on the extended surfaces, and natural convection on the rest of components remains constant. This does not mean that the air temperature remains constant in the entire room. This assumption only allows using a constant air temperature for defining the boundary conditions on the heat dissipative components.

Constant temperature in forced and natural convection could also be challenged by the fact that regular HVAC systems monitor the average air temperature instead of localized temperatures. Moreover, delivering the cold air to the fan inputs may not always be possible due to compact configuration of the control panel. Since this assumption overestimates the cooling capacity of the HVAC unit, results of the study can only represent the performance of this cooling mechanism under ideal conditions.



**Figure 4.66. Heat transfer mechanisms for solution I.**

#### 4.6.2 Solution II: Roof Fan Only

An industrial fan can be mounted on the roof of the room to blow air constantly onto the control panel. Considering the large space of the workshop, one can assume that the temperature of the air blown onto the control panel remains constant. This does not mean that the air temperature remains constant within the entire room. This only facilitates the simulations by using constant temperature in defining the boundary conditions for the control panel components.

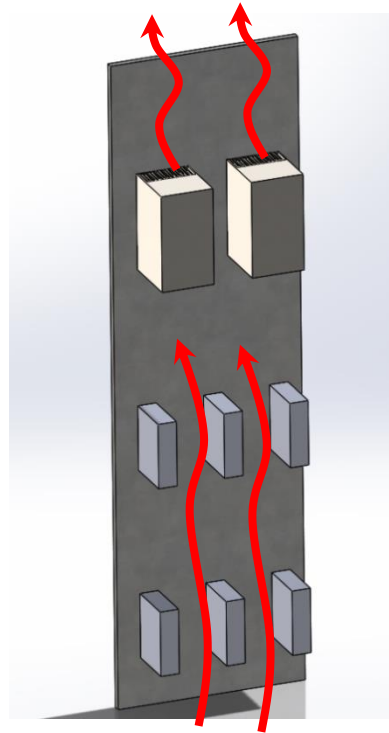
This mechanism needs a big fan for air intake and another one for exhaust (possibly on the side wall). However, in order to consider the worst case scenario, it is assumed that there is only one intake fan and air temperature inside the clean room can change. Similar to S772 fans, assuming an average-size roof fan, one could calculate the air speed as below:

$$\text{Air Flow} = 93\text{CFM}$$

$$D_{\text{roof fan}} = 370\text{mm} \rightarrow A = 0.10752\text{ m}^2 \tag{32}$$

$$V = 5.59 \frac{\text{m}}{\text{s}}$$

Forced convection  
 $T_{\text{Air}} = 303.15\text{ }^\circ\text{K}, V_{\text{Air}} = 5.59\text{ m/s}$



Forced convection front and back  
 $T_{\text{Air}} = 303.15\text{ }^\circ\text{K}, V_{\text{Air}} = 5.59\text{ m/s}$

**Figure 4.67. Heat transfer mechanisms for solution II.**

#### 4.6.3 Solution III: Finned Plate and Roof Fan

Similar to case II, a roof mounted fan can be used to blow air on the control panel components. Considering the large workshop space, it is reasonable to assume that the temperature of the air temperature blown onto the control panel remains constant. Air speed is assumed to be constant throughout the length of the fins.

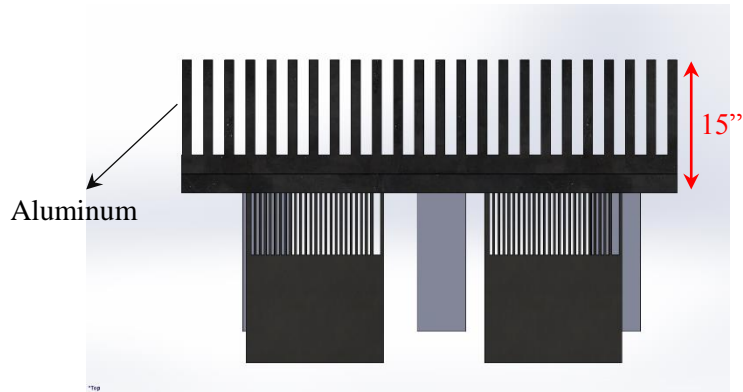


Figure 4.68. Fins on the back of mounting plate.

Three boundary conditions can be defined for this case: forced convection over the back fins, forced convection on the fins of the S772 drives, and forced convection over the surface of the mounting plate and drives. Figure 4.69 summarizes these heat transfer mechanisms.

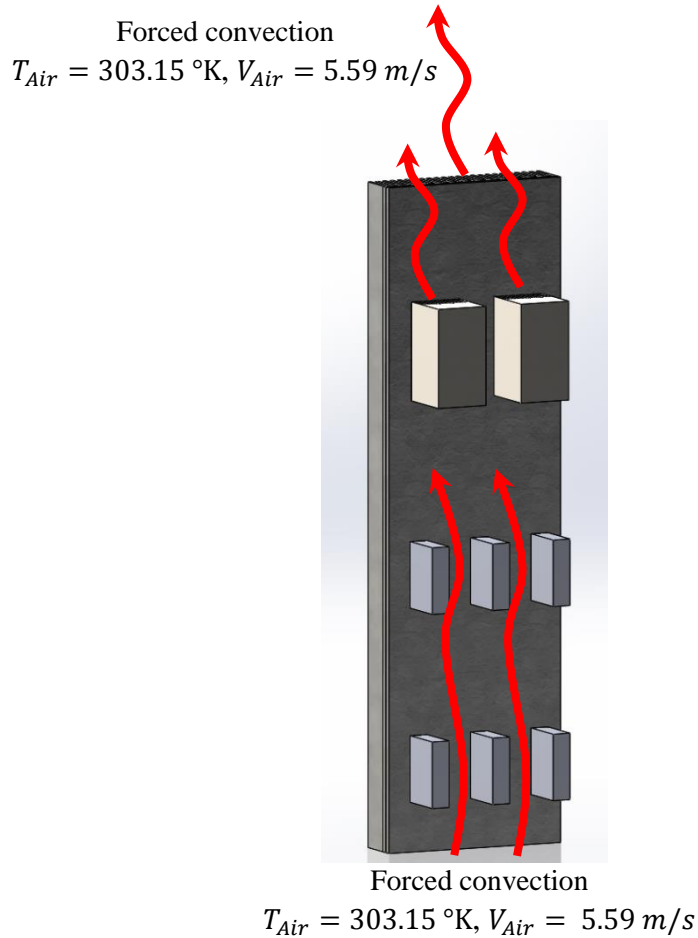


Figure 4.69. Heat transfer mechanisms for solution III.

#### 4.6.4 Solution IV: Liquid Cold Plates plus HVAC unit

Liquid cooling is a natural evolution beyond air cooling where either due to thermal requirements or footprint requirements, the desired performance can no longer be economically met by air cooling. There are many ways to accomplish liquid cooling, but the most common method is to have a plate with a flow path that moves liquid under the devices. After the heat is absorbed into the liquid, it is taken out of the plate and into the larger system. While water or water/glycol are the most common fluids used in liquid cooling, gasoline, oil, and refrigerant are other fluids that can be utilized.

There are lots of ways to construct a cold plate, and the methods can be driven by the level of performance needed, the materials needed, or the environmental requirements. One construction method is to use a series of cross-drilled holes on a plate. The holes intersect in the plate to determine the flow pattern and unneeded patterns are plugged. This construction method can be cost effective, but the pattern is limited to straight lines.

Another method is to embed a tube in a plate by machining a groove in the plate. The tube can either be placed toward the top surface of the plate to provide better cooling to devices mounted on that surface, or it can be embedded further into the plate so that it cools devices mounted on both sides of the plate. This option provides greater flexibility, but the thermal performance is limited because of the surface area of the tube perimeter.

To get more performance, extended surface area in contact with the fluid is required, and this leads to machined cold plates. The cold plate is constructed of a plate that has been machined to form some flow passages and then a cover is assembled to capture the flow. The extended surface area can be machined in place or installed by use of a piece of folded fin. The cover can be flat or be another machined plate. The method of assembly of the two parts can be done by gasket/screw, glue/screw, brazing, or welding and is dependent on the required performance and the requirements of the environment. Below is a sample of AavFin (Aavid Thermalloy LLC) plates that increase the surface area in contact with the cooling fluid by using fin structures in the flow path thereby increasing thermal transfer performance. Cold plates can be custom configured for length, width and fluid path to meet specific application requirements.

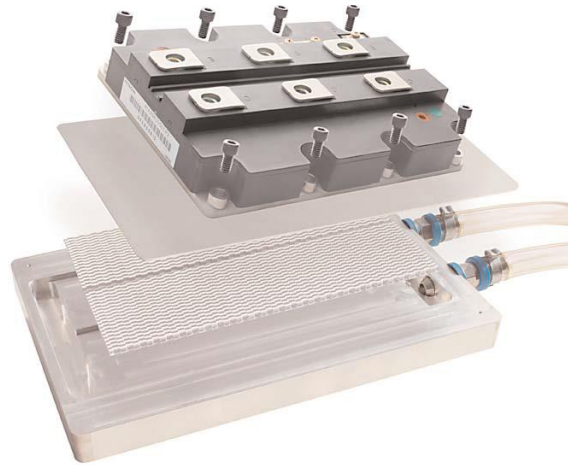


**Figure 4.70. AavFin liquid cold plate (courtesy of Aavid Thermalloy) [117].**

Besides design characteristics, the performance of cold plates depends on flow rate, pressure drop, and contact thermal resistance. The figure below shows the effect of these parameters on the performance of an AavFin liquid cold plate.

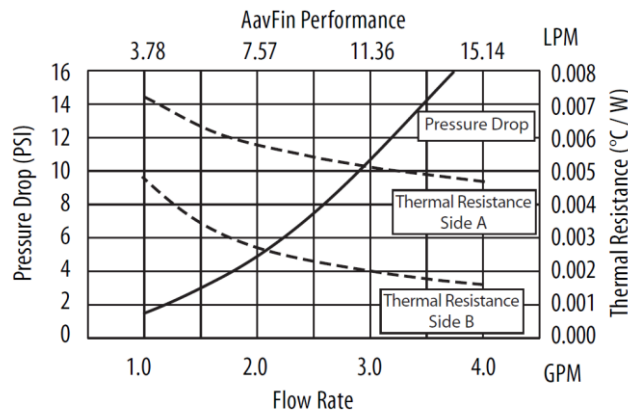


**Figure 4.71. Effect of flow rate, pressure drop and thermal contact resistance on the performance of AavFin liquid cold plates (courtesy of Aavid Thermalloy) [117].**

The following design is proposed for cooling the control panel down using AavFin liquid cold plates. Temperature and flow rate of the liquid can be adjusted via the external cooling system (LCS). Regular cooling systems can provide the full range of 0-55 °C at 0-62 Linear feet Per Minute (LPM).

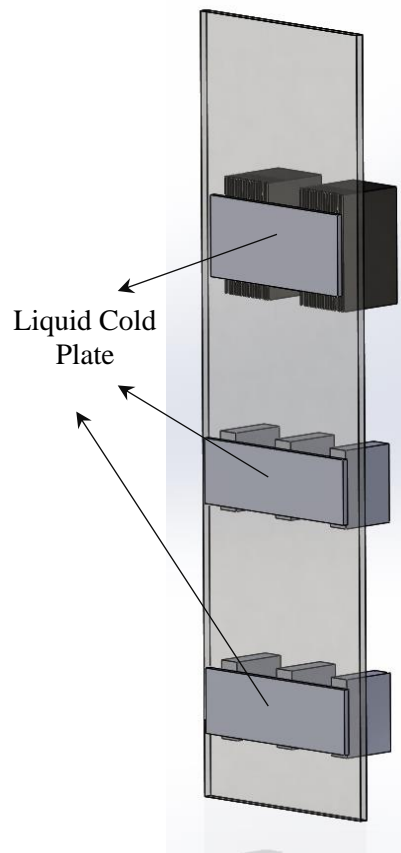


**Figure 4.72. Proposed design for cooling the control panel down using liquid cold plates.**

For the case of this application, a low flow rate (3.78LPM) at 20°C is used. Based on Figure 4.71, this leads to thermal resistance of 0.005°C/W. This resistance could be decreased by increasing the flow rate or decreasing the liquid flow set temperature.

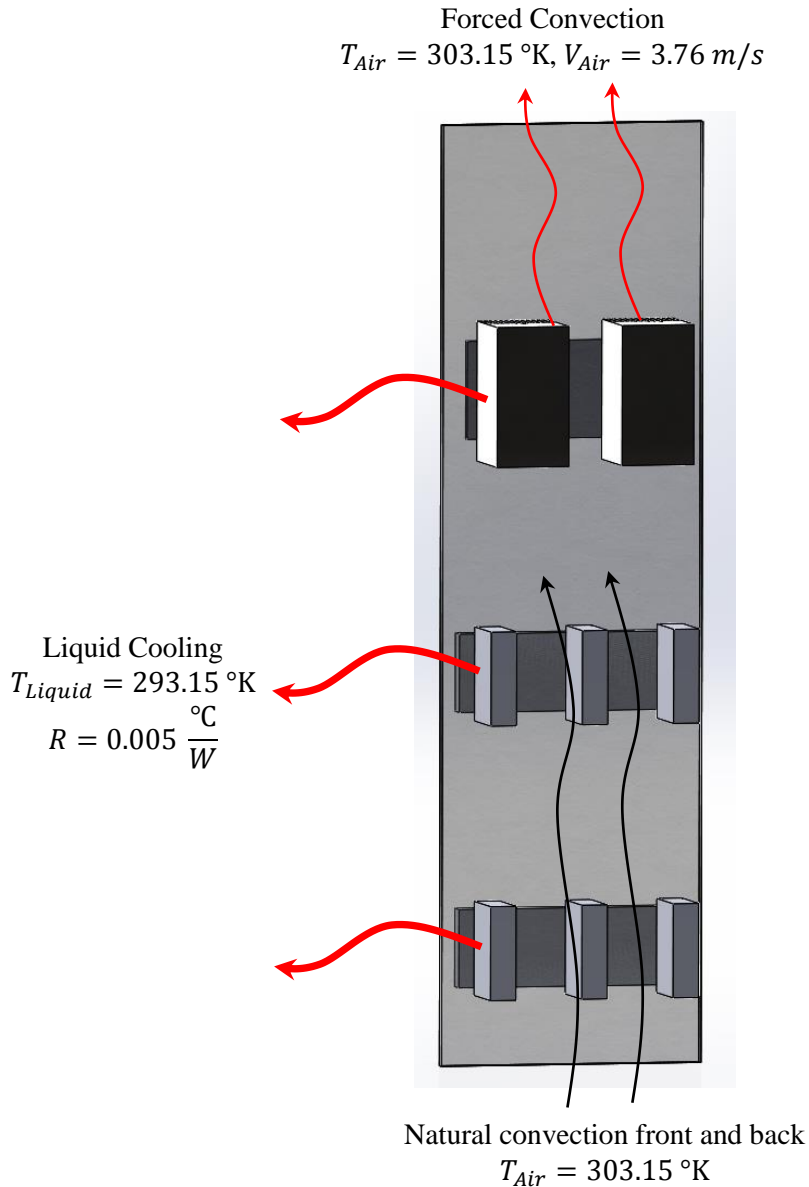


**Figure 4.73. Heat transfer mechanisms for case IV.**

4.6.5 Solution V: Liquid Cold Plates plus Roof Fan

This case is basically the combination of cases II and IV. If further cooling capacity is needed, case II could be replaced by case III. The figure below shows the boundary condition for these combined heat transfer mechanisms.

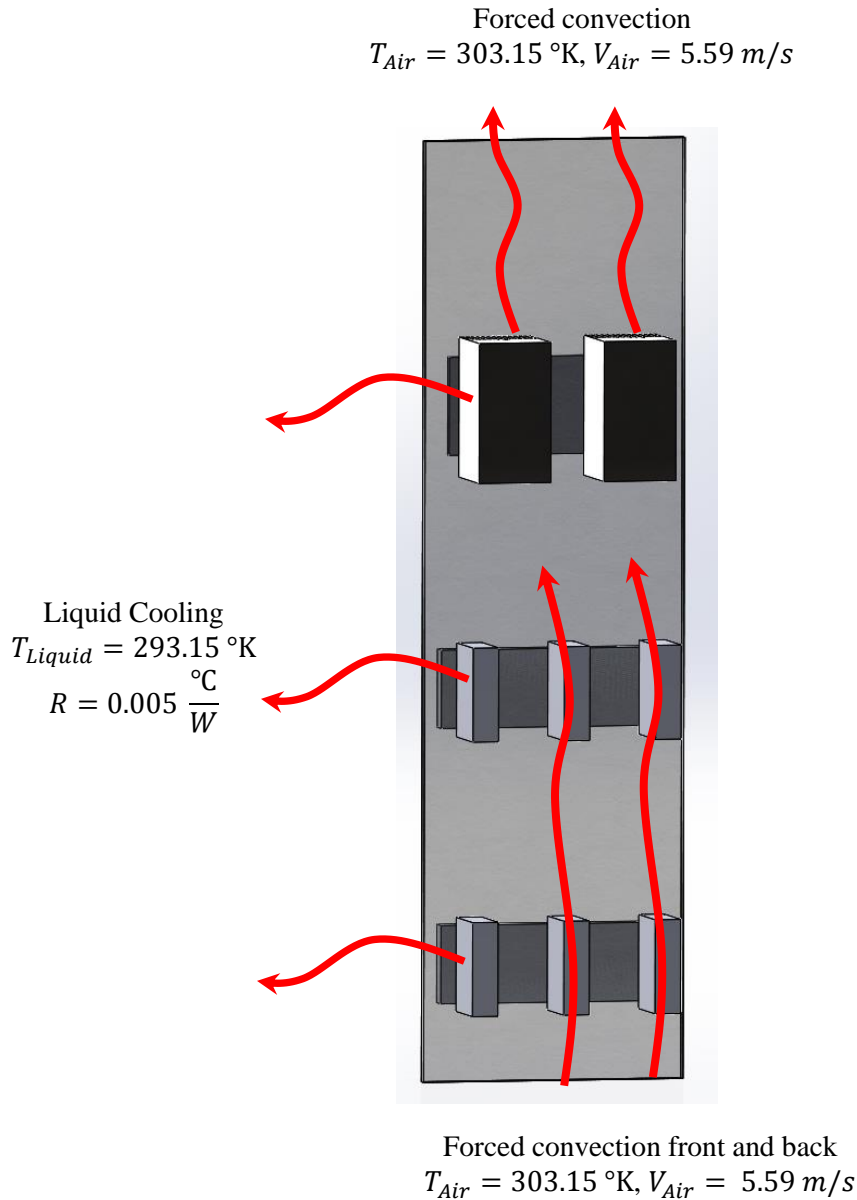


**Figure 4.74. Heat transfer mechanisms for case V.**

#### 4.6.6 Outcome and Discussion

Wall boundary conditions for all case studies is  $T_{wall} = 303.15^\circ\text{K}$ . Table 4.10 summarizes the results for the five studies. The maximum allowable ambient temperature is  $313.15^\circ\text{K}$  ( $40^\circ\text{C}$ ). Unsatisfying cases are marked in red.

**Table 4.10. Results of the 5 case studies.**

Case Number	Cooling Setup	Max Temp (°K)	Average Control Panel Temp (°K)
<b>I</b>	HVAC unit	398.49	379.70
<b>II</b>	Roof Fan	373.9	347.48
<b>III</b>	Fins for Control Panel Plate and Roof Fan	345.92	317.37
<b>IV</b>	Cold Plate for Control Panel plus HVAC unit	334.24 (Tc = 293.15 and R=0.005)	310.47 (Tc = 293.15 and R=0.005)
<b>V</b>	Cold Plate for Control Panel plus Roof Fan	331.75 (Tc = 293.15 and R=0.005)	308.7 (Tc = 293.15 and R=0.005)

Figure 4.75 through Figure 4.79 show the temperature distribution for each case. Streamlines represent the temperature gradient lines.

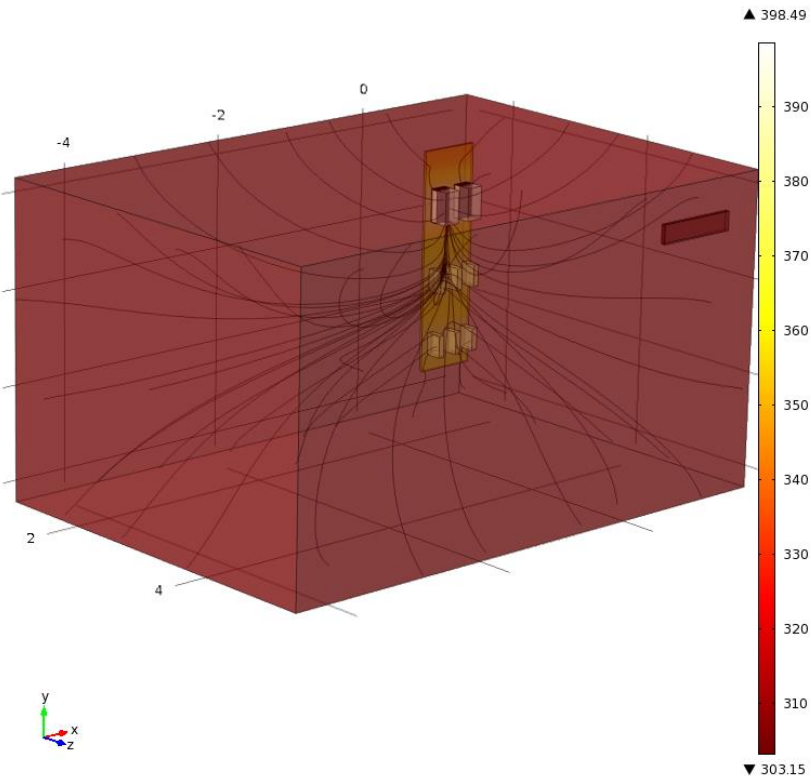


**Figure 4.75. Temperature distribution for case I. Colors show the temperature and streamlines represent the temperature gradients.**

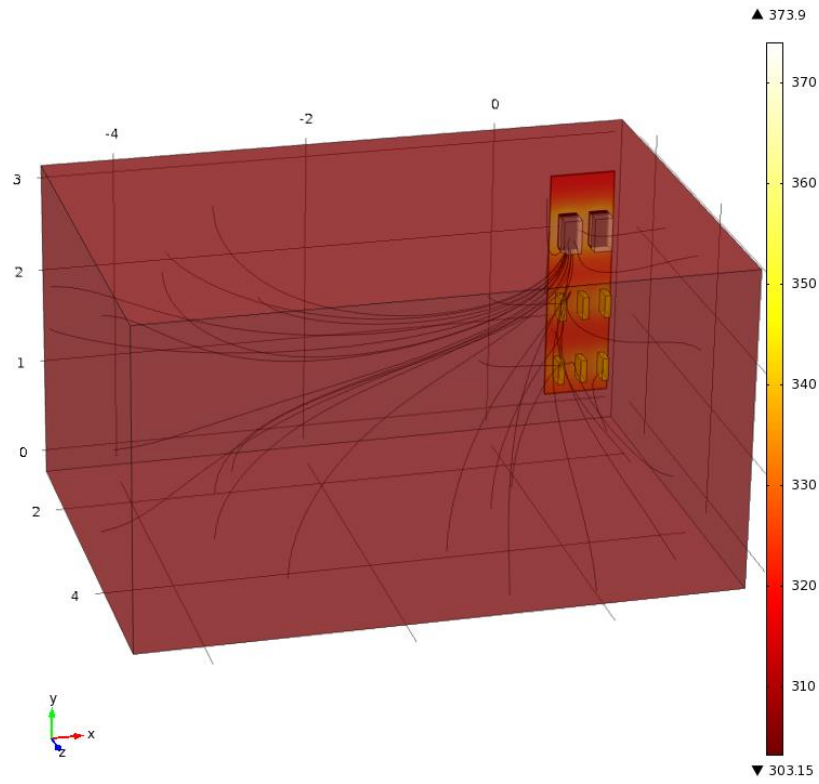


Figure 4.76. Temperature distribution for case II. Colors show the temperature and streamlines represent the temperature gradients.

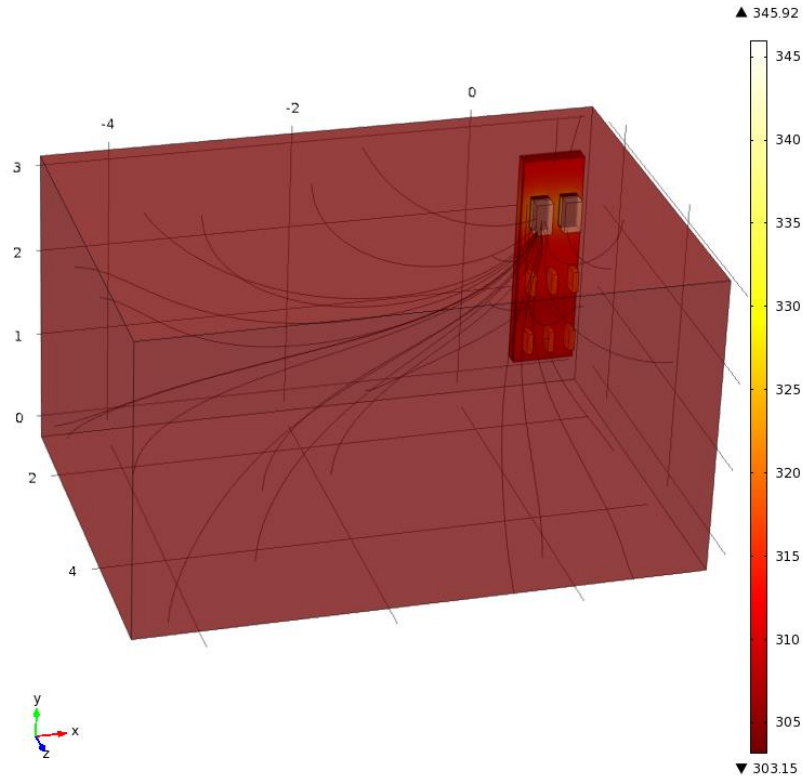


Figure 4.77. Temperature distribution for case III. Colors show the temperature and streamlines represent the temperature gradients.

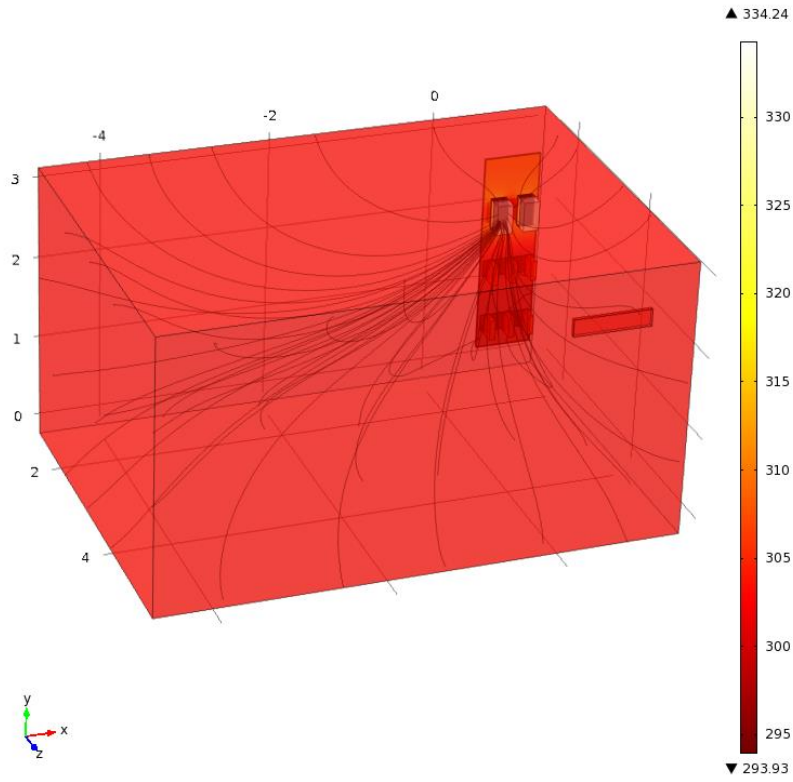


Figure 4.78. Temperature distribution for case IV. Colors show the temperature and streamlines represent the temperature gradients.

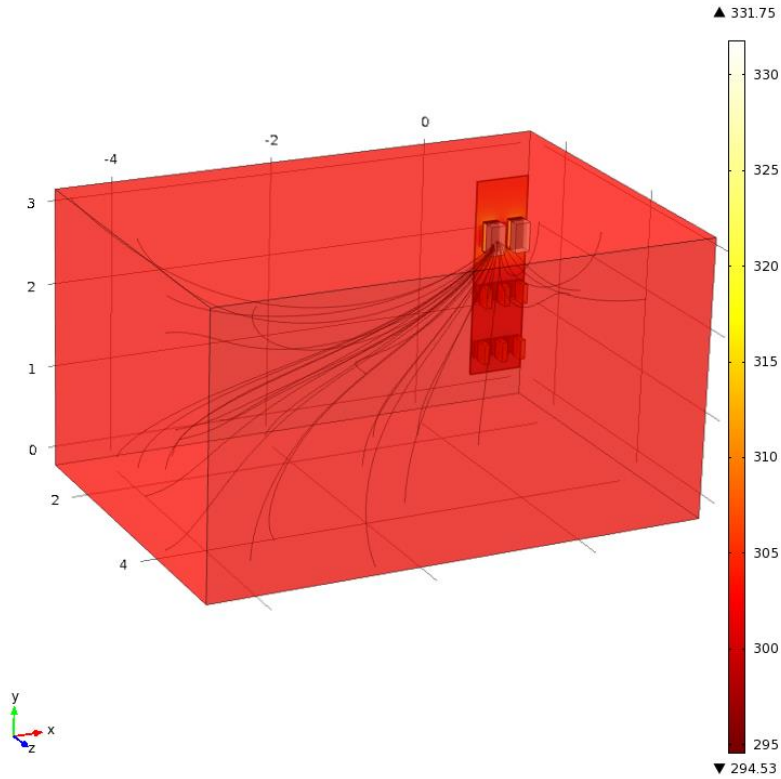


Figure 4.79. Temperature distribution for case V. Colors show the temperature and streamlines represent the temperature gradients.

The following three figures compare cases I, II and V regarding the affected volumes inside which the temperature is above 308.15°K (35°C). Motor manufacturer specs 403.5°K as the maximum ambient temperature and 35°C provides some safety factor to the design.

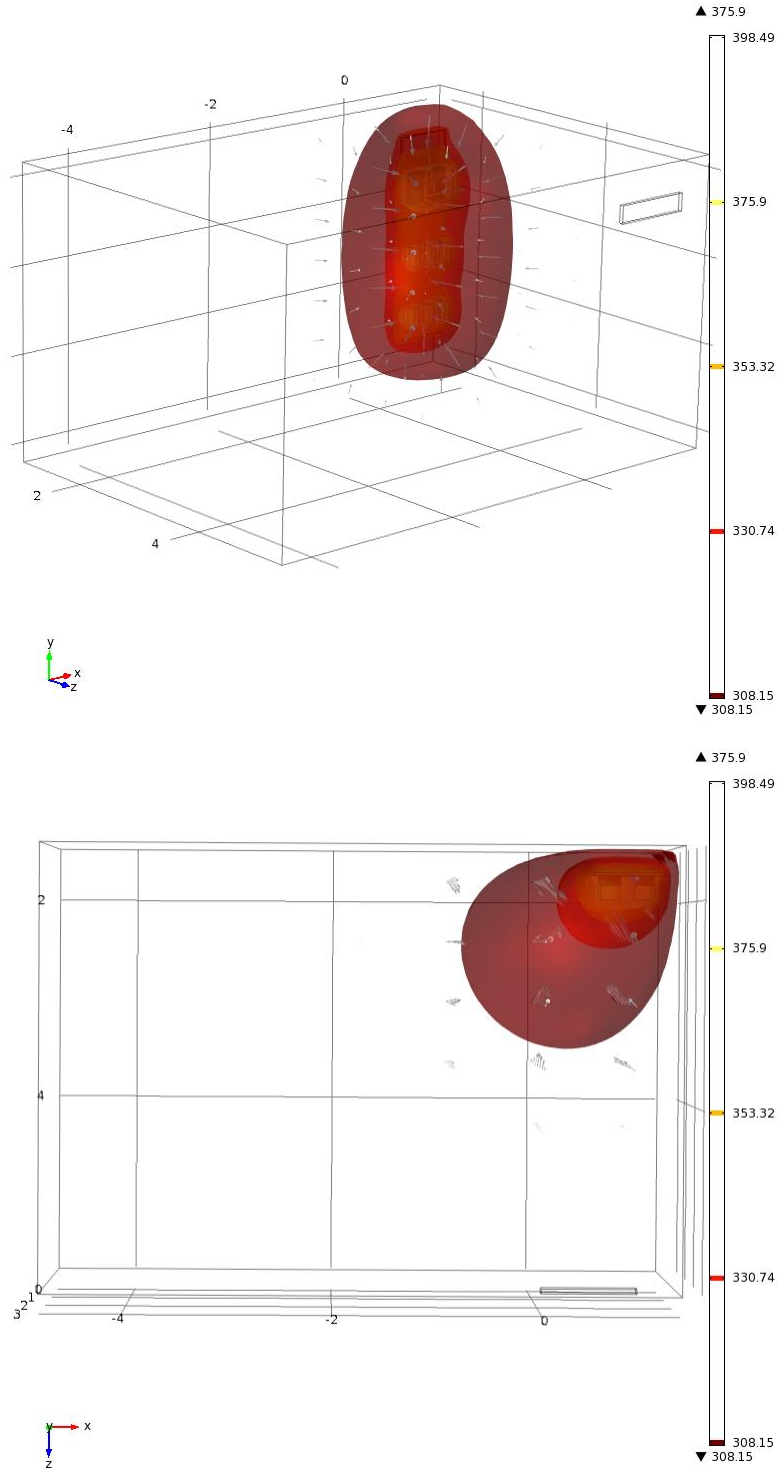


Figure 4.80. Isotherm surfaces for  $T=308.15\text{K}$  (35°C) and above in case I. Arrows represent the temperature gradient.

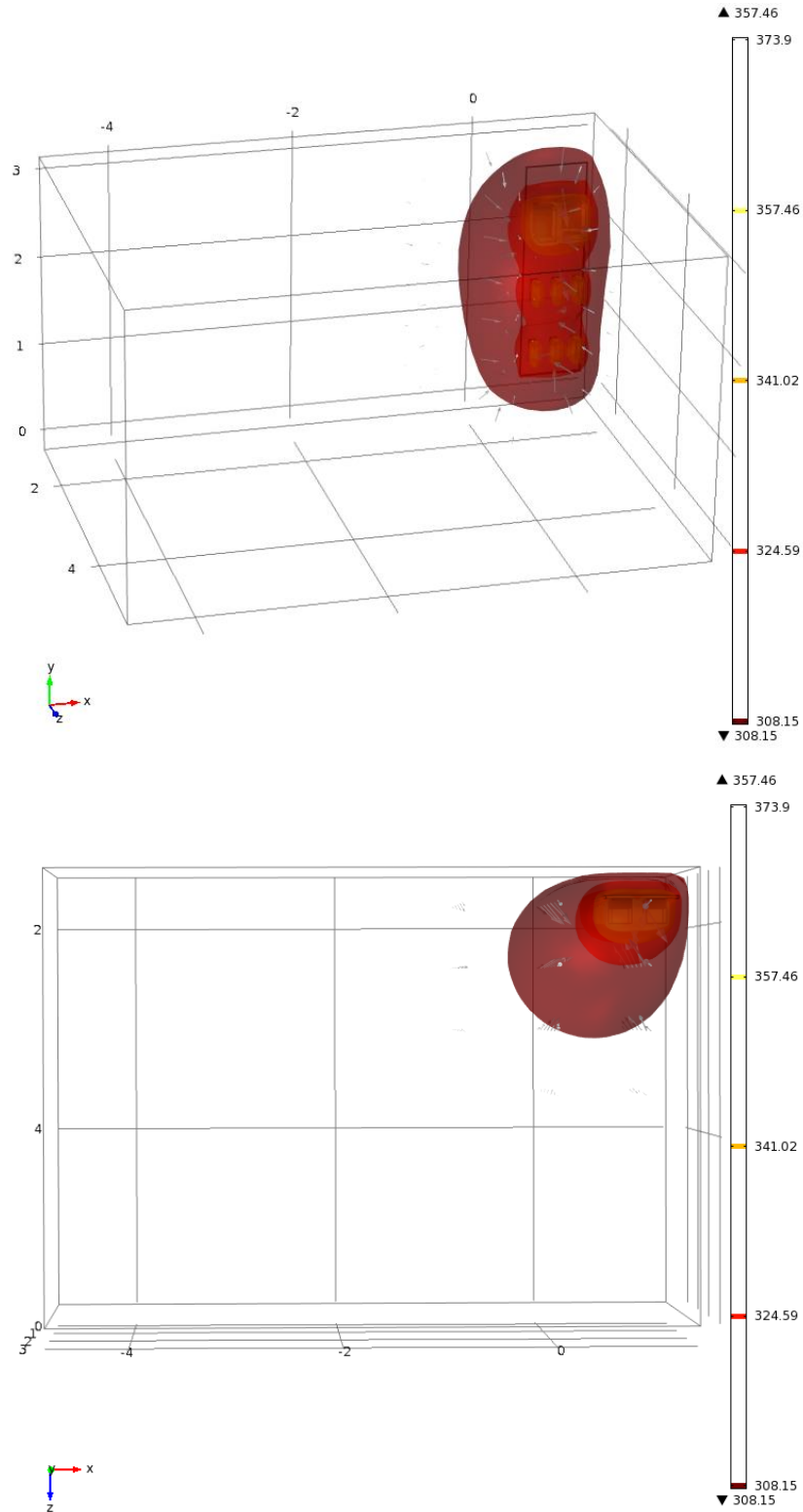


Figure 4.81. Isotherm surface for  $T = 308.15^{\circ}\text{K}$  ( $35^{\circ}\text{C}$ ) and above in case II. Arrows represent the temperature gradient.

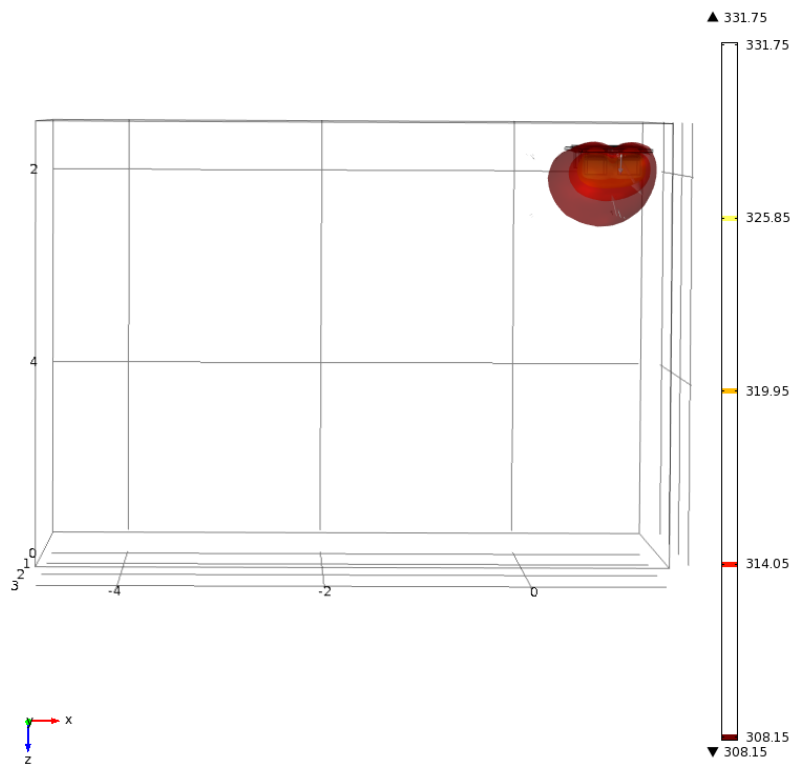
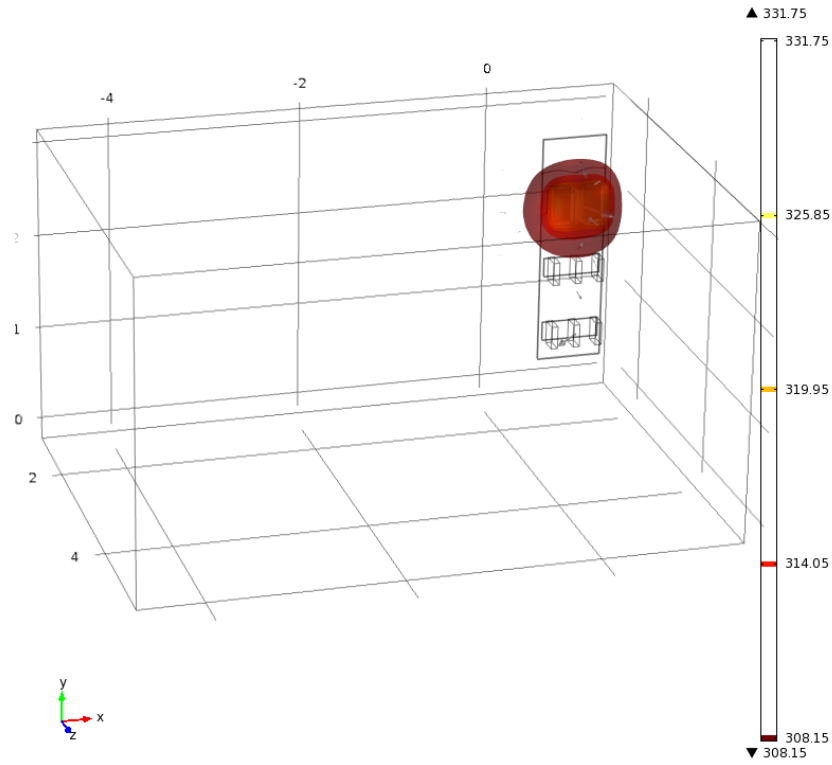


Figure 4.82. Isotherm surface for  $T = 308.15 \text{ K}$  (35°C) and above in case V. Arrows represent the temperature gradient.

By comparing the size of isothermperature surfaces in cases 1, 2, and 5 one can realize the average temperature of other sensitive electronics that are going to be mounted next to the heat dissipative components. This provides another tool for deciding which cooling mechanism delivers the highest performance at lower cost. Based on the results in Table 4.10, and Figure 4.77, case III was chosen for the cabinet, with provisions for adding the cold plates used in case IV.

## Chapter 5. Safety and Monitoring

The Stop function is used to shut down the machine in normal operation. The Stop functions are defined by IEC 60204. The Stop Category must be determined by a risk evaluation of the machinery.

**Category 0:** Shut-down by immediate switching-off of the energy supply to the drive machinery (i.e. an uncontrolled shut-down). Such functionality can be implemented with Safe-Torque-Off (STO) circuit (Section 5.1).

A wiring example for stop Category 0 is given in Figure 5.1. The switching sequence is precisely determined by this circuit to avoid undesirable fault messages and servo amplifier failures. It is not possible to achieve a Category 0 shut-down with the servo amplifier alone since hard-wired electromechanical components are compulsory for this type of disconnection. To meet Category 0, a brake that is built into the motor must have an additional electromechanical control circuit, as well as the control by the servo amplifier,

Usually, a brake in a servo motor only functions as a holding brake (Section 5.5), not means for deceleration. To ensure an emergency stop function, the braking torque that is required for decelerating the entire mechanical system is calculated. Using the holding brakes for deceleration leads to significantly increased wear in the motors.

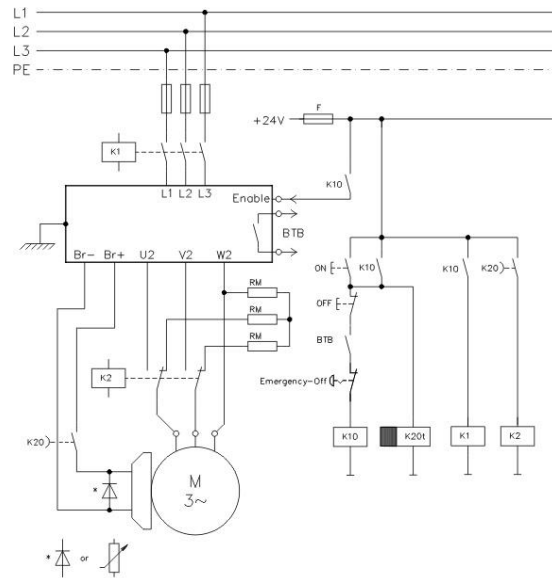


Figure 5.1. Wiring example for stop Category 0 (courtesy of Kollmorgen) [73].

**Category 1:** A controlled shut-down, whereby the energy supply to the drive machinery is maintained to perform the shut-down, and the energy supply is only interrupted when the shutdown has been completed. This function can be implemented with a Hardware Enable circuit (Section 5.2)

A wiring example for stop Category 1 is given in Figure 5.2. The logic power (often 24V) supply for the servo amplifier must remain on for Category 1 stop. The drive is braked in a controlled manner during the stopping (disabling) procedure. If the speed drops below a certain threshold, the holding brake will be applied, and the output stage will be disabled.

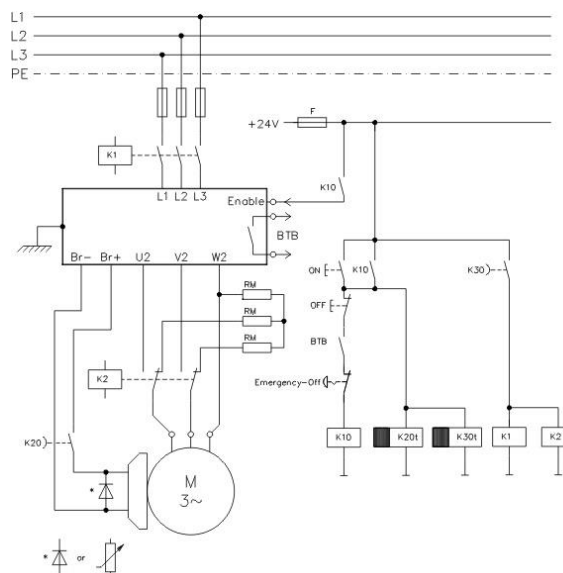


Figure 5.2. Wiring example for stop Category 1 (courtesy of Kollmorgen) [73].

**Category 2:** A controlled shut-down, whereby the energy supply to the drive machinery is maintained. This functionality is often implemented in motion controlling software. A wiring example for stop Category 2 is given in Figure 5.3. The drive is braked in a controlled manner during the stopping (disabling) procedure. If the speed drops below a threshold, the holding brake is applied, and the output stage remains enabled. In this case, there is no interruption of the electrical supply.

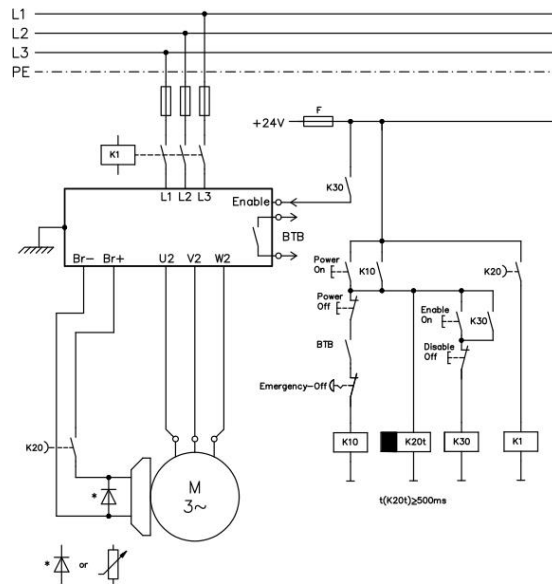


Figure 5.3. Wiring example for stop Category 2 (courtesy of Kollmorgen) [73].

The Stop Category must be determined by a risk evaluation of the machine. Also, suitable means must be provided to guarantee a reliable shut-down. Category 0 and Category 1 Stops must be operable independently of the operating mode, whereby a Category 0 Stop must have priority. Stop functions must be implemented by **disconnection** of the appropriate circuitry, and take precedence over assigned start functions. Figure 5.4 compares the controlled and uncontrolled stops. In Category 1 and 2 stops, the brake will get engaged after velocity drops below a certain threshold or when a speed threshold timeout saturates. In Category 0 stop, the brake will be engaged after the disable timeout saturates.

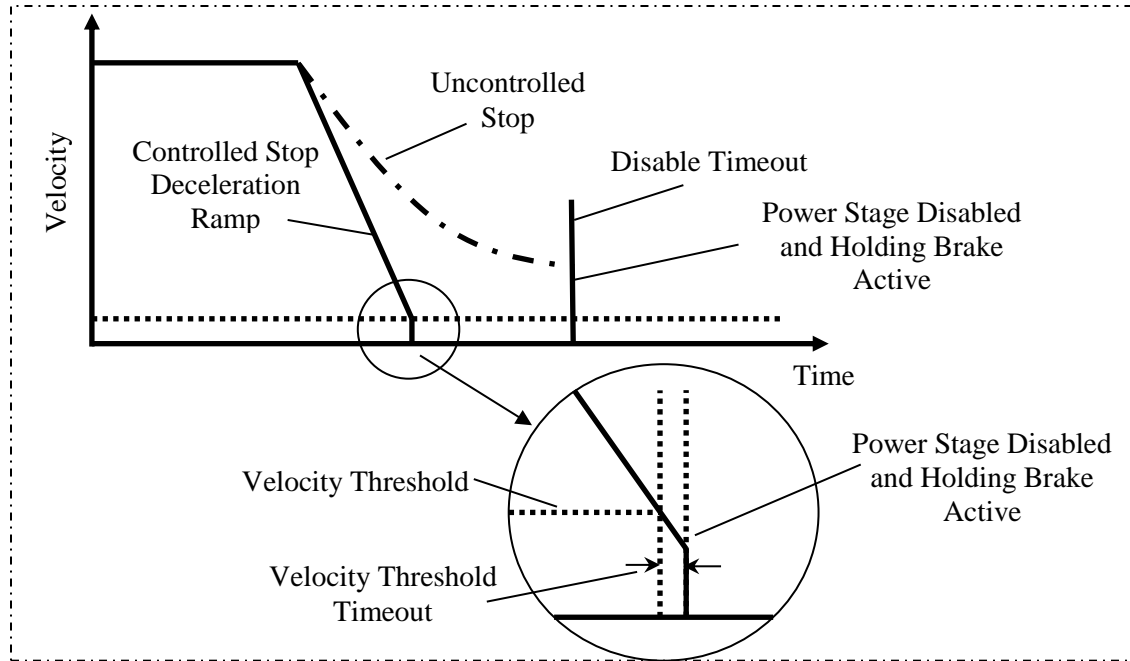


Figure 5.4. Comparison between stop categories.

If necessary, provision must be made for the connection of protective devices and lock-outs. If applicable, the Stop function must signal its status to the control logic. A reset of the Stop function must not create a hazardous situation.

Table 5.1. Function of safety circuits in the VT Roller Rig.

Safety Circuit	Function
Safe Torque Off	Monitoring the safety gate and unintentional restart prevention
Hardware Enable	Activating the output stage of servo amplifiers
Ready-to-Operate	Monitoring internal faults of servo amplifiers
Logic On-Off	Turning the drive logics ON and OFF
Emergency Stop	Implementing emergency stop
Dynamic Braking	Activating the dynamic brake resistors for electrodynamic braking
Holding Brake	Controlling the holding (static) brake
Temperature Monitoring	Monitoring the temperature of other electronic components and notify the user if over-temperature occurs

## 5.1 Safe-Torque-OFF (STO) Safety Circuit

A frequently required application task is the safe torque off and the protection of personnel against unintentional restarting of drives. With the functional, safe restart lock STO, the drive can be secured on standstill using its internal electronics so that even when power is being supplied, the drive shaft is protected against unintentional restart. The 772 servo amplifier offers a two-channel Safe-Torque-Off (STO) function. The function blocks the trigger pulses of the power transistors (pulse inhibitor). The STO safety function corresponds to stop category 0 (uncontrolled stopping) according to EN60204-1. When STO is engaged during operation, drives generates a fault, and the motor runs down out of control, and there is no possibility of stopping the drive controllably.

The STO function is exclusively intended to provide functional safety, by preventing the restart of a system. To achieve this functional safety, the wiring of the safety circuits must meet the safety requirements of IEC 60204, ISO 12100, IEC 62061 respectively ISO 13849-1. The STO function must not be used if the drive is to be made inactive for the following reasons:

- Cleaning, maintenance and repair operations, long inoperative periods: In such cases, the entire system should be disconnected from the supply by the personnel, and secured (Section 5.4).
- Emergency-stop situations: In an emergency-off situation, switched off the main contactor (Section 5.7).

The safety function STO can be operated from external safety relays, from a safe external control (semiconductor output or driven contact) or the built-in safety card. It can be implemented with single-channel or dual-channel control with simple safety switching devices (corresponding to SIL CL2 in EN62061 and PLd Cat3 in EN13849-1).

### **Advantages of the safety function STO:**

- The DC bus link remains charged up since the mains supply line remains active
- Only low voltages are switched, so there is no contact wear
- Simple wiring is required
- Single or dual channel control possible

In the case of single channel usage of STO, erroneous engaging will not be recognized. Therefore, the output of the control unit must be supervised for possible malfunction. With the dual-channel monitoring of the STO safety function, the switch-off paths are switched separately by two outputs of a safety switching device (e.g. safety relay). To reduce the risk of relay malfunction, a control

circuit with dual-channel SIL CL2/PLd Cat3 is designed for all eight axes (2 AKM84T and 6 EC4). Figure 5.5. shows the circuit diagram for both wheel and roller axes.

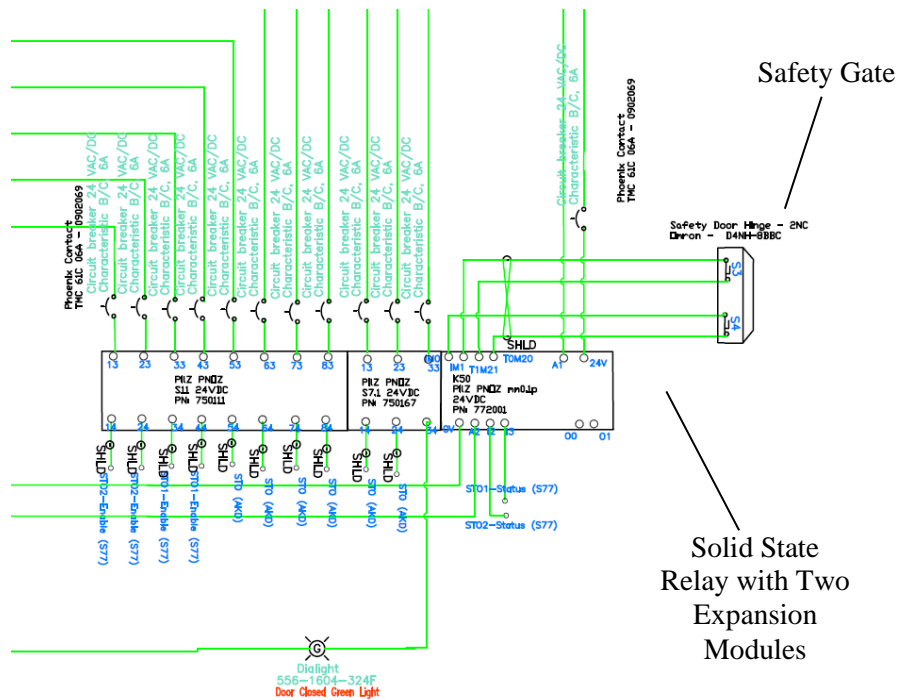


Figure 5.5. Dual-channel SIL CL2/PLd Cat3 STO control circuit for eight axes.

The STO of the drives is switched by a dual channel normally-closed safety door hinge. The hinge is mounted on the door of a protective screen that encloses the Rig. The safety switch gears used in this circuit include a programmable solid-state safety relay with two input channels, an extension solid-state relay with three normally-open contacts, and another extension solid-state relay with eight normally-open contacts. Shielded AWG16 load lines are protected with twelve 6-Amp circuit breakers. A green indicator light visually represents the status of STO signals.

## 5.2 Hardware Enable Safety Circuit

Two enable commands are required for activating the output stage of the drive:

- Enable signal for the servo amplifier, Hardware-Enable with 24V signal
- Software-Enable command by setup Software, Fieldbus or permanently set

Both are required for enabling the amplifier. Software enable means that motion program is properly uploaded on the drive and motion control is ready. However, this can also be permanently enabled and monitor the output stage of the drive through Hardware Enable safety circuit. Enable

is possible only if both inputs of STO have a 24V signal. Table 5.2 clarifies the possible status that may happen between STO and Hardware Enable.

**Table 5.2. Possible servo amplifier status between STO and HW-Enable.**

STO1 and STO2	Hardware Enable	Motor Torque	Drive Status
0V	0V	No	Error
0V	+24V	No	Error
+24V	0V	No	Normal
+24V	+24V	Yes	Normal

Voltages between -3 and 5V are considered low, and 15 to 30V are considered high. When Hardware Enable has low voltage (like an emergency stop), drive generates a fault, and speed-controlled braking with an emergency ramp (Category 1 stop) will bring the motor to stop. When the speed drops below a certain threshold, the output stage will be disabled, and the amplifier will not be ready to operate (not RTO, Section 5.3). Standard operation is possible when the error has been quit (Emergency Stop released). Figure 5.6. shows the Hardware Enable circuit for the VT Roller Rig. The circuit constitutes of a dual input solid-state relay with two normally-open contacts, a solid-state extension relay with eight normally-open contacts, an illuminated momentarily pushbutton (reset), Eight 6-Amp circuit breakers, a green indicator light, and AWG16 shielded wires. The circuit implements Hardware Enable for eight axes. Inputs of these relays are taken from the emergency stop circuit.

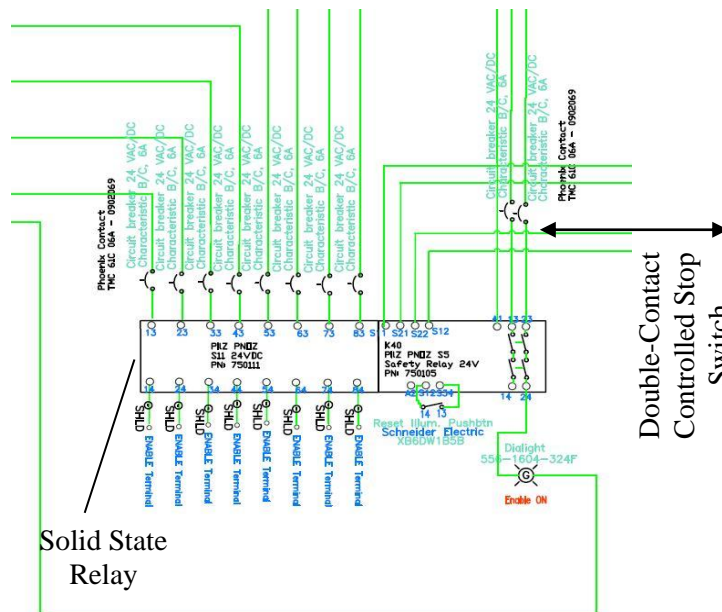


**Figure 5.6. Hardware Enable control circuit for eight axes.**

### 5.3 Ready-to-Operate (RTO) Safety Function

Ready-to-Operate (RTO) function is an internal contact of the ServoStar servo amplifier that is signaled by a floating relay. The contact is closed when the servo amplifier is ready for operation, and the signal is not influenced by the Hardware Enable signal, or the brake threshold (Sections 5.1 and 5.5.1). Unlike STO and Hardware Enable that monitor external events, RTO is dedicated to internal faults. RTO is implemented by the manufacturer with high sensitivity to the possible abnormal conditions. All faults cause the RTO contact to open and the output stage to be switched off. Table 5.3 provides a list of most significant internal faults that will cause the RTO contact to open. The third column of the table gives reference to the section of this document where more information about that fault can be found. If the RTO contact is open, the output stage of the drive is disabled and has not power output to the motor.

While the servo amplifiers would open the RTO contacts in case of the above faults, an intermittent circuit is required to integrate the VT Roller Rig emergency stop circuit and the two RTO contacts of the servo amplifiers. The output of this circuit would be turned off if any fault occurs, either internally or externally. This signal is a summarized representation of all safety and monitoring systems of the Rig. For the initial tests with the VT Roller Rig, this signal is fed into the shunt tripping circuit of the I-Line panel (mains 3-phase circuit breakers). Figure 5.7. shows this circuitry.

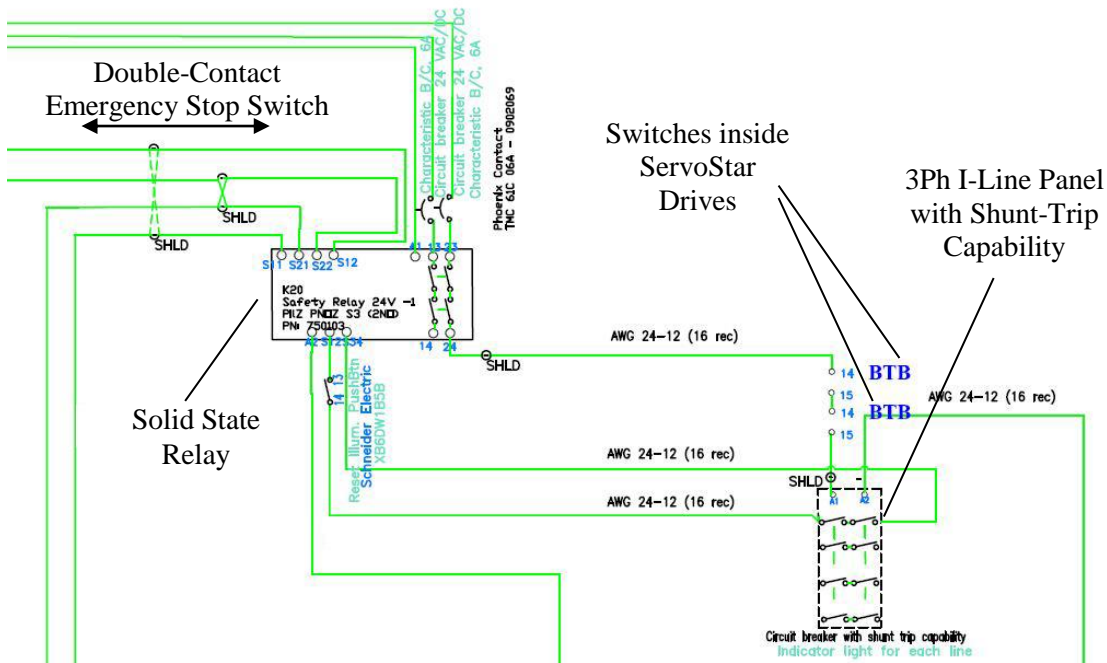


Figure 5.7. RTO intermittent circuit.

**Table 5.3. Internal faults that cause the RTO contact to open.**

Fault	Reason
Overvoltage	Overvoltage in DC bus link. Limit depends on the electrical supply voltage
Undervoltage	Undervoltage in DC bus link (default: 100 V)
Internal Voltages	Internal supply voltages not ok
Heat Sink Temperature	Heat sink temperature too high (default: 80 °C)
Motor Temperature	Motor temperature too high or temperature sensor is defective
Ambient Temperature	Ambient temperature too high
Overspeed	Motor speed is too high
Motor Phase	One or more motor phases are missing (e.g. cable break)
Output Stage	Fault in the power output stage, also with wrong motor cable or insufficient cable shielding
STO	Operational error with STO
Emergency Stop	Emergency stop circuit is activated, or Emergency stop timeout has reached
Brake Circuit	Brake circuit faulty or incorrect setting
Feedback	Cable break, short-circuit, short to ground
System Software	System software not responding correctly

#### 5.4 Logic ON-OFF

This section describes the circuit that controls the logic power of the ServoStar and AKD drives. It is important to note that motors may be in stand-still position, or the output stage of the drives may be deactivated while the logic power is still ON. If the Logic ON-OFF is switched OFF, the following circuits will lose control over the system or switched OFF: Hardware Enable, Emergency Stop, and Motor-Short Dynamic Braking. However, the following will remain ON: STO, RTO, Regenerative Dynamic Braking, Holding Brake, and Thermal Monitoring. The second group should never be switched OFF, even if the Logic ON-OFF is deactivated. As described in Section 4.1.3, the power to these circuits is backed up by interruptive power supplies. The only way to kill these systems is via the mains service switch, and manually removing both back up UPSs.

This circuit constitutes of a normally-open illuminated momentarily pushbutton (ON), a normally-closed illuminated momentarily pushbutton (OFF), a 4-pole-double throw mechanical relay, a protective lock for the OFF button, a red indicator light, a green indicator light, and AWG16 shielded cables. When the ON button is pressed, the 4PDT relay is energized, and the emergency stop relay is activated. One of the contacts of the emergency stop relay is fed back to the 4PDT relay after the ON switch. This means that, as the ON switch is released, the 4PDT relay remains energized. The OFF switch sits between the emergency stop relay and the 4PDT relay. If it is pressed, the feedback line opens and the 4PDT relay halts. Figure 5.8 shows the Logic ON-OFF circuit for the VT Roller Rig.

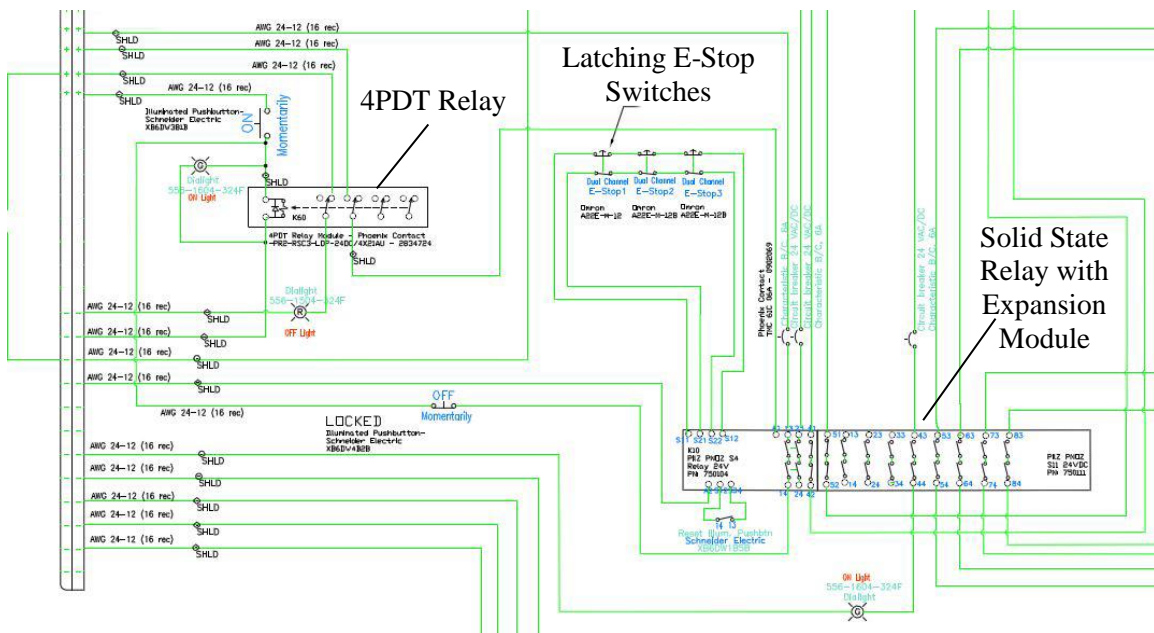


Figure 5.8. Logic ON-OFF and Emergency Stop circuits for the VT Roller Rig.

### 5.5 Dynamic Braking

Dynamic braking is a general term that denotes application of various electrical or mechanical systems for bringing the AKM84T motors to stop from a non-zero speed. For the VT Roller Rig, different mechanical and electrical systems were considered for dynamic braking. Integration of mechanical disk brakes into the powertrain adds significantly to the complexity of the driveline. On the other hand, engaging mechanical brakes while the output stages of the drives are active can lead to over-voltage in the motor or DC-bus. Applying mechanical brake should also be synchronized between both wheel and roller drivelines. Otherwise, excessive torque will be enforced to one brake mechanism. Considering the rotational speed of the drivelines, any possible breakage in the brakes can lead to serious safety hazards. Moreover, synchronizing the two

mechanical brakes will require additional control and monitoring gears. After numerous discussions with application engineers of the motors and gearheads suppliers, two alternative approaches were selected for dynamically braking the Rig.

### 5.5.1 Regenerative Dynamic Braking

In this method, mechanical energy is converted into electrical energy using the motor regeneration and is fed back into the servo amplifier. A part of this braking energy is stored in the DC link bus capacitors of the servo amplifier. If these capacitors are filled, the brake energy is led to the regenerative resistors to be dissipated as heat. The regenerative resistors are switched in by the brake circuit. The setup software can be used to adapt the brake circuit (thresholds) according to the electrical supply voltage.

Electric power stored in the DC Link capacitors ( $E_c$ ), depends on the mains supply voltage.  $E_c$  is the amount of additional energy that can be stored in the bus capacitors during motor regeneration before the shunting resistor circuit is closed. This is the difference between the peak energy (Joules) in the bus capacitors and the nominal energy stored. Specifically:  $\frac{1}{2} CV^2$ , (where C is the capacitance in farads and V, is the peak bus voltage when the shunting transistor turns on, minus the minimal energy value  $\frac{1}{2} CV^2$  based on the nominal bus voltage. ServoStar servo amplifier have 900  $\mu F$  capacitors. The rated voltage of the motors must be at least as high as the DC bus link voltage divided by  $\sqrt{2}$  produced by the servo amplifier ( $U_{n \times Motor} \geq UDC / \sqrt{2}$ ). Based on motor manufacturer data at 3Ph 480V,  $E_c$  is 110J. From that the reduced speed due to the power storage in DC capacitors can be found with [118]:

$$n_2 = \sqrt{n_1^2 - E_c \times \frac{219}{J + J_{ext}}} \quad (33)$$

where  $n_1$  is the maximum speed of the motor,  $J$  is the inertia of the motor in  $kg/m^2$ ,  $J_{ext}$  is the inertia of the load, and  $n_2$  is the reduced speed of the motor. The rest of mechanical energy is dissipated in regenerative resistors ( $E_{Brems}$ ). It can be calculated as:

$$E_{Brems} = \frac{(J + J_{ext}) \times n_2^2}{228} \quad (34)$$

From this energy, the number of turns until the motor stops ( $N$ ), and time to stop ( $t$ ), one can calculate the required brake power for regenerative resistors as:

$$P_{Brems} = \frac{N \times E_{Brems}}{t} \tag{35}$$

Considering the large inertia of the roller driveline 495(kg.cm<sup>2</sup>), regenerative resistor should be sized properly. On the other hand stop time greater than 1s and less than 5s is desirable. Small stop time not only increases the required resistor size, but puts the driveline under excessive braking torque. Considering the recommendations of the resistor manufacturer for allowable range of power, 6kW rated power per regenerative resistor is used for selecting the proper part. The regenerative dynamic braking circuit is shown in Figure 5.9. The circuit constitutes of two ServoStar servo amplifiers, two regenerative resistors, DC-Bus link, four 125-Amp fuses, and shielded twisted pair AWG2 cables.

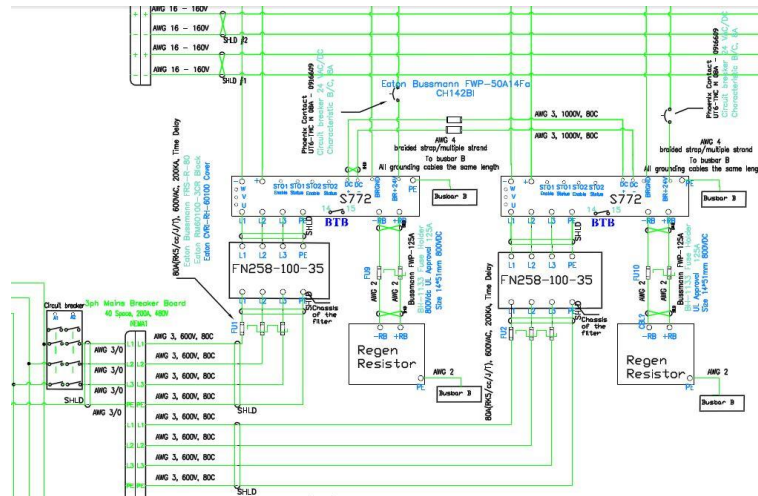


Figure 5.9. Regenerative Dynamic Braking circuit.

### 5.5.2 Motor-Short Dynamic Braking

In this approach, motor leads are disconnected from servo amplifiers and external dynamic brakes short the U, V and W leads of the motor to dissipate the mechanical energy as heat. Unlike regenerative braking, no energy will be stored in DC bus link, and servo amplifier will have no control over the motor after external dynamic brakes are switched on. This method assures minimum stop time but does not allow for Category 1 or 2 stops. Therefore, this approach is only recommended for emergency stop or safety hazards.

The equations for calculating the stopping time with the motor-short dynamic braking of a 3Ph permanent magnet (PM) brushless motor are adapted from a Kollmorgen application note originally derived from a PM DC motor [119]. A typical connection for 3-phase PM motor for dynamic braking is shown in the figure below.

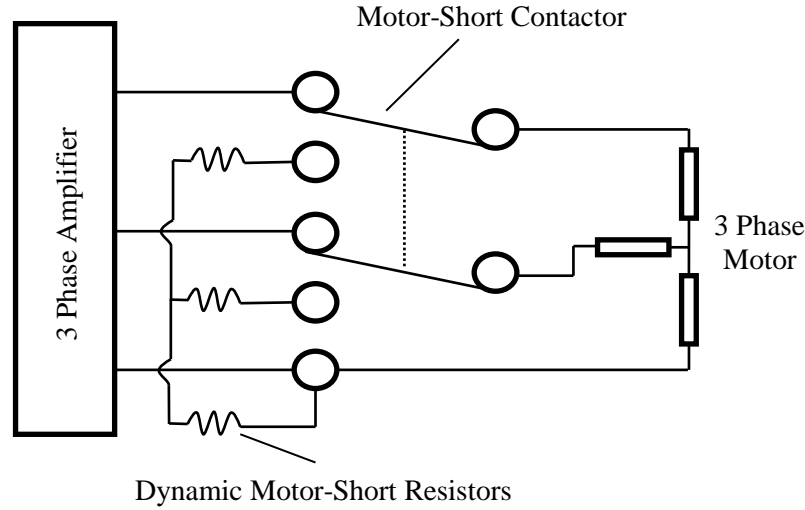


Figure 5.10. Typical connection for 3-phase PM motor for dynamic braking.

Assuming a motor-short dynamic brake resistance of  $R_{DB}$ , the current in each phase resistor ( $I$ ) can be calculate as:

$$I = \frac{\omega K_B}{R_o} \quad (36)$$

where  $\omega$  is the motor speed in  $\frac{rpm}{sec}$  or  $\frac{rpm}{9.55}$ .  $K_B$  is the motor BEMF constant in  $\frac{V \times sec}{rad}$  or  $\frac{V \times 104.7}{kRPM}$ .  $R_o$  is the resistance per phase of the motor plus  $R_{DB}$  in ohms. The total inertia ( $J_o$ ) can be defined as:

$$J_o = J_M + J_{RL} \quad (37)$$

where  $J_M$  is the motor inertia in  $lb \times ft \times s^2$ , and  $J_{RL}$  is the reflected load inertia on the motor in the same unit.  $J_{RL}$  is found as:

$$J_{RL} = \frac{J_L}{g^2} + J_{GI} \quad (38)$$

where  $g$  is the gearhead ratio, and  $J_{GI}$  is the inertia of the gearhead at the input.

From that, parameters  $P$  and  $Q$  will be defined as:

$$P = \frac{(K_B - L \times PP)K_T}{J_o R_o}$$

and

$$Q = -\frac{T_F}{J_o} \quad (39)$$

where  $L$  is the phase inductance in  $L - L$  Henrys,  $PP$  is the number of motor pole pairs,  $K_T$  is the motor torque constant in  $\frac{lb \times ft}{\frac{amp}{phase}}$ , and  $T_F$  is the static friction in  $lb \times ft$ .

Finally, motor stop time with motor-short dynamic braking can be calculated as:

$$t = \left(\frac{1}{P}\right) \ln\left(\frac{\omega_1 - \frac{Q}{P}}{\omega_2 - \frac{Q}{P}}\right) \tag{40}$$

where  $\omega_1$  is the beginning speed in  $\frac{RPM}{9.55}$  and  $\omega_2$  is the ending speed in the same unit. If  $\omega_2 = 0$ , then equation 40 can be simplified to the following:

$$t = \left(\frac{1}{P}\right) \ln\left(1 - \left(\frac{P}{Q}\right) \omega_1\right) \tag{41}$$

If friction is neglected, equation 41 leads to:

$$t = \left(\frac{1}{P}\right) \ln\left(\frac{\omega_1}{\omega_2}\right) \tag{42}$$

From equation 42, one can assume a motor-short dynamic brake resistance and find the equivalent stop time in the worst case scenario. With iterative calculations, the proper resistance size can be found. For the purpose of the VT Roller Rig, stop time less than 2s is desirable. After numerous discussions with Kollmorgen application engineers, peak braking torque was limited to 50% of the nominal motor torque ( $0.5 \times 680 = 340Nm$ ). Table 5.4 shows some of the calculations towards finding the proper size resistance. For these calculations  $\omega_1 = 2000rpm$ ,  $\omega_2 = 0$ ,  $T_F = 0$ . From the gearbox manufacture data sheet, gearbox efficiency is set 94%.

**Table 5.4. Iterative calculations for sizing motor-short dynamic braking resistors.**

$R_{DB}$ ( $\Omega$ )	Estimated Stop Time (s)	Peak Watts/Phase (W)	Braking Torque (Nm)
1.6	0.53	25261	340
3.3	0.90	12630	170
6.6	1.49	6315	85
8.2	1.73	5052	68
17.0	2.76	2452	33
82.6	6.07	505	6.8

Not every desirable size dynamic resistor is available off the shelf. From the above calculations, the 8.2 $\Omega$  resistor will stop the motor in 1.73s and imposes 10% of motor nominal torque to the

motor during braking. The motor-short dynamic braking circuit is constituted of two AKM84T motors, 8 T-connectors, two 3Ph contactors, a dual-channel time-delayed solid-state relay with two normally-open contacts, six 8.2Ω dynamic resistors, two 6-Amp circuit breakers, a green indicator light, a red indicator light, shielded AWG4 motor cables, shielded AWG16 cables, and shielded twisted pair AWG16 cables. Inputs of the solid-state relay are taken from the emergency stop circuit.

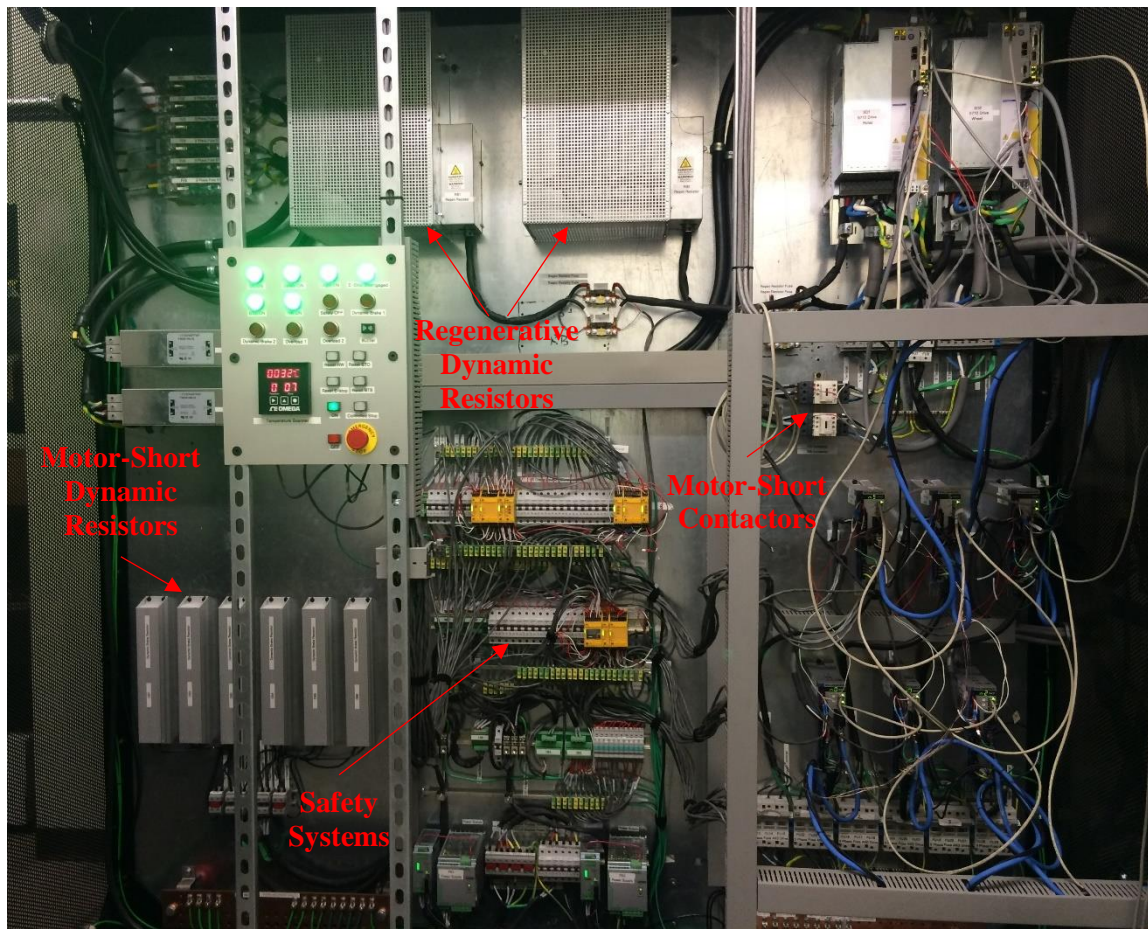


Figure 5.11. Motor-Short Dynamic Braking circuit.

## 5.6 Holding Brake

All AKM84T and EC4 motors are equipped with an internal holding brake mechanism that is intended to be used in “static/stationary” conditions. The application of this brake in “dynamic/moving” condition will result in dramatic wear of the brake mechanism. This brake is only intended for holding the motor in stalled condition. The holding brake is not field-replaceable, and two possible scenarios can damage it:

- Using the holding brake for reducing speed of the motor
- Applying power to the motor while the holding brake is engaged

The holding brake can be controlled directly with the servo amplifier with 24V voltage level. The following scenario describes the function of the holding brake in an emergency stop condition (Hardware Enable off). The same procedure can be followed for normal circumstances when the motor is stopped manually and holding brake is being engaged.

When the Hardware Enable signal drop, after a delay time of 100ms, the speed setpoint of the servo amplifier is internally driven down with an adjustable ramp to 0rpm. The output for the holding brake is switched on when the speed has reached 5rpm, at the latest after 5s Hardware Enable signal drops. The release delay time (tbrH) and the engage delay time (tbrL) of the holding brake are built into the motor for preventing instantaneous engagement of the holding brake. Figure 5.12 shows the proper sequence for switching off the output stage of the servo amplifier with the Holding Brake signal.

The holding brake is not intended to be used as a single stage functional safety during maintenance. An additional mechanical brake is required to hold falling loads. Turning the logic or power systems off will disengage the holding brake.

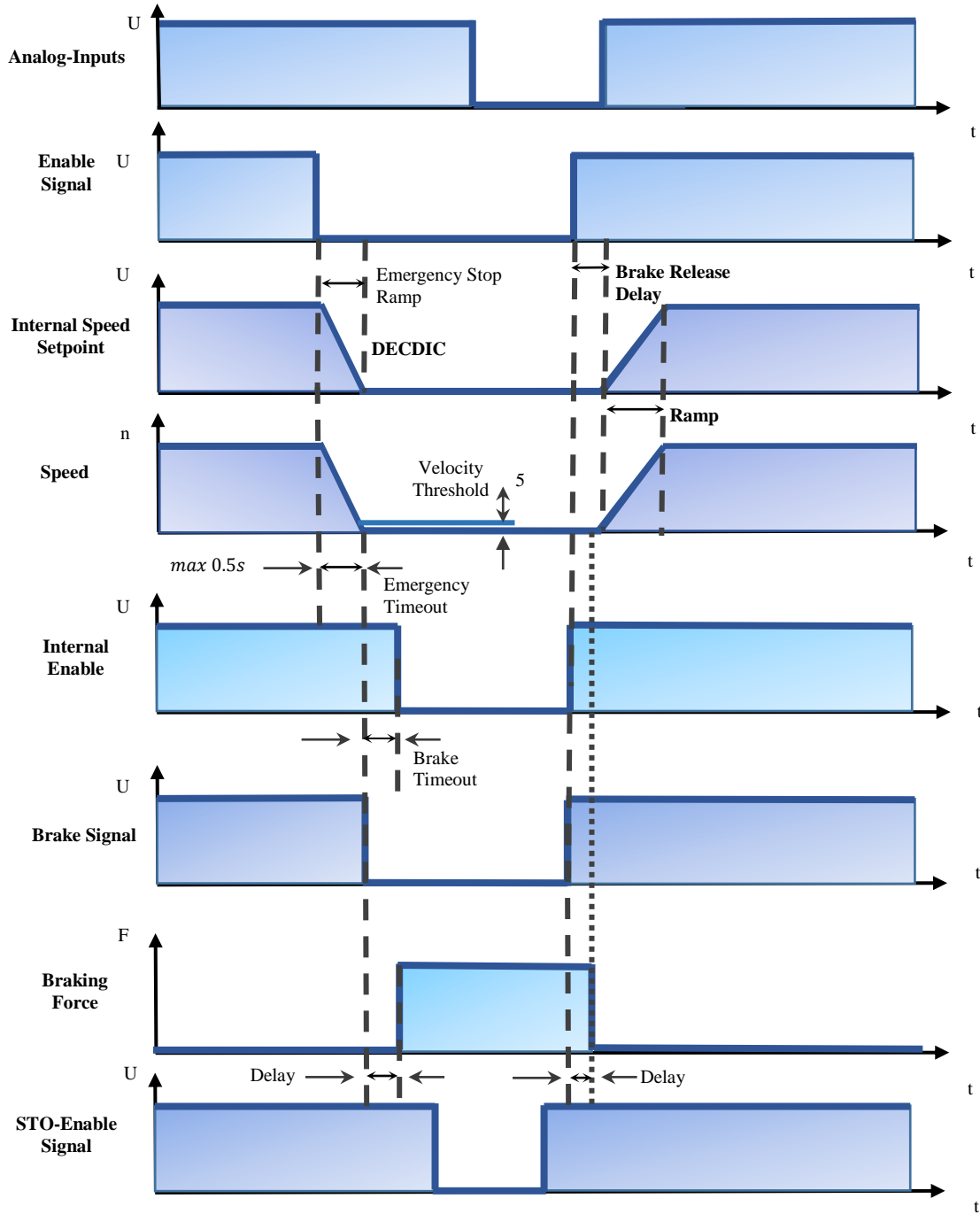


Figure 5.12. Special sequence for switching off the output stage of the servo amplifier with the Holding Brake signal [73].

### 5.7 Emergency Stop

The stop categories described at the beginning of this chapter, classify the general STOP functions, and may be used for normal stopping as well as e-stop. Stop categories and control reliability

categories are not the same, and there are significant differences between them. Control reliability categories are defined and described in ISO 13849-1, and they are used to describe system architectures for safety-related control systems. Each architecture includes a range of reliability performance that can be related to the degree of risk reduction in the system. The following control circuits could fall within the scope of these architectures: STO, Hardware-Enable, RTO, Logic On-OFF, Dynamic Braking, and Holding Brake.

Three standards define the requirements for emergency stop categories, and they are relatively consistent.

- ISO 13850, Safety of machinery: Emergency stop function
- IEC 60204-1, Safety of machinery: Electrical equipment of machines (aka EN 60204-1)
- NFPA 79, Electrical Standard for Industrial Machinery

The three stop category definitions match well with the regulations given in these three standards. All standards require all machines to have at least a Category 0 stop. This is identical to physically killing the power source through a master control relay, or through an emergency stop. However, this does not require all machines to have an emergency stop. The VT Roller Rig can perform Category 0 stop with each one of STO, RTO, Hardware-Enable, Logic ON-OFF, and Motor-Short Dynamic Braking control circuits without having a dedicated emergency stop circuit. Therefore, it well satisfies the requirement. However, stopping the system with Category 0 stop can impose certain risks to the personnel and machinery. First, all moving objects coast to stop out of control. Considering the high kinematic energy stored in the wheel and roller drivelines, broken components should be treated as serious safety risks. In addition to that, increasing the number of turns before the machine stops, can lead to more damage to the machinery. Categories 1 and 2 are favorable for three reasons:

- The machinery has a significant amount of inertia, meaning that it will not coast to stop in a short time
- The machinery can be stopped more quickly under control than when the power is simply removed
- The machinery needs to be stopped on a regular basis during operation. This means that there are devices that require power to keep them in a safe state. In this case, certain precautions should be taken into account as leaving high power on the machinery exposes user to electrical shock hazards

Category 2 stop is not allowed for emergency stopping, although it may be used for normal stop functions. ISO 13850, IEC 60204-1, and NFPA 79 explicitly limit emergency stop functions to Categories 0 and 1. For the VT Roller Rig, emergency stop circuit is intended to serve two purposes:

- Give the highest priority to Category 0 stop
- Allow for Categories 1, and 2 stop using the same system architectures

The emergency stop circuit is not a safeguard by itself, but can be considered as a complementary prioritizing measure. Understanding the hazards that need to be controlled by the user, provides specific direction on the stop category required and the degree of control reliability necessary to deliver the expected risk reduction.

The emergency stop circuit is fed by the Logic ON-OFF circuit, and feeds the Hardware Enable, and Motor-Short Dynamic Braking circuits. Emergency stop circuit provides a bypass for the momentarily ON pushbutton of the Logic ON-OFF circuit. This allows the Logic ON-OFF circuit to feed the safety systems without relying on a single pushbutton. The Emergency Stop circuit further feeds the inputs of the Hardware Enable through two normally-open contacts and Motor-Short Dynamic Braking circuit through two normally-closed contacts. This means that if one of the emergency stop switches are pressed, it will kill the Hardware Enable signals while it activates the Motor-Short Dynamic Brakes. As the Hardware Enable signals drop, the output stage of the servo amplifiers will get deactivated, and the Motor-Short Dynamic Brakes stop the motors in the shortest possible time. This gives the highest priority to Category 0 stop.

The Motor-Short Dynamic Braking circuit is equipped with a time delayed relay. This allows for performing Category 1 stop even when the emergency stop switch is depressed. This is possible by giving the servo amplifiers enough time to stop the motors controlled before the Motor-Short Dynamic Brakes kick in. The default setting for the time delay relay is 0ms for providing the highest degree of safety. This setting should only be changed if the user is fully aware of the risks and understands the operational parameters of the servo amplifiers.

Categories 1 and 2 stops are possible if all emergency stop switches are released, or within the time delay of Motor-Short Dynamic Braking. In either case, Regenerative Dynamic Braking and Holding Brakes are responsible for stopping and holding the system, respectively. The emergency stop circuit is constituted of a dual-input solid-state relay with two normally-open contacts and a normally-close contact. This relay is extended with another solid-state relay with eight normally-open contacts and one normally-closed contact. The inputs of the circuit are taken from three dual-channel emergency stops. Dual-channels provide redundant safety on the switch contacts in case

of contacts fusion or shortcut. One of the normally-open contacts bypasses the momentarily ON pushbutton of the Logic ON-OFF circuit while four other ones feed the inputs of Hardware Enable and Motor-Short Dynamic Braking circuits. Two other normally-open contacts input a dual-channel solid-state relay that is in series with the RTO contacts of the ServoStar servo amplifiers. The purpose of this relay is tripping the shunt of the 3Ph circuit breaker that feeds all servo amplifiers. This relay is energized, it kills the 3Ph power to all servo amplifiers, allowing the Motor-Short Dynamic Brakes to dissipate the stored energy in the motors while the output of the servo amplifier dead. Three 6-Amp circuit breakers protect the incoming power of this circuit through shielded AWG16 cables. Figure 5.8 shows the Logic ON-OFF circuit for the VT Roller Rig.

## Chapter 6. Commissioned Capabilities of the Virginia Tech Roller Rig

### 6.1 Novel Motion Control and Data Acquisition Architecture: Fast, Low-Noise, High-Performance, and Plug-n-Play

The Virginia Tech Roller Rig's motion control and data acquisition are based on SynqNet Technology, provided by Kollmorgen (Radford, VA). The communication protocol between components of the Roller Rig was selected based on the following criteria:

- Unified between servo drives, motion controller computer, and data acquisition units
- Maximum performance with minimum wiring
- Minimum skew and jitter
- Does not require additional diagnostic tools. Simply serviceable
- Easily expandable without modifying the existing network

SynqNet is a digital communication protocol for multi-axis motion control applications. It is globally renowned for high-performance, low-noise, and synchronous command and feedback. SynqNet replaces the noise-prone analog communication protocols ( $\pm 10V$  + Encoder) with a real-time digital network. The digital communication provides additional diagnostic, performance and reliability benefits to the Roller Rig.

A unique feature of SynqNet is adaptability to servo drives, motion controllers, and data acquisition units. This eliminates the need for any data conversion between these units, thus maximizing the network bandwidth to 48kHz for torque updates (4 axes). For the Virginia Tech Roller Rig, SynqNet was successfully implemented on S772 and AKD servo drives, QMP motion controller, SQIO-SQID data acquisition boards (all from Kollmorgen).

The centralized QMP motion controller transmits regular synchronization data to every component around the Roller Rig network. Each receiving component uses advanced digital time correction

techniques to minimize both skew and jitter to less than  $1\mu\text{s}$ , and cycle time latency to  $\sim 25\mu\text{s}$ . These values are constantly reported to the user.

Altogether, Roller Rig includes more than 3200ft of cable in various gauges. Adding more cables not only makes the cable management more difficult but increases the risk of cross-talk between adjacent cables. An important criterion in selecting the motion communication protocol for the Roller Rig was maximum performance with minimum required wiring. The physical layer of SynqNet is based on IEEE 802.3 standards for 100Base-TX, the physical layer of Ethernet [120]. The 100BASE-TX protocol is based on specifications published in the ANSI TP-PMD physical media standard. The 100Base-TX system operates over two pairs of wires, one pair for ‘receiving’ data signals and the other pair for ‘transmitting’ data signals. Each link is full duplex, i.e. capable of transmitting and receiving simultaneously [121]. 100Base-TX Ethernet cables are inexpensive and can transfer more data than traditional serial cables.

SynqNet has built-in query mode that allows for querying components regarding a variety of information without additional diagnostic tools. For the S772 and AKD drives, a user can simply acquire drive information via the motion communication protocol and the Roller Rig motion programming interface (Section 6.2).

Each component on the SynqNet network, regardless of physical role, is called a ‘node.’ The nodes are enumerated sequentially according to the wiring order of the network. Roller Rig does not require a DIP ID switch or EEPROM to hold the node numbers. The Roller Rig nodes are:

- Wheel S772 digital servo drive
- Roller S772 digital servo drive
- Lateral AKD digital servo drive
- AoA AKD digital servo drive
- Vertical 1 digital servo drive
- Vertical 2 digital servo drive
- Cant 1 digital servo drive
- Cant 2 digital servo drive
- SQIO-SQIO data acquisition board 1
- SQIO-SQIO data acquisition board 2
- SQIO-SQIO data acquisition board 3
- SQIO-SQIO data acquisition board 4

The signaling scheme between the nodes is strictly point-to-point, meaning that one transmitter is connected to one receiver. A schematic of node-to-node signaling is given in Figure 6.1. SynqNet is compatible with two standard connectors: RJ-45 and Micro-D. The RJ-45 connector is standard for commercial 100Base-TX applications and conforms to CAT-5. Micro-D is used in environments where additional tolerance of vibration is required. All sensitive electronics of the VT Roller Rig are secured in the control tower, isolated from vibration. Therefore, RJ-45 connectors are used for implementing the network.

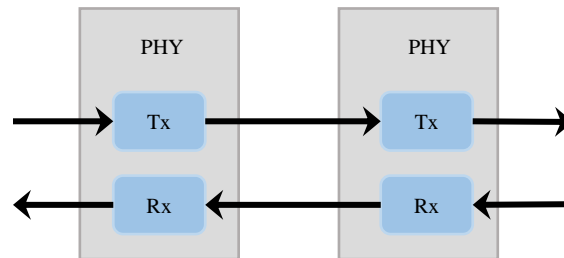


**Figure 6.1. Node-to-node signaling in the Virginia Tech Roller Rig is full duplex.**

Frequently, motion designers think of each axis regarding a single motor; however, the Roller Rig motion controller platform allows the user to expand this model. For example, the X-Y cradle on a three-axis machine can be simply controlled by two motors, each of which represents a single, independent axis. However, it may be advantageous to “map” a second motor to each axis, to obtain independent, rapid-coarse motion and slow-fine motion. Currently, the motion axes of the Roller Rig are:

- Wheel rotation
- Roller rotation
- Lateral linear motion
- AoA linear motion
- Vertical 1 linear motion (tied to Axis 6)
- Vertical 2 linear motion (tied to Axis 5)
- Cant 1 linear motion (tied to Axis 8)
- Cant 3 linear motion (tied to Axis 7)

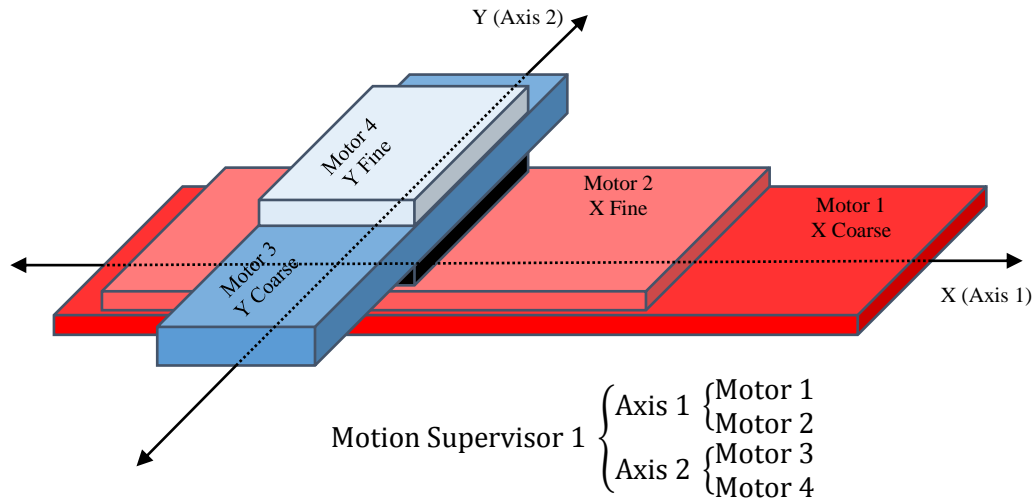


Figure 6.2. An illustration of motor axis mapping concept.

A concept similar to mapping multiple motors to the one axis is Gantry. The term “Gantry” defines a system with two motors controlling a single linear axis. The vertical and cant axes in the VT Roller Rig are examples of Gantry (Figure 6.3). Each motor/bearing system is separated a finite distance orthogonal to the direction of the axis. Small rotational motion about the center of the gantry due to differential motion of the two motors is usually undesirable and will lead to mechanical binding if the rotational motion is excessive [122].



Figure 6.3. Gantry axes of the VT Roller Rig (left: vertical, right: cant).

A goal of the gantry system is to move both separate motor systems together so that negligible “crabbing” occurs, wherein one motor leads or lags the other. Since each side of the gantry receives the same linear command position (with zero yaw command), a lagging motor/encoder provides a greater error signal to that respective control loop [122]. Due to the mechanical coupling of the Gantry beam, motion from one motor can appear as a disturbance on the other motor, particularly within the same bandwidth, since they have identical or similar control elements. This coupling of disturbances can reduce system performance. In a Gantry control scheme, separate controllers directly control each motor. The standard gantry configuration results in a control loop that controls each motor the same as if they were separate (non-gantry) motors. It provides the convenience of commanding the linear motion, thereby simplifying programming and lab testing. Figure 6.4 illustrates the Gantry motion control concept. The Gantry axes in the VT Roller Rig are 5&6 for vertical motion and 7&8 for cant. In the Roller Rig, six motion supervisors are responsible for commanding the four independent axes and the two Gantry ones. These supervisors are:

- Wheel
- Roller
- Lateral
- AoA
- Vertical
- Cant

Nodes 1 and 2 each incorporates an S772 digital servo drive connected to an AKM84T servo motor and a single-turn EnDat 2.2 absolute sine encoder. Nodes 3 through 8 each have an AKD servo drive that commands an EC4 linear actuator and receives feedback from its multi-turn EnDat 2.2 absolute sine encoder. Nodes 9 through 11 each have an SQIO-SQID data acquisition board connected to an SQIO-MIXEDMODULE. SynqNet supports up to 64 motion axes, 64 nodes, and 32 bits of configurable I/O per axis. Figure 6.6 shows the VT Roller Rig SynqNet network. The blue arrows represent the digital communication network.

The VT Roller Rig’s control and data acquisition architecture are Plug-n-Play. Expanding the network includes connecting two RJ45 cables to its adjacent components and refreshing the Roller Rig MPI. Nodes are all updated and queried at the same time, while the data is processed in the order reported to the motion controller.

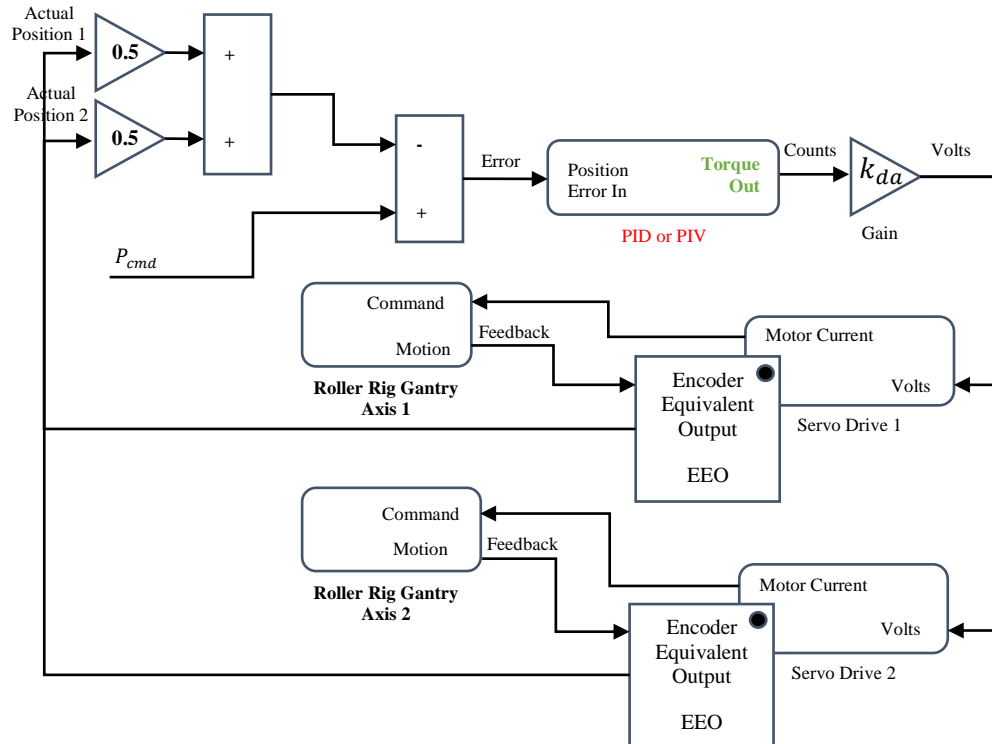


Figure 6.4. Gantry motion control scheme using two encoders.

Common motion control architectures are String without termination, Dual String without termination, String with termination, Dual String with termination, and Ring. Figure 6.5 compares these topologies with each other. In some non-standard applications, Ring-of-Rings and Tree topologies have also been used. The String topology is the most basic network configuration [121]. Packets are sent downstream from the motion controller to the nodes, and upstream from the nodes to the controller. Each node repeats the downstream and upstream data to the next node. If a cable breaks, the nodes downstream from the break will be lost. A String topology has nodes connected to either IN or OUT ports. If nodes are connected to both ports, the topology is called Dual String. If the end of String or Dual String topologies are left unterminated, a timeout period is required to detect the end of the string. To reduce this discovery time, a loopback connector can be added to String and Dual String topologies. The loopback allows the motion controller to deterministically find the last node on the network.

The VT Roller Rig control architecture is set up in a Ring topology (closed-loop). The Ring topology is similar to String topology, except with an idle link that is added between the last node and the motion controller. In a Ring topology, if any one of the cables fails, the network will redirect packet data around the break, and the motion controller will notify the user in the Roller Rig MPI with an event. The location of the break can be determined by the motion controller [123].

Furthermore, if one or more nodes fail, the network will continue to operate and communicate with the good nodes, while the motion controller notifies the user of bad nodes.

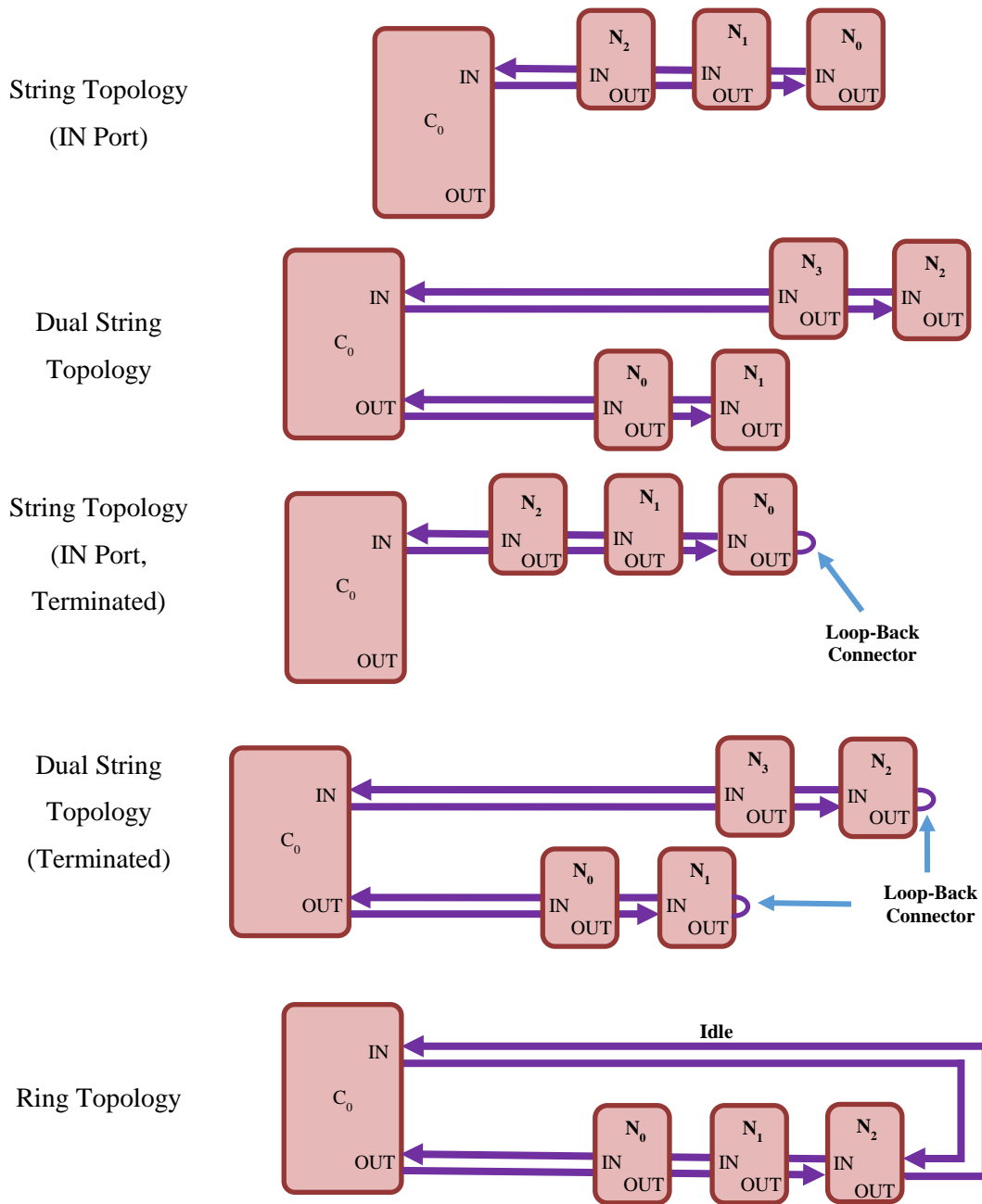


Figure 6.5. Common motion control network topologies.

The Roller Rig network topology can be saved to the motion controller's flash memory. After a reset, the controller will automatically initialize the Roller Rig and verify that the number and type of discovered nodes match the expected topology. Figure 6.6 shows the Virginia Tech Roller Rig control and data acquisition architecture. The green arrow indicates the data acquisition channels,

while the brown arrow indicates incoming power. The command and feedback loop between each drive and the motor is represented by red and purple arrows, respectively. For more information on the yellow and gray arrows (regen and dynamic brake resistors), see Section 5.5.

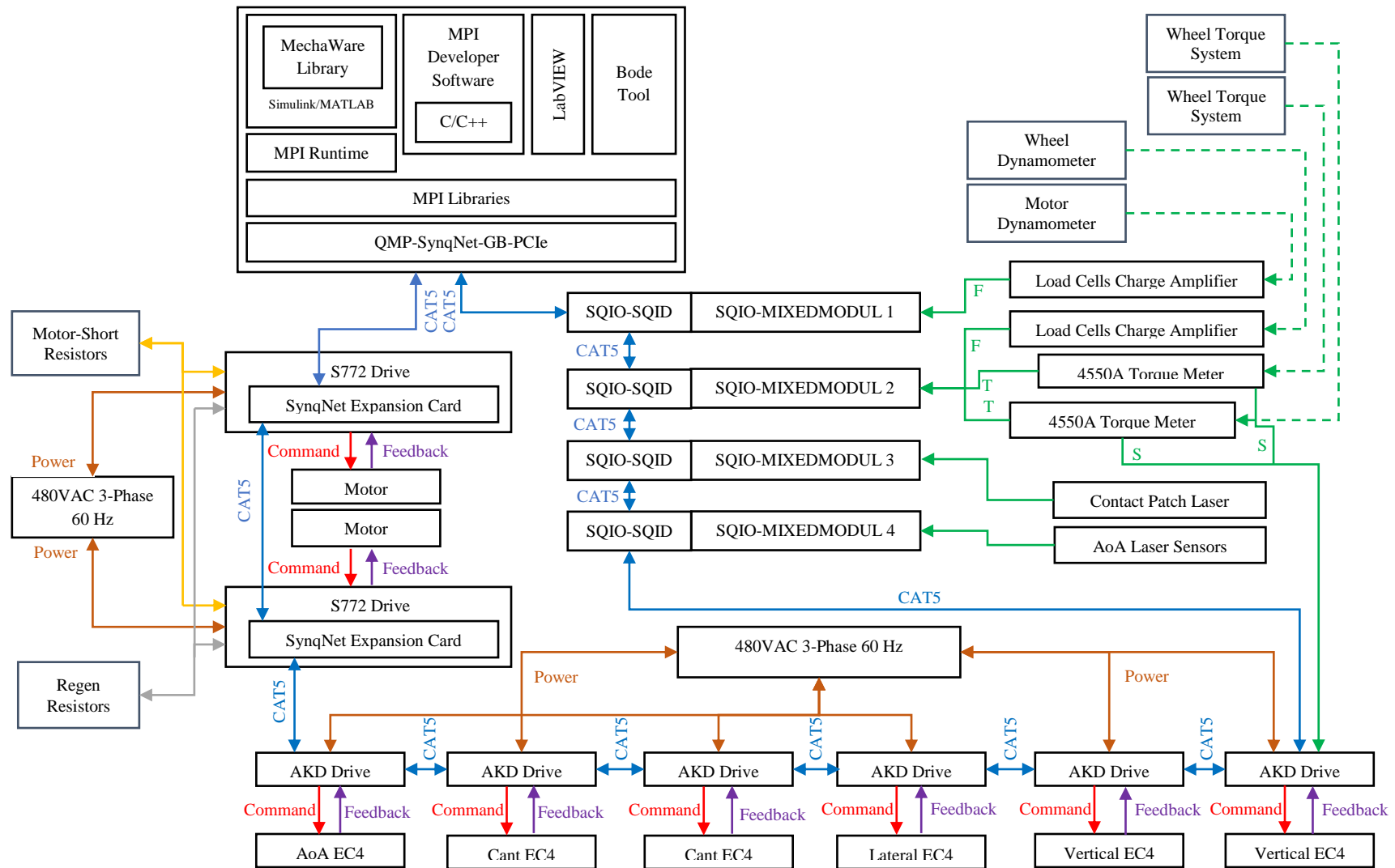


Figure 6.6. The Virginia Tech Roller Rig’s control, power, and data acquisition architecture.

### 6.1.1 Motion Controller

The motion controller is responsible for the real-time trajectory calculations, closed-loop control, handling the dedicated I/O, updating status, event messages, data recording, SynqNet network data processing, plus many other features. The controller's processor load is based on the number nodes, axes, supervisors, and enabled features [124,125]. The ultra-high-performance QMP-SynqNet card (Figure 6.7) incorporates a 64-bit Freescale QorIQ P2010 1200MHz PowerPC for optimum flexibility and speed. The controller offers servo update rates up to 48kHz and can support up to 64 axes, 64 nodes, and 32 bits of configurable I/O per axis [126].



**Figure 6.7. QMP-SynqNet-GB-PCIe-RJ motion controller.**

The central motion processor performs matrix computations based upon multiple inputs generating multiple outputs. MIMO (Multiple-In-Multiple-Out) control systems use demand and feedback inputs, such as the actual torque and velocity, to compute new target data for output components such as drives and motors.

The QMP motion controller splits the operations into two tasks: foreground and background [124]. The foreground task is the main task and is triggered by an internal interrupt that fires when the sample period timer expires. After the foreground task completes, then the background task executes. If the background task does not complete within one sample period, it is interrupted to begin the foreground task in the next sample. Each time the foreground cycle completes, it begins the background task from the point it was adjourned in the last reporting period.

All sample period critical functions are performed in the foreground: trajectory calculations, closed-loop servo calculations [124], SynqNet data processing, data recording, linking, camming, position compensation tables, capture, compare, program sequencers, etc. Less critical functions are performed in the background cycle: status update, dedicated I/O processing, motor limits, actions, event messages, etc.

The motion controller maintains the previous sample's actual position and calculates the actual velocity. If the feedback packet is corrupted, the controller will interpolate the expected actual position [123]. This feature prevents motor jumps due to network data integrity problems.

EMI shielding for the motion controller follows standard 100BT NIC design conventions: the RJ-45 connector shell is tied to the bracket or front panel, and not directly connected to the controller's local digital ground. The host computer chassis is responsible for grounding the chassis [127]. It is tied to the Roller Rig isolated ground rod at a central point along with the digital ground. The cable shield is also related to an isolated plane section on the motion controller PCB to minimize EMI. To prevent ground loop formation in the control Ring, the RJ-45 connector is isolated from local node chassis, as well as from ground and power signals. Instead, the connectors are AC coupled via internal capacitors (one for each port) to a nearby earth point on the node. Figure 6.8 illustrates this technique [127].

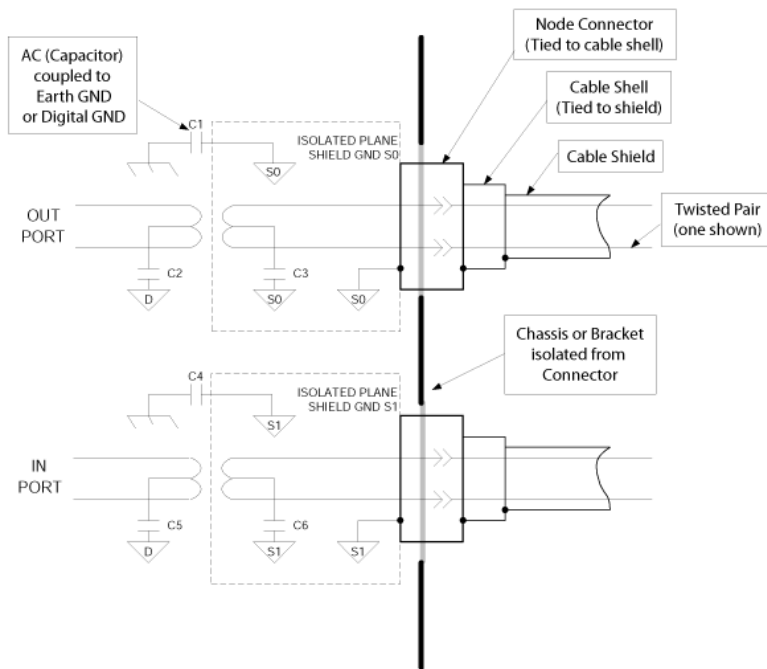


**Figure 6.8. Cable shield grounding at local nodes to prevent ground loop in the VT Roller Rig control loop (courtesy of Kollmorgen) [127].**

### 6.1.2 Data Acquisition Units

Roller Rig data acquisition units have a modular architecture based on SQIO Technology developed by Motion Engineering (now part of Kollmorgen). SQIO is a modular system, in which each data acquisition unit is considered a node in the SynqNet network. Each node is comprised of the following:

- An SQID, which serves as the SynqNet network interface and power source for all connected I/O boards
- One or more board modules that can be cascaded to provide as much I/O as is required . Available modules are DIN32DOUT32, ADC4DAC4, and MIXEDMODULE. DIN32DOUT32 provides 32 isolated digital inputs and 32 isolated digital outputs. ADC4DAC4 provides 4 ADC and 4 DAC channels. The most versatile of the three, MIXEDMODULE, features 64 isolated digital inputs, 64 isolated digital outputs, 16 ADC channels, and 8 DAC channels [127].

Communication between the board modules and the SQID is implemented through four SPI-type<sup>5</sup> serial buses [128]. Each SPI bus either passes through the logic circuitry of a board module or is merely tracked-through. Figure 6.9 illustrates the SQIO communication through the SPI busses. The SPI rates on the digital input SPI, digital output SPI, analog input SPI and analog output SPI are completely independent.

For adding more modules to an existing SQID board, the following two criteria should be satisfied:

- A 2A fuse limits SQID's incoming current

$$(d \times 0.02) + (a \times 0.10) + (m \times 0.20) + 0.06 < 2 \quad (43)$$

- SQID's 5W DC-DC converter can provide maximum 800mA spare capacity

$$(d \times 0.05) + (a \times 0.12) + (m \times 0.65) < 0.8, \quad (44)$$

where  $d$  is the number of DIN32DOUT32 modules,  $a$  is the number of ADC4DAC4 modules, and  $m$  is the number of MIXEDMODULE1 modules.

Table 6.1 summarizes the SPI rates. Connecting ADC4DAC4 to an existing assembly of SQID+DIN32DOUT32 will not affect the SPI rate of either. However, when a unit with a MIXEDMODULE is connected to a DIN32DOUT32, the lesser clock rate will prevail on the affected SPIs.

---

<sup>5</sup> A trademark of Motorola

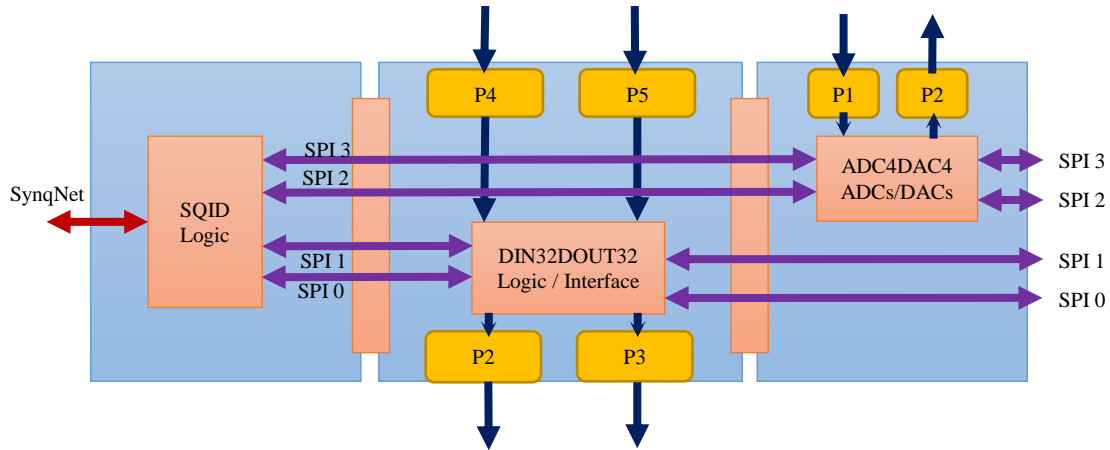


**Figure 6.9. SQIO communication through SPI serial busses. A digital module (DIN32DOUT32) and an analog module (ADC4DAC4) are cascaded to the SQID.**

**Table 6.1. SPI rate of different data acquisition modules.**

Module	SPI Rate
DIN32DOUT32	6.25MHz
ADC4DAC4	6.25MHz
MixedModule1	12.5MHz

To SynqNet, the board modules appear as a “chain of bits.” i.e. a knowledge of the SPI busses is all that is required to design a custom data acquisition unit. Neither special controller software nor special SQID FPGA logic is required [128]. As mentioned earlier, motion control and data acquisition units are similarly interpreted as nodes in the SynqNet network. This allows for expanding or modifying the network with minimum adjustments. Adding an entirely new node only requires connecting two RJ45 cables to its adjacent components and refreshing the Roller Rig MPI.

Each SPI bus on each SQID node can support up to 256 bits. In a standard scheme, therefore, there can be up to 256 digital inputs, up to 256 digital outputs, 16 sixteen-bit ADC channels, and 16 sixteen-bit DAC channels attached to each SQID node. Up to eight board modules can be connected [129]. This is a constraint of the I2C2 EEPROM<sup>6</sup> addressing scheme on the SQID. The Roller Rig MPI will check the setup at initialization to verify compatibility and report an error if it is not valid. Currently, the VT Roller Rig has four SQID boards, each slotted with a MIXEDMODULE. The SPI rate of this configuration, shown in Figure 6.10, is 12.5MHz.

<sup>6</sup> The EEPROM (U801) is a 2kbit memory that is used to hold certain data required for the correct start-up of the network.

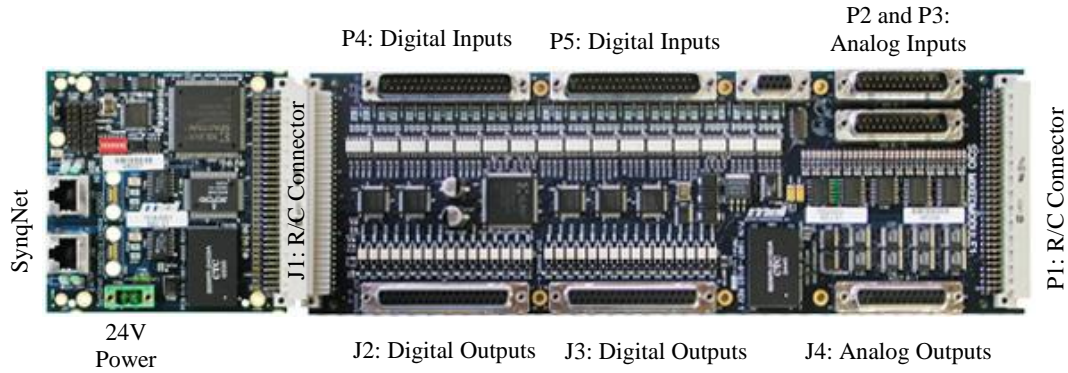


Figure 6.10. Current configuration of each data acquisition node on the VT Roller Rig SynqNet network.

### 6.1.2.1 Latency

The load on each SPI affects the delay between consequent updates. The SPI delay is defined as:

$$SPI\ delay = \left( \frac{Number\ of\ bits\ on\ the\ SPI}{SPI\ Clock\ Rate} \right) + 2\mu s \quad (45)$$

For the configuration shown in Figure 6.10, the SPI delay is tabulated in Table 6.2.

Table 6.2. SPI delays for the VT Roller Rig data acquisition units depending on the SPI load.

SPI Clock Rate (MHz)	Number of Bits on the SPI			
	32	64	128	256
6.25	7.12	12.24	22.48	42.96
12.5	4.56	7.12	12.24	22.48

The overall latency between the acquired bits depends on:

- SPI delay
- Network update rate (Section 6.1.3)
- Opto-isolator delay

The SynqNet network latency for each update rate is given in Table 6.4. Optoisolators are components that transfer digital signals between two isolated circuits in the SQIO module using light. For a standard optoisolator, the delay is  $1\mu s$  when the input is energized and  $500\mu s$  when the input is de-energized. For digital outputs, the delay is  $5\mu s$  when the output is turned ON and  $80\mu s$  when the output is turned OFF. Below is the equation for the worst-case latency between a digital input changing and the value appearing at the Roller Rig MPI:

*Worst Case Latency*

$$= \text{Opto Isolator Delay} + \text{SPI Delay} + \text{Network Delay} \quad (46)$$

Assuming full load on an SPI (256bit), with an SPI clock rate of 12.5MHz, and network update rate of 4kHz, the worst case ON latency is:

$$\text{Worst Case ON Latency: } 1 + 22.48 + 250 = 273.48 \mu\text{s}$$

Moreover, the worst case OFF latency under the same condition is:

$$\text{Worst Case OFF Latency: } 500 + 22.48 + 250 = 772.48 \mu\text{s}$$

For analog inputs, the optoisolator delay is substituted with ADC conversion delay. To include the number of analog channels, worst case analog latency is defined as:

*Worst Case Latency*

$$= [(\text{ADC Conv. Time} \times \text{Num. of Channels}) + \text{SPI Delay}] + \text{Network Delay} \quad (47)$$

To use Table 6.2, the resolution of ADC should be known. All Roller Rig data acquisition units, report analog inputs with 16bit resolution. The standard ADC conversion delay for the ADC4DAC4 and MIXEDMODULE is 8μs. So, the worst case latency for a full load (16 channel) ADC input node with an SPI clock of 12.5MHz and a network update rate of 4kHz is:

$$\text{Worst Case Latency: } (8 \times 16) + 22.48 + 250 = 400.48\mu\text{s}$$

For analog outputs, the DAC delay is represented by slew rate. The slew-rate delay varies with the change of voltage, but for most purposes, a lumped figure of 10μs can be used.

### 6.1.3 Network Update Rate

The network update rate determines the update frequency for the motion controller and the SynqNet network. Every sample, the motion controller must read the cyclically sampled data from the network hardware (sense), process the data (think), and write the transmit data to the network (act). The maximum controller/sample rate and servo control latency of the Roller Rig depend on the various factors:

#### 6.1.3.1 Network Load

At higher update rates, the servo performance improves. However, more nodes require more data packets and more features within a node will require larger data packets. The limitation to the servo

update rate is the network loading. The bandwidth usage must be kept below 100% at all time. Based on the initial tests on the Roller Rig, the servo update rate is limited by the motion controller's processing power and not by the network bandwidth. For example, at 4kHz, the Roller Rig only uses 16% of the motion control network bandwidth. In the future, with more features within each node, the user should pay attention to the maximum sample rate and data packet load. Data packets can be optimized to remove unused features in case of sample rate limitations due to network bandwidth.

6.1.3.2 Digital Servodrive Update Rate

S772 and AKD digital servo drives update torque, velocity, and/or position loop at specific frequencies. To make sure the motion controller's closed-loop control loop is synchronized with the drives' loops, the motion controller update period must be a multiple of the drive's update period. Currently, the S772 and AKD drive update rates are set to those given in Table 6.3.

**Table 6.3. Update rate of digital servo drives used in the Virginia Tech Roller Rig.**

Drive	Drive's Control Loop Update Rate	Drive's Control Loop Update Period
S772	16kHz	62.5μs
AKD	4kHz	250μs

Such restriction guarantees that the drive phase-locked loop (PLL) can lock to an even sample period of the motion controller. Since the drives on the Roller Rig network have different update rates, then the motion controller sample period must be a common multiple of all drives on the network. With current settings, valid network update rates are 1kHz, 2kHz, and 4kHz. The SynqNet network latency for each sampling frequency is given in Table 6.4.

**Table 6.4. Network latency for each update rate.**

Network Update Rate (kHz)	Latency (μs)
1	1000
2	500
4	250
8	125
16	62.5

### 6.1.3.3 Cyclic Data Transmit ( $T_x$ ) Time

The transmit time ( $T_x$ ) determines when the cyclic data is sent within the motion controller's sample period. The  $T_x$  time is expressed as a percentage from 0% to 100%. Smaller  $T_x$  time values will cause the cyclic data to be transmitted earlier in the sample period.

Smaller  $T_x$  time values will reduce the latency between the feedback data from the node and the servo demand value sent from the motion controller to the node. Decreasing the latency will improve the servo closed-loop performance. The ( $T_x$  time  $\times$  controller period) must be larger than the controller's foreground calculation time.

$$T_x \times \text{Controller Period} > \text{Controller Foreground Calculation Time} \quad (48)$$

Larger  $T_x$  time values will cause the cyclic data to be transmitted later in the sample period. Larger  $T_x$  time values will increase the latency between the feedback data and the demand value. Nevertheless, using a larger  $T_x$  time value may allow the controller to operate at a higher sample rate, thereby increasing the servo bandwidth.

For S772 and AKD servo drives, the latency change is only effective if the magnitude of the  $T_x$  time change is large enough to cross the boundary of the drive's sample period. For example, suppose the Roller Rig cyclic period is 250 $\mu$ s (4kHz) and the AKD drive period is 62.5 $\mu$ s. Changing the  $T_x$  time by 2% will cause a 5 $\mu$ s change in the transmit time. To cross the drive period boundary, the  $T_x$  time would need to be changed by about 26% (or less). Since the transmit data timing may not be exactly lined up with the drive's update time, the actual amount of  $T_x$  time change to cross the drive period boundary may be significantly less.

The default  $T_x$  time for the Roller Rig Time is 75%. A reasonable range for  $T_x$  time values is from 65% to 95%.

**Example:**

$$\begin{aligned} \text{Sample Rate} &= 4000 \text{ (period} = 250\mu\text{s)} \\ T_x \text{ time} &= 75\% \text{ (} 187.5\mu\text{s)} \end{aligned}$$

$$\begin{aligned} \text{Foreground Time} &= 238\mu\text{s} \\ \text{Background Time} &= 11.98\mu\text{s} \\ \text{Delta} &= 1 \end{aligned}$$

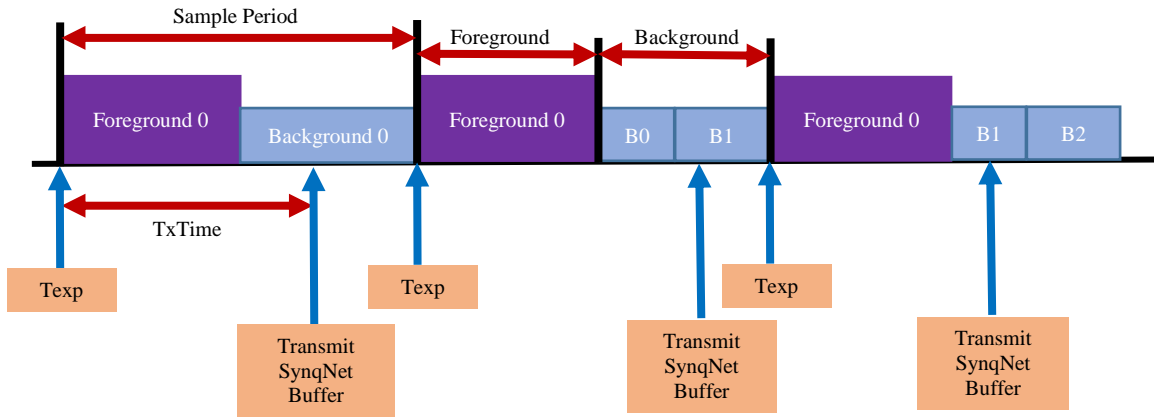


Figure 6.11. The relation between background, foreground, and transmit times.

Delta is the maximum number of times a full background task is interrupted by the foreground task. A value of zero means the background task executed to completion without being interrupted by the foreground cycle [123]. Larger deltas can degrade controller performance. Figure 6.12 shows an example of Roller Rig controller timing.

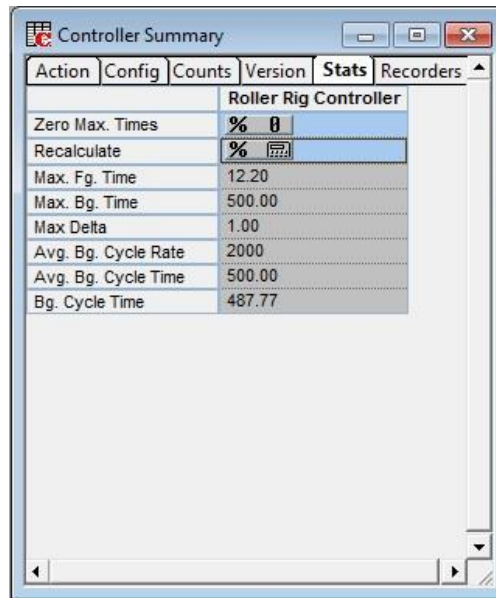


Figure 6.12. An example of the Roller Rig controller timing.

## 6.2 Flexible Motion Programming Interface (MPI)

The Virginia Tech Roller Rig’s motion programming interface (MPI) is founded on a set of object-oriented, C-language functions and data types developed by Motion Engineering (now part of Kollmorgen). These libraries are independent of the motion controller hardware used, as well as the platform (operating system and compiler) on which the motion control application is built.

These libraries can be used directly to develop motion control applications. Programs written using these tools range from simple, single-task, single-controller applications to complex multi-task applications that use multiple motion controllers. These libraries provide direct memory access to all motion controller firmware components, delivering much more performance than other systems that use command-based controllers or ASCII interfaces. Motion programming for the VT Roller Rig is made possible using the following objects [130,131]. Figure 6.13 illustrates the relation between these objects:

- **Control object:** A Control object manages the motion controller. One Control object is created for the Roller Rig motion controller. This object can read and write device memory using I/O ports, memory-mapped or device driver methods. All communication with the Roller Rig motion controller firmware is handled by this Control object. The Control object can also provide a memory snapshot of the controller stored in a file.
- **Axis objects:** An Axis object is associated with a single physical axis on the Rig's motion controller, and corresponds to a geometric axis used for calculation of a path of motion. An Axis may be controlled by one or more Motion objects. The Roller Rig Axis objects were introduced in Section 6.1. The concept of an Axis is a "geometric" idea, but the main purpose of an Axis object is to generate the desired path (trajectory calculations, i.e., to generate command positions) on every sample, using the path-planning data provided by a Motion Supervisor. An Axis object is mostly a computational block .
- **Motion objects:** Motion object, aka Motion Supervisor object, corresponds to a coordinate system or collection of axes. The primary function of the Motion Supervisor is to provide data in a synchronized manner to the Axis objects for use in path creation. Roller Rig Motion Supervisors were introduced in Section 6.1. A second important function of the Motion Supervisor is to monitor the status of all of the Axes under its control (and all of the Motors, and Filters associated with these Axes), so that motion can be stopped or resumed in a controlled manner, especially in the event of errors. The Motion Supervisor is the primary handle for the Roller Rig MPI on the motion.
- **Motor objects:** The Motor object corresponds to a physical motor used to cause motion. The main function of the Motor object is simply to provide an interface to the S772 and AKD digital servo drives. The data of the Motor object contains the state of motion feedback, limit switches, home sensors, amplifier control and status signals (demand, amplifier enable, fault, warning, step, and direction), and motor related general purpose digital I/O.

- **Filter objects:** The Filter object implements the controller's closed-loop servo control loop, i.e., what should the controlled output be based on the position error. The Filter is primarily a computational block, taking command positions and actual positions and computing errors. The Filter object calculates the demand output (representing a torque or velocity command) that controls a physical motor or motors, using data (command positions) computed by the Axis object. PID, PIV and Biquad filter calculations are all parts of the Filter object.
- **Event objects:** An Event object contains information about an asynchronous event that has occurred. Event messages are generated and stored in the controller's memory buffer. When an event occurs, an interrupt is generated to the Roller Rig MPI and the control event service retrieves the event messages and distributes them to the application threads waiting for a notification.
- **Notify objects:** A Notify object is used by a thread to wait for event notification. Notify object can be configured to wait and look for specific events and specific event sources.
- **Recorder objects:** The Recorder objects allow for recording any data from the Roller Rig motion controller's memory. The data is stored in a controller memory buffer and retrieved by the host application. Multiple recorder objects can be enabled and can be started/stopped from the application or by using trigger conditions in the controller memory.
- **Sequence objects:** A motion application can issue individual motion commands, or can create a series of the movement commands (that are executed in sequence by the controller). Sequence object can be used to download commands that are implemented by the motion controller, and not carried out by the host. A typical Sequence might be:
  - Wait for 60ms
  - Change Cant angle
  - Turn on a specific I/O bit
  - Start a motion
  - Wait for motion to finish
  - Wait for another I/O bit
  - Change AOA and Vertical
  - Start a new motion
- **Command objects:** A Command object specifies a single action that is executed by a Sequence, such as motion, conditional branch, computation, time delay, wait for a condition, etc. Any Command object that specifies motion must have a Motion object associated with it.

- **Coordinate systems:** To create a coordinate system for a motion application, the Axis numbers are mapped to the Motion Supervisor in the Roller Rig controller’s memory. The axis count and list of axis numbers define the coordinate system.

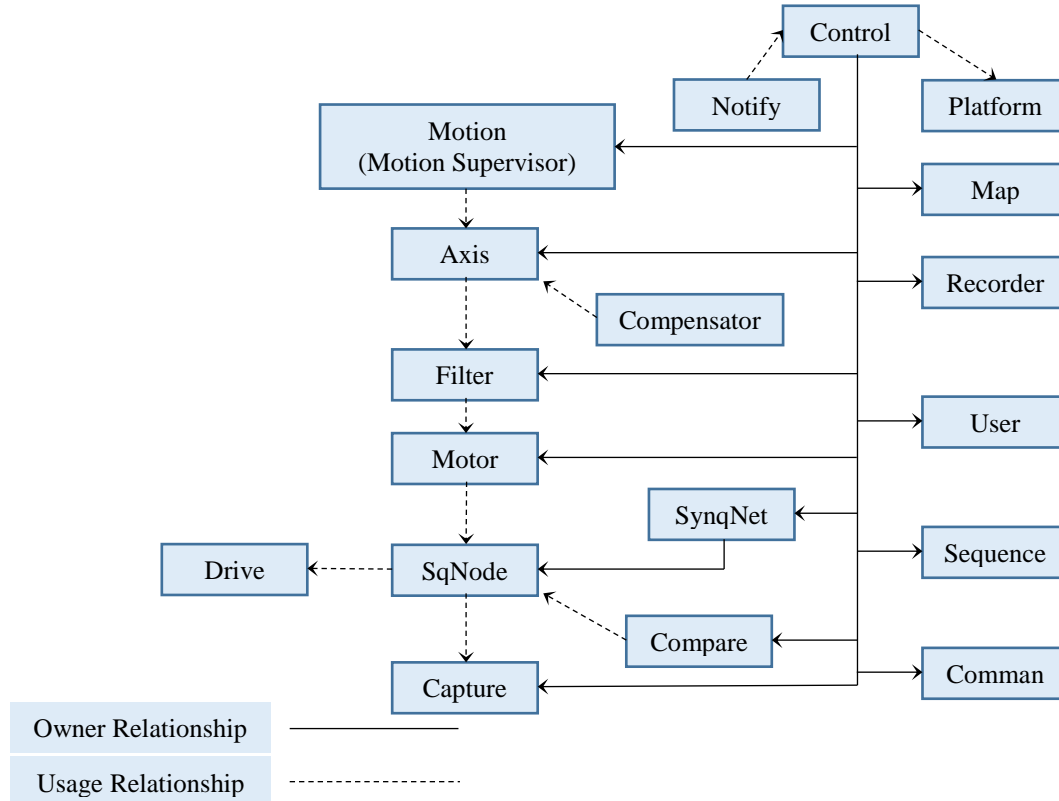


Figure 6.13. Objects used in the VT Roller Rig Motion Programming Interface.

### 6.2.1 High-Level Motion Programming Interfaces

For non-programmer users, four high-level interfaces are provided on the VT Roller Rig. These interfaces hide platform-specific and firmware implementation details while providing a rich set of functions for controlling motion at any desired level. These interfaces are all developed by Motion Engineering:

#### 6.2.1.1 MPX .NET API

The MPX is a .NET API (application programming interface) for the Roller Rig MPI Libraries [132]. It is an alternative way of writing code for users who do not want to write C code using the standard tools. It is programmed using the standard libraries, so everything that is possible with the MPX is possible with the MPI libraries. However, the MPI libraries can only be employed by C

and C++ compilers while the MPX can be utilized by any language that supports .NET, including .NET scripting languages.

### 6.2.1.2 MechaWare Matlab/Simulink Plugin

MechaWare is rich Matlab/Simulink control topology designed to provide the ability to design, implement, and load user-defined control algorithms onto the Roller Rig motion controller. MechaWare is built on top of MPI libraries using 64-bit double data types. The user defines and designs a new control algorithm in the user-friendly environment of Matlab/Simulink [133]. This environment provides an easy-to-use graphical interface for defining the control algorithm and also takes advantage of Matlab's data analysis capabilities.

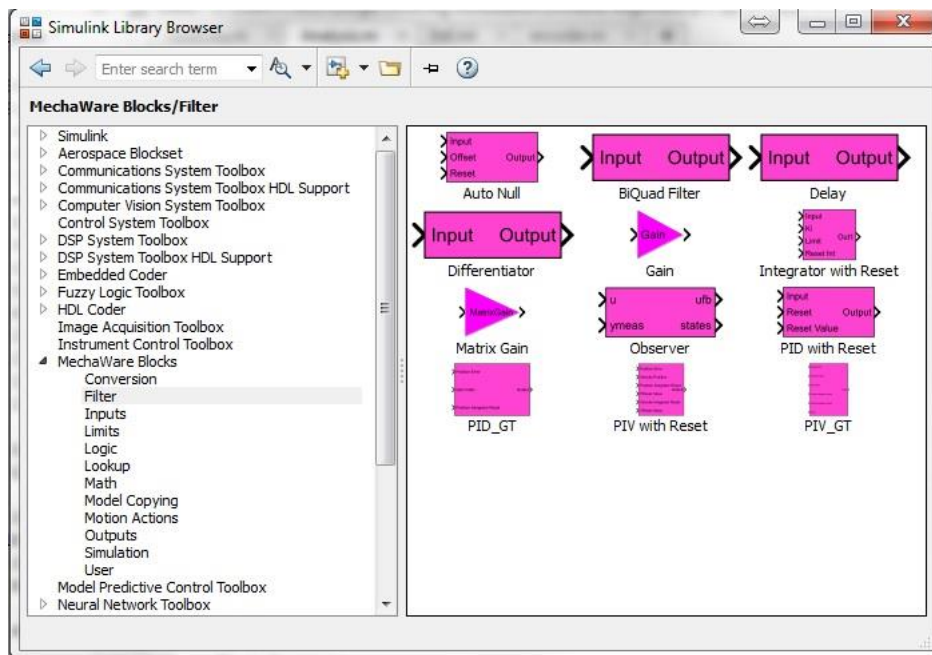


Figure 6.14. MechaWare Simulink Plugin.

MechaWare simplifies addressing more complex control system problems, particularly the issues of system resonance, vibration control and improved settling time performance. It is made up of time-proven basic building blocks used in PID and PIV algorithms. MechaWare allows the user to graphically define a combination of essential components for a desired algorithm (or control law). The Matlab/Simulink workspace provides the user with a graphical user interface for algorithm definition and access to the full functionality of Matlab [134]. The user is also able to load the control algorithm directly into the Roller Rig controller and gives the non-software engineer the ability to download custom control solutions onto the controller. MechaWare can collect and



or MechaWare allows the user to command and plot the data in real time. Motion Scope plots, traces, and exports I/O signal data from the motion controller [135]. It also provides a utility for checking and troubleshooting motion control systems. Motion Scope is a purely "passive," read-only utility, with no ability to write data or control motion. Figure 6.16 shows a snapshot of the software.

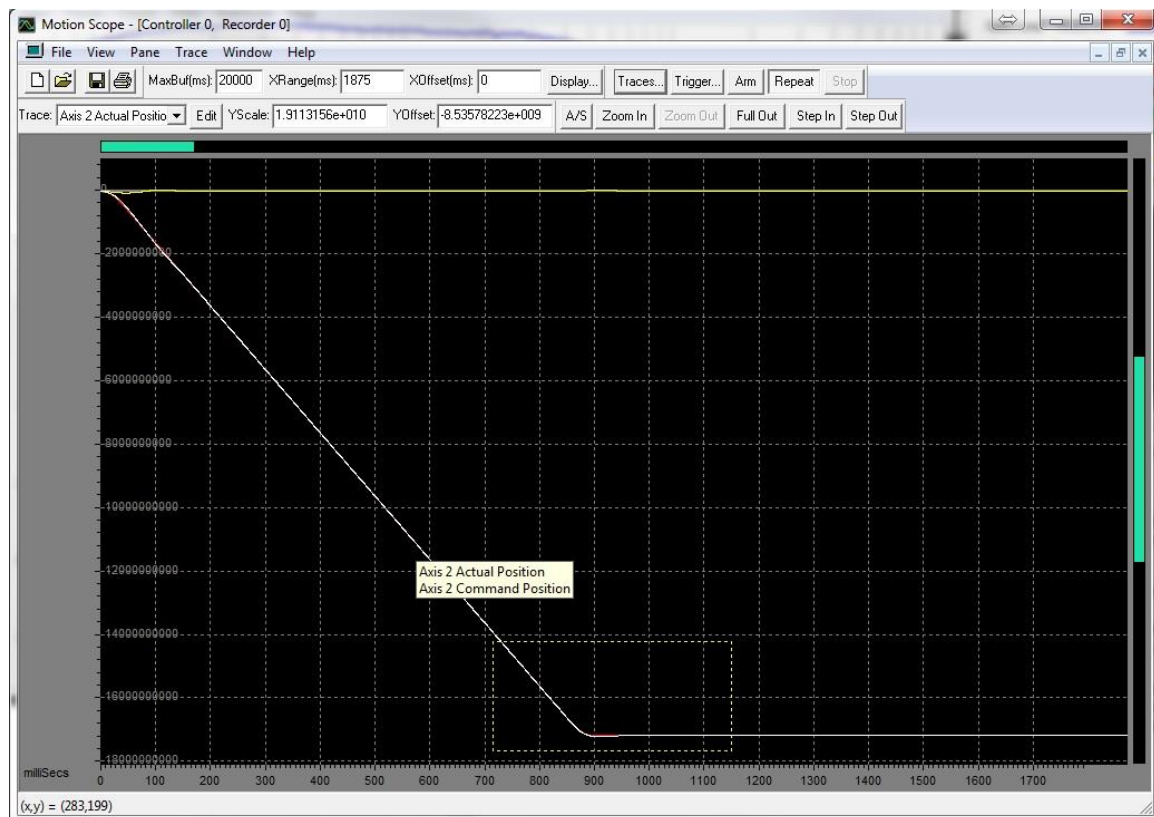


Figure 6.16. An overview of the Roller Rig Motion Scope user interface (data for lateral axis).

#### 6.2.1.6 Bode Tool

The Bode Tool is a tool for capturing frequency domain data from the Roller Rig. The Bode Tool is intended to make it easy to get the data a controls engineer needs to set up and tune the control system properly [136]. The Bode Tool can be used for the following measurements:

- **Measurement of Closed-Loop Response:** Provides measurement of the closed-loop frequency response of a single axis using sine sweep and white noise excitation methods.
- **Measurement for Two-Axis Systems:** Provides measurement of a two-axis system simultaneously using the sine sweep method, exciting the two axes in or out of phase. This is useful for systems with cross-coupled axes (gantries, SCARA robots, etc.)

- **Direct Measurement Using White Noise Excitation:** Provides direct measurement of closed, open, plant, and controller frequency response of the Rig using a white noise excitation method. The Bode Tool allows users to specify controller addresses for FFT inputs and output points to create specific dual channel measurements.
- **Control loop Configuration and Simulation:** Allows configuration of control loop parameters for PID, PIV, and Biquad post filters for quick, intuitive experimentation of controller response in simulation or on a live system. Additionally, can simulate changes to the control system without retesting, allowing control loop iteration cycles to be measured in seconds.
- **Plotting of Frequency Response Data:** Allows plotting of frequency response data in Bode, Nyquist, real/imaginary vs. frequency, and amplitude vs. phase formats. The results are also made available as tab-delimited text files for use in external analysis programs.
- **Automatic Stability Measurements:** The Bode Tool automatically makes quantitative stability measurements on both measured and simulated responses.
- **Command Line Operation:** Extensive command line parameter flags allowing automated testing from a batch file which useful for diagnosis and production line testing.
- **Plant Measurement of the Roller Rig:** Allows for plant measurement of the Rig and simulate tuning, which provides the user to go from no tuning to high-performance tuning in one step.
- **Open-Loop Response Simulation:** Provides simulation the open-loop response of the Rig from the closed-loop response. A filter can be simulated, and the filtered open- and closed-loop responses can be simulated.

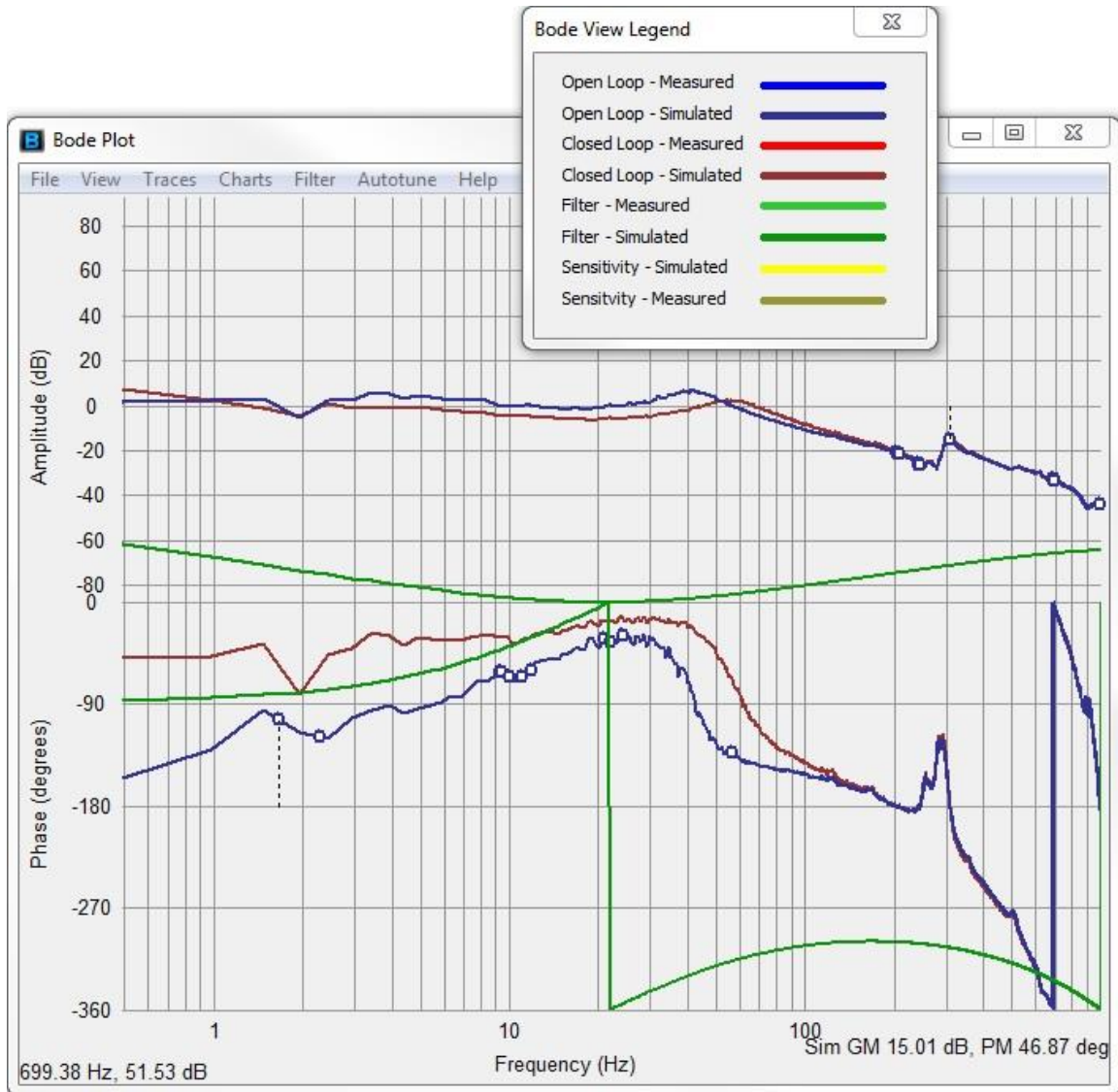


Figure 6.17. A snap-shot from the Roller Rig Bode Tool user interface (plant frequency response).

## 6.2.2 Packet Timing

A vital task in all layers of the Roller Rig motion programming interface is proper packet timing for on-time control and data capture. The MPI automatically configures the packets during network initialization based on the type of nodes. MPI also estimates the cable length between the nodes and the motion controller. Then, it scales the packet timing based on the node number, order, estimated cable length for on-time delivery.

For estimating the cable lengths, motion MPI sends a packet to each node, waits for the node to repeat the packet back, and measures the elapsed time [137]. In Ring topology, the last cable requires the packet to travel around the network and return to the motion controller. The motion

controller reads the clock values for each measurement packet and stores the values. The MPI converts the raw time values into cable length (meters). The MPI also uses the propagation delay values to calculate the packet spacing.

The estimated cable length measured during initialization has an uncertainty factor that can affect control latency. For systems such as Roller Rig, the uncertainty is small ( $\pm 0.160\mu\text{s}$  for an 8 node network) and is completely hidden when latency schedule is rounded up to  $N \times \text{drive period}$ . For the expected sample rates on the Roller Rig, the cable length uncertainty has no effect on control latency. For ultra-high speed tests, however, even a tiny uncertainty can bump the latency by a full drive period. For these tests, the cable lengths can be set manually (0 uncertainty in this case). Typical CAT-5 cable propagation delays are roughly  $0.005\mu\text{s}/\text{m}$ . Actual values are affected by cable construction and will vary, but the variation will be small for any reasonable cable. The propagation delay can be estimated by a cable propagation velocity of 70% the speed of light, using the formula:

$$\text{delay} = \text{meters} \times \frac{1,000,000}{0.7 \times 299,722,458} \quad (49)$$

The minimum sample rate is 1kHz. The MPI also supports user-configurable packets for customized node types. The MPI allows for time-based position capture. Time-based capture is a special technique useful for high accuracy position capturing when the motion controller reads the interpolated position feedback from the drive (encoder equivalent output or EEO), not the encoder itself. The position interpolation is required for increasing the resolution of the encoder, which is limited by physical constraints.

The MPI calculates the SynqNet control latency for each node. This is the time from when the feedback input is sampled at the node to the time when the demand output available on the node. This duration of time includes internal node delays, packet scheduling, network delays, controller delays, and controller calculation time. It does not include delays for serial encoders, drive feedback delays, or drive demand delays [130].

### 6.3 Precise Independent Velocity Control

Each axis object executes a servo loop at a constant rate. The following steps briefly summarize the sequence of operations that are performed each servo loop period:

- The servo drive calculates the encoder equivalent output and velocity of the axis using the information captured from the encoder.

- New command position and velocity are computed from the trajectory data of a Motion object.
- The position error is calculated from the difference between the Command and Actual positions.
- A filter algorithm calculates the demand signal that is applied to the drive.

The Virginia Tech Roller Rig supports Torque and Velocity demand modes. The demand mode determines the size and type of control signal between the controller and the drive. The demand mode is configurable when the amplifier is disabled. On-the-fly switching requires some special techniques to transition smoothly between demand modes.

### 6.3.1 Roller Rig Demand Modes

During network initialization, the nodes are discovered, and the demand mode is automatically set to default, based on the particular drive model (S772 or AKD). The number of 16-bit demand fields per motor is configured and connected to the controller's filter (closed-loop servo algorithm). The default is the recommended mode, but the user can change the demand mode [127].

#### 6.3.1.1 Torque Mode

In Torque Mode, the output of the closed-loop servo algorithm is a 16-bit value representing torque. Figure 6.18 shows a schematic of PID servo algorithm in this demand mode. The 16-bit demand value is sent cyclically to the drive in a special packet. Torque motion applies the specified torque to the motor shaft for acceleration or load bearing. The axes will continue to accelerate (with no load) at the specified torque until a new torque is commanded.

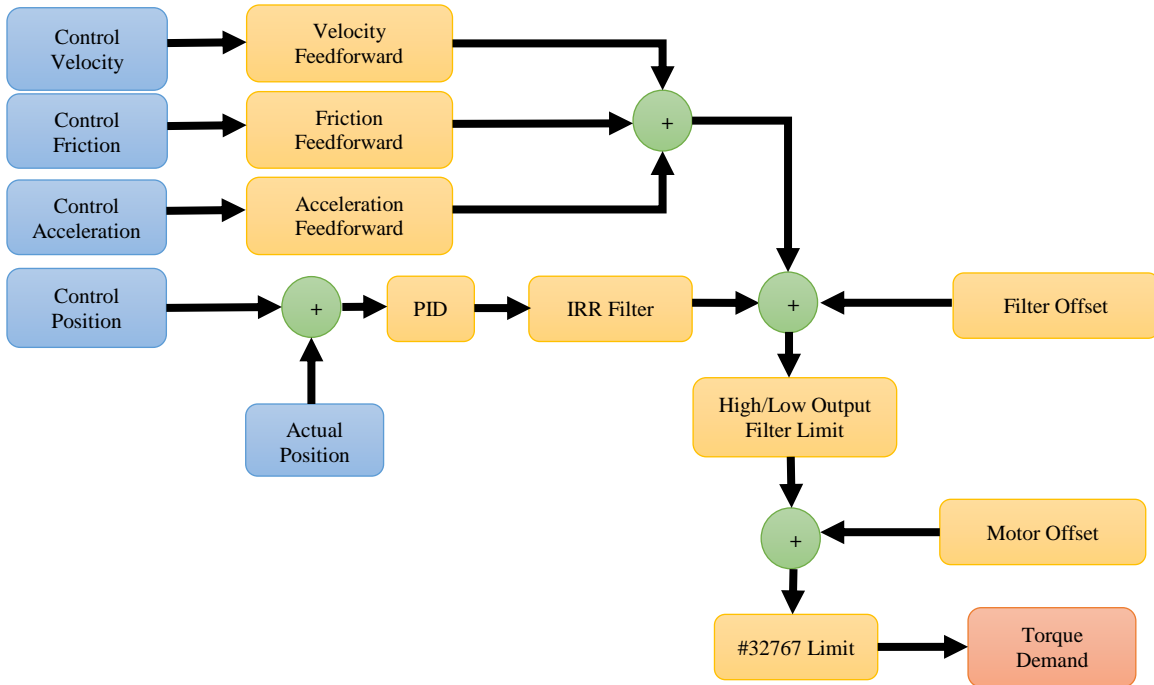


**Figure 6.18. MechaWare schematic of PID servo algorithm in Torque Mode.**

PID is a control algorithm based on position error. It is a very common control algorithm in motion control industry. Another servo control algorithm is PIV. It consists of an inner velocity loop and an outer position loop. PIV is a control algorithm based on velocity error for its inner loop and position error for its outer loop. It is similar in concept to a velocity drive that has a position loop around it. Systems that care more about velocity regulation than position error will likely have better velocity regulation with PIV than PID. For any application, it is recommended to try both PID and PIV to get the best performance. Figure 6.19 shows a schematic of PIV servo control algorithm in Torque mode. Position and velocity compensators are further illustrated in Figure 6.20 and Figure 6.21.

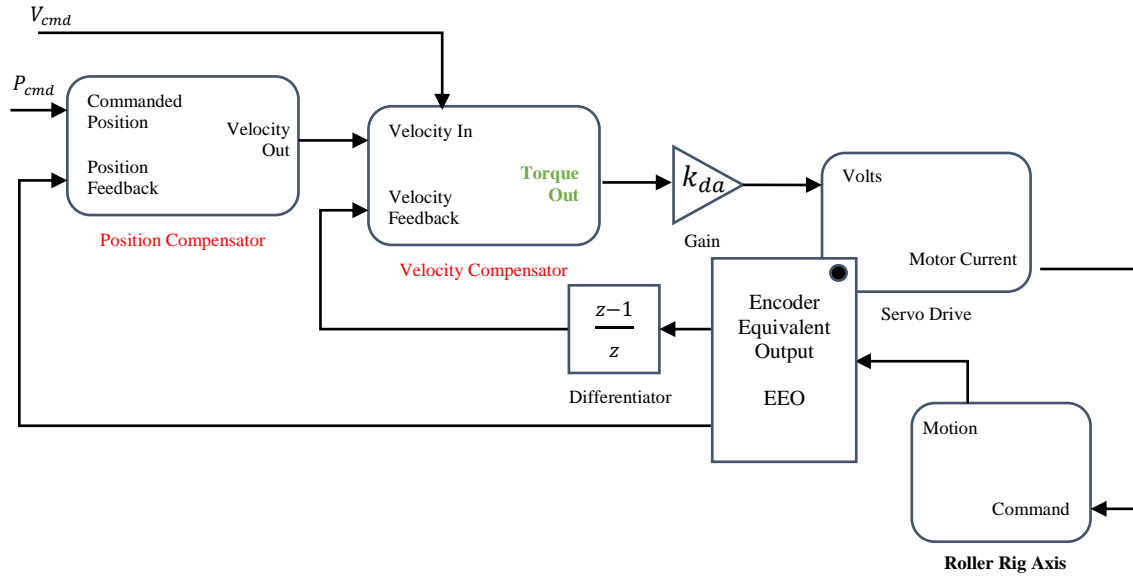


Figure 6.19. MechaWare schematic of PIV servo algorithm in Torque Mode.

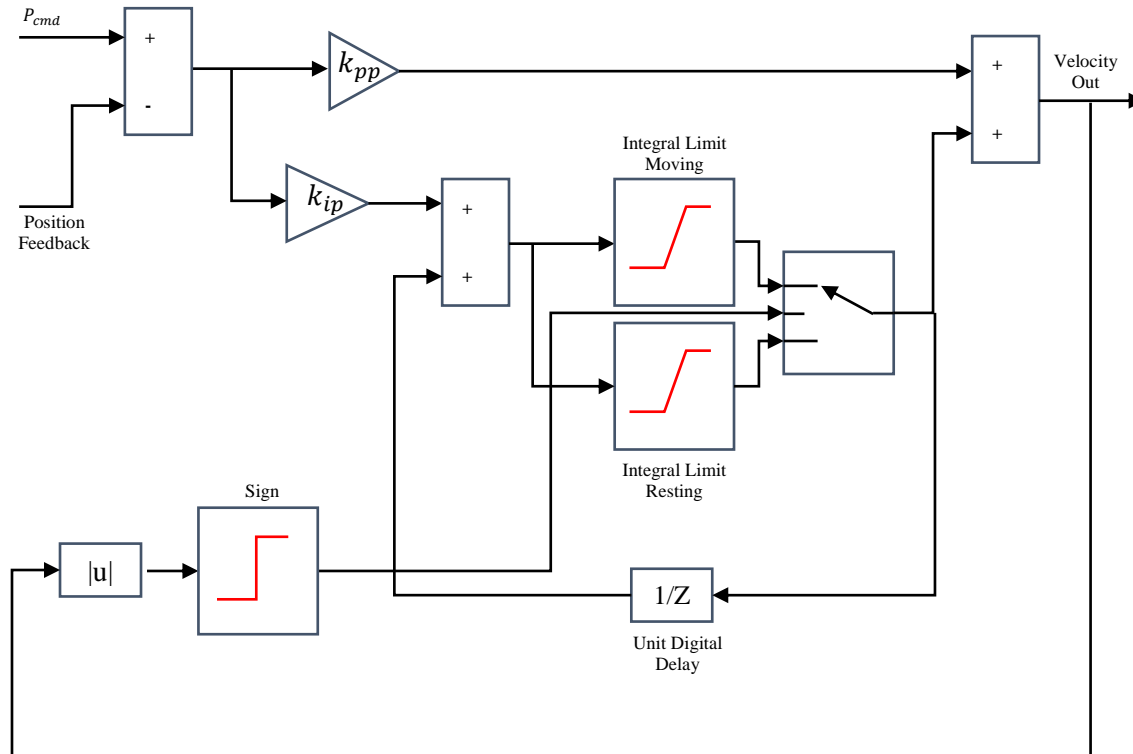


Figure 6.20. MechaWare schematic of the position compensator in PIV servo algorithm.

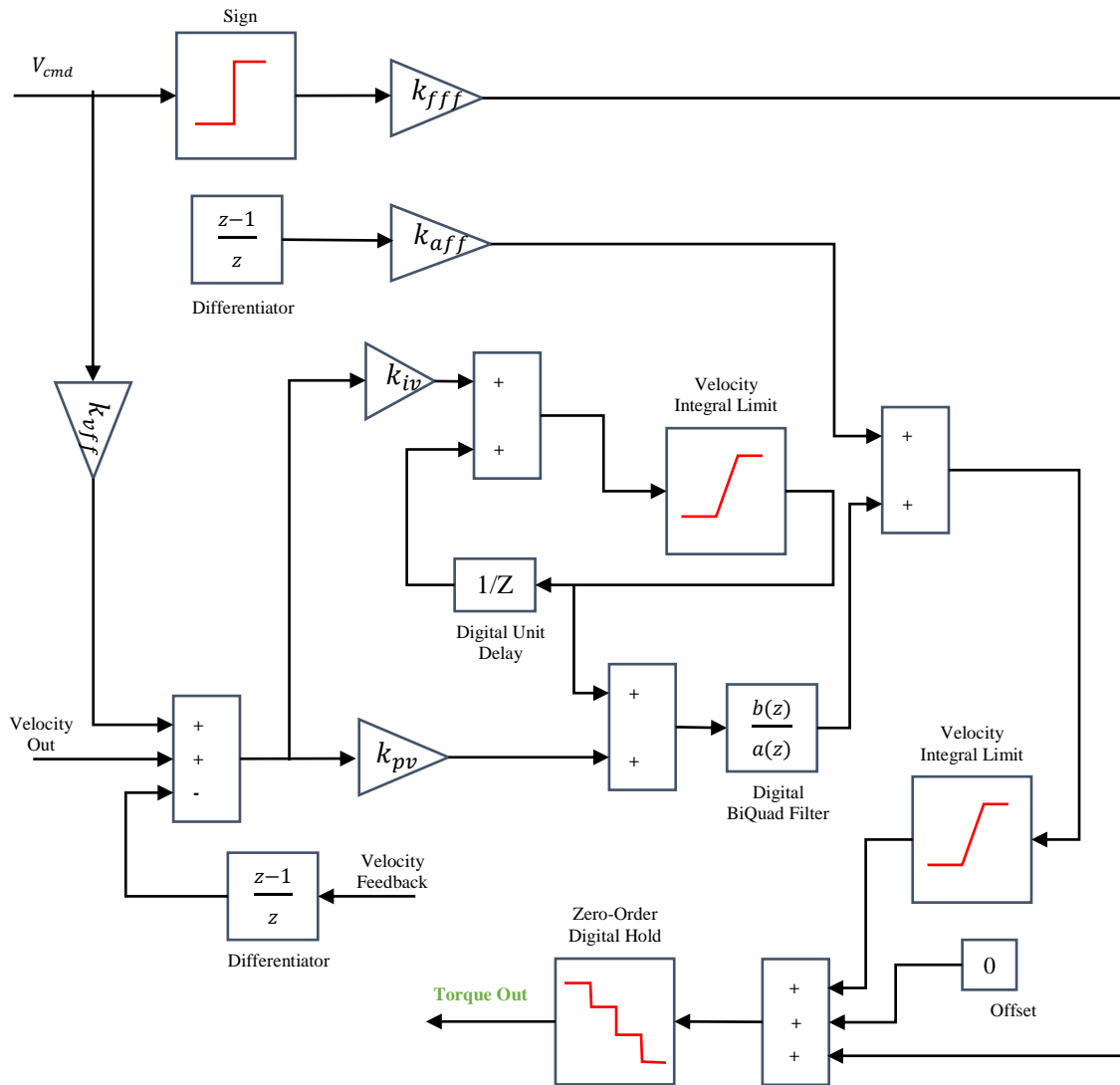


Figure 6.21. MechaWare schematic of the velocity compensator in PIV servo algorithm.

### 6.3.1.2 Velocity Mode

In Velocity mode, the output of the closed-loop servo algorithm (PID or PIV) is a 16-bit value representing velocity. The S772 and AKD drives automatically scale the velocity demand input so that the 16-bit range is used effectively. Velocity motion accelerates the axes to a specified speed. The axes will continue to move at the specified velocity until a new velocity is commanded.

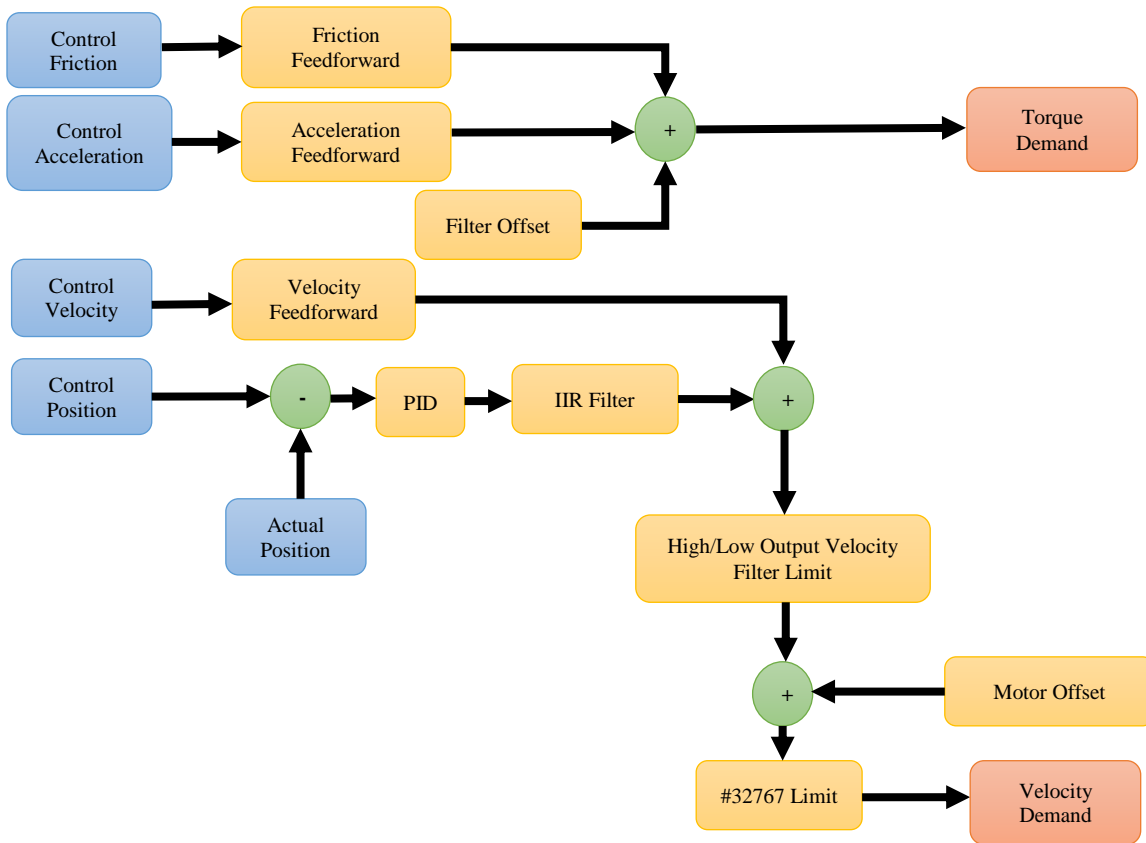


Figure 6.22. MechaWare schematic of PID servo algorithm in Velocity Mode.

### 6.3.2 Servo Tuning

The object of tuning is to tweak the different gains and motion parameters of a servo machine so that the resulting motion is optimized for production purposes. A machine is considered "tuned" if its servo performance meets the specified requirements. There are some common signs that a servo is tuned:

- Visibly smooth motion
- Little to no audible noise produced during and after a commanded motion
- Acceptable measured overshoot on a step input (e. g. 25%)
- Little to zero position error after the completion of a commanded motion

Furthermore, key points in tuning the Roller Rig servo controllers are:

- For point-to-point moves, total motion time is the main concern, not the rise time. A longer move time with less ringing cycles is a better choice than a shorter move time with longer ringing cycles.
- Larger underdamped peaks should be omitted to prevent long ringing cycles.

- Ringing is caused by moves that are shorter than the closed-loop bandwidth and no acceleration feedforward ( $K_{aff}$ ).
- Sometimes a longer move time is better than a shorter move time because it is more stable (less ringing) and no overshoot.

Various methods are available for tuning a servo system to deliver the above specification.

**Table 6.5. Comparison between common servo tuning methods [138].**

Servo Tuning Method	Ease of Use	Stability	Speed of Tuning	Ease of Getting Data	Experience Required	Servo Algorithm	Summary of the Method
Step Overshoot	✓✓✓✓	✓✓	✓✓✓	✓✓✓	average	PID	$K_d \rightarrow K_p$ $\rightarrow K_i$
Step Stability	✓✓✓✓	✓✓	✓✓✓✓	✓✓✓	average	PID	$K_p \rightarrow K_d$ $\rightarrow K_i$
Under/Over damped	✓✓✓	✓✓✓	✓✓✓	✓✓✓	average	PID	$K_p \& K_d$ $\rightarrow K_i$
Frequency Response	✓✓	✓✓✓	✓✓	✓	expert	PID	-
Velocity/ Position Loop	✓✓✓	✓✓✓	✓✓✓	✓✓	above average	PIV	Velocity Loop $\rightarrow$ Position Loop
Frequency Shaping	✓	✓✓✓✓	✓	✓	expert	PID and PIV	-

Trial-based iterative methods require some move to be made. The response of the system is observed in the time domain and an adjustment towards the goal is made based on the response of the system. This is iterated until the control goals are satisfied. One of the important features of trial-based iterative methods is that the simplicity of commanding a move and getting the time domain response of the system. The common problem with these methods is that they can easily get unstable for unexperienced user. Roller Rig Motion Console and Motion Scope are two interfaces that can be used for getting time domain response of the system in iterative tuning.

Frequency shaping is a method for tuning a control loop in the frequency domain with more flexibility than time domain methods. It can address problematic elements of a system more directly than simpler methods can provide. Frequency shaping is a tuning method that is largely based on frequency analysis and requires accurate frequency response data of the Rig. It has numerous more adjustments than a standard PID tuning method. It is necessary that the controls engineer has specific knowledge about the problems to be solved to apply correct solutions. Roller Rig Bode Tool is an interface that can be used for performing frequency shaping servo tuning.

PIV and Lead/Lag frequency shaping followed by fine tuning were used for tuning the wheel and roller rotational axes. PID frequency shaping and fine tuning were utilized for the linear axes. Bode Tool provides an excellent Auto-tuning feature for frequency shaping. The Auto-tuner only operates in “Plant” measurement mode with white noise excitation.

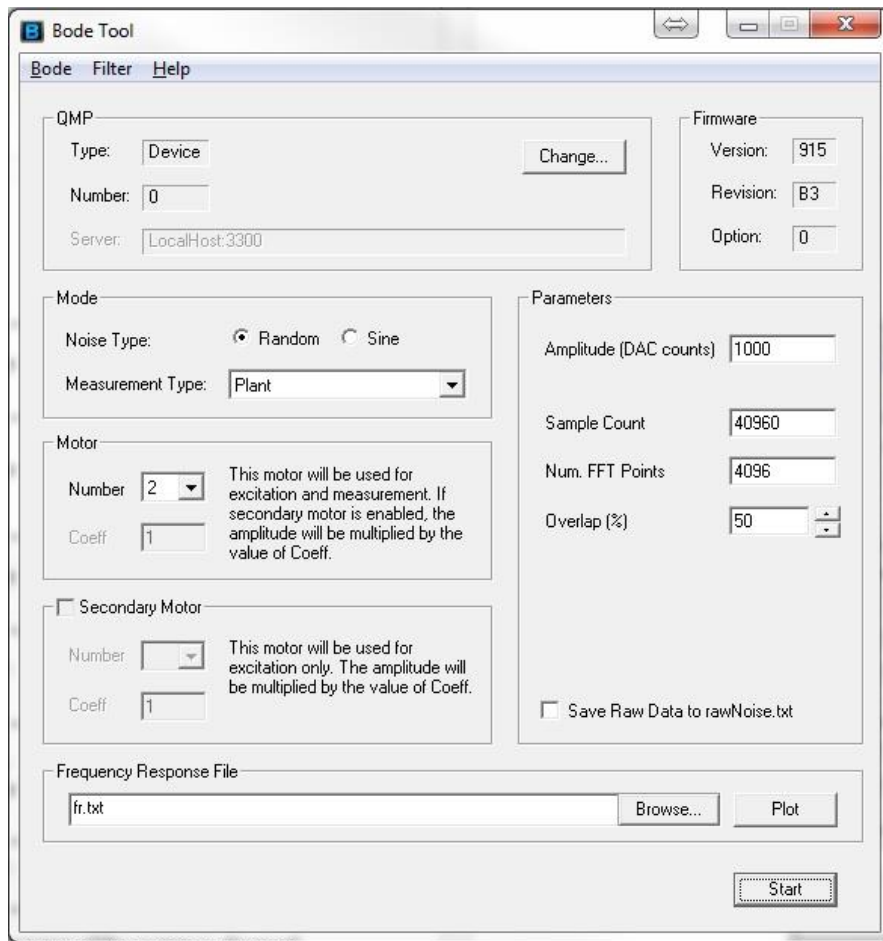
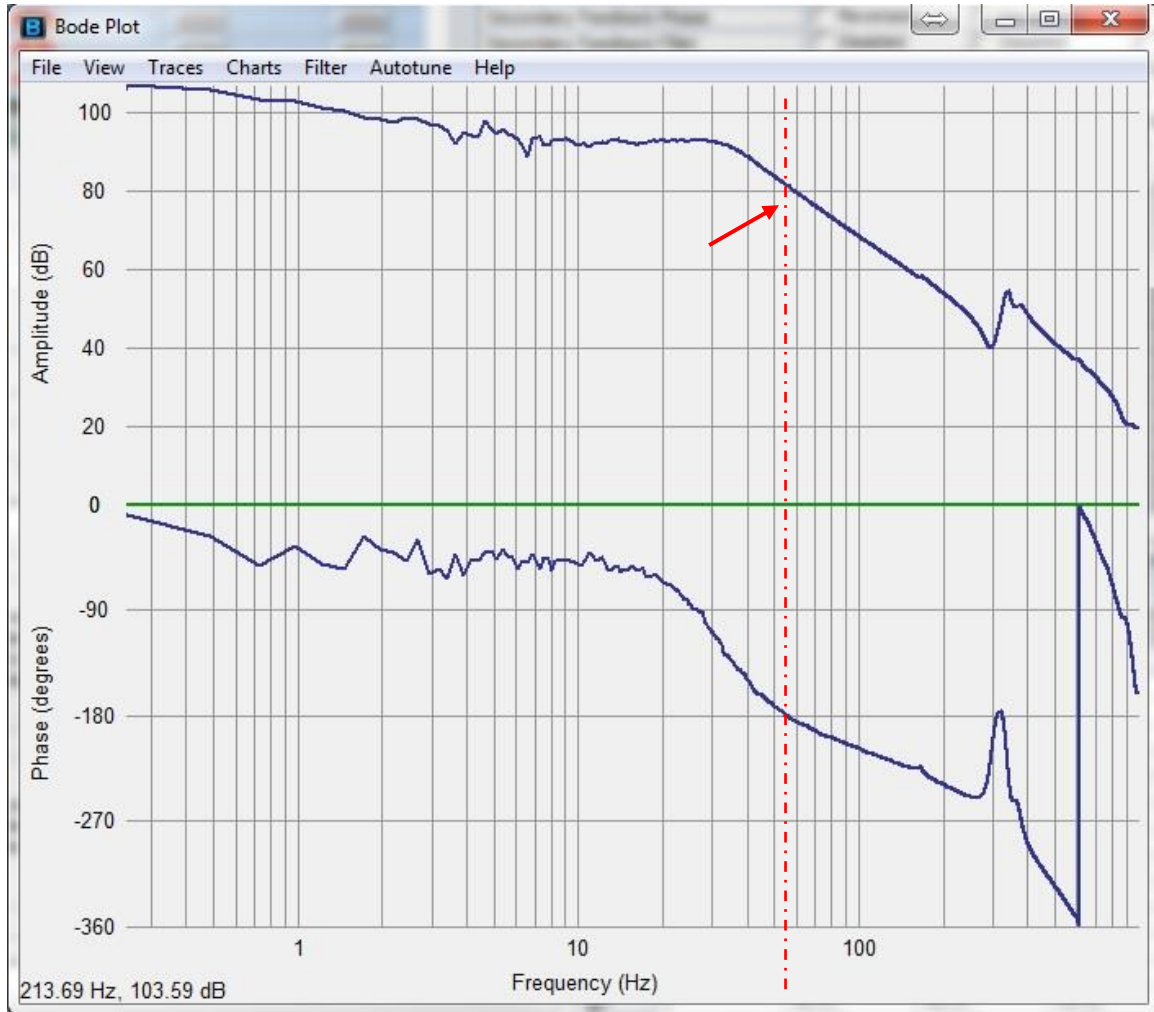


Figure 6.23. A snap-shot of Bode Tool ready for FFT measurement.

Once the Bode Plot is displayed, the drive should be disabled to prevent unexpected moves during tuning. The Autotuner takes most of the guesswork out of tuning. It does require a reference point

for it, as a safety precaution. It is recommended to use the point where the open-loop phase crosses through the -180-degree point (bottom blue trace). The red arrow shows this point for the example below.



**Figure 6.24. Selecting the reference point for the Bode Tool Auto-tuner (plant frequency response). The simulated and measured open-loop responses are identical.**

There are four auto-tuning methods available:

- Resonator
- PID
- PIV
- Lead/Lag

Each method should be checked for achieving the best performance. Clearing out tuning parameters will set PID and post filter settings to 0.

The Auto-tuner will always return a set of tuning parameters. These parameters should be checked manually to make sure they are stable for Rig. The easiest way to verify this is to turn on the closed-loop simulation and ensure that the frequency response is reasonable. Any peak in the simulated closed-loop response (dark red/brown) of more than +6 dB or so is unacceptable. An example is shown below that show acceptable Auto-tuning with the Lead/Lag method (3% smoothing used to make the results easier to see).

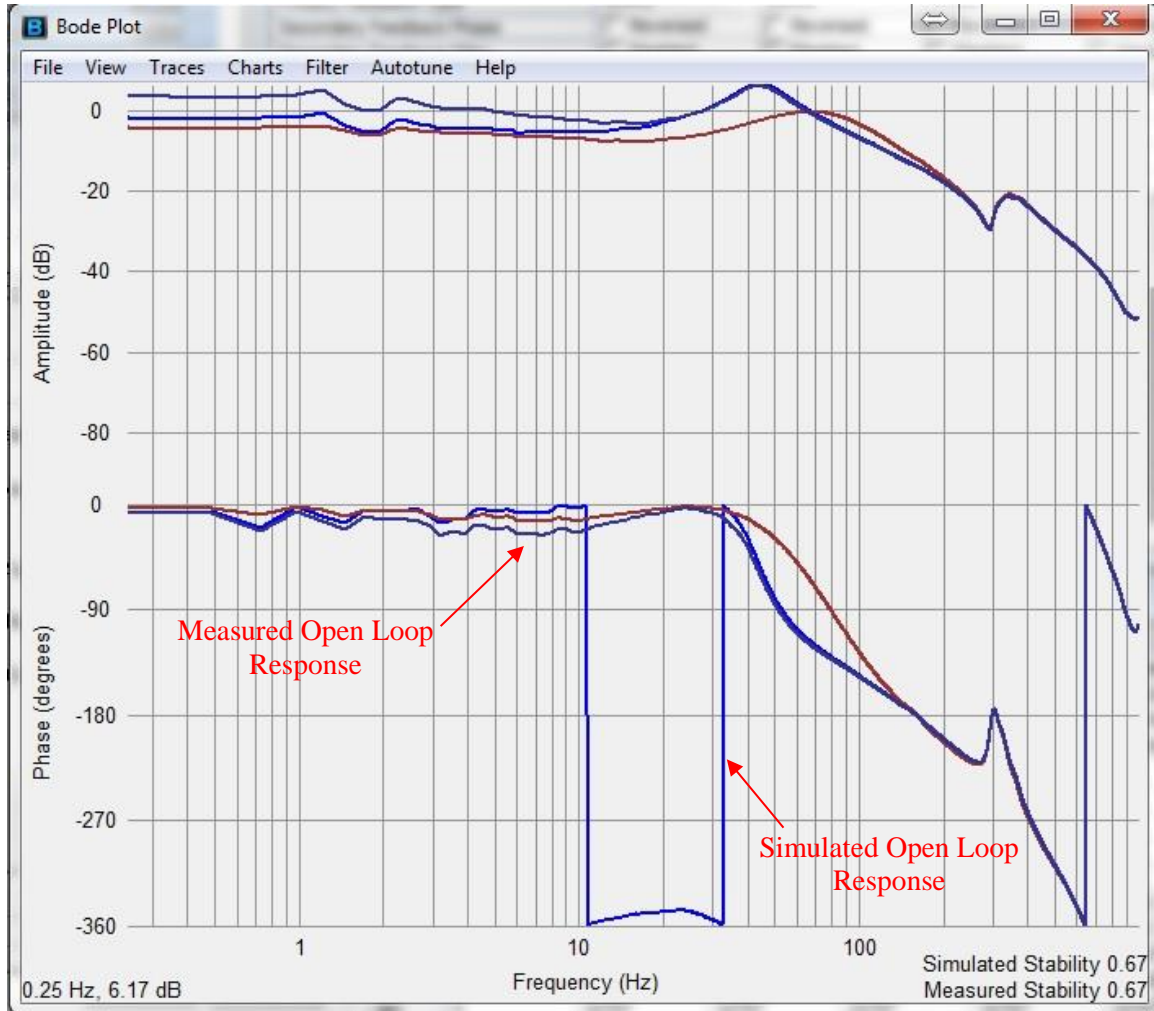


Figure 6.25. An example of acceptable Auto-tuning results using the Lead/Lag method.

### 6.3.2.1 Stability Measurement

A quantitative stability measurement is made when a bode test is run. The measurement is displayed quantitatively in the bottom right-hand corner of the plotting window [136]. The stability measurement is performed on both the measured open-loop and the simulated open-loop responses. The measured and simulated response are identical if the control tuning has not been changed since

taking the measurement. When simulating control loop response, the user can compare the stability of the measured vs. simulated response.

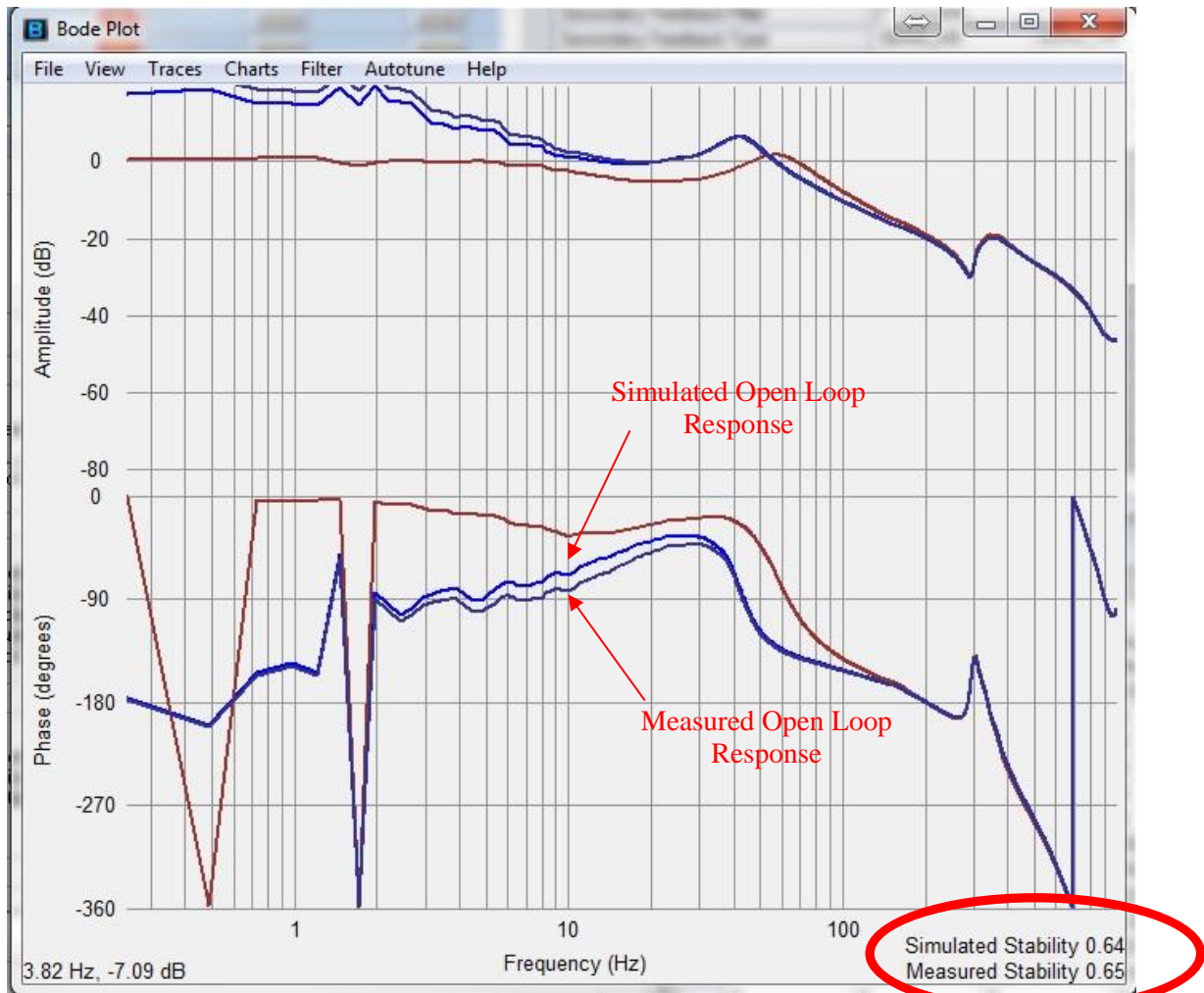


Figure 6.26. Simulated and measured stabilities using PID (compare with Figure 6.25).

Bode Tool can also provide a visual representation of the stability measurement in Nyquist plot. If different, the measured and simulated responses will be shown separately with arrows. The length of the arrow is equal to the stability measurement value, which is also shown in the plotting window. The stability measurement is the distance between 0dB, -180 degrees and the closest open-loop response point [139]. The 0dB, -180-degree point represents an oscillator. In the figure below, the stability measurement is 0.70.

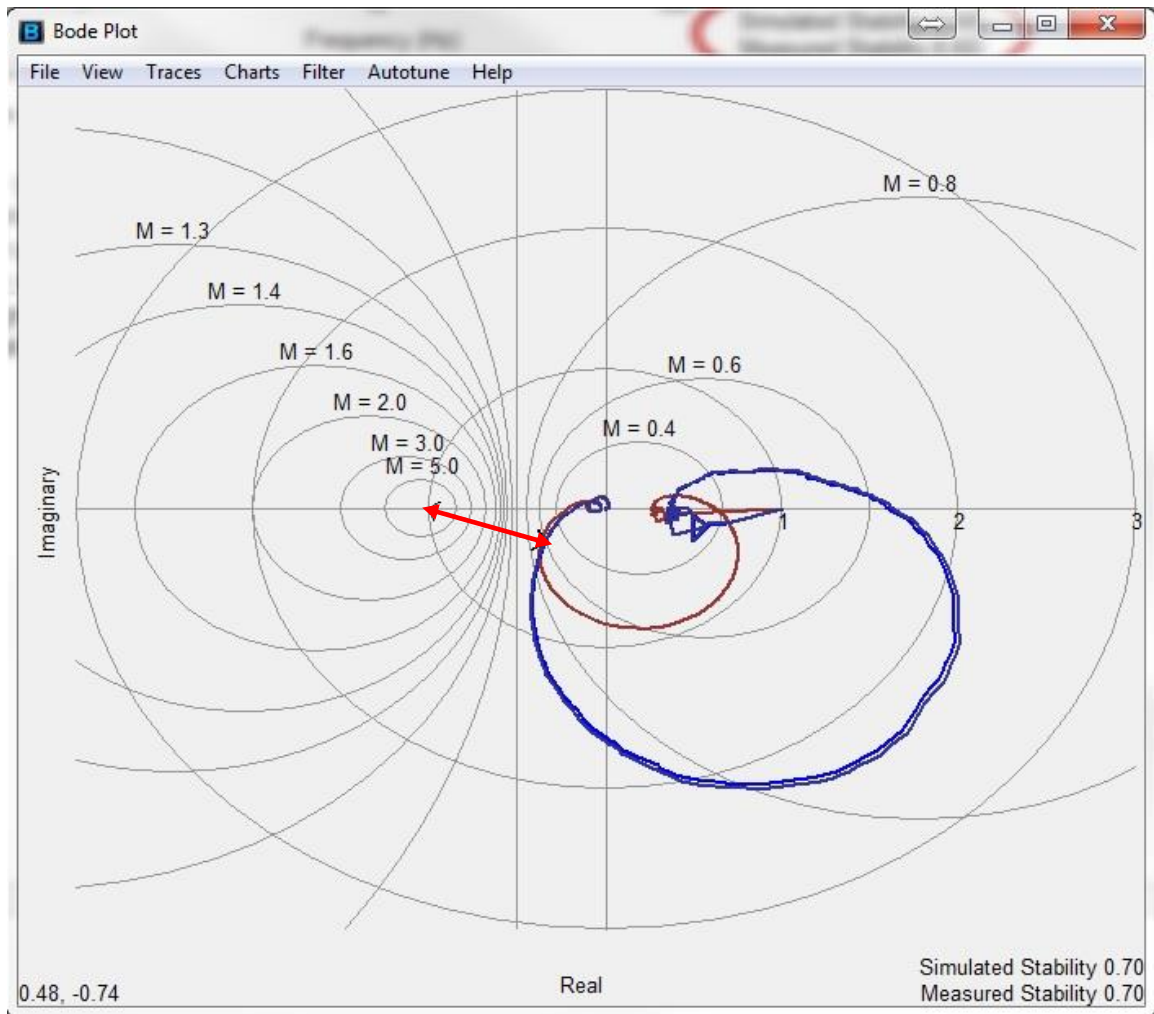


Figure 6.27. Simulated and measured stability in Nyquist plot.

The stability value ranges from 0 on up ( $x > 0$ ). However, a realistic upper limit value of 1 would be normal. A stability measurement of 0 would represent an extremely unstable system. A stability measurement of 1 would represent an extremely stable system [139]. It is not uncommon for Roller Rig Axes to end up with a stability figure in the range of 0.3 - 0.5 after all tuning is finalized.

### 6.3.2.2 Gain and Phase Margin

The gain and phase margins are commonly used in controls to quantitatively determine how stable a system is. The gain and phase margins are separate measures of the stability of a system. Gain and phase margins are only calculated based on the open-loop system response. They are not valid measures of the closed-loop response [140].

Gain and phase margin measurements serve two purposes: 1) They ensure that the system is sufficiently damped and stable to reduce overshoot, ringing effect, and other undesirable behaviors and 2) They ensure the controller is stable enough to deal with any unknowns in the system, such as different motors on the production line having slightly different performance [139]. A normal system would do well with a minimum of 12 dB gain margin and 45 degrees of phase margin.



Figure 6.28. Multiple gain and phase margin in the bode plot.

The gain margin of a system is the amount of amplitude below 0dB at the frequency which the phase crosses -180 degrees. This can occur more than once. A common way to deal with multiple gain margin measurements is to consider the worst one, i.e. the smallest gain margin. The bode tool automatically does this. It shows all gain margin measurements with a dot and shows the worst with a dot and dotted line. Gain margin values are shown in the lower left of the screen for both measured and simulated data. These concepts are presented below [136].

The phase margin of a system is the amount that the phase of a system is more than -180 degrees at the frequency where the open-loop amplitude crosses 0 dB. This can happen more than once. The easiest way to deal with multiple phase margin measurements is to concentrate on the worst one (smallest phase margin) [141]. The bode tool does this automatically. It will show all phase margin measurements with a dot and show the worst with a dot and dotted line. Phase margin values are shown in the lower left of the screen for both measured and simulated data. These concepts are shown above.

Both stability measurement and Gain/Phase margin can be used to evaluate the performance of the Rig. The table below provides a comparison of the two methods:

**Table 6.6. A comparison between phase and gain margin versus stability measurement.**

Method	Pro	Con
Stability Measurement	It is excellent at finding the worst frequency of instability in a system. It is an automated way of looking at the Nyquist plot, which is the most efficient simple way of looking at stability. It will not miss resonances that are not near 0 dB or -180 degrees [139].	It is much less common than gain and phase margin.
Gain and Phase Margin	It is the most common way to specify or measure the stability of a system.	It can miss critical resonances that don't occur near the 0 dB or -180-degree crossover frequencies.

**Table 6.7. Stability of the VT Roller Rig Axes.**

Axis	Servo Control Algorithm	Stability	Gain Margin (dB)	Phase Margin (deg)
Wheel	PIV with feedforward	0.61	11.45	50.56
Roller	PIV with feedforward	0.93	3.21	62.95
Lateral	PID with feedforward	0.65	18.02	47.70
AoA	PID	0.41	5.00	48.76
Vertical	PID	0.65	13.25	51.65
Cant	PID	0.61	8.41	62.68

The diagrams below outlines the main steps of PIV velocity loop tuning [140]:

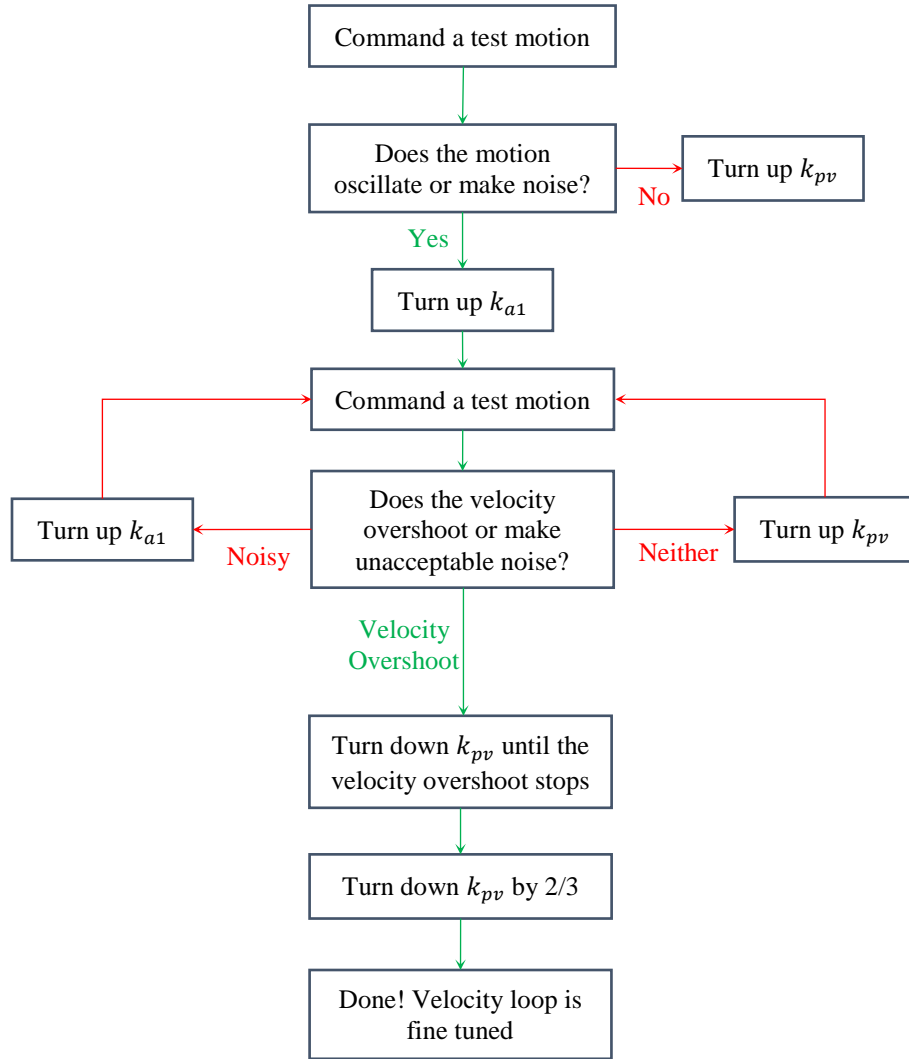


Figure 6.29. Flowchart of PIV velocity fine tuning.

Table 6.8 summarizes the velocity control accuracy of the VT Roller Rig after servo tuning. Figure 6.30 and Figure 6.31 show the raw velocity feedback. As discussed later, this data is subjected to quantization error in encoder equivalent output. In other words, not all of the error shown in these two figures is happening in reality. A major part of it is an artifact caused by the digital interpolation and quantization operations applied by the drive to the encoder output for increasing the performance of positioning servo algorithm. The mathematical modeling and filtering technique for de-noising the velocity data is extensively discussed later in this document. The 90% probability band for the error using the noisy raw data is 0.206rpm for the wheel, and 0.104rpm for the roller. Figure 6.32 and Figure 6.33 show the histogram of the error for both axes and the 90% probability band.

**Table 6.8. Velocity control accuracy of the VT Roller Rig after servo tuning.**

Axis	Maximum error after frequency shaping	Maximum error after fine tuning (improvement)	90 <sup>th</sup> percentile error after fine tuning
Wheel	1.516rpm	0.526rpm (65.30%)	0.206rpm
Roller	1.282rpm	0.221rpm (82.76%)	0.104rpm

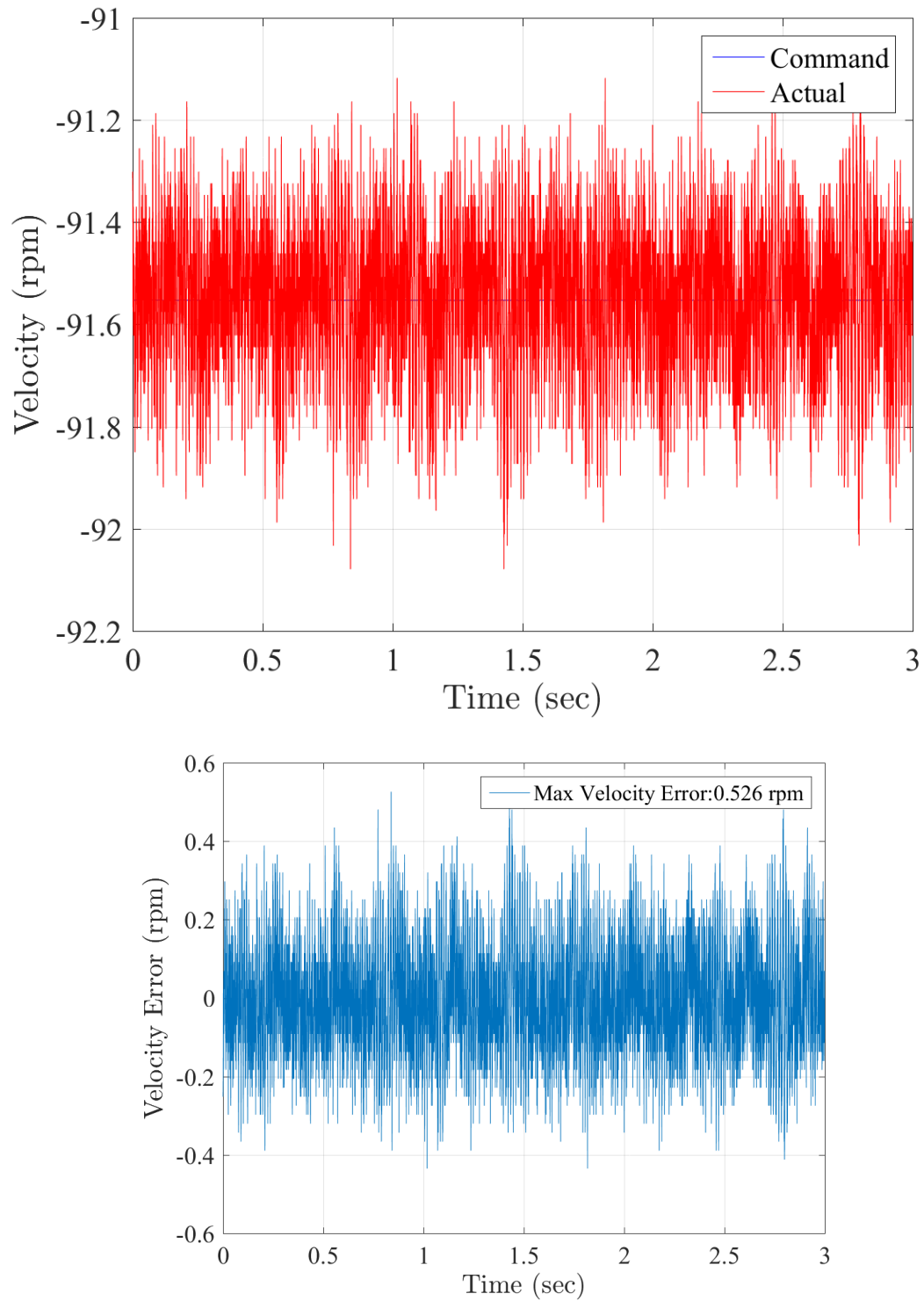


Figure 6.30. Instantaneous velocity error of the wheel axis at 91.553rpm.

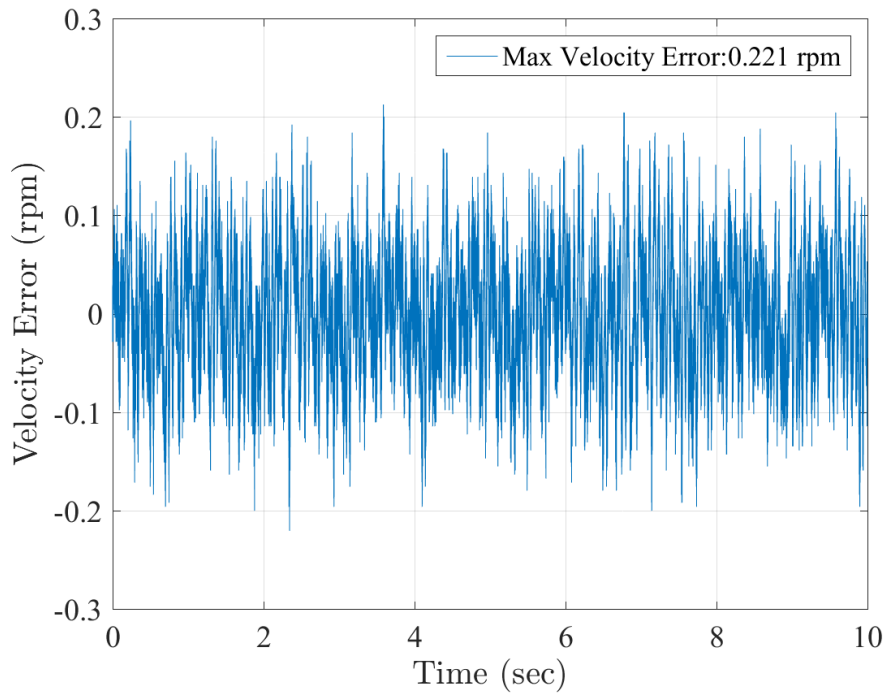
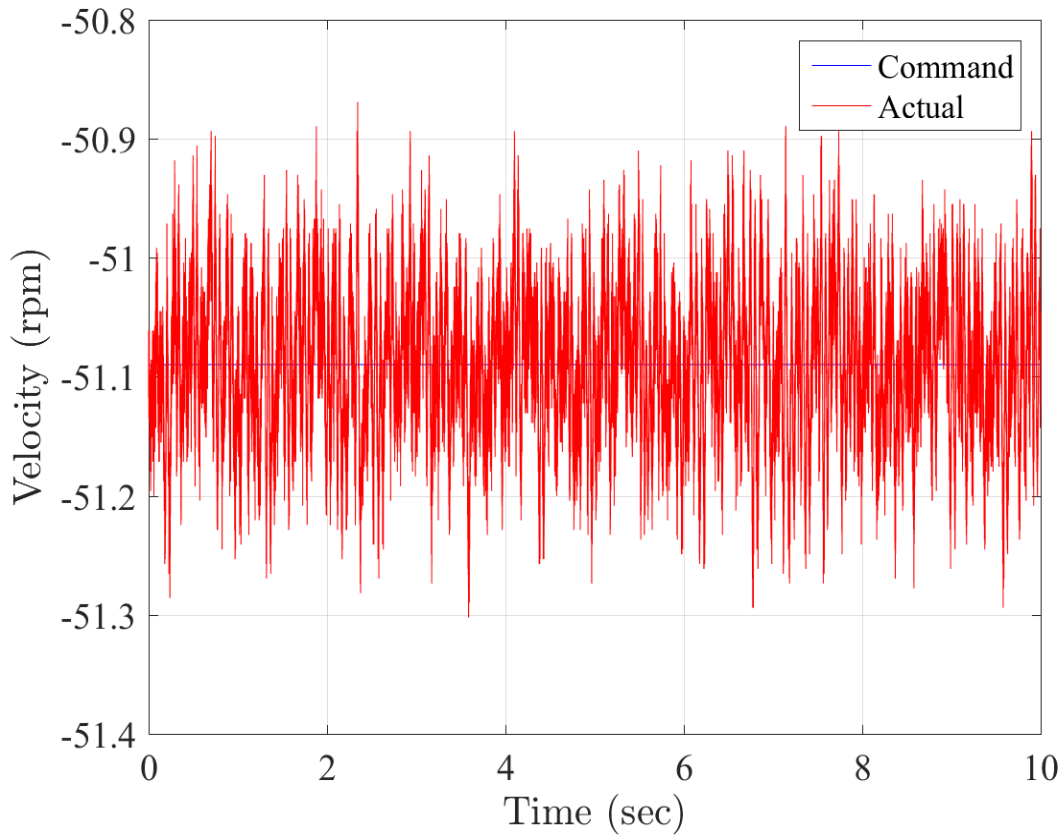


Figure 6.31. Instantaneous velocity error of the roller axis at 51.090rpm.

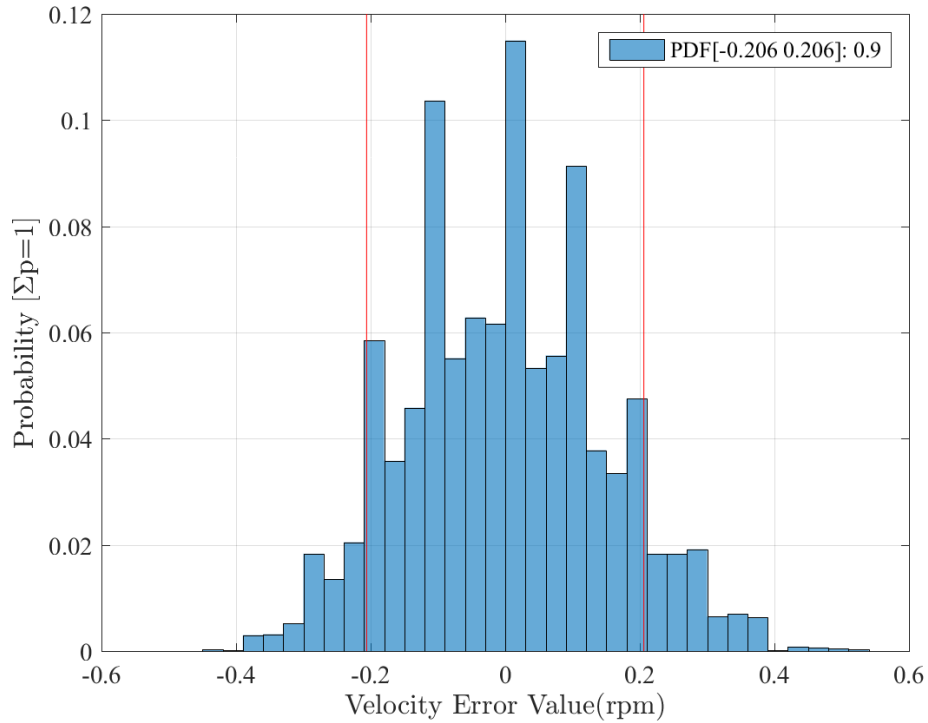


Figure 6.32. Velocity control accuracy of the VT Roller Rig for the wheel axis at  $91.553rpm$  with 90% probability band:  $0.206rpm$ .

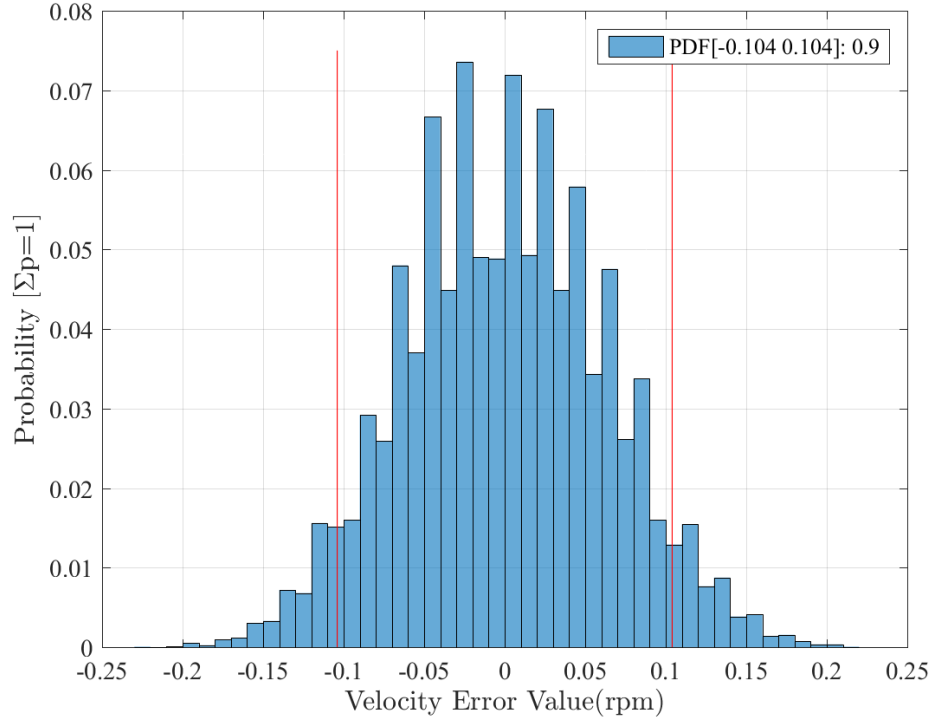


Figure 6.33. Velocity control accuracy of the VT Roller Rig for the roller axis at  $51.090rpm$  with 90% probability band:  $0.104rpm$ .

### 6.3.3 D-Rate

D-Rate is a derivative averaging method in PID servo algorithm. When used, the PID derivative term is applied to the velocity that is measured in the last  $n$  samples where  $n = D\text{-Rate} + 1$ . D-Rate is valuable when it is not possible to use filters due to some environmental or design constraint. D-Rate can only be set in integer values with the default value of 0. To conserve computational horsepower and memory, D-Rate is limited to a maximum of 7 [142].

The derivative is applied to the measured velocity over some samples. It is not applied to the average velocity during that period. Therefore, a change in D-Rate influences the effective gain of  $K_d$ . Since the derivative term can be measured over several samples, some aliasing factors can also have an effect. An increase in D-Rate will increase the effective  $K_d$  at frequencies far below the Nyquist Frequency (1/2 sample rate). The effective increase in  $K_d$  at low frequencies will be:

$$(D\text{Rate} + 1) \times K_{d \text{ without } d\text{-rate}} = K_{d \text{ effective}} \quad (50)$$

D-Rate has the effect of changing the sample rate for the derivative term. This has two effects:

- A comb filtering effect occurs at high sample rates. This consists of two effects: Notches in the amplitude response of the control algorithm that are dependent on the D-Rate value, and distortions in the phase response that correspond to the notches.
- Because of the comb filtering effect, there is an effective cap in  $K_d$  gain that is relatively the same regardless of D-Rate.

The gain of D-Rate at very high frequencies (near the Nyquist frequency) will be lower than the gain if  $K_d$  is raised to an equivalent level (equivalent  $K_d = K_d \times (D\text{Rate} + 1)$ ).

### 6.3.4 Electronic Gearing / Master-Slave configuration

Electronic gearing provides a position command to a servo amplifier that depends on the motion of another device. That device is typically an encoder (or its equivalent) connected to a motor. However, it can also be a hand-driven encoder used to accept input from an operator or an output from a stepper motor controller. For the VT Roller Rig, either wheel or roller servo amplifiers could provide the position command for the other one to follow. In this case, the master encoder must connect as both the feedback for the master drive and input for the slave drive. This is different from internal profile generation where position commands are calculated inside the drive based on motion parameters such as distance, velocity, acceleration, and torque.

The external encoder signal provides an input to the gearing software. The following types of external encoders can be used as a master signal source for electronic gearing.

**Table 6.9. External encoders for providing input in electronic gearing.**

Feedback Type	Frequency Limit
SinCos Encoder BISS digital	1.5MHz
SinCos Encoder ENDAT 2.1	350kHz
SinCos Encoder ENDAT 2.2	1.5MHz
SinCos Encoder HIPERFACE	350kHz
SinCos Encoder without data channel	350kHz
ROD* (AquadB) 5V	1.5MHz
ROD* (AquadB) 5V	350kHz
ROD* (AquadB) 24V	100kHz
SSI 5V	1.5MHz
Step/direction 5V	1.5MHz
Step/direction 24V	100kHz

For cases where the feedback device of the master servo motor is something other than a physical encoder, the S772 and AKD-B00707 provide encoder emulation. For example, neither a sine encoder nor a resolver directly produces signals compatible with encoders. The S772 and AKD-B00607 encoder emulation circuit produce output signals equivalent to an encoder from any feedback device that is used as the main feedback device. Figure 6.34 shows the electronic gear architecture using S772 servo amplifiers for the VT Roller Rig.

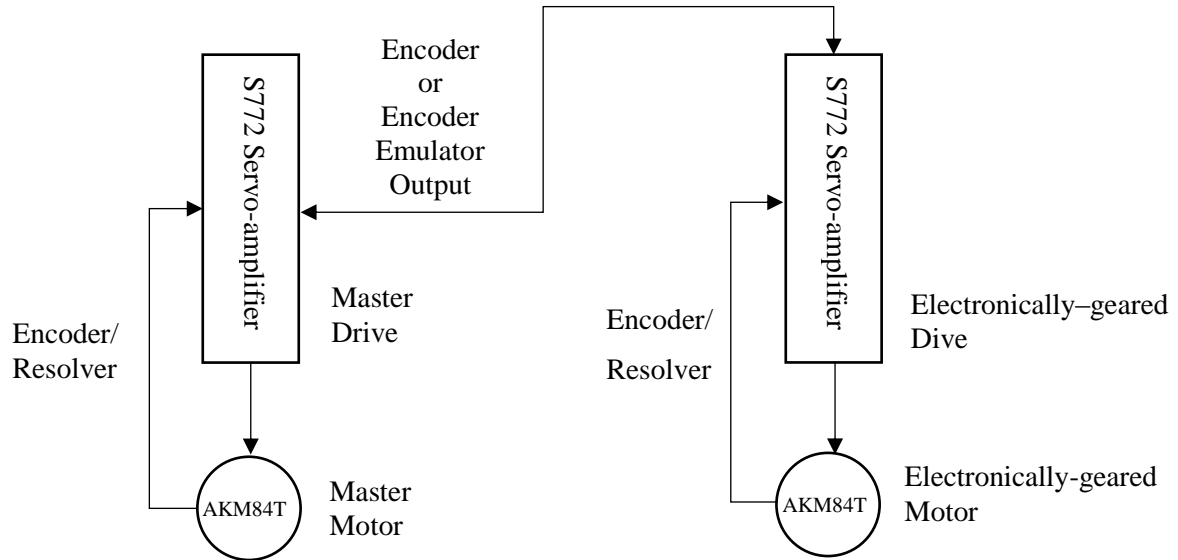
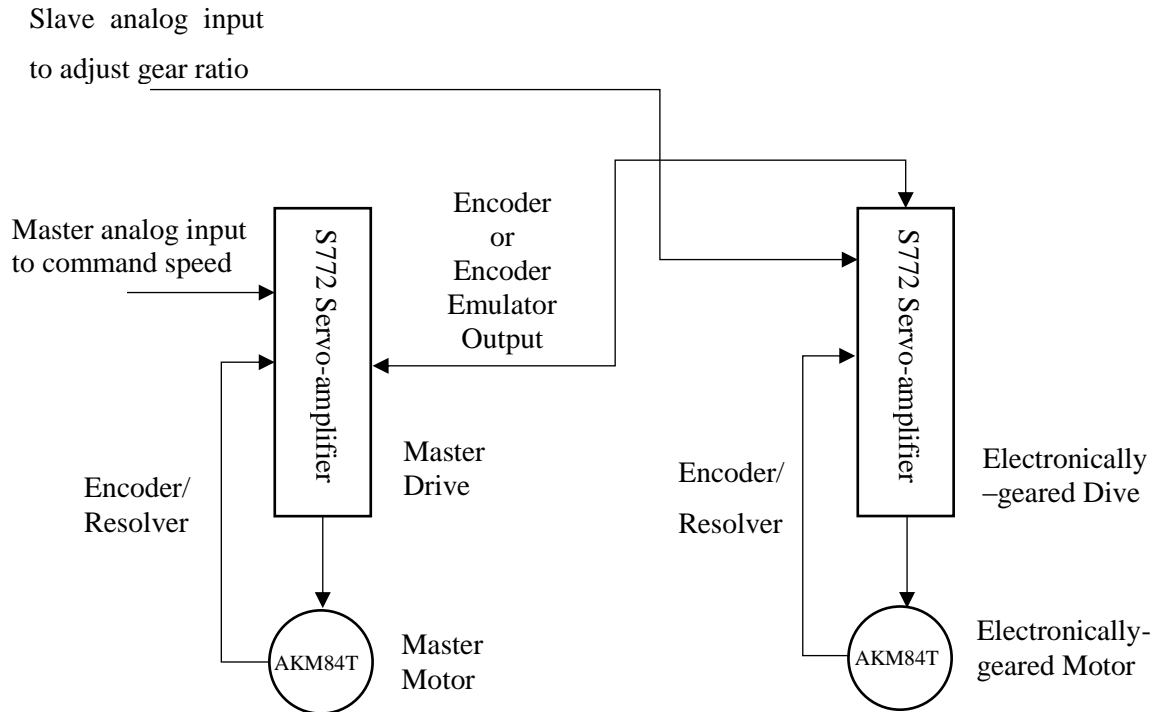


Figure 6.34. VT Roller Rig electronic-gearing architecture (the same holds for AKD-B00607).

In many applications, the motor follows the input each step, where one revolution of the input device should create one revolution in the electronically-gearred motor. This is called one-to-one gearing. Other times, it is necessary to have a non-unity scale factor. The gear ratio may be a non-integer, such as 1:3. It is important that the gearing software not introduce round-off errors when the gear ratio is non-integer. Otherwise, the round-off error accumulates and causes the electronically-gearred motor to drift with respect to the input over an extended period. If the gear ratio needs to be controlled in real-time, one of the analog inputs of the slave servo amplifier can be used to adjust the gear ratio. Figure 6.35 shows a control scheme where one analog input commands speed of the master axis and the slave axis follows that command according to the gear ratio.

The distance between the command generated from the encoder input and the electronically-gearred motor is called position error (PE) or following error. If a servo loop is poorly tuned so that the geared motor is sluggish, the motor will not follow the input signal well. It is important to tune the geared motor with servo gains as high as possible to minimize this problem. High values of velocity feed-forward (GPFFV) are also helpful in reducing following error. In fact, if GPFFV is set to 1.0, all following error is eliminated during steady-state operation. However, such large values of GPFFV can cause an overshoot of rapidly-accelerating commands. If the following error exceeds a certain threshold, the slave servo amplifier generates a fault.



**Figure 6.35. VT Roller Rig electronic-gearing architecture with adjustable gear ratio (the same holds for AKD-B00607).**

In S772, the analog input is the fastest way to change the gear ratio, allowing up to 4000 adjustments per second. However, analog inputs are subject to noise. This is avoided by using a field bus or serial port. These methods are slower than an analog input. Field bus input allows for approximately 50 to 100 gear adjustments per second, while serial input only allows for 20 to 30 updates per second.

For the AKD-B00607, only digital inputs can be used for electronic gearing. Depending the voltage level of the commanding signal, two ports are available. With 5V (TTL level) signals, incremental encoder or encoder with EnDat could be accepted. This allows for up to 500kHz updates. With 24V signals, only incremental encoder can be used. However, this allows for up to 3MHz update rate.

## 6.4 Precise Wheel-Rail Positioning

Point to point motion will start a move on all the axes mapped to the Motion object from the current command position to a new position. There are two main point-to-point motions, each taking a different set of arguments and generating different velocity profiles as the axis/axes are moving:

**Trapezoidal:** This type of the movement has a trapezoidal shape for the velocity with constant acceleration and deceleration phases.

**S-Curve:** This kind of move has an "S" shape to the acceleration and deceleration phases. It uses a "Jerk Percent" argument to decide how much of the acceleration and deceleration phases are curved. A Jerk Percent of zero produces a trapezoidal profile. These motion profiles are illustrated in Figure 6.36 and Figure 6.37.

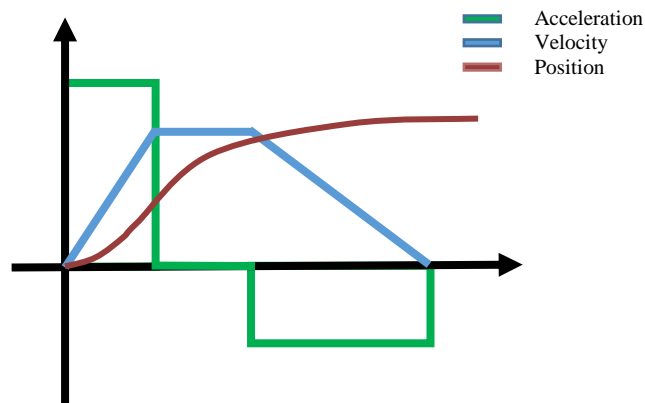


Figure 6.36. Trapezoidal motion profile.

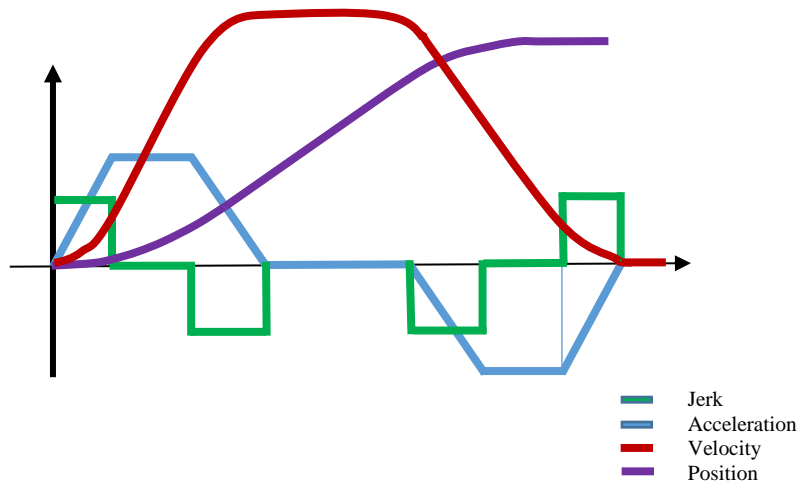


Figure 6.37. S-Curve motion profile.

The following table summarizes the arguments that each of the motions needs. The Position argument is always required, but all the other arguments are optional.

**Table 6.10. Comparison between Trapezoidal and S-Curve motion parameters.**

	Position	Speed	Acceleration	Deceleration	Jerk Percent	Attributes
<b>Trapezoidal</b>	Mandatory	Yes	Yes	Yes	No	Yes
<b>S-Curve</b>	Mandatory	Yes	Yes	Yes	Yes	Yes

If an optional argument is omitted, then the value used is taken from the corresponding properties starting with default in either the Axis or Motion objects. The Attributes argument modifies the default behavior of each of these motions enabling a large number of variations of the basic motion to be generated. The Attributes argument does not have a corresponding default property and must be specified for each motion.

Frequency shaping followed by PID tuning with step behavior were used for tuning the wheel-rail positioning axes. Where needed, feedforwards were added to correct small remaining errors and achieve faster settling time.

PID tuning with step behavior is accomplished by turning up a gain parameter until unwanted behavior (oscillation or noise) is reached and then turn down the gain parameter until the desired behavior is achieved and the stage is stable. This method primarily focuses on tuning the position overshoot parameter. The diagram below shows the natural progression of steps for this tuning method. To create a disturbance on the stage, a small commanded step is made. To create a step, a highly large acceleration, deceleration, and velocity is used ( $1e^{10}$  counts/sec<sup>2</sup> should be enough for all axes). Figure 6.38 summarizes the steps involved in tuning a PID servo loop with step behavior [140].

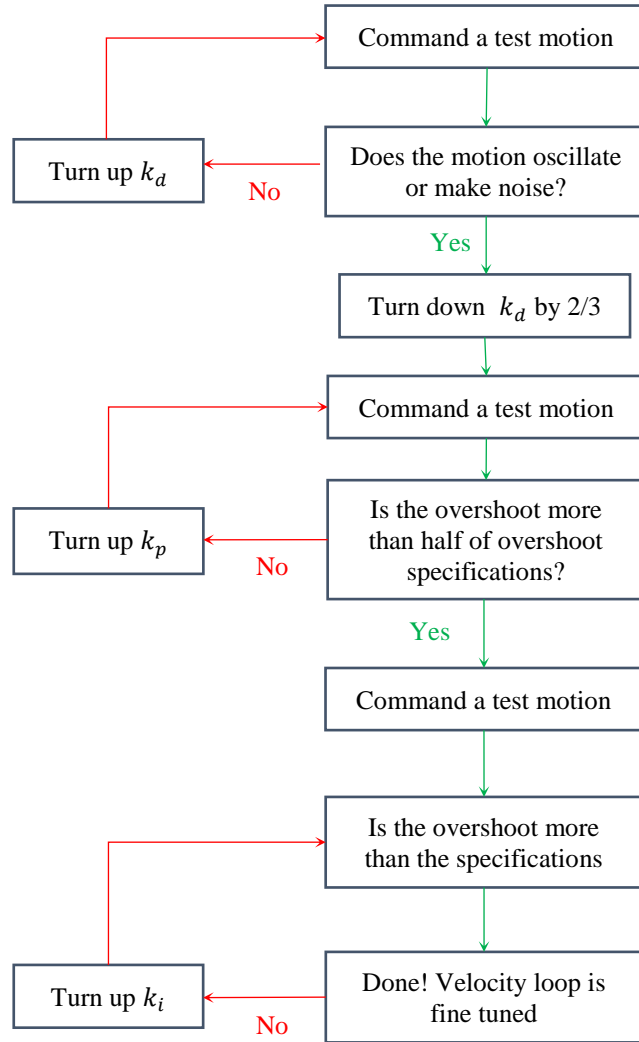


Figure 6.38. PID servo tuning with step behavior.

Feedforwards result in a virtually instantaneous response of the system. Feedback control loops (PID, PIV, or similar) take a finite amount of time before reacting. Feedforwards rely on an imperfect model of the system. This means that the feedforwards need help from the feedback control loop to get accurate motion. Feedforwards make the bulk of the move very quickly, while the feedback control loops correct the small errors that remain. As a result, a faster settling time is achieved than if feedforwards were not used.

On the other hand, feedforwards are open-loop, so they cannot suffer from closed-loop instability. Feedforwards are typically less sensitive to being misadjusted than closed-loop parameters. Feedback control systems can be excited into instability by grossly misadjusted feedforwards. However, the amount of maladjustment in feedforwards that is necessary to cause such instability is very rare.

Table 6.11 summarizes the positioning accuracy of the VT Roller Rig after servo tuning. Figure 6.39 through Figure 6.42 show the actual errors in motion and at steady state. All motion profiles are trapezoidal. The maximum positioning error of the VT Roller Rig on the move is 66.35 $\mu$ m, and 16nm while holding a constant position.

**Table 6.11. Positioning accuracy of the VT Roller Rig after servo tuning.**

Axis	In motion		Steady	
	after frequency shaping	after fine tuning (improvement)	after frequency shaping	after fine tuning (improvement)
Lateral (mm)	0.1058	0.06635 (37.29%)	8.516e-6	5.398e-6 (36.61%)
Vertical (mm)	0.0515	0.00358 (93.05%)	0.00323	8.567e-6 (99.74%)
Cant (mm)	0.04832	0.01779 (63.18%)	0.00668	1.607e-5 (99.76%)
AoA (mm)	0.04304	0.02114 (50.88%)	1.365e-5	1.017e-5 (25.50%)

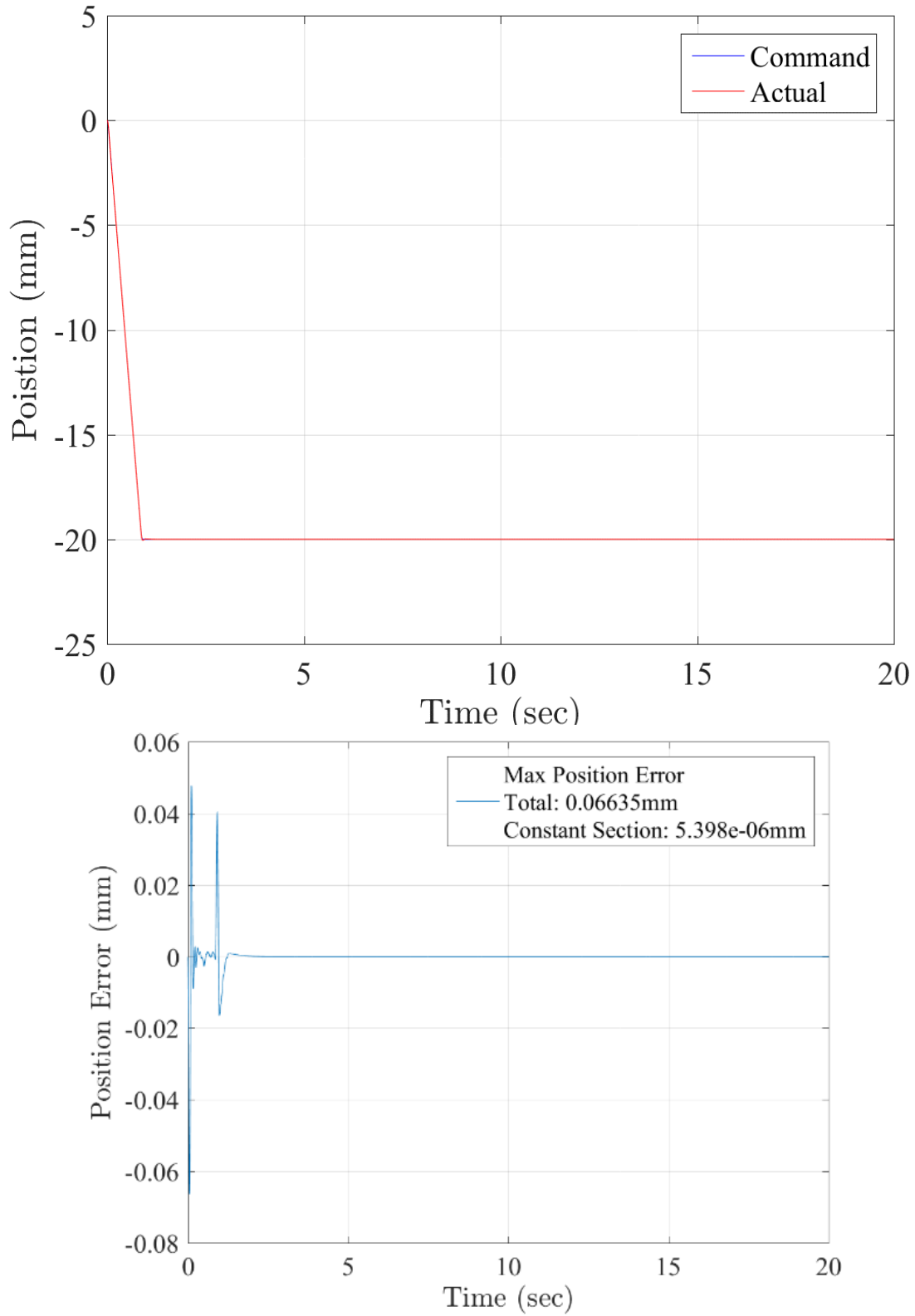


Figure 6.39. Positioning accuracy of the VT Roller Rig in a 20mm lateral motion at 22.52mm/s: 66.350 $\mu$ m error in motion, 5.398nm error at steady state.

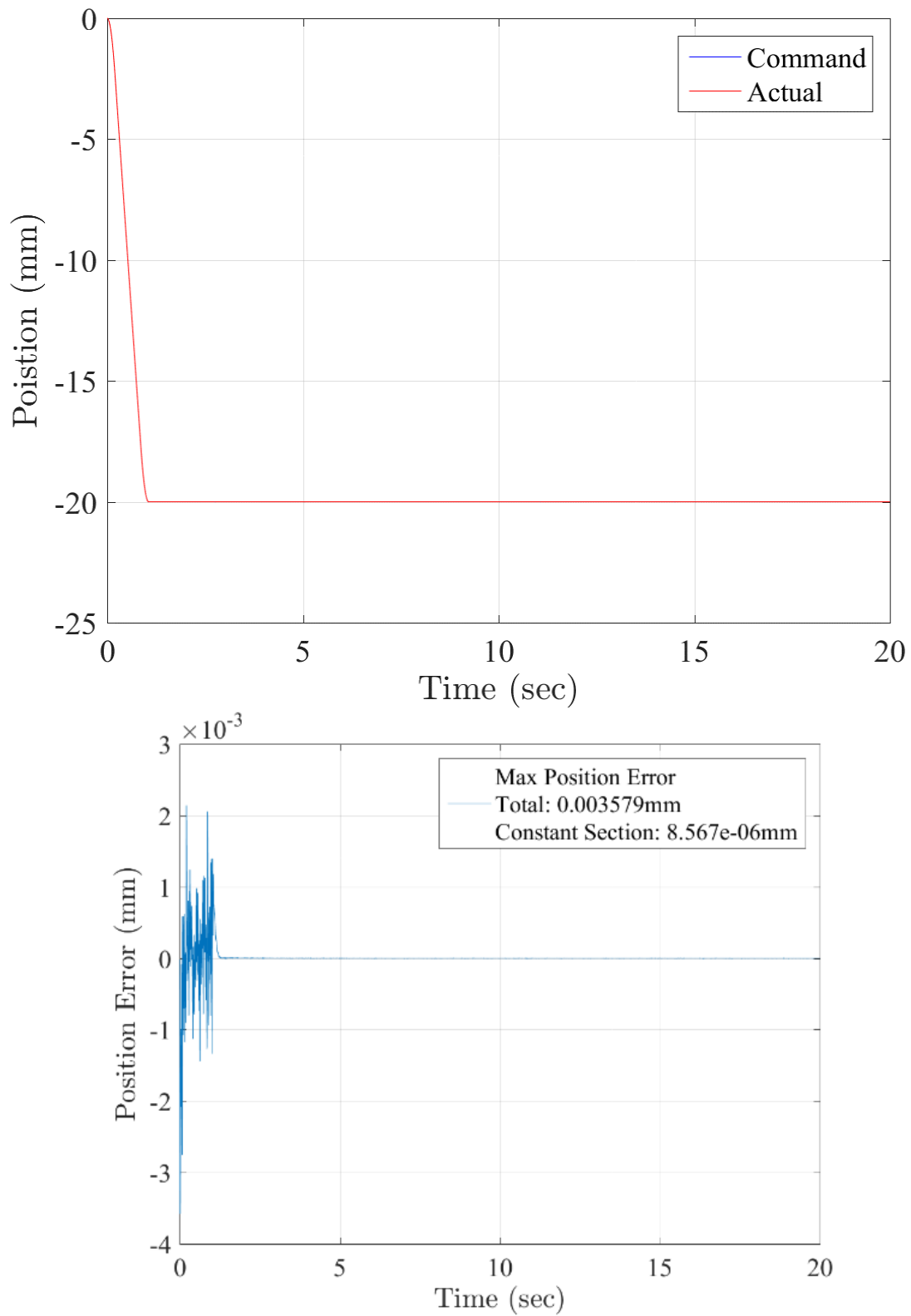


Figure 6.40. Positioning accuracy of the VT Roller Rig in a 20mm vertical motion at 19.3mm/s: 3.579 $\mu$ m error in motion, 8.567nm error at steady state.

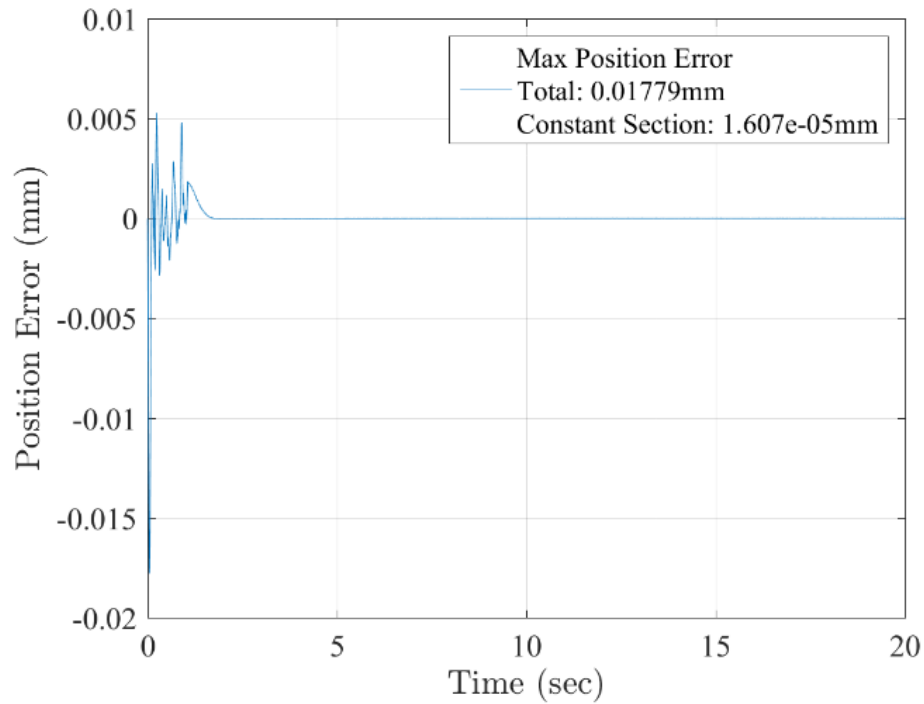
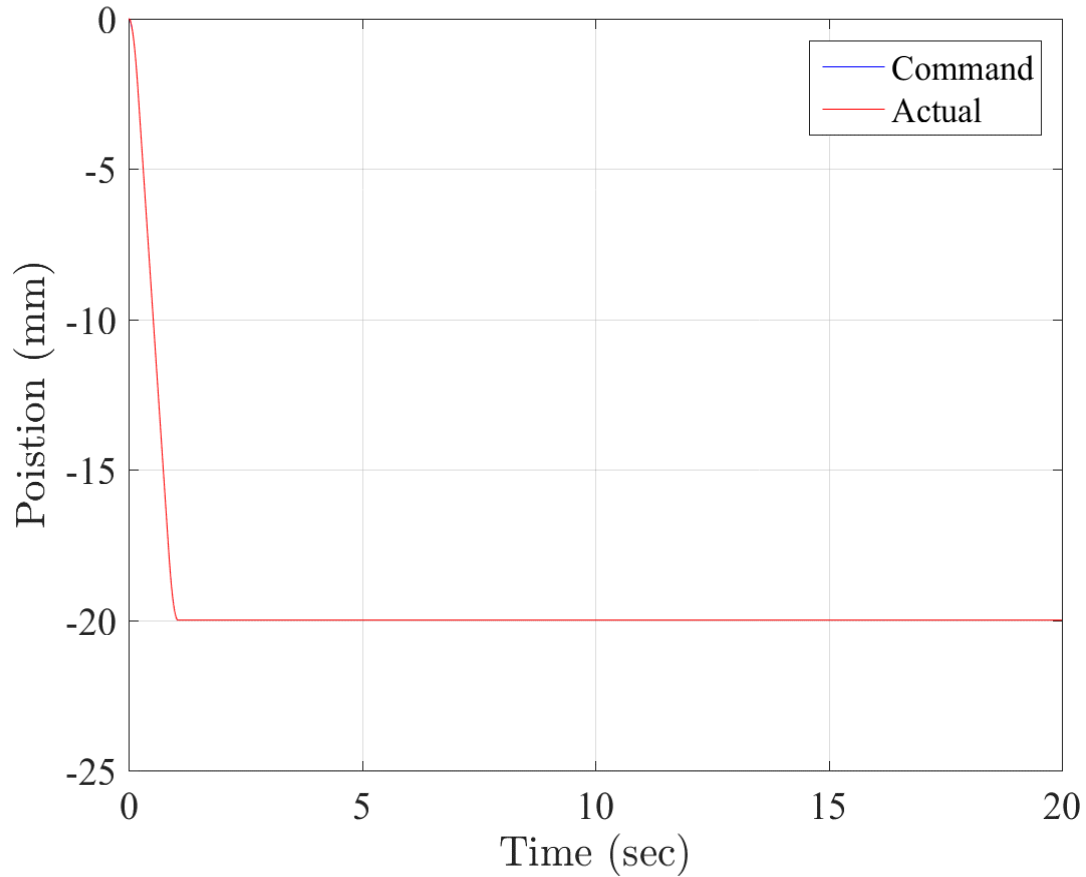


Figure 6.41. Positioning accuracy of the VT Roller Rig in a 20mm cant motion at 19.15mm/s: 17.79 $\mu$ m error in motion, 16.07nm error at steady state.

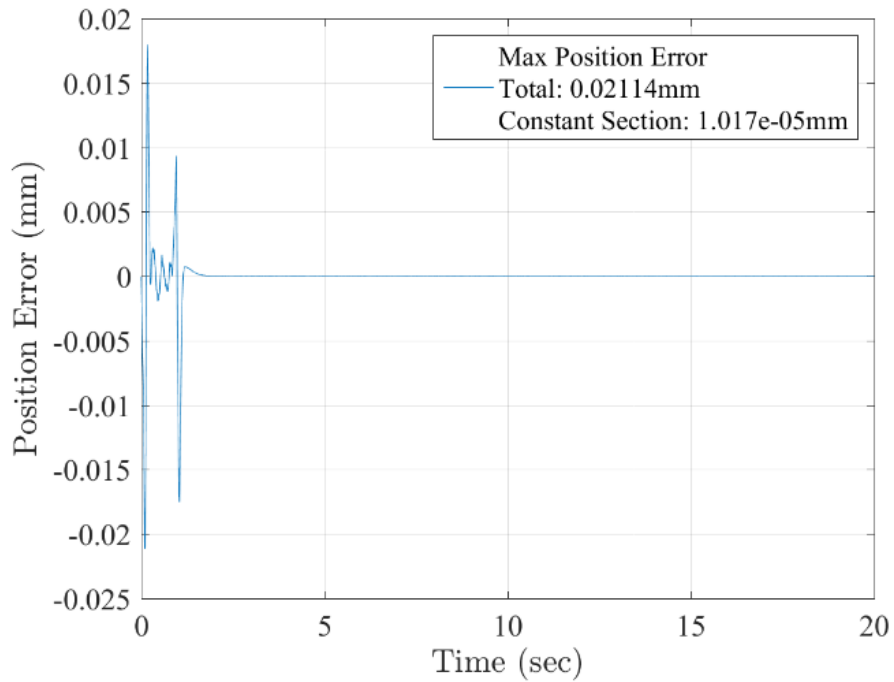
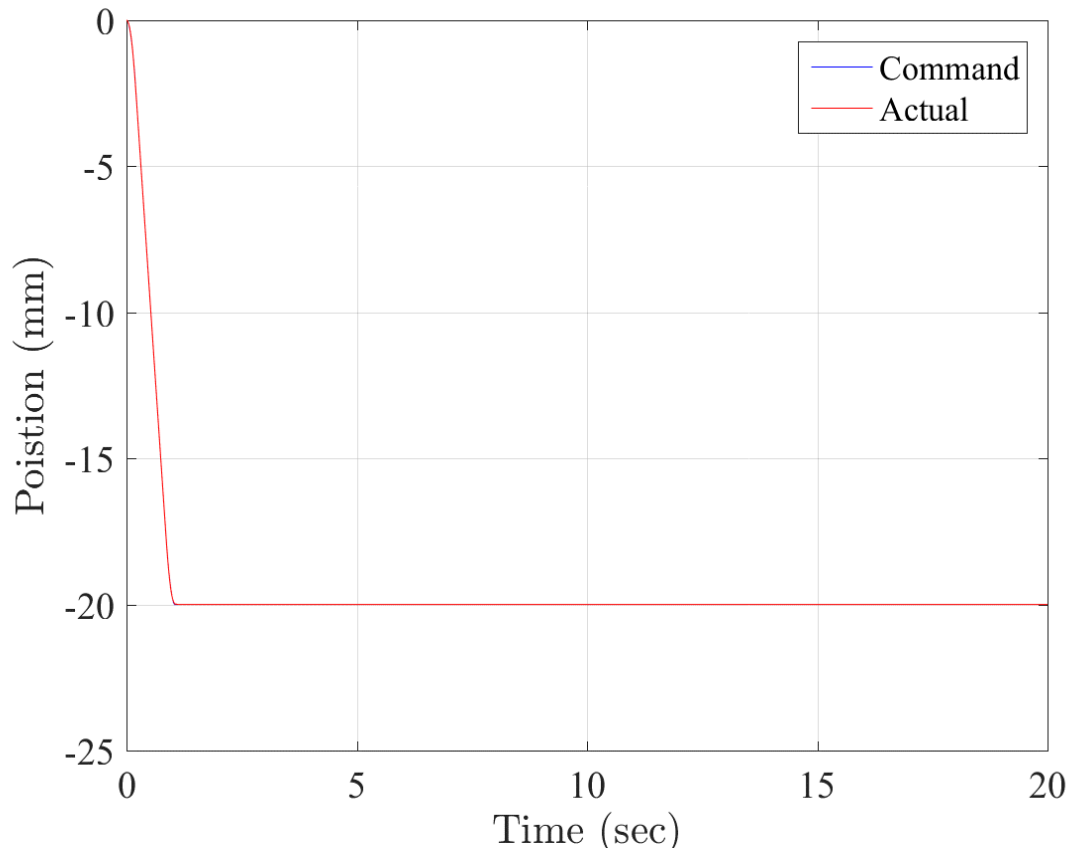


Figure 6.42. Positioning accuracy of the VT Roller Rig in a 20mm AoA motion at 17.2mm/s: 21.14 $\mu$ m error in motion, 10.17nm error at steady state.

### 6.4.1 Scaling PID Parameters for Different Controller Update Rates

When tuning the Roller Rig, it may be necessary to adjust the controller's sample rate for optimum performance. Changing the sample rate will directly affect the closed-loop response of the PID control algorithm. To maintain stability and performance, the PID parameters must be scaled to match the change in sample rate. The table below has been taken from a document published by Motion Engineering (now part of Kollmorgen) [143]. It explains how to scale the tuning parameters properly. This document only addresses scaling for the PID closed-loop algorithm. It does not compensate for resonances caused by increased system bandwidth or system nonlinearities.

**Table 6.12. Compensations for PID parameters at different controller update rates.**

Term	Compensation
Proportional - $K_p$	None
Integral - $K_i$	$\text{new } K_i = \text{old } K_i \times (\text{old SR} / \text{new SR})$
Derivative - $K_d$	$\text{new } K_d = \text{old } K_d \times (\text{new SR} / \text{old SR})$
Acceleration Feedforward - $K_{aff}$	$\text{new } K_{aff} = (\text{new SR} / \text{old SR})^2 \times \text{old } K_{aff}$
Velocity Feedforward - $K_{vff}$	$\text{new } K_{vff} = (\text{new SR} / \text{old SR}) \times \text{old } K_{vff}$
Friction Feedforward - $K_{fff}$	None
Position Feedforward - $K_{pff}$	None

### 6.5 Accurate Measurement of Contact Forces and Moments

The maximum tangential, and normal forces at the contact patch of the VT Roller Rig are calculated based on the scale factor of 1/4<sup>th</sup> (1/6<sup>th</sup> for loads), and 300,000lbs weight of railcar taken by four wheelsets in a typical railcar. These forces are tabulated in Table 6.13. Figure 6.43 shows how these contact creep forces are reacted at the positioning systems. Considering the forces in Table 6.13 and the position of dynamometers, the reaction moments taken by the transducers are calculated.

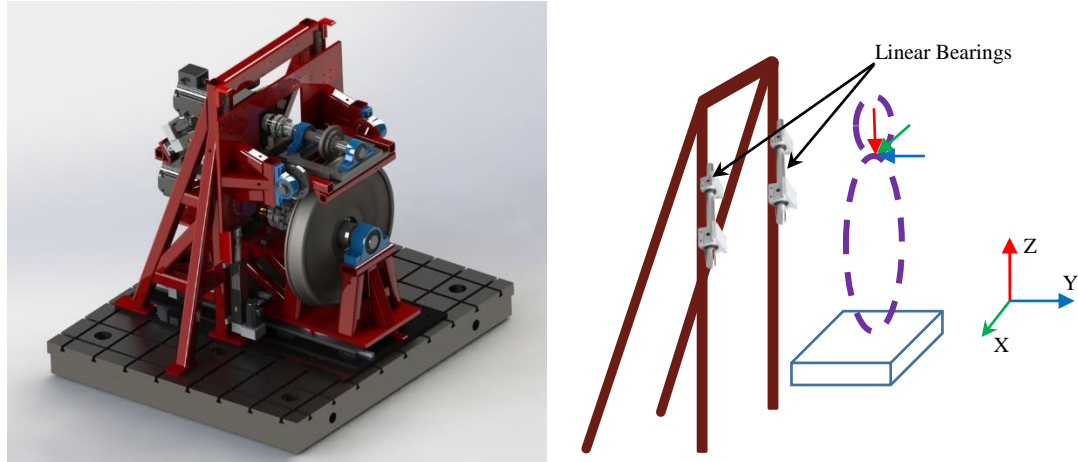


Figure 6.43. Contact creep forces are reacted by the positioning system.

Table 6.13. Maximum estimated creep forces at the contact patch.

Longitudinal ( $F_x$ )	Lateral ( $F_y$ )	Vertical ( $F_z$ )
$\pm 4265N$	$\pm 4265N$	$-10664N$

As discussed in powertrain chapter, a direct driveline is selected to rotate the wheel and roller via two independent motors, without any flexible joints. This causes a contact force shunt through the driveshaft connected to the wheel. In other words, the load path of the contact forces to ground is not solely through the wheel bearings (Figure 6.44). This can affect the load cell readings using only one force measurement system under the wheel. The loading component that passes through the driveline needs to be measured and compensated in the sensor readings for obtaining accurate contact forces. To this end, a secondary force platform is implemented under the motor. Figure 6.45 shows both force platforms (dynamometers) installed under the wheel driveline.

If there are any other elements such as shear loading that passes through the driveline, the motor dynamometer will be able to resolve them from the readings. The motor platform measures the motor torque in addition to the force shunt components. Assuming the motor is mounted exactly between left and right sensors, the motor torque can be resolved to the left and right sensors as a force couple. Therefore, it can be subtracted from the sensor readings, and it would be possible to resolve all force shunt components of the driveline from the motor dynamometer's readings.

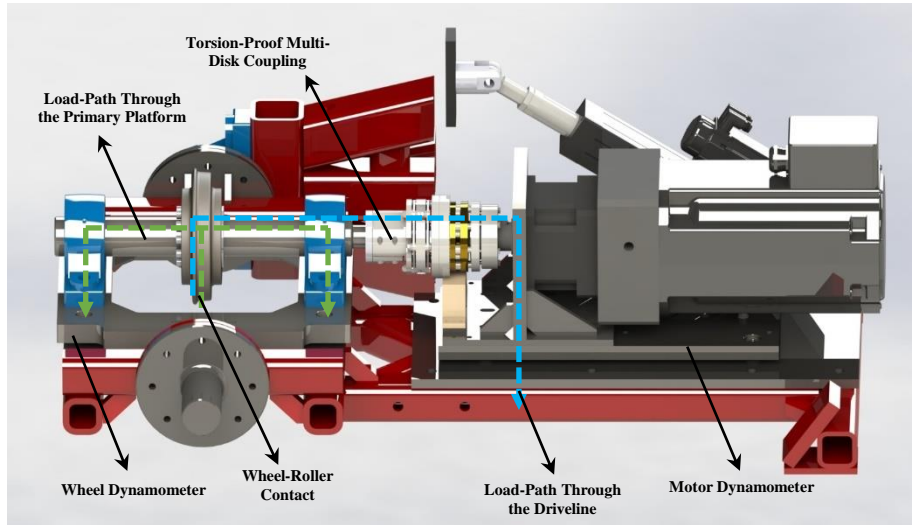


Figure 6.44: The path for the contact forces to the ground includes two routes: one through the wheel bearings, and the other one through the motor mounting plate (force shunt).

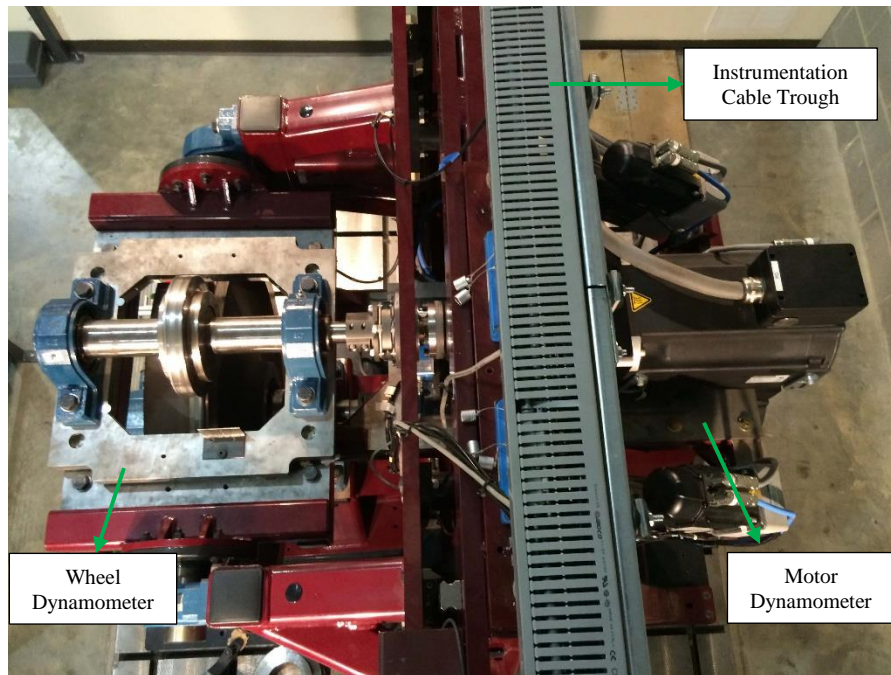


Figure 6.45: Top view of the Rig showing wheel and motor dynamometers installed under the wheel driveline.

Two specially designed dynamometers are used to measure the contact forces and moments. The dynamometers are embedded in the load-path of the contact forces from the wheel-roller interface to the ground. The positions of the dynamometers are selected such that they minimize the reaction moments of the contact forces, and simplify resolving the contact forces from the sensor readings. Each dynamometer is comprised of four triaxial piezoelectric load cells (Kistler, Amherst, NY) preloaded between two plates. The four triaxial sensors are aligned and installed on the base plate. The cover plate and pretensioning set are then installed to preload the sensors. Figure 6.46 shows

the motor (left) and wheel (right) dynamometers. Figure 6.47 illustrates the arrangement of loadcells in each dynamometer.



Figure 6.46. Contact force measurement dynamometers consist of four triaxial sensors preloaded between two plates (left: motor, right: wheel).

Each triaxial loadcell<sup>7</sup> is capable of conducting dynamic and quasi-static measurements. The preloading of the sensors between the base and cover plates would ensure that tensile forces are measured as a relief of the preloaded sensor, shear forces are transmitted between sensor and plates, and micro-gaps are closed ensuring high rigidity and a wide frequency range. Each triaxial loadcell is a quartz force sensor that works based on the piezoelectric principle. The generated electrostatic charges are picked up by built-in electrodes and transferred to the corresponding connector. Table 6.14 summarizes the technical specification of triaxial loadcells.

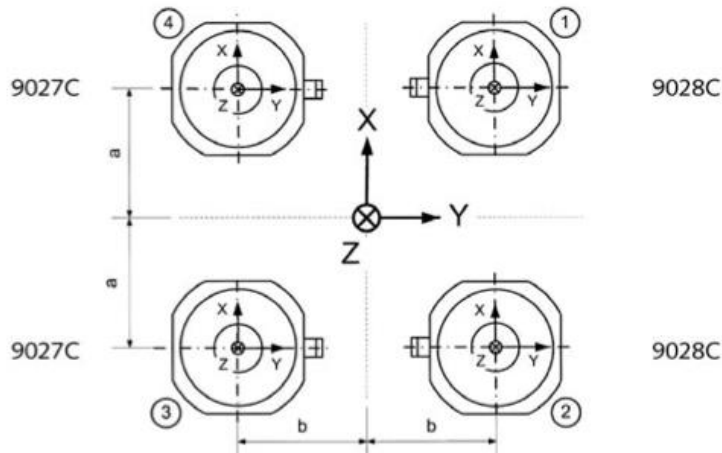


Figure 6.47. Arrangement of loadcells in each dynamometer (courtesy of Kistler Holding AG) [102].

<sup>7</sup> Type 9027C and 9028C

**Table 6.14. Technical specification of piezoelectric triaxial loadcells [102].**

Range	$F_x, F_y$	kN	-4 ... 4
	$F_z$	kN	-8 ... 8
Sensitivity	$F_x, F_y$	pC/N	$\approx -7.8$
	$F_z$	pC/N	$\approx -3.8$
Overload	$F_x, F_y$	kN	-5/5
	$F_z$	kN	-10/10
Linearity, each axis		%FSO	$\leq \pm 0.25$
Hysteresis, each axis		%FSO	$\leq 0.25$
Crosstalk	$F_z \rightarrow F_x, F_y$	%	$\leq \pm 0.5$
	$F_x \leftrightarrow F_y$	%	$\leq \pm 2$
	$F_x, F_y \rightarrow F_z$	%	$\leq \pm 2$

The electrostatic measurement signals of the four sensors in each dynamometer can be summated via a summing box<sup>8</sup> (Kistler, Amherst, NY) to reduce the number of outputs from 12 to 8. The summated signal corresponds to the total algebraic charge of the individual sensors. The summing box provides the following summated and individual outputs:

- $F_{x1+x2}$
- $F_{x3+x4}$
- $F_{y1+y4}$
- $F_{y3+y4}$
- $F_{z1}$
- $F_{z2}$
- $F_{z3}$
- $F_{z4}$

---

<sup>8</sup> Type 5417

The eight outputs from each summing box are conditioned and amplified by a multichannel charge amplifier<sup>9</sup> (Kistler, Amherst, NY). The charge amplifier converts the eight measuring electrostatic signals into the following fourteen  $\pm 10\text{VDC}$  signals [144]:

- $F_{x1+x2}$
- $F_{x3+x4}$
- $F_{y1+y4}$
- $F_{y3+y4}$
- $F_{z1}$
- $F_{z2}$
- $F_{z3}$
- $F_{z4}$
- $Sum F_x$
- $Sum F_y$
- $Sum F_z$
- $M_x$
- $M_y$
- $M_z$

The output signals of the charge amplifier are put into the SynqNet MIXEDMODULE data acquisition units. Figure 6.54, Figure 6.51, and Figure 6.48 show the accumulative baseline error of both dynamometers in X, Y, and Z directions with no motion and the wheel drive disabled. The measurements are taken when the wheel and roller are not in contact, i.e. zero dynamic force in the three directions. The error in these figures can be attributed to the imperfections in the sensors, summing boxes, charge amplifiers, data acquisitions units, and cables.

Figure 6.55, Figure 6.52, and Figure 6.49 show the baseline error when the wheel is rotating at  $91.553\text{rpm}$ , not in contact with the roller. The added error can be contributed to the vibrations of the motor. To find the force measurement accuracy of the dynamometers, the force histograms with probability normalization are plotted in Figure 6.56, Figure 6.53 and Figure 6.50. The force measurement accuracy of the VT Roller Rig in the X, Y, and Z directions with 90% probability band are found 13.59N, 11.48N and 10.57N, respectively. Table 6.15 summarizes these results.

**Table 6.15. Force measurement accuracy of the VT Roller Rig in three directions.**

Direction	Standard deviation ( $\sigma$ ) of the baseline error with no motion and drive disabled	Standard deviation ( $\sigma$ ) of the baseline error on the move (motor contribution)	90 <sup>th</sup> percentile baseline error in motion
X	1.003N	13.923N (92.80%)	13.59N
Y	1.046N	11.342N (90.78%)	11.48N
Z	2.036N	8.801N (76.87%)	10.57N

<sup>9</sup> Type 5070A

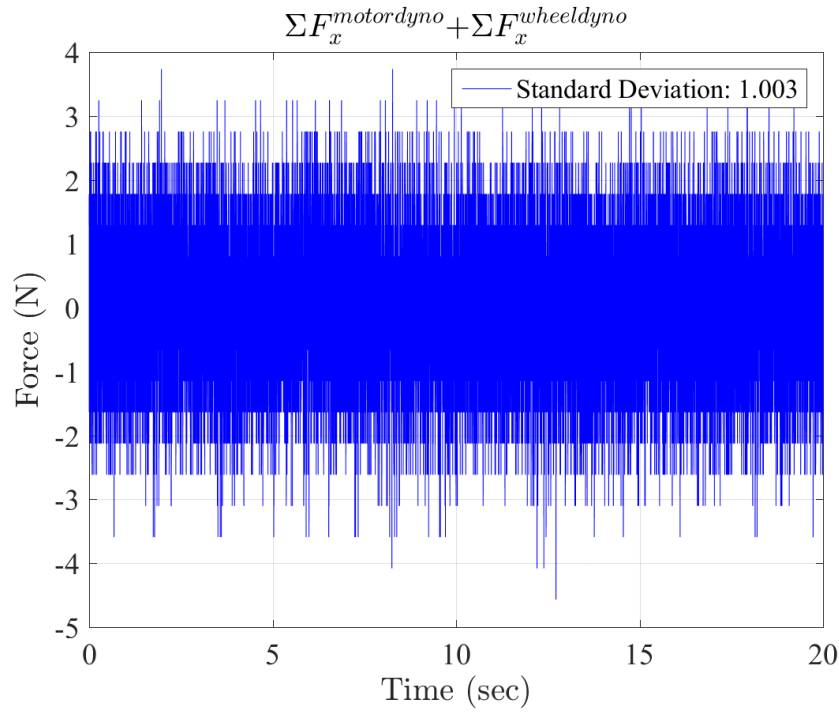


Figure 6.48. Accumulative baseline error of both dynamometers in X direction with no motion and wheel drive disabled ( $\Sigma F_x^{motor\ dyno} + \Sigma F_x^{wheel\ dyno}$ ).

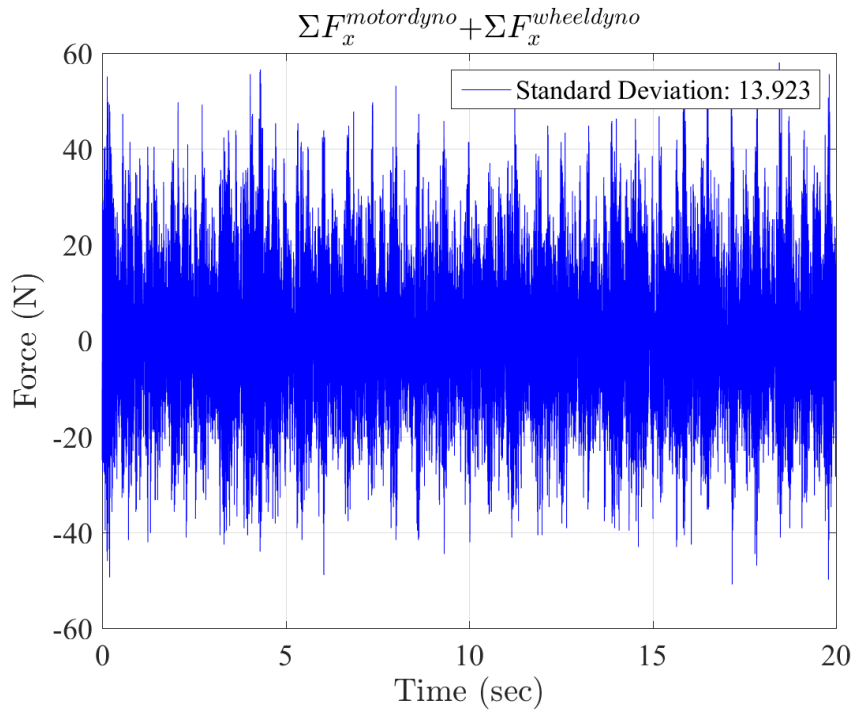
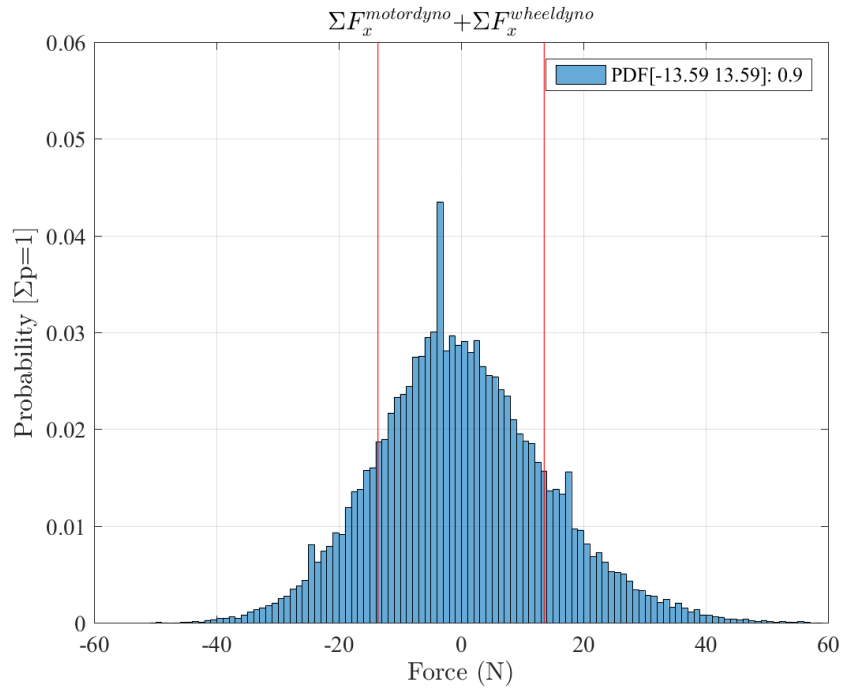
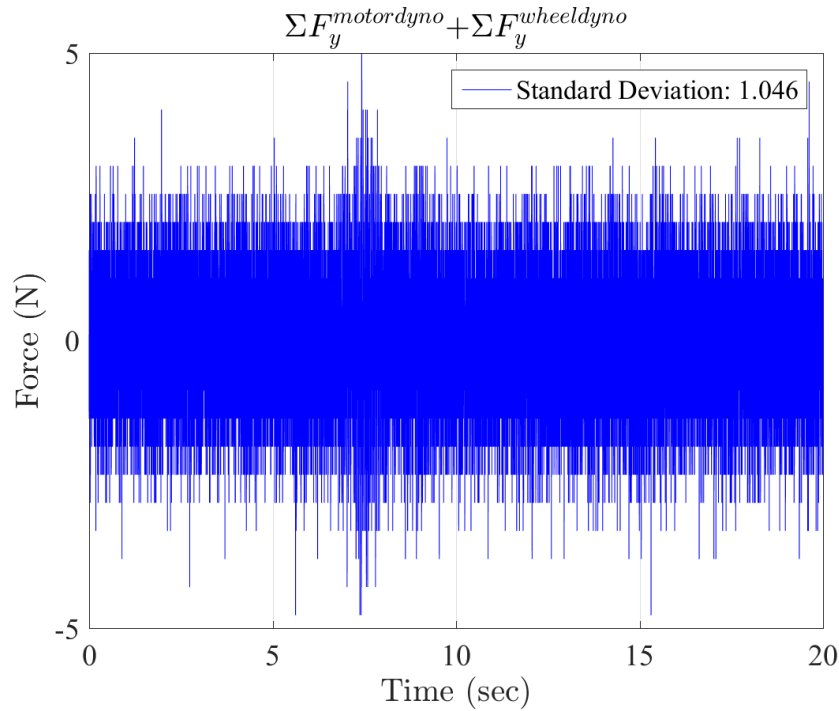


Figure 6.49. Accumulative baseline error of both dynamometers in X direction at 91.553rpm ( $\Sigma F_x^{motor\ dyno} + \Sigma F_x^{wheel\ dyno}$ ).



**Figure 6.50. Force measurement accuracy of both dynamometers in X direction at 91.553rpm with 90% probability band ( $\Sigma F_x^{motor\ dyno} + \Sigma F_x^{wheel\ dyno}$ ): 13.59N.**



**Figure 6.51. Accumulative baseline error of both dynamometers in Y direction with no motion and wheel drive disabled ( $\Sigma F_y^{motor\ dyno} + \Sigma F_y^{wheel\ dyno}$ ).**

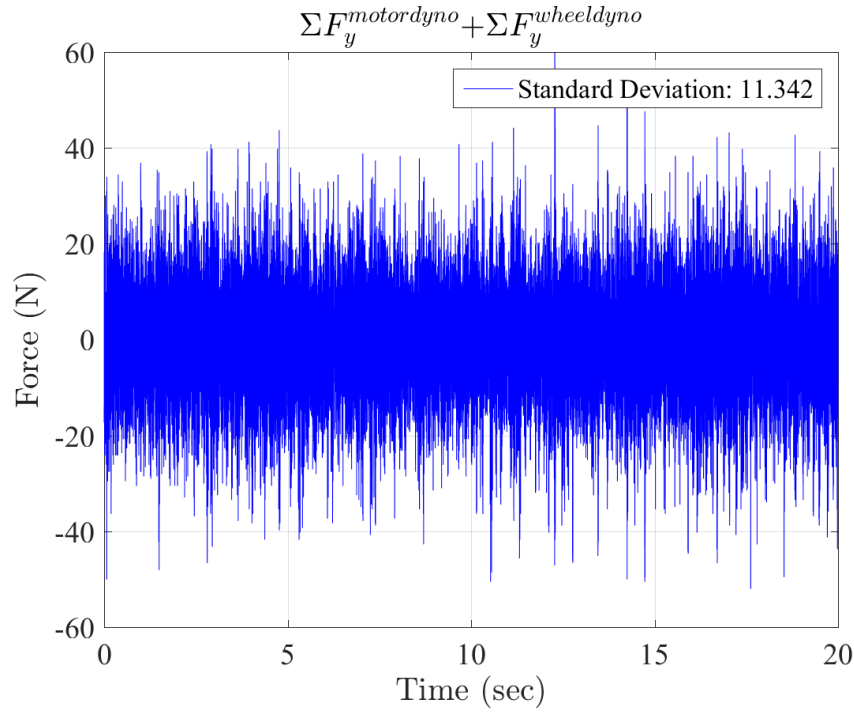


Figure 6.52. Accumulative baseline error of both dynamometers in Y direction at 91.553rpm ( $\Sigma F_y^{motor dno} + \Sigma F_y^{wheel dno}$ ).

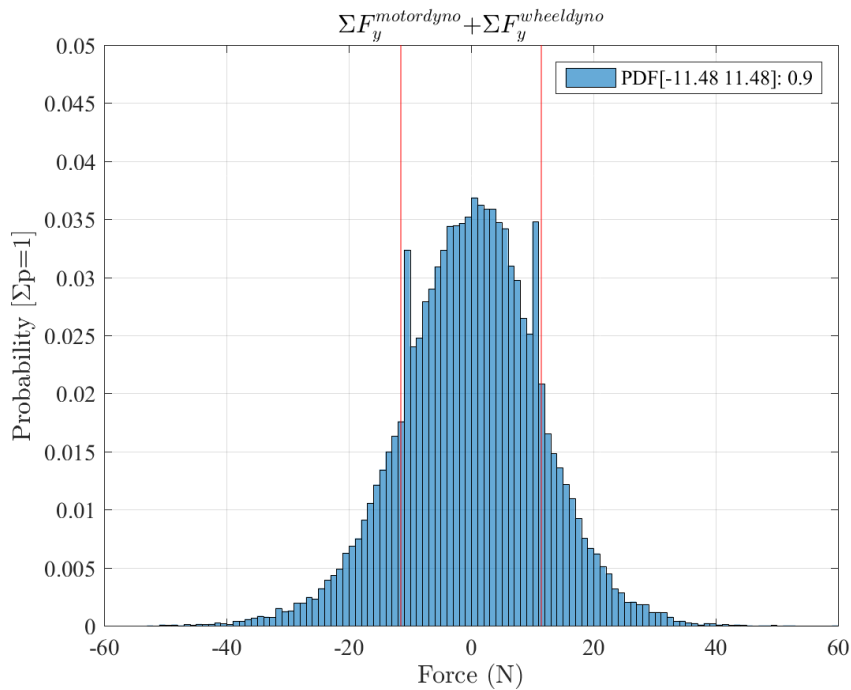


Figure 6.53. Force measurement accuracy of both dynamometers in Y direction at 91.553rpm with 90% probability band ( $\Sigma F_y^{motor dno} + \Sigma F_y^{wheel dno}$ ): 11.48N.

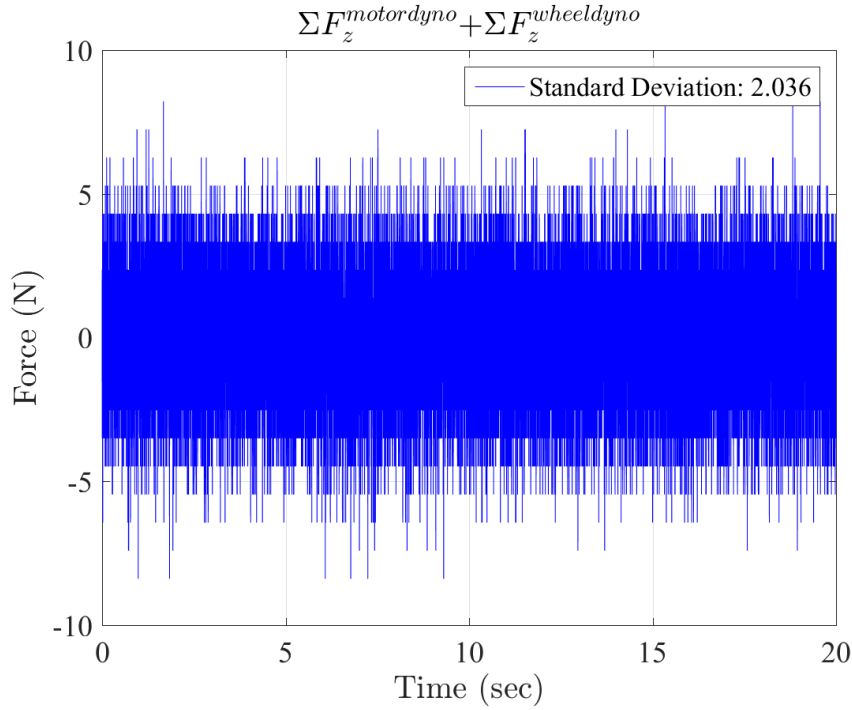


Figure 6.54. Accumulative baseline error of both dynamometers in Z direction with no motion and wheel drive disabled ( $\Sigma F_z^{motor\ dyno} + \Sigma F_z^{wheel\ dyno}$ ).

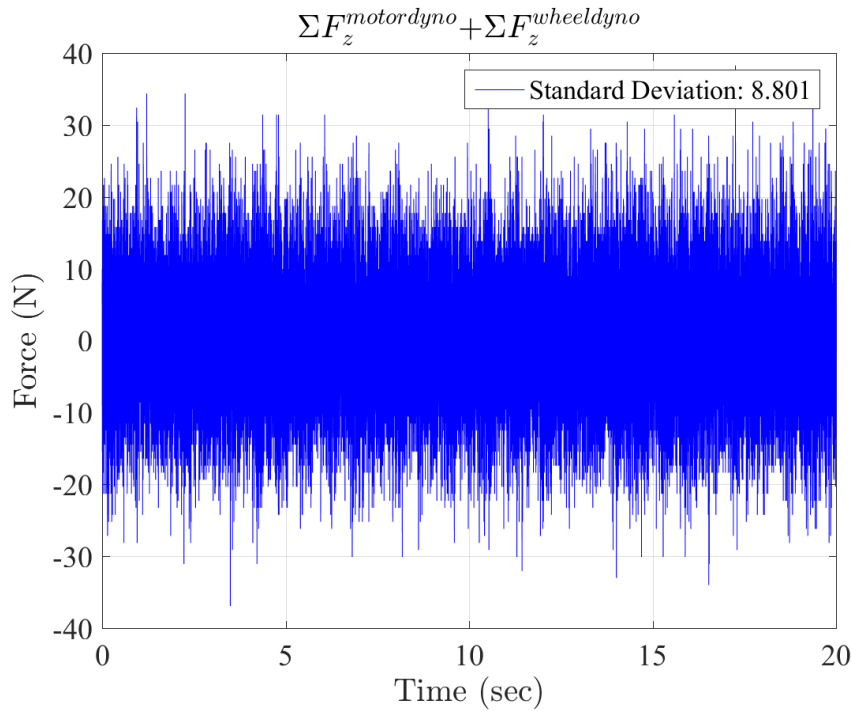
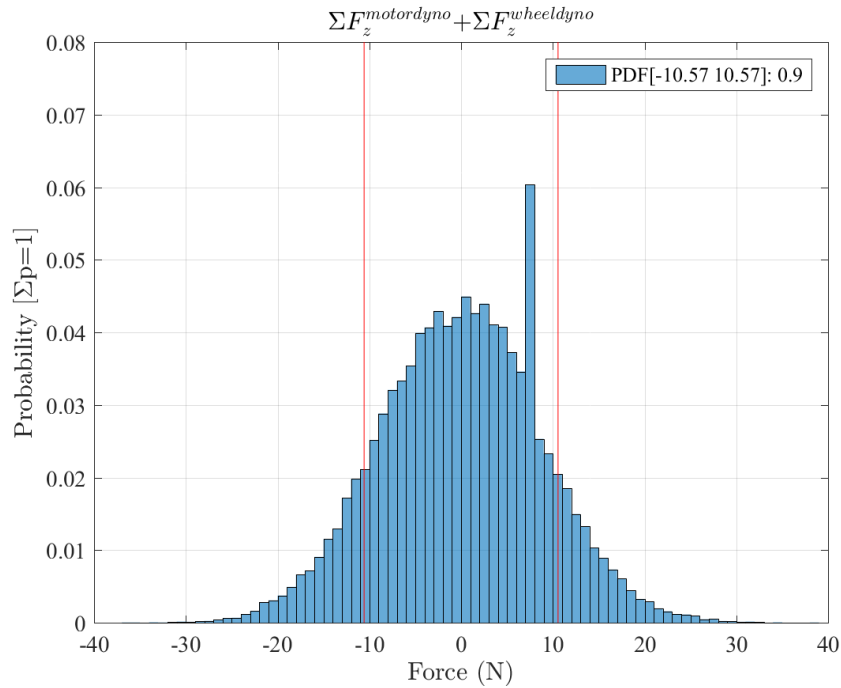


Figure 6.55. Accumulative baseline error of both dynamometers in Z direction at 91.553rpm ( $\Sigma F_z^{motor\ dyno} + \Sigma F_z^{wheel\ dyno}$ ).



**Figure 6.56. Force measurement accuracy of both dynamometers in Z direction at 91.553rpm with 90% probability band ( $\Sigma F_z^{motor\ dyno} + \Sigma F_z^{wheel\ dyno}$ ): 10.57N.**

## 6.6 Accurate Torque Measurement

A flange torque sensor is embedded in each driveline to measure the instantaneous torque between the rotating bodies and the motor. Each sensor is comprised of two parts: a measurement flange, and an evaluation unit (Figure 6.57). KiTorq<sup>10</sup> measuring unit (Kistler, Amherst, NY) is used in both drivelines. It measures the torque using strain gauges. The measuring range for the wheel and roller drivelines are 1000Nm and 5000Nm, respectively. The measurement specifications of the KiTorq units are summarized in Table 6.16.

A KiTorq<sup>11</sup> stator torque evaluation unit (Kistler, Amherst, NY) inductively samples the measurements picked up by the strain gages inside the measurement unit at 35kS/sec. It conditions and amplifies the analog and digital output signals while powering the measuring unit. The evaluation unit is equipped with an integrated speed-measuring encoder and provides both torque and speed measurements. It provides the same outputs on different digital interfaces. This makes it possible, for instance, to use the output for measuring the torque with a different low-pass filter

<sup>10</sup> Type 4550A

<sup>11</sup> Type 4542A

than a second torque output used for control purposes. It also allows converting speed into a voltage signal.

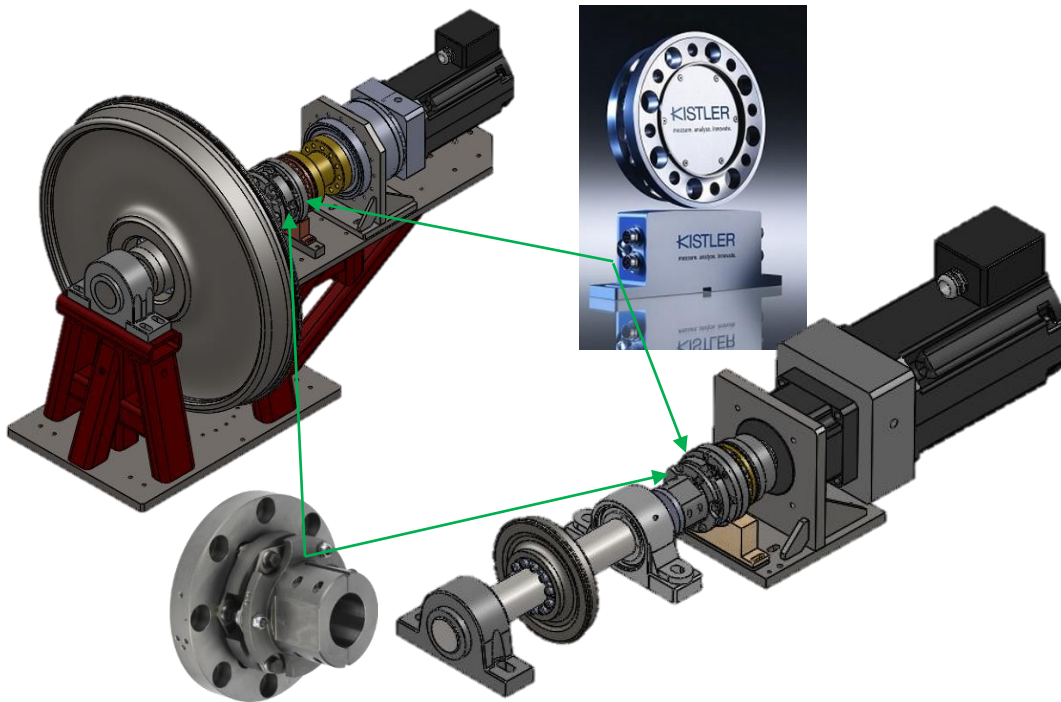


Figure 6.57. KiTorq measuring system comprising a KiTorq measuring flange and a KiTorq stator evaluation unit. Each torque flange is connected to the shaft via a torsion-proof multi-disk coupling [145,146].

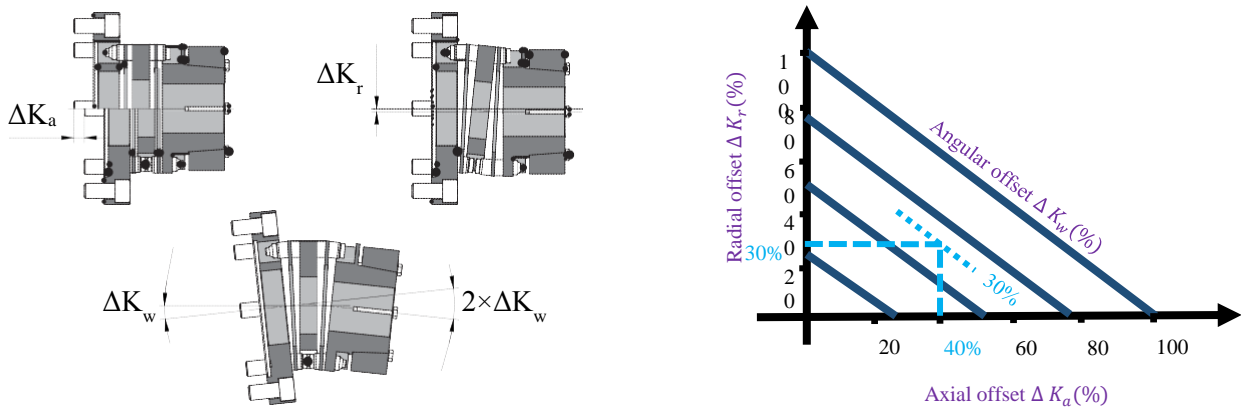
Table 6.16. Measurement specification of the Roller Rig torque measuring system (Including a KiTorq-4550A measuring unit and a KiTorq-4542A evaluation unit) [103,145].

Accuracy class	0.05
Linearity (% FSO)	0.03
Hysteresis (% FSO)	0.03
Limit Frequency -3 dB (kHz)	10
Scanning rate (kS/Sec)	35
Speed resolution (pulse/rev)	60
Speed pulse level	Active TTL
Jitter – Oscillation Period (%)	2
Temperature influence on the zero point TK0 (% FSO/10k)	0.05
Temperature influence on the nominal value TKC (% FSO/10k)	0.05

Each flange is connected to the driveline via torsion-proof multi-disk couplings (Kistler, Amherst, NY). These particular couplers allow for minor misalignments when incorporating the measuring flange into the shaft assembly. Table 6.17 shows the permissible shaft misalignments in the wheel and roller torque flange couplings. These multi-disc couplings use a two-disc assembly to compensate for angular, axial, and radial shaft offsets. If multiple offsets occur simultaneously, they influence one another. The permissible values for displacement, therefore, depend on each other. The sum of the actual displacements, in percent of the maximum values, may not exceed 100%. Figure 6.58 illustrates the shaft misalignments and the chart for calculating the maximum value for the third misalignment if two are known. The blue dashed line depicts an example where the axial offset is 0.16mm that corresponds to 40% of permissible value in the wheel driveline. With an angle offset of 0.06deg, the maximum permissible radial offset will be 30% or 0.03mm.

**Table 6.17. Permitted misalignments in the wheel and roller multi-disk couplings.**

Offset Type	Wheel	Roller
Permitted axial offset $\Delta K_a$ (mm)	0.4	0.5
Permitted radial offset $\Delta K_r$ (mm)	0.1	0.1
Permitted angle offset $\Delta K_w$ (deg)	0.2	0.2



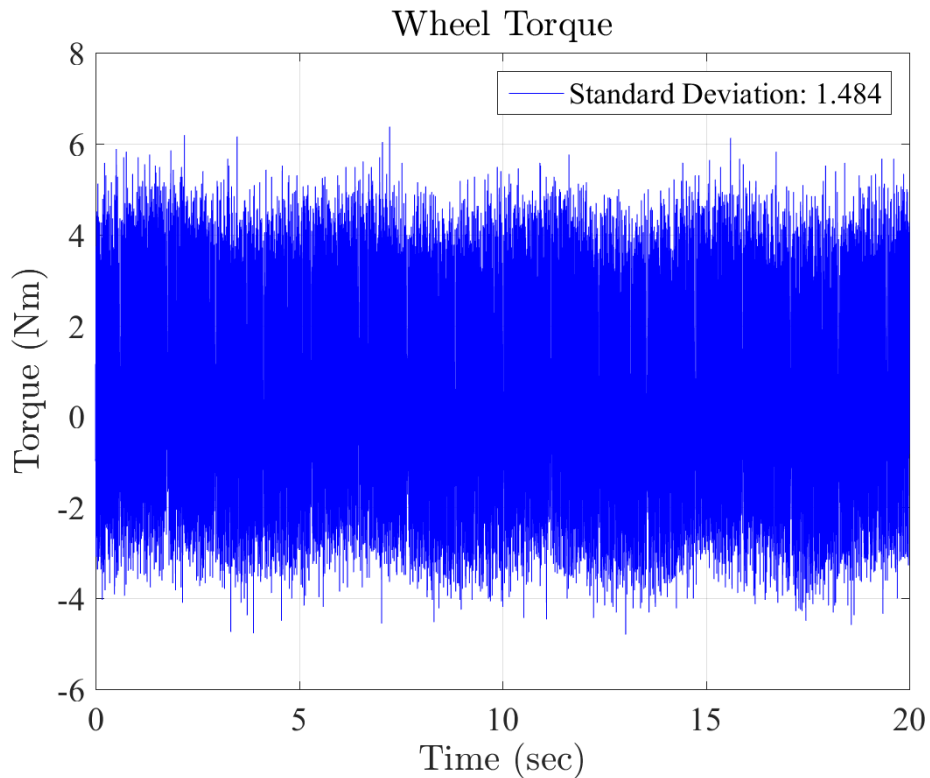
**Figure 6.58. Permissible shaft misalignments in the wheel and roller drivelines (courtesy of Kistler Holding AG) [146].**

Figure 6.59 and Figure 6.60 show two examples of wheel and roller torque measurements with no motion and drives disabled. Since there is no motion, the motors cannot have any contribution to the noise shown in these two figures. These baseline noises are attributed to the sensor and calculations unit, or the noise picked up by Kistler cables between the summing boxes and charge amplifiers. Figure 6.61 and Figure 6.63 show the same measurements in motion. The difference

between the two measurement sets can be attributed to the motor vibrations. Similar to the analysis for velocity control accuracy, the torque measurement accuracy of the VT Roller Rig for the wheel and roller axes in motion using 90% probability band are found 4.94Nm and 6.10Nm, respectively. Figure 6.62 and Figure 6.64 show these probability band measurements. Table 6.18 summarizes these results.

**Table 6.18. Torque measurement accuracy of the VT Roller Rig for the wheel and roller axes.**

Axis	Standard deviation ( $\sigma$ ) with no motion and drives disabled	Standard deviation ( $\sigma$ ) at constant speed (motor contribution)	90 <sup>th</sup> percentile at constant speed
Wheel	1.484Nm	3.874Nm (61.69%)	4.94Nm
Roller	7.908Nm	7.951Nm (0.54%)	6.10Nm



**Figure 6.59. An example of torque measurements in the wheel axis of the VT Roller Rig (no motion and drive disabled).**

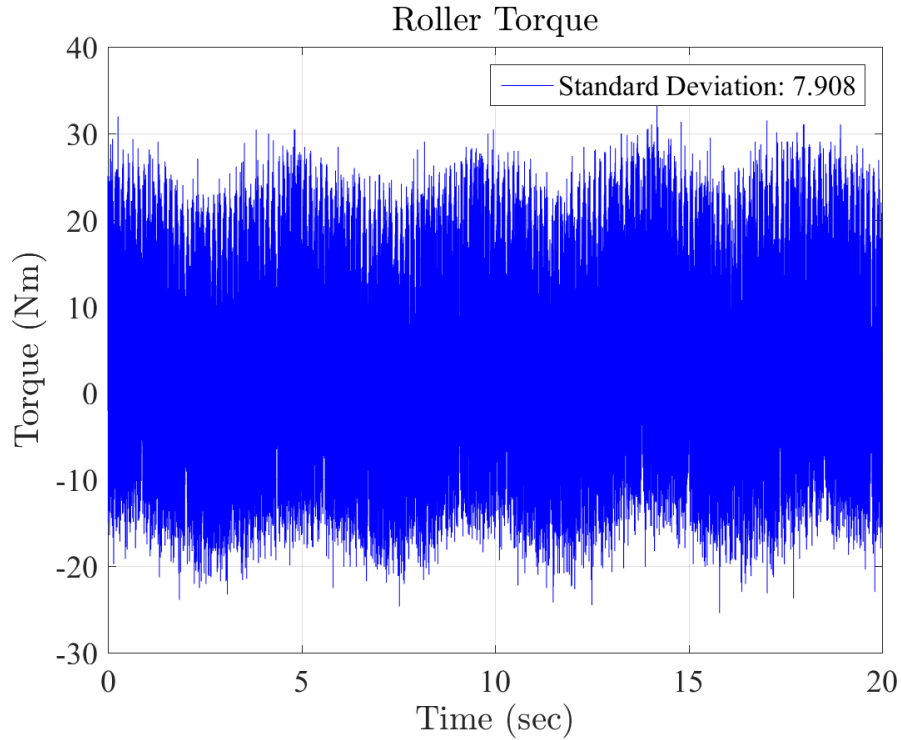


Figure 6.60. An example of torque measurements in the roller axis of the VT Roller Rig (no motion and drive disabled).

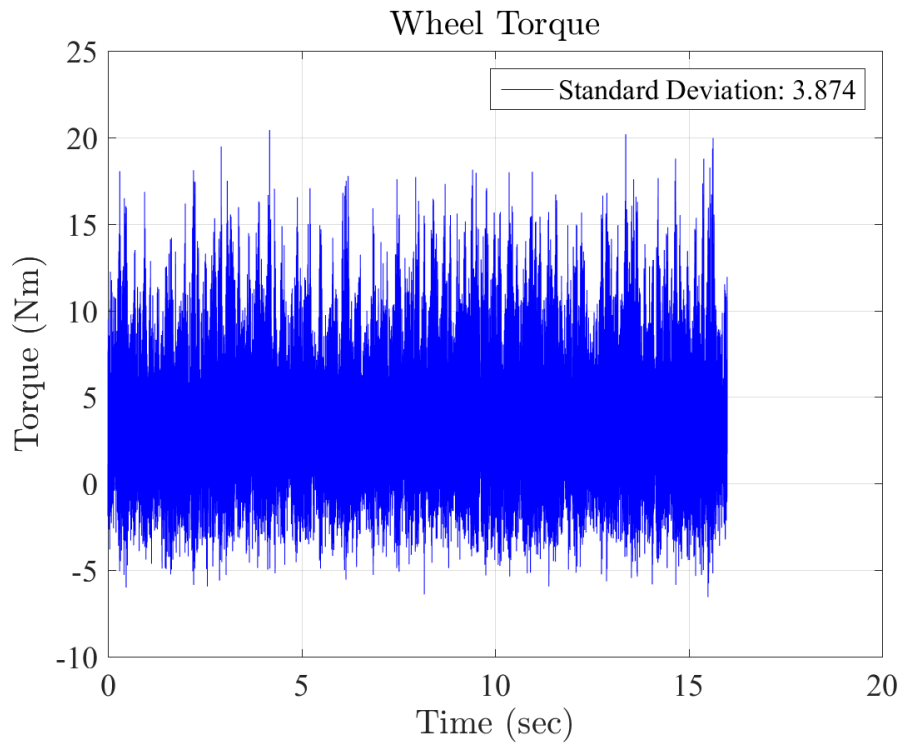


Figure 6.61. Wheel torque measurement in the VT Roller Rig at 91.553rpm constant speed.

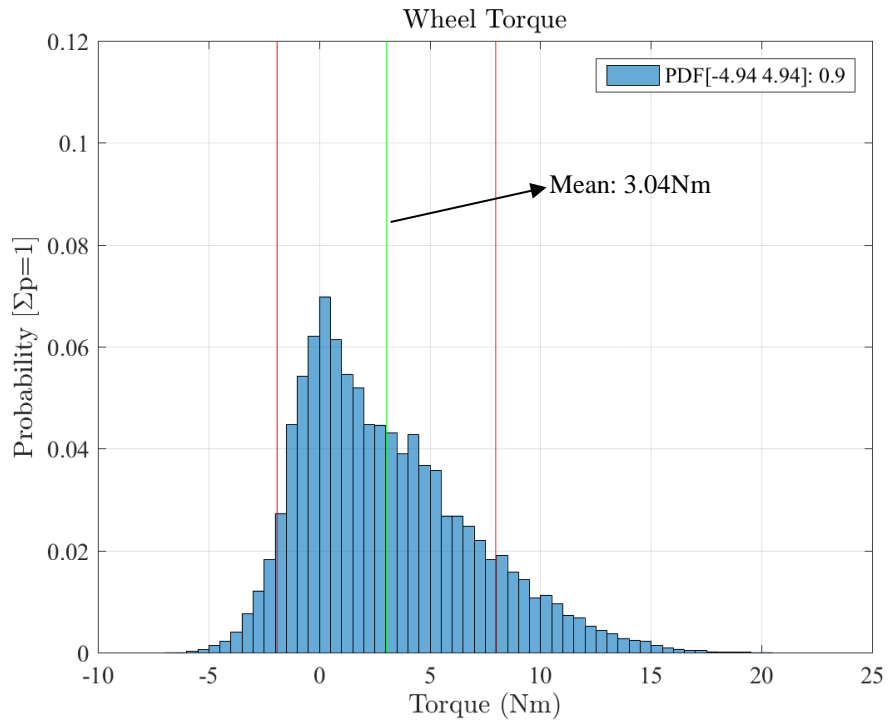


Figure 6.62. Torque measurement accuracy of the VT Roller Rig for the wheel axis at 91.553rpm with 90% probability band: 4.94Nm.

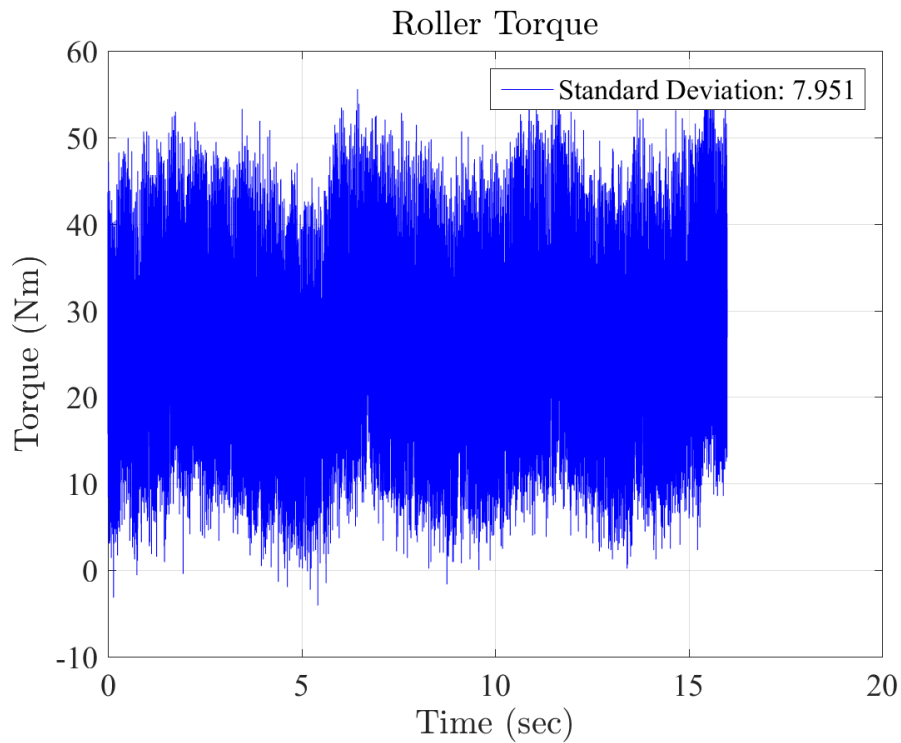
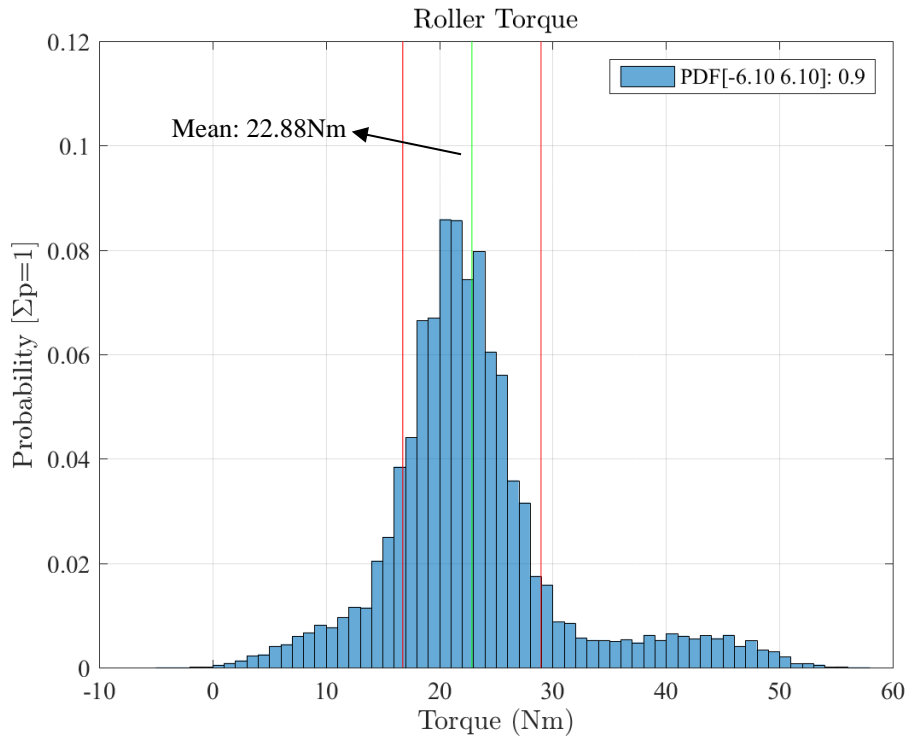


Figure 6.63. Roller torque measurement in the VT Roller Rig at 91.553rpm constant speed.



**Figure 6.64.** Torque measurement accuracy of the VT Roller Rig for the roller axis at *51.090rpm* with 90% probability band: *6.10Nm*.

### 6.7 Unified Operating User Interface for Non-Electrically Certified Personnel

The powering scheme of the Rig provides 150kVA power for the 200A load of the Rig at 480VAC 3-phase. It guarantees the least susceptibility to electromagnetic noise and assures safe operation for the Rig and the personnel based on IEC and ISO standards. A control tower, shown in Figure 6.65, is configured for providing a unified user interface for control, safety, and power systems. It facilitates the cable management.

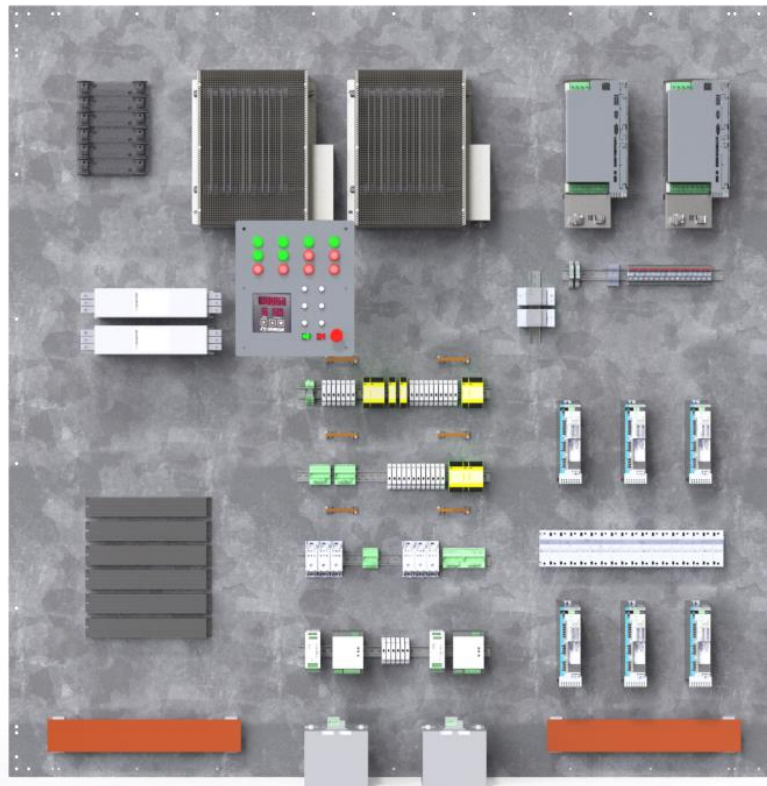


**Figure 6.65. The control tower of the Rig includes S772 drives, AKD drives, regenerative and dynamic brake resistors, safety/control circuits, etc. All the components are placed inside a Faraday cage and are controlled through operator interface panel.**

To have the best isolation between the control cabinet including the digital drives, and the Rig, a dedicated electronics room, right next to the mechanical setup, is devoted to accommodating the control cabinet and all the safety, and powering elements. The room is equipped with an industrial cooling system for controlling the temperature and humidity of the electronics room.

All power electronics, safety circuits, and motion control systems of the VT Roller Rig are enclosed within a control panel inside the electronics room. This enclosure serves different purposes:

Various high voltage and high amperage lines feed the power electronics. Any unintentional, unsupervised exposure to these hotlines can have maximum lethality risk for the users. Although various safety, short circuit, and grounding apparatus are developed for this Rig, it is desired to minimize the exposure of unnecessary personnel and users to electrically risky components. This control cabinet serves as a barrier between the users and the high voltage power electronics inside it. A unified user interface is installed on the door of this enclosure. During normal operations, users have no need to open the door of the control cabinet to change a parameter, reset a circuit, or diagnose an issue. This interface provides enough access to all circuits described in Chapter 5 of

this document, that only authorized personnel could be allowed to open the control cabinet. In case that control cabinet needs to be opened, certain procedures should be followed for ensuring the safety of the user and machinery.

As discussed in Section 4.4 of this document, VT Roller Rig power electronics are not only victims of EMI, but also generate a broad range of electromagnetic noise at high amplitude. Shielding and grounding the other victims, especially data acquisition systems, helps to reduce the effect of these waves on their performance. However, a Faraday Cage for the sources of electromagnetic noise can significantly reduce the leaking waves by attenuating the interference. Extensive discussion on the material, thickness, and geometry of proper shielding enclosure was given in Section 4.4, and the results of that study will be used for both EMI victims and sources. This cabinet, like the enclosure of most important electromagnetic noise sources, plays a major role in noise suppression and signal to noise ratio improvement.

Numerous subsystems are working to run the VT Roller Rig properly. They include the power network, power filters, safety circuits, motion control system, and many more electromechanical components. Each one of these subsystems includes quite a few components. An important task in the development of the VT Roller Rig was arranging, mounting, and wiring these components. Altogether more than 350 pieces of cable (3200ft) and 600 shield grounding wires needed to be properly routed and secured for driving the circuits. Cables vary from AWG3/0 to AWG16. Even the bend radii of these cables vary drastically from each other. The total mass of the electronics exceeds 150kg, which have to be safely mounted on a structure. This cabinet not only serves as a safe structure for mounting and holding these components, but also allows for easily planning for the cable-runs and cable ducts.

Each electrically driven system has some power loss through heat loss. When power ranges go up to 150kVA, heat dissipation can lead to significant temperature rise in the environment. This increased temperature is both inconvenient for the users of the VT Roller Rig and also affects the performance of the components. Heat transfer analysis and computational fluid dynamics showed that this much heat dissipation can increase the temperature to above 140°C, not permissible by any of the component manufacturers. On the other hand spreading the components away from each other is not possible, first because the cable lengths are limited, and second due to the space limitation inside the electronics room. IEC has certain regulations for the minimum distance around the high voltage electrical equipments, and that limits how big the control cabinet can be. This cabinet serves as a base for mounting auxiliary cooling systems and temperature monitoring

apparatus for maintaining the environment temperature within the permissible range by the manufacturers.

The control cabinet structure is made of  $2 \times 2 \times 1/8$  L brackets welded together. The back plates are 14GA G90 galvanized steel that assures proper grounding of the electronics housings. The side plates and doors are made of 16GA steel sheets with 1/4 inch holes at 3/8 inch centers. The plates are powder coated with a  $4 \times 4$  inch area masked for properly sized grounding cable.



**Figure 6.66. CAD model of the VT Roller Rig control cabinet.**

For more safety of the users, easier cable management, and better thermal management of the control cabinet, a dedicated electronics room, right next to the mechanical setup is devoted for accommodating the control panel, and all the safety and powering components. The room is equipped with an industrial roof fan ventilating the air.



Figure 6.67. Rear view of the VT Roller Rig control cabinet.

## 6.8 Hardware-In-The-Loop Testing Infrastructure

The VT Roller rig provides the required infrastructure for performing hardware-in-the-loop testing for validation of complex railcar dynamics models, traction/braking controllers, and derailment prevention measures in real-time. This study will also include the tasks associated with developing the software tools for connecting commonly used simulation environments to the VT Roller Rig motion control architecture that can be used for future studies that FRA and railroad industry wishes to carry out. A research proposal for HIL testing using the VT Roller Rig is currently submitted to the Federal Railway Administration. It is fully recognized that the studies proposed here do not encompass the complete domain of studies that can be performed on the Rig. Other studies are expected to materialize after the initial studies included here, based on the FRA and industry's needs. Such studies will form follow-up efforts that can be included in future proposals.

Hardware-in-the-loop testing is a real-time experiment for validating models of complex physical systems. It is a well-known procedure in other fields such as automotive and aerospace [147] It is ideal for the design and test of complex equipment such as traction and braking systems, active steering controllers, and active tilting algorithms. Much of the test environment is replaced with mathematical models. For unknown complex physics, such as contact mechanics, the system is replaced with a controlled test setup. HIL allows for comparing the performance of models against actual measurement in real-time to calibrate parameters, find singularities in models, and develop smarter models. HIL has significant benefits in measuring the performance of controllers. HIL testing shows how the controller responds, in real-time, to realistic virtual stimuli. Without HIL, validation of controllers involves using the actual complex system in the field. Using precise test setups, HIL testing offers benefits in cost and practicality.

There are several areas in which HIL testing offers safety and cost saving over field testing. HIL testing is significantly safer when it comes to testing hazardous conditions. Design changes are considerably less expensive using HIL. Finding problems before field implementation includes these benefits:

- Testing and diagnostics are less expensive
- Controlled laboratory environment minimizes the safety risks
- Design changes are more likely to be approved

Regarding scheduling, HIL testing is less expensive and more practical than field testing because it can be set up to run on its own. Benefiting from the safety systems embedded in the VT Roller Rig, the HIL can be adjusted to improve itself iteratively. HIL testing is the most reliable means for testing a dynamic system's response to unusual events. For example, it is possible to model extreme weather conditions like earthquakes and blizzards, or abnormal working conditions due to damaged components caused by natural causes or terrorism. The laboratory setting will provide for precise measurements of the software and hardware performance in real-time, thereby enabling us to achieve the earlier-stated goals of the study.

The work will be performed by the Virginia Polytechnic Institute and State University (VT) that is in the final stages of commissioning a new wheel/rail test Rig to enhance the government's capability to study wheel/rail contact interaction. The Rig also provides experimental tools to the government to study the effects of the various wheel and rail profiles on wheelset and truck performance, and the elements that can cause a derailment.

To meet the objectives of HIL research program, the work that is proposed here will continue the efforts that are underway at VT. Specifically, VT needs to perform the following tasks during this project:

**HIL Workflow:** VT can provide a hardware-in-the-loop workflow that combines new numerical solvers and software tools with Rig's digital communications, data acquisition, instrumentation and motion control. It describes how the Rig will be utilized to simplify development and design processes for complex systems as well as their testing and validation.

**Developing Modeling Libraries:** VT can develop libraries in MATLAB and a common programming language like C or C++ for connecting complex dynamic models to the motion control of the Roller Rig. The modeling libraries are important because they will provide the basis for interfacing existing third-party software with existing hardware at the Virginia Tech. Once developed, these libraries can be used as elements of future HIL tests that the government or railroad industry wish to perform.

**Assessing HIL Areas of Research:** VT can prepare a white paper on the key opportunities for HIL testing of ongoing researches in railroad systems and controllers that are compatible with the tools developed in 0. One key area of research is how to achieve numerical solutions of existing wheel/rail contact models at sufficient speed for real-time applications. Other possible topics of research are:

- Real-time software for rail vehicle dynamics
- Real-time testing in conjunction with multibody simulation software
- HIL prototyping of complex systems and their components
- Test automation processes based on HIL
- Real-time simulation of rail geometry for better ride comfort
- Communication interfaces between software and hardware products

**HIL Testing:** VT will perform HIL testing in one area of research in 0 based on FRA's feedback using the tools developed in 0. The validity of the models will be checked versus realistic results of the Roller Rig to calibrate the model parameters. Controller's response to desired disturbances will be measured to allow for real-time tuning. If required, closed-loop HIL-tests will be set up to perform reinforced learning on the models or controllers for smarter optimization.

**Verification of HIL Results:** VT will verify the validity of the HIL testing results through running cases that can be crossed check with analytical data or, possibly, field measurements. Any sources

of error will be identified, and steps will be taken to eliminate or reduce errors. Particular attention will be paid to standardizing the developed modeling libraries for future HIL testing on the VT Roller Rig in other areas of research that the FRA or railway industry wish to perform.

## Chapter 7. Identification and Modeling of the Quantization Error in Encoder Equivalent Output

The quantization error in encoder equivalent output is introduced, identified, and modeled for the first time. Methods for filtering the noise are discussed. Encoder equivalent output is widely used in modern industrial drives equipped with tools for improving the encoder resolution. A standard application for this output is electronic gearing for controlling slave amplifiers via the encoder equivalent output of a master drive. If left uncorrected, this noise would report unreal low performance of motion controllers to the user, or lead to unstable motion in electronic gearing applications. A survey of the known noise sources in encoder output classifies this error with respect to the previously known errors. A discussion on the encoder resolution improvement and output emulation sheds light on the mechanism behind quantization error generation in encoder equivalent output. This invention provides a deterministic mathematical estimator for modeling the noise harmonics. Experimental data is provided for identifying this artifact and validating the deterministic noise estimator. Noise characteristic such as speed and update rate dependency are illustrated with both experimental and numerical results. Numerical results show full agreement with the experimental data. The computationally inexpensive estimator allows for adjusting the accuracy of estimations to adapt the model for existing FPGAs on the drives. The model provides the training data for filtering this noise online. Due to simple mapping structure of the model, it can be adapted for all rotary and linear encoders in conjunction with any modern drive that generates encoder equivalent output. The model can be incorporated into a drive firmware for detecting the noise, anti-aliasing the harmonics, and performing one of the various techniques used in telecommunication interference reduction to filter specific frequencies and protect the rest of data. Without this estimator, all frequencies above the first noise harmonic have to be eliminated using a low-pass filter.

## Nomenclature:

PPR [pulse-per-revolution]: physical pulses of an incremental encoder

LPR [line-per-revolution]: quadrature encoded resolution of an incremental encoder

QPL [quadrature-per-line]: resolution improvement factor through quadrature decoding

CPQ [count-per-quadrature]: interpolation factor of the drive

CPR [count-per-revolution]: improved resolution of the encoder

EEO [encoder equivalent output]: encoder emulated output generated by the drive

### 7.1 Description of the Related Art

The terms sampling (discretization) and magnitude quantization (or just quantization) are sometimes used interchangeably. However, they describe two different procedures. In 1948, Bell Laboratories defined quantization of magnitude as the case when it is not permitted to select a continuous range of magnitudes but only certain values [148]. Quantization error is defined when a signal is to be replaced by a wave constructed of quantized magnitudes selected from an available set based on minimum error [148]. An important goal for quantization of magnitudes is to suppress interference in the transmission medium. Using precise receiving electronics, it is possible to restore the transmitted quanta, provided the superposed interference does not exceed half the difference between adjacent quantized magnitudes [148].

Encoders provide position feedback to a control device that performs drive control of a motor. For example, a rotary encoder generates a series of pulses or sine waves in relation to the motion for the drive. Methods for detecting the error in actual encoder output are known. For example, an encoder error detection method is disclosed in US Patent 20140306635A1 [149] if pulses from the rotary encoder are not uniformly generated. The error detection is performed by properly determining the rotational direction and computing the number of counts generated by the encoder. Interpolation techniques for increasing the resolution of encoders are available. Methods for detecting the error in such interpolation techniques are known. For example, the servo mechanism disclosed in US Patent US6037735A [150] proposes a method for controlling the phenomenon of runaway.

Absolute encoders and TTL incremental encoders quantize the motion in magnitude. At each slot, a value is selected from a predefined set to report the position of the disk. For absolute encoders, the set length is equal to the binary (or Gray) numbers that can be generated with the tracks on the encoder disk. A TTL incremental encoder, reports on of the two values high or low.

A sin/cos incremental encoder provides the means for increasing the number of time intervals from the encoder sampling rate to the much faster ADC sampling speed (Section 7.5.1). Digital electronics further quantize the magnitude between the two consecutive slots of the encoder to a much larger set and report the value from that subset based on the electrical phase of the ADC output. This process is often referred to as interpolation (Section 7.5.2). For example, US Patent US4429267A [151] and US Patent US4623831A [152], related to high accuracy servo positioning systems, propose using trigonometric functions for the interpolation. In US Patent US5005089A [153] and US Patent US4954905A [154], related to high-performance disk drives, a position control approach is used. The actual crossover of sine and cosine waves is performed as a coarse measurement. A digital controller carries out a fine interpolation using a look-up table or algorithm based on an arctangent function. The result is the ability to position at higher resolutions than the base resolution of the encoder. Regardless of the approach, faster ADC sampling and interpolation are proven methods for increasing the resolution of the motion measurement.

The effect of sampling rate on the resolution of measurements between the original continuous signal and, a stream of numbers sampled and quantized to a predefined set is known. Quantization and sampling error in such scope can be minimized using a sufficient number of steps using high-speed ADCs and FPGAs. However, digital drives perform a further transformation between the digitized encoder output and the encoder equivalent output. The effect of mapping the encoder measurements from one quantized set to another is unknown to the researchers and industry. This mapping process is of interest in encoder equivalent output generation (Section 7.5.3).

The encoder equivalent output is generated by the drive after applying the interpolation techniques to increase the accuracy of position calculations. Such output is generated via a mapping between two digitized domains that may lead to unreal errors added to the initially errorless position data. This output is either reported to the user as the actual location of the motor shaft or fed into other slave drives for electronic gearing. In the first case, the erroneous output shows an artifact that is not happening in reality. User controller programs that use this signal as feedback to command the drive try to correct this unreal phenomenon, leading to an undesirable performance or unstable motion. If used in electronic gearing, such noise commands the slave drive to generate such erroneous motion in reality. This can lead to low positioning accuracy in the slave drive, although the motion in the master drive is noiseless. Drives can be daisy-chained, and the effect of this noise can be further amplified. Multiple drives can be controlled in master/slave configuration through the encoder equivalent output of the master drive.

## 7.2 Background

An encoder is an optical or magnetic sensor that generates signals in response to the motion. Shaft encoders measure rotation while the linear encoders react to linear movement. Optical sensing provides high resolution, high operating speed, and durability. Magnetic sensing is often used in rugged applications such as steel and paper mills. It provides maximum resistance to dust, moisture, and thermomechanical shock [155].

Optical encoders use a disk or strip with a pattern of lines deposited on it. Light from a LED shines through the lines onto one or more photodetectors, which produce the encoder's output. Based on how encoders report the position within one revolution, they are divided into two categories. *Absolute* encoders return the actual position by a multi-bit digital word. *Incremental* encoders produce a series of pulses as they move. An incremental encoder has one or more tracks on its disk while an absolute encoder has one track for each output bit [156]. An encoder may or may not contain a data track for multi-turn. In a single-turn encoder, the outputs are repeated for every revolution of the encoder's shaft. Multiturn absolute encoders, report unique digital words for each shaft position, usually up to 4096 revolutions or 12 bit [155]. Figure 7.1 shows an incremental encoder disk compared with the one of an absolute encoder.



Figure 7.1. Typical incremental encoder disk (left) and absolute encoder disk (right, courtesy of Kollmorgen) [155].

The performance of an encoder is typically stated as *resolution*, rather than accuracy of measurements. The reason for that is that the encoder does not compensate the tolerances in the machinery. As an instance, if there are deflections in loaded machine elements, or if there is a drive screw with 0.1 inches of backlash, using a 1000 line-per-revolution (LPR) encoder with an output resolution of 0.001 inches will not improve the 0.1-inch tolerance on the measurement. Resolution is the number of measuring lines or units in one revolution of an encoder shaft or one unit of a linear scale.

The number of bits in the output word defines the resolution of an absolute encoder. This output can be in straight binary or in Gray code, which produces only a single bit change between two consecutive steps to reduce error [157]. The total number of bits is often limited to 32 [158]. A quick search in the market shows that depending on the communication protocol, an absolute encoder may or may not provide an incremental signal when higher resolution is needed.

Lower resolution incremental encoders provide a specific number of equally spaced pulses-per-revolution (PPR) or-per-unit of linear motion. When higher resolution is desired, pulses will be replaced with sine waves. As explained further below, the sine wave encrypts information that can be used for increasing the resolution of the encoder. For common communication protocols, the incremental signal is TTL or 1Vpp sin/cos [159]. Since the on-demand encoder data can come in too slowly for many high-speed motion control loops, most modern communication protocols provide the 1 Vpp sin/cos output for real-time control [5]. Where sensing the direction of the movement is not important, a single channel output is used. *Quadrature* output is used when direction sensing is required. It consists of two channels 90 electrical degrees (one quadrant) out of phase. Circuitry determines the phase relationship between the quadrature signals to measure the direction and increase the resolution. Quadrature encoding is useful for bidirectional processes, or those maintaining net position when idling. A common scenario is when machine vibration while stopped causes a unidirectional encoder to produce a series of pulses that would be erroneously counted as motion. The motion controller would not be fooled when quadrature counting is used [155].

The digital output of an encoder can be transmitted in either parallel or serial form. The advantage of parallel output is that it is fast: all channels are available in real-time. Disadvantages include expensive and bulky cables, as well as limited cable length. Data rate is directly related to resolution and inversely related to cable length. Encoder handbooks recommend reducing data rate 100kHz for every 50m of cable [156]. Most parallel encoders come with cables a meter or two long. Using a parallel differential output and proper cable shielding can extend the cables length to 100m, at a reduction in speed.

The viable alternative to parallel output is to encode the data and send it in serial form. Several dedicated serial buses are available. Tradeoffs among these include availability, proprietary versus nonproprietary nature, hardware requirement, bandwidth, update rate, and wire count. Table 7.1 puts four of the most common dedicated serial interfaces side-by-side [160–163].

**Table 7.1. Dedicated Serial Interfaces.**

	HIPERFACE®	SSI + sin/cos	EnDat®	BiSS
<b>Open Protocol</b>	No	No (License available)	No	Yes
<b>Connection</b>	RS-485: Bus or Point-to-Point Analog: Point- to-Point	Point-to-Point	Point-to-Point	Bus or Point-to-Point
<b>Analog Signals Available</b>	Yes	Yes	Yes	No
<b>Transmission Mode (Digital)</b>	Bidirectional, asynchronous	Unidirectional, synchronous	Bidirectional, synchronous	Bidirectional, synchronous
<b>Digital Data Transmission Rate</b>	38.4 kBaud	1.5 MHz	4 MHz	10 MHz
<b>Cable Length Compensation</b>	No	No	Yes	Yes
<b>Protocol Length Adjustable</b>	No	No	Yes	Yes
<b>No. of Wires</b>	8	6–8	6 to 12	6
<b>Alarm/Warning Bit</b>	No	Definable	Yes	Definable

EnDat (Encoder Data) is one of the most widely used interfaces. It is a proprietary protocol developed by Heidenhain, Traunreut, Germany. It is available in EnDat 2.1 and EnDat 2.2 versions. EnDat 2.2 provides some benefits over 2.1 regarding self-configuration, system security, and additional information [162]. EnDat can include the 1V<sub>pp</sub> sin/cos quadrated output for real-time control. Compared with SSI, EnDat can carry more information. It provides the means for accessing an internal memory in the encoder for diagnostics, identification, and alarm status. Also, the controller can set the encoder’s zero reference point, which aids in equipment setup.

### 7.3 Motivation

A scaled vertical Roller rig is under development at Virginia Tech’s Railway Technology Laboratory (RTL) [2,3,56]. The VT Roller Rig is aimed to shed more light on the wheel/rail contact mechanics with an unprecedented level of accuracy. The rig is comprised of a wheel and a roller that simulate the single-wheel/rail interaction. The machine is equipped with two independent, direct drivelines that provide the required power to drive the wheel and roller as well as precisely control the differential speed at the contact (creepage).

Each driveline is driven by an AKM84T 3-phase permanent magnet AC servo motor manufactured by Kollmorgen, Radford, VA. An 11-bit resolution absolute sine encoder EnDat 2.2 manufactured by Heidenhain, Traunreut, Germany is embedded in each motor as the primary feedback. An S772 digital servo drive (Kollmorgen, Radford, VA) controls the position and speed of each driveline.

These drives increase the resolution of the encoder to 20bit through quadrature decoding (Section 7.5.2.1) and interpolation (Section 7.5.2.2).

An important task in the development of the Rig has been designing the motion controllers that can control the differential speed between the two rotating bodies with 0.1rpm accuracy. During the controller implementation phase, VT engineers noticed an irregular high-frequency noise in position, velocity, and acceleration data that is speed and update rate dependent. The sub 100Hz peaks in Figure 7.2 are attributed to motor cogging and gearbox resonance frequencies. While the 500Hz peak remains unexplained. This study reports how further investigation in this noise led to the development of tools for identification, modeling, and filtering of quantization error in encoder equivalent output.

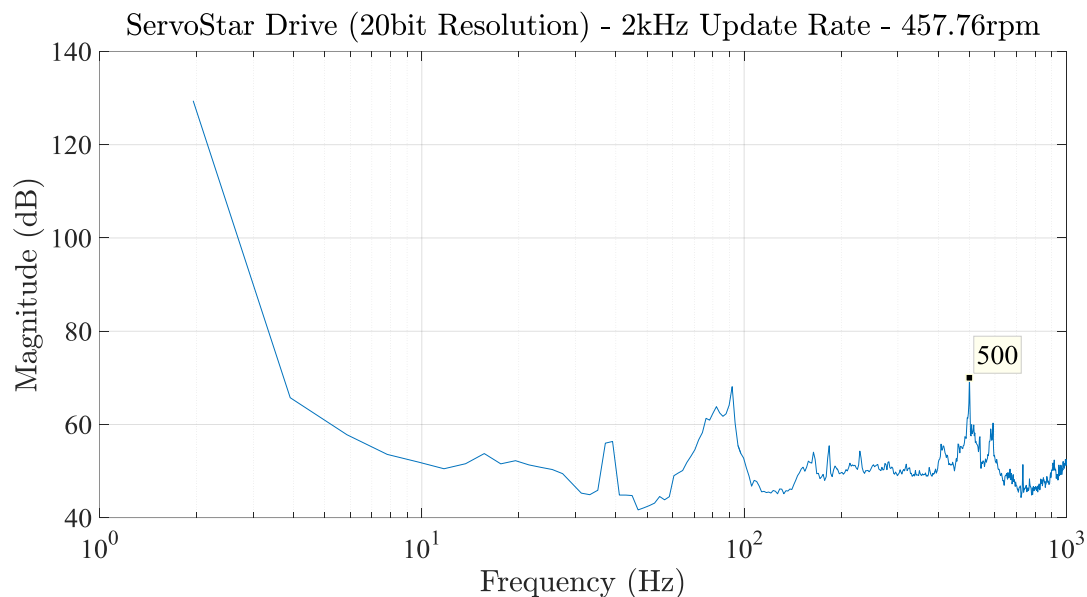


**Figure 7.2.** An example of how the high-frequency noise manifests itself in position and velocity data.

Upon further investigations and discussions with the manufacturer, a slew of experiments was designed to identify the noise and resolve it. Various noise sources were investigated including, but not limited to, the following:

- Electromagnetic interference
- Equipment malfunction: encoder, motor, drive, data acquisition unit
- Motion controllers
- Discretization, magnitude quantization, data rounding, and data transmission
- Noisy input power

This study summarizes the experimental techniques that were used to identify the noise. Extensive tests revealed that the noise is present in position and velocity data, however, it is not detectable on motor current. Incorporated into each driveline, a torque sensor measures the instantaneous shaft torque and speed. Direct torque and speed measurements with the torque flange did not show the noise. Two dynamometers are configured in the Rig to measure the contact forces and moments accurately. The force measurements by the dynamometers were also clean from the high-frequency noise. There is enough evidence to conclude that the noise is an artifact of digital signal processing. Characteristics described in Section 7.7 suggest that this noise does not fall under any of the known noise categories. A review of the known encoder noise varieties is available in Section 7.4. The two major characteristics of this artifact are high sensitivity to speed and dependence on the user update rate. A deterministic estimator for this noise reveals the source of this noise in Section 7.6. Sections 7.7 and 7.8 verify the proposed deterministic estimator by comparing the observations and estimated noise behavior. Section 7.7 provides a discussion on identifying this noise in other systems and filtering it.

### 7.4 Other Errors in Encoder-Based Measurements

Encoder related noises can originate from various sources including, but not limited to: discretization, rounding, data transmission, and hardware.

#### 7.4.1 Sampling Error

Bennet used the term “sampling” interchangeably with the term “quantizing of time” [148]. In sampling, time is divided into equal (or unequal) divisions and the magnitude of the signal is reported at each discrete time. Only one magnitude can be captured for each quantum of time. The magnitude can be selected from a continuous range. Ideally, if magnitudes are assigned at a sufficiently close spacing in time, the continuous and sampled (discretized) signals become indistinguishable. A familiar example is sampling rate of an ADC.

Following the definition above, an encoder quantizes the motion in time by sampling it at intervals that depend on the number of slots on the encoder disk and the speed of motion. Assuming constant speed, increasing the LPR increases the sampling rate of the encoder. Figure 7.4 shows the effect of LPR and count-per-quadrature (CPQ) on the resolution of the encoder. See Section 7.5.2 for more information on how these numbers are generated.

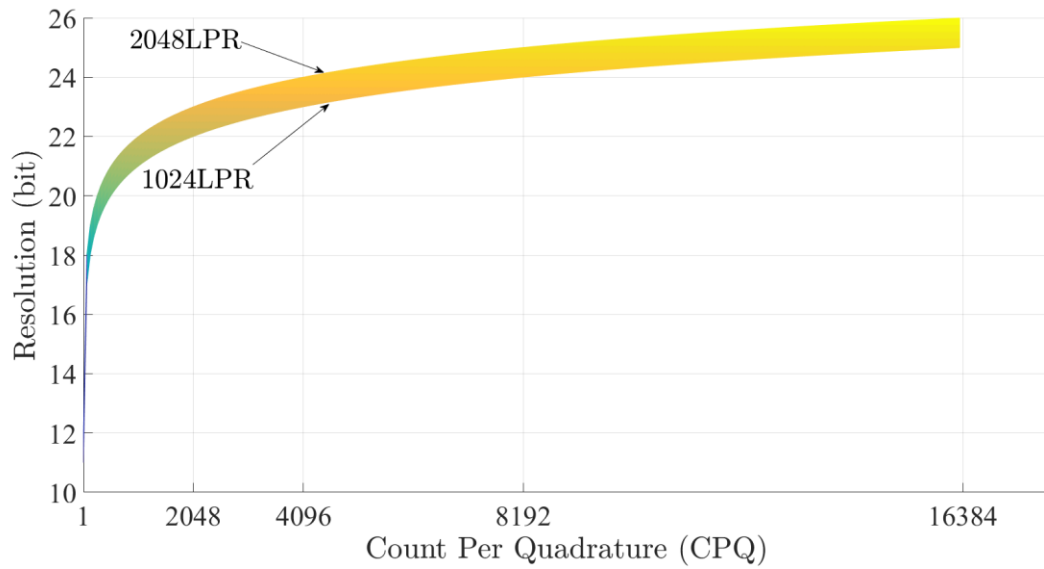


Figure 7.3. The effect of LPR on the resolution of encoders.

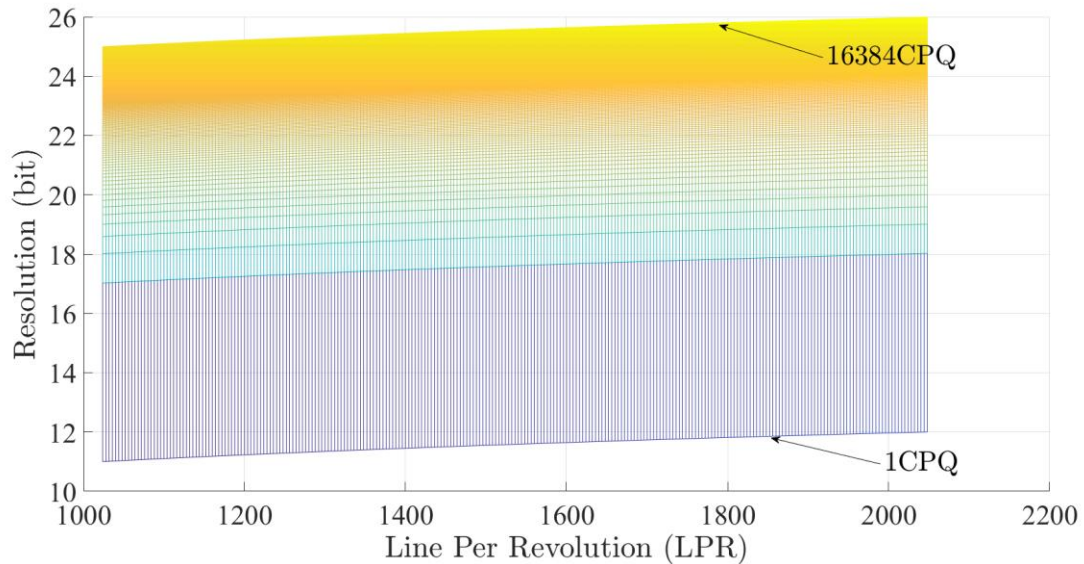
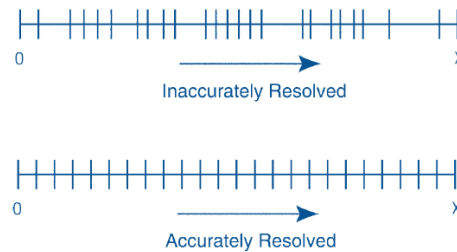


Figure 7.4. The effect CPQ on the resolution of encoders.

While the number of slots on the encoder disk defines the resolution of the encoder, the spacing between them defines the accuracy of the sensor. Accuracy and resolution are different, and it is possible to have one without the other. Figure 7.5 shows a distance  $X$  divided into 24 increments. If  $X$  represents  $360^\circ$  of shaft rotation, then one revolution has been resolved into 24 parts. While the resolution on both encoders is 24, the 24 parts are not uniformly distributed on both encoders. The top transducer could not be used to measure position, velocity or acceleration with desired accuracy [156].



**Figure 7.5. Difference between accuracy and resolution (courtesy of Kollmorgen) [156].**

A system accuracy is a direct function of the accuracy of its encoder. Typical values are  $\pm 20$  and  $\pm 60$  arc-seconds. It has been shown that the onboard electronic decoder on the receiver electronics usually adds another 1% of one sine wave period to the total system error [164]. For example, using a 2048 line encoder rated for 20 arc-seconds accuracy, the electronics add another 6.5 arc-seconds of inaccuracy for a total of  $\pm 26.5$  arc-seconds.

#### 7.4.2 Rounding Error

In 1982, Zador provided an extension to the following theory of asymptotic quantization error of continuous signals [165]:

*“The mean squared error due to rounding a random signal number to the nearest  $n$  place decimal fraction tends to zero as  $1/12n^2$  when  $n$  increases if the signal is uniform over the unit interval.”*

Rounding can be considered as a form of quantization, namely quantization in precision. In ADC devices, there is often a trade-off between sampling rate and the number of bits used to quantize (round) each sample [166]. The ideal resolution of the encoder receiver electronics is a function of the sin/cos encoder’s LPR and the resolution of the ADC. The ADC noise includes the rounding as well as the noise contributed by ADC internal circuitry (Section 7.4.4). The data in Table 7.2, Figure 7.6, and Figure 7.7 has been published by Texas Instruments, Dallas, TX to outline the impact of an ADC resolution, offset, gain, or phase error on the resolution of the receiver electronics.

In Figure 7.6, note that the phase error introduced due to offset has the same frequency as the input signals. The phase error caused by the phase shift between the input signals A and B exhibits twice the frequency of input signals. These signatures can be leveraged for detection and correction of a constant phase shift using signal processing algorithms.

**Table 7.2. Analysis of Phase Error Examples [167].**

Error Source	Example	Maximum Phase Error
Resolution of ADC	12-bit	0.012% [0.045°]
Offset error of signals A and B	0.1%	0.05% [0.18°]
Gain error of signals A and B	0.1%	0.04% [0.15°]
Phase shift between input signals A and B	$90 + 0.36^\circ$ [0.1%]	0.1% [0.36°]

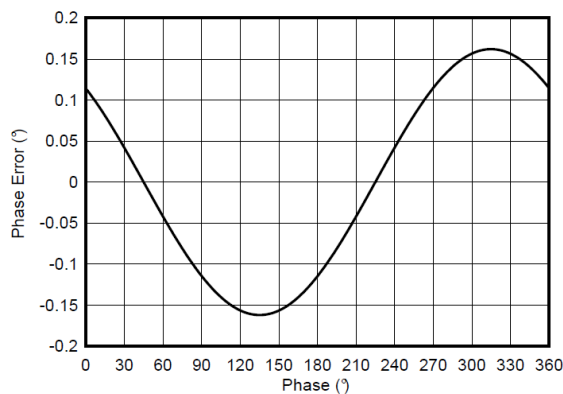


**Figure 7.6. Phase error with +0.1% offset in both signals A and B (courtesy of Texas Instruments) [167].**

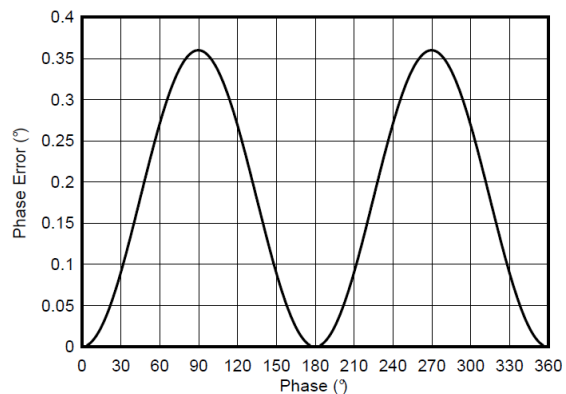


**Figure 7.7. Phase error with  $(90 + 0.36^\circ)$  phase shift between signals A and B (courtesy of Texas Instruments) [167].**

Various FFT-based measures have been proposed in the literature to quantify the noise and distortion performance of an ADC. These measures include signal-to-noise-ratio (SNR), total harmonics distortion (THD), signal-to-noise and distortion (SINAD), and an effective number of bits (ENOB).

#### 7.4.3 Data Transmission Error

Signal distortion and electrical noise are the most frequent problems encountered in transmitting an encoder’s signals to receiving electronics. Either can lead to gain or loss of encoder counts. The code of practice for avoiding many of these problems is proper wiring and installation. Transients in the encoder power supply can adversely influence operation. Typically, encoder power should be regulated to within  $\pm 5\%$ , and it should be free of induced transients. Radiated noise from nearby relays, transformers, and electric drives may be picked up by the signal lines causing undesired signal pulses. Likewise, the encoder may induce noise into sensitive equipment adjacent to it [155]. Machine power and signal lines should be routed separately. Signal lines should be twisted,

shielded and routed in separate conduits or harnesses spaced at least 12 inches from power leads [156].

Cable length, or more specifically, cable capacitance, is considered the primary cause of signal distortion. As with any feedback device, cable capacitance should be kept less than 47pF-per-foot [164]. Increasing the cable length increases the potential for signal distortion (see Figure 7.8). The receiving electronics will respond to an input signal that is either a logical 0 or 1. The region between 0 and 1 is undefined, and the transition through this region must be less than about 1 microsecond [156].

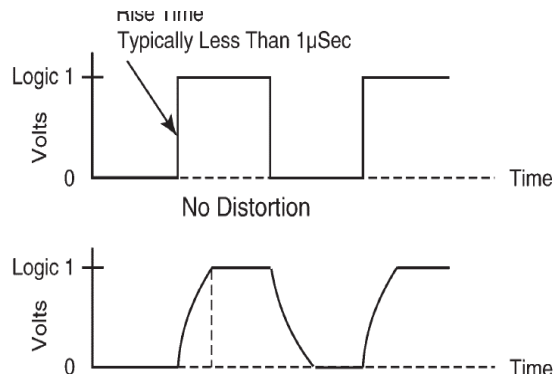


Figure 7.8. Typical signal distortion due to cable capacitance (courtesy of Kollmorgen) [156].

#### 7.4.4 Hardware Error

The continuous sin/cos outputs of the encoder are converted to digital TTL-level signals for fine motion control purposes. In practice, the digitized signals have a phase shift compared to the analog signals. This is mainly due to hysteresis and propagation delay of the comparators [168], as well as due to non-ideal synchronization between latching the incremental count and sampling the analog inputs. At the transition to the next quadrant, the incremental counter is not updated immediately because of the phase lag, e.g., as shown in the first quadrant in Figure 7.9.

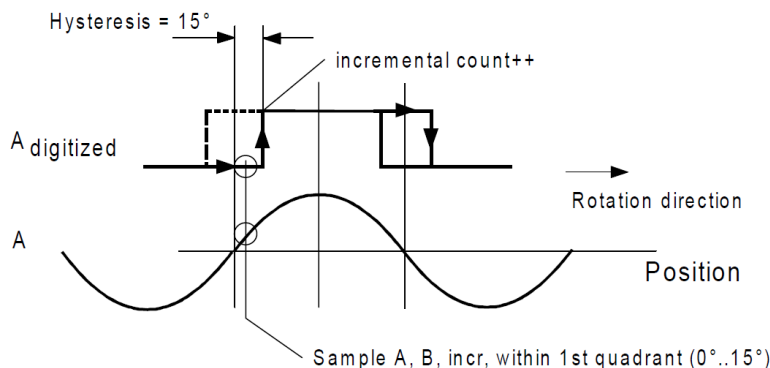


Figure 7.9. Phase shift of  $A_{TTL}$  to  $A$  due to hysteresis (courtesy of Texas Instruments) [169].

The impact of the hysteresis on the phase shift is almost independent of the signal frequency but almost inversely proportional to the signal amplitude. The impact of a propagation delay and a non-ideal synchronization between sampling the analog signal and latching the incremental count is almost independent of the amplitude but proportional to the frequency. Therefore, the maximum phase shift occurs at maximum sin/cos encoder frequency with minimum amplitude. This means that at each transition to the next quadrant, the incremental counter is not updated immediately because of the phase lag [167]. The factors outlined cannot be omitted and hence correction methods such as those given in [167] and [169] are applied to detect and correct these corner cases.

Pitch errors arise mainly due to encoder disk manufacturing tolerances and mounting distortion [170]. Encoders are very susceptible to mounting misalignment. If the encoder's physical dimensions are close to tolerance limits, then the encoder may not provide the design accuracy. Five major factors should be considered when mounting the encoder to motor shaft [171]:

- Concentricity of encoder housing with the centerline of the motor shaft
- Perpendicularity of motor shaft center line to motor mounting surface
- Axial end play of motor shaft that supports the hub and disk assembly
- Tolerance between encoder hub, disk assembly, and motor shaft
- Runout of hub, disk assembly, and motor shaft assembly

A common number for the Total Indicator Reading of errors due to these factors is  $\pm 0.002''$ . These errors can be compensated via the same procedures that are carried out for geometrical error compensation [170].

### 7.5 Quantization Error in Encoder Equivalent Output

The quantization error discussed here is different from the errors caused by discretization, quantization in magnitude, and rounding. While similar in nature, the mechanism behind generation of each noise is different. The rest of this paper attempts to introduce this error and provide a mathematical model that can estimate it based on the line count of the encoder, speed of motion, and output update rate. The update rate is the rate at which data is reported to the user. It is inherently different from the sampling rate of the ADC, clock rate of the FPGA, and frequency of motion control loops.

### 7.5.1 ADC Sampling

The sin/cos encoders modulate a beam of light whose intensity is sensed by photo-electrical cells, producing two 90° electrically phase-shifted sinusoidal signals “A” and “B” (AquadB). The convention is that B lags A in clockwise rotation viewed from the shaft side of the encoder [169]. The number of periods of A and B over one mechanical revolution equals the line-per-revolution (LPR) of the encoder. In Figure 7.10, the incoming sine signals from the encoder are complementary presenting a single-ended signal waveform of 500mVpp riding on a 2.5VDC carrier for each signal. When these signals are presented to a differential receiver, the resulting waveform is 1Vpp riding on 0VDC. Theoretically, a scope plot with the A-channel on the x-axis and the B-channel on the y-axis produces a circle with a radius of 0.5 volts [172]. A second track carries a reference mark that modulates the reference mark signal “R” at a maximum once-per-revolution. The reference marker allows for an absolute angle position measurement.

These signals are sampled with analog-to-digital converters at  $f_{ADC}$ Hz. The resultant digital words are handled with digital electronics (FPGA) providing arithmetic processing to decode the interpolated position. The resulting position word is fed to internal capture registers, for use in the control algorithms and to an accumulator that outputs the Encoder Equivalent Output signal for the user. There is a limit to the amount of position change that is allowed in each  $\tau_{ADC}$ , ( $1/f_{ADC}$ ), that establishes the  $f_e$  input frequency limit [164]. A common code of practice is:

$$f_e = \frac{f_{ADC}}{5} \quad (51)$$

Few manufacturers use the alternative  $f_e = f_{ADC}/4$  for limiting the input frequency [167]. For the sake of this paper, the more conservative form given in equation 51 is used. The sinus inputs to the drive must not exceed  $f_e$ . Assuming sampling rate of 625kHz for Figure 7.10, the maximum input sine frequency is 125kHz. Using an encoder with 2048LPR, the maximum shaft speed is 3662rpm.

In addition to electronic speed limitations, all transducers have inherent mechanical limitations that exceeding them may result in incorrect data or premature failure. For a given application, the maximum operating speed is the encoder’s maximum mechanical RPM specification ( $f_m$ ), or maximum electronic operating speed of the encoder and the electronics to which it is connected ( $f_e$ ), whichever is less [155].

$$f_{sine} \leq \min\{f_e, f_m\} \quad (52)$$

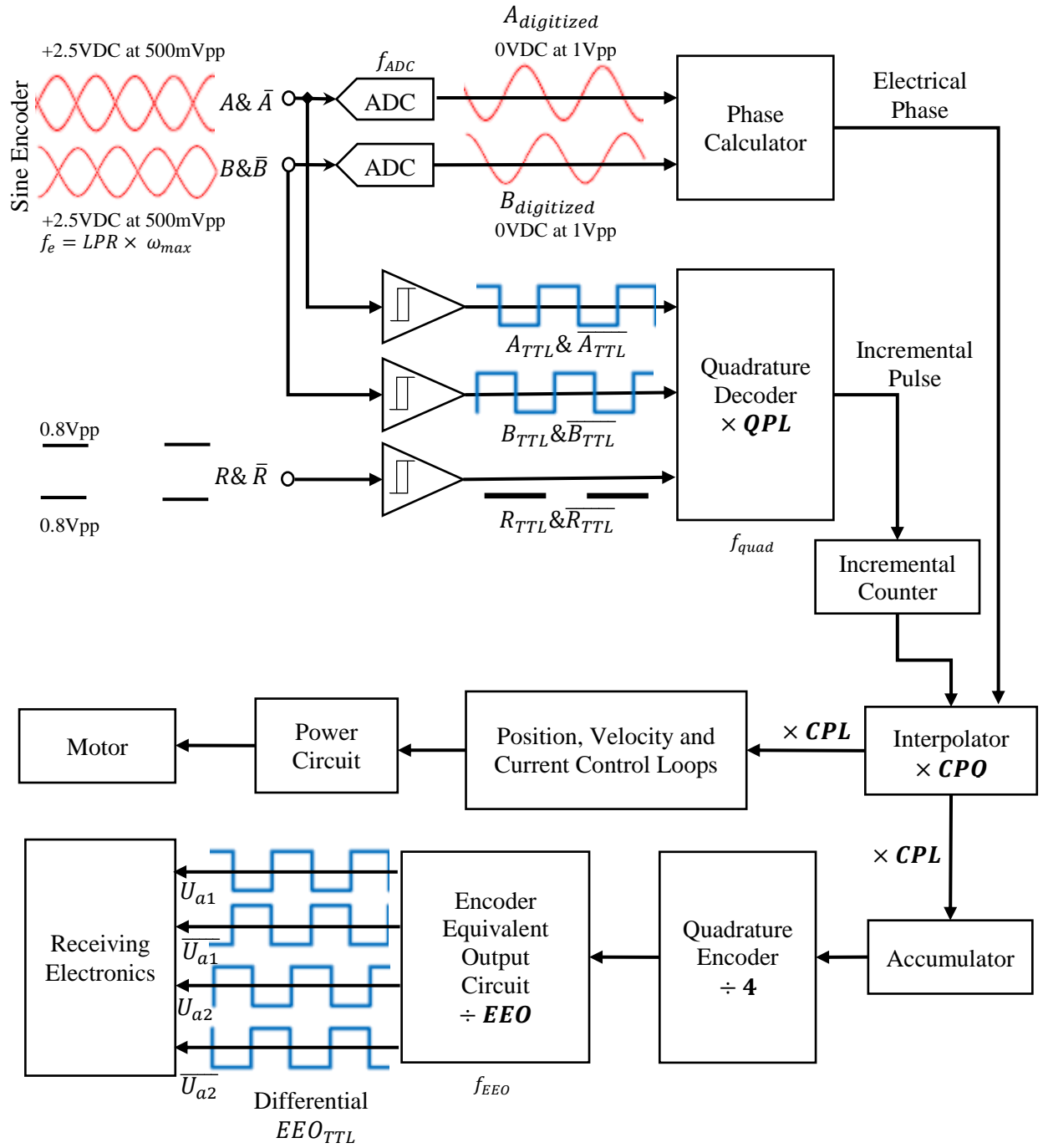


Figure 7.10. Simplified diagram of encoder circuit in a digital drive ( $\times$  and  $\div$  denote resolution change).

In most cases,  $f_e < f_m$  [159]. In practice, the maximum revolution speed at which the electronics can track the high resolution position depends on the following [169]:

- LPR: line count of the encoder
- $\alpha_{hys}$ : hysteresis angle of the digitizing circuit
- Propagation delay between the analog and the digitized signals
- $t_{delay}$ : delay time between sampling the analog signals and capturing the incremental counter

$$n_{max}[rpm] = \frac{60}{LPR \cdot t_{delay}} \left(90^\circ - \frac{\alpha_{hys}}{360^\circ}\right) \quad (53)$$

The quadrature-per-line (QPL) and count-per-quadrature (CPQ) boxes shown in Figure 7.10 represent the internal interpolation. These values can be adjusted if the servo controller requires lower encoder resolution, count-per-revolution (CPR).

### 7.5.2 Interpolation

Interpolation is the process of decoding the AquadB sine waves into a very fine resolution. This is the main advantage of sine encoders over pulse incremental encoders. The disadvantage is that analog signals are notably susceptible to noise pickup and require good wiring installation practices [164]. Various interpolation approaches have been suggested in the literature since the 1990s. Few of these methods are: fringe fractioning [173], code compensation [174], Radial Basis Functions [170], DSP-based [175], look-up table [176], and phase-lock loop [177].

In all interpolation techniques, the drive interpolates internally each sine wave to certain counts, often called count-per-line (CPL) [178]. Depending on the number of LPR on the encoder, high CPR can be achieved. For example, the output of Heidenhain ECN1313 absolute sine encoder (2048LPR) can be interpolated with Kollmorgen ServoStar drive (1024CPL) to reach an improved resolution of  $2^{21}$ CPR, or 0.62 arc-seconds. The equation 54 summarizes the interpolation process.

$$CPR = LPR \times CPL \quad (54)$$

A serial interface such as EnDat 2.1 is needed to transmit both absolute and incremental signals. Below is a typical wiring of a single turn or multi-turn sin/cos encoder with EnDat 2.1 interface as a feedback system.

The increased resolution improves the system's velocity performance by giving more information to the velocity loop controller which, in turn, reduces truncation and discretization errors and allows

higher loop gains. These are critical characteristics for high inertia and mass loads typical of direct-drive rotary and linear motors [178].

Increased position resolution of the sine encoder system provides a higher gain for position and velocity loops resulting in superior system stiffness [178]. The higher resolution also allows for higher proportional gain to correct for torque disturbances. High velocity and position loop gains typical of direct-drive rotary and linear applications can cause a motor to dither back-and-forth by a least-significant-bit of the feedback resolution. Increased resolution reduces dither by reducing the significance of least-significant-bit.

The increase in feedback resolution (down to  $\pm 0.62$  arc-seconds compared to  $\pm 600$  arc-seconds for original encoder output) has obvious benefits when attempting to position a load but also provides the advantage of reduced velocity ripple.

CPL interpolation consists of two steps: quadrature decoding (course angle calculation) followed by phase calculation (fine angle calculation).

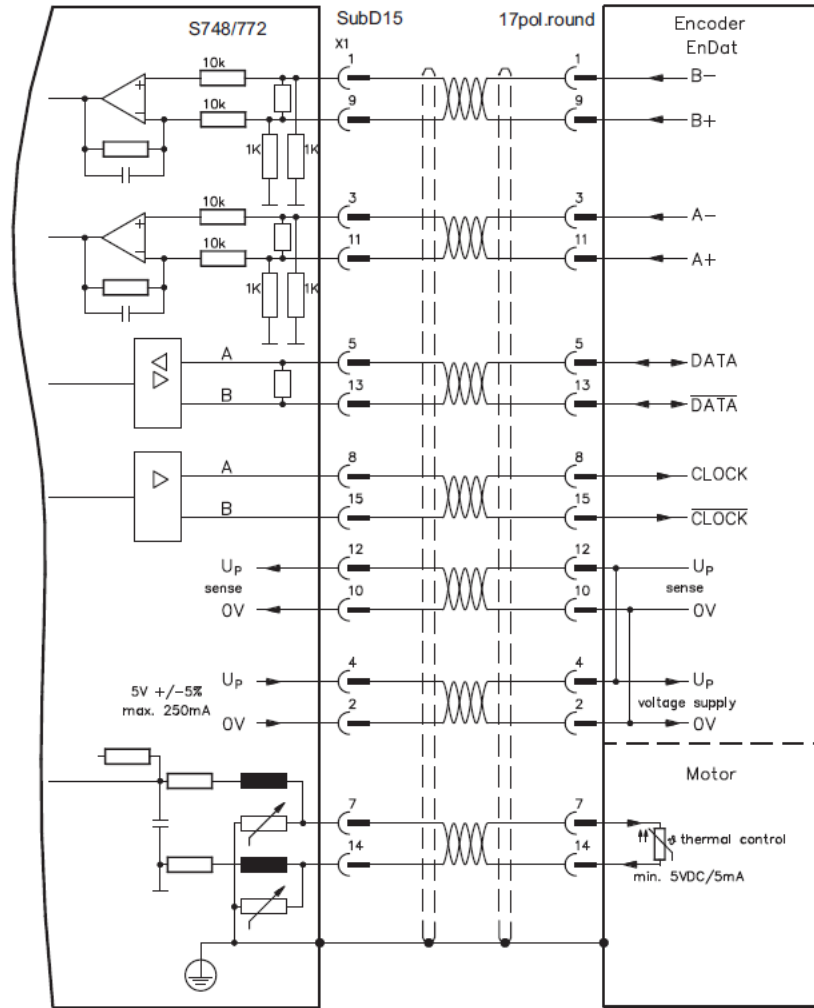


Figure 7.11. Absolute sine encoder connected to Kollmorgen S772 drive with EnDat 2.1 (courtesy of Kollmorgen) [73].

### 7.5.2.1 Quadrature Decoding

Because encoder outputs are differential, the complementary channels (A& $\bar{A}$  and B& $\bar{B}$ ) combine to create the 1V<sub>pp</sub> signal to the control electronics with good noise immunity. Through quadrature decoding, a drive is capable of multiplying the original resolution (LPR) by a factor of 1, 2, or 4. This method is often referred to as edge-detection, and the multiplication factor is called QPL [164]. The quadrature resolution in an encoder with LPR original resolution is:

$$\text{Quadrature Resolution} = \text{LPR} \times \text{QPL} \quad (55)$$

### 7.5.2.2 Electrical Phase Calculation

Through a method called phase calculation, the drive breaks down each quadrature with additional internal counts (CPQ). The electrical angle is then rounded to the closest sub-quadrature count. Typical CPQ values are 128 and 256 [164]. Applying fine angle calculation to equation 55 gives:

$$CPR = LPR \times QPL \times CPQ \quad (56)$$

In other words, since each encoder line corresponds to one sine cycle:

$$CPL = QPL \times CPQ \quad (57)$$

The first term on the right side of equation 57 shows the coarse position calculation (quadrature decoding) and the second term shows the fine position calculation (electrical phase). Almost all modern quadrature decoding circuits are capable of detecting both edges, or in other words, full quadrature count (4QPL). Evidently, the sinusoidal signals A and B, and the incremental count must be sampled simultaneously. The interpolations happen at  $f_{interp}$  that depending on the interpolation technique may be different from  $f_{ADC}$ . For instance, if the interpolation method involves averaging, the same ADC and accumulator register number may be used for consecutive iterations.

Assuming that the shaft in the system of Figure 7.10 rotates at the maximum electrical speed ( $f_e = 125kHz$ ), the quadrature decoder frequency will be  $f_{quad}$  is  $500kHz = 4 \times 125kHz$ . The interpolator should operate at or above this clock rate. A Heidenhain absolute sine encoder with incremental signal specifies a resolution of 2048LPR. Regardless of the actual interpolation technique, the highest achievable interpolations within a quadrature determines the improved resolution of the encoder. A Kollmorgen ServoStar drive provides 128CPQ, therefore, the improved resolution of Heidenhain absolute sine encoder will be:

$$2048 \times 4 \times 128 = 2^{20} \text{alternatively, 20-bit resolution}$$

Modern digital drives allow for adjusting the CPQ value programmatically. If the encoder above is connected to a Kollmorgen AKD digital drive that provides 524288CPQ, the improved resolution will be:

$$2048 \times 4 \times 524288 = 2^{32} \text{alternatively, 32-bit resolution}$$

In practice, the FPGA runs at a clock speed higher than  $f_{interp}$  to allow for more intensive interpolation multiplication-accumulations (MACs). Also, the motion controller calculations are

usually performed at a clock rate lower than  $f_{interp}$ . For a Kollmorgen ServoStar drive, FPGA runs at 16MHz to perform the closed loop motion control operations at 16kHz [71].

### 7.5.3 Encoder Equivalent Output

For a TTL incremental encoder using serial communication bus, the output is in the form of complementary TTL, i.e.  $U_{a1}, U_{a2}, \overline{U_{a1}}, \overline{U_{a2}}$ . For the receiver electronics, this is equivalent to 4x higher data rate [179]. This section discusses the challenge of reporting the improved encoder resolution (CPR) to the normal receiving electronics, as if the TTL signals were generated by a hypothetical encoder with  $LPR = CPR$ . A common application of encoder equivalent output is electronic gearing in master/slave systems [108].

The overall improved resolution of a conventional Heidenhain encoder using Kollmorgen ServoStar digital drive was found in the previous section. A hypothetical incremental encoder with this improved resolution would generate  $2^{18}$  (quadrature encoded) TTL PPR. The pulses are often complimentary for noise rejection purposes. Assuming that the shaft of this encoder is rotating at max speed (3662rpm), the receiver electronics of the encoder would receive complementary TTL signals at 16MHz. This is equal to 64MHz data rate to the processor of the electronics.

Using AKD digital drive would lead to even higher frequency and data rate. Recognizing that user will attach the improved output of the encoder to equipment incapable of receiving such high data rates, the Encoder Equivalent Output (EEO) should be scaled down to allow a reduction in the output resolution and keep the output frequency within limits after considering maximum system speed. Upon receiving each count at the accumulator register, the EEO circuit outputs pulses, while limiting the maximum frequency to a drive-specific output frequency,  $f_{EEO}$  (quadrature encoded). If the accumulator gets more than 1 count-per- $\tau_{ADC}$ , EEO outputs the signals at  $f_{EEO}$ , which can distort the  $90^\circ$  edge separation. This is normally not a problem, but is worth noting and another reason to keep the design limit to  $f_{EEO}/2$  to allow for overshoot [164].

Some FPGAs have a small accumulator to allow for pulse storage beyond the  $f_{EEO}$ . If this buffer overflows, an error is generated and, encoder equivalent pulses from the output port are lost. The maximum count transfer rate via quadrature encoded EEO is:

$$f_{out} = 4 \times f_{EEO} \quad (58)$$

Following the notation used by Zador [165], consider  $N$  angular positions of a rotational encoder,  $x_n$ , to be randomly distributed over a linear metric space,  $D$ . The cardinality of  $N$  is determined by the frequency of interpolations. A predefined set of code points  $y_m \in M$  are uniformly disturbed in

$D$  such that  $|N| \geq |M|$  and  $|M| = CPR$ . The interpolation function  $Y$ , maps or quantizes  $x_n$  to  $y_m$ , if  $y_n$  is the nearest neighbor to  $x_n$  with respect to the metric distance of  $|y_m - x_n|$ . Such notation can then be used to find quantization power distortion to measure the noise. In one approach, Zador found the mean sth power distortion [165].

$$\begin{aligned} Y: N \ni x_n &\mapsto y_m \in M, \\ N \subset D, M &\subset D, \\ |N| \geq |M|, |M| &= CPR, \end{aligned} \tag{59}$$

where  $|N|$  and  $|M|$  are the cardinality of  $N$  and  $M$ , respectively. Discussing such metrics is beyond the scope of this paper. However, such notation can be expanded to evaluate the effect of EEO quantization. EEO replicates a secondary mapping function  $P$ , between  $y_m$  and  $|H|$  uniformly distributed code points in  $D$ ,  $p_h$ . While equation 59 still holds,  $P$  can be defined as:

$$\begin{aligned} P: M \ni y_m &\mapsto p_h \in H, \\ H \subset D, \\ |H| &= \frac{|M|}{4 \times EEO} \end{aligned} \tag{60}$$

Unlike  $Y$ , the EEO quantization function  $P$  relates two discrete domains. The mathematical representation of  $P$  is given in the next section.

## 7.6 Deterministic Estimator for Quantization Error

Because this noise source is in discrete domain, aliasing effects can manifest themselves upon changing the user update rate. Equations 61 through 66 develop a model for predicting the pre-aliased error on the quantized EEO. These equations are derived for a bidirectional single-turn rotational encoder. The same derivations can be applied for multi-turn rotational and linear encoders, provided that the lower and upper movement boundaries be known.

The following parameters are based on the manufacturing specifications of the encoder and drive:

- $f_{out}$
- $LPR$

The following variables are often adjustable by the user:

- $QPL$
- $CPQ$
- $EEO$

$$\circ f_{update}$$

The time spacing between the generated counts is defined as:

$$\tau = \frac{1}{f_{out}} \quad (61)$$

Particular attention should be paid to  $\tau$ . Equation 61 is valid only if the EEO is quadrature encoded. Otherwise,  $f_{EEO}$  should be used instead of  $f_{out}$ . If the instantaneous speed of rotation,  $v$ , is known, then the  $M$  set is:

$$y_i = t_i \times v + \varphi_0, \quad 0 \leq t_i < T, \quad i = 0, \dots, \left(\frac{t}{\tau}\right) - 1, \quad \varphi_0 \sim \cup [0,1] \times 360^\circ, \quad (62)$$

where  $\varphi_0$  is an arbitrary number in  $D$  that denotes the initial location of the encoder.  $T$  is the duration of motion, larger than  $1/f_{sine}$ . The cardinality of  $H$  is determined by the resolution of emulated output:

$$|H| = \frac{LPR \times QPL \times CPQ}{4 \times EEO}, \quad EEO \sim \{1, 2, 4, 8 \dots, CPQ\} \quad (63)$$

If both edges have been detected for quadrature decoding, then equation 63 simplifies to:  $|H| = LPR \times QPL/EEO$ . Finding the quotient and remainder of  $y_i$ :

$$q_i = \text{sgn}\left(\frac{y_i}{360^\circ}\right) \left\lfloor \left\| \frac{y_i}{360^\circ} \right\| \right\rfloor, \quad (64)$$

$$r_i = y_i \text{ mod } 360^\circ,$$

one can define the EEO mapping function as:

$$Q_i = \text{sgn}\left(\frac{r_i}{|H|}\right) \left\lfloor \left\| \frac{r_i}{|H|} \right\| \right\rfloor, \quad (65)$$

$$R_i = r_i \text{ mod } |H|,$$

$$\bar{p}_i = |H| \times (Q_i + 1) + q_i \times 360^\circ$$

From which the EEO quantization error can be found

$$\epsilon_i = p - \bar{p}_i \quad (66)$$

In practice, the user update rate  $f_{update}$  is less than  $f_{out}$ . In such cases the generated output,  $\bar{p}_i$ , is resampled with the output rate while maintaining the magnitudes found in equation 65.

$$\ddot{\bar{p}}_i = S(\bar{p}_i, f_{EEO}, f_{update}) \quad (67)$$

where  $S$  is the resampling function. The  $\ddot{p}_i$  further incorporates the effect of user update rate into encoder equivalent output. The next section validates the deterministic estimator for quantization error in encoder equivalent output against experimental results.

### 7.7 Experimental Noise Identification

This section describes the characteristics of the noise, first observed in the VT Roller Rig motion control system. Nine major characteristics of this noise depart it from the previously known errors reported in the literature. All DFT results presented here are performed using  $2^{11}$  point Hamming windows with  $2^{10}$  points overlap.

- I. The noise is independent of the interpolation factor (CPQ)
- II. It is also independent of the interpolation method [see Section 7.5.2.2 on interpolation]

To evaluate the effect of interpolation process on the noise, similar tests were performed using different drives and motors. The position and velocity data were captured for 20s of rotation at 457.76rpm. Figure 7.13 presents the results. Similar peaks are evident between the two measurements. This suggests that the noise cannot be related to malfunction, interpolation factor, or interpolation method. According to the manufacturer, the electronic parts and circuits are also different between the two drives. However, due to proprietary specification, the one-to-one comparison is not possible.

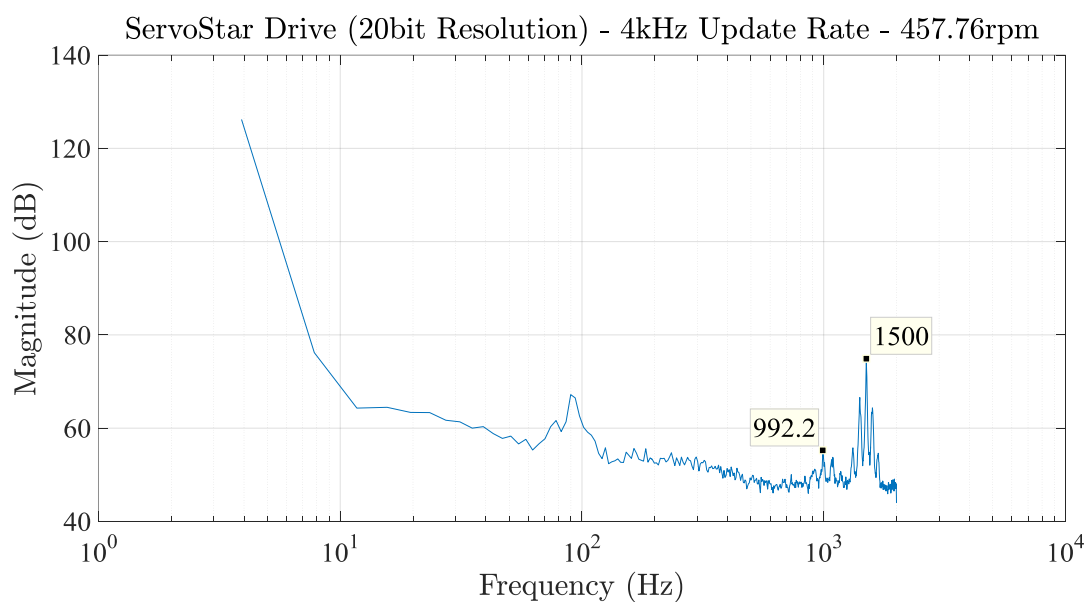
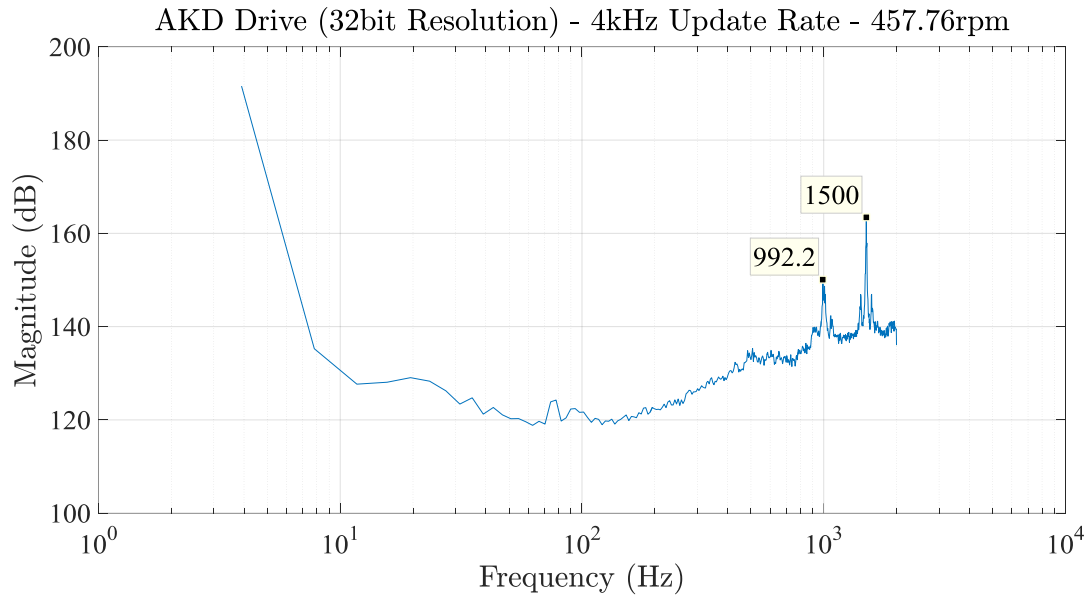


Figure 7.12. Position DFT from 20s of rotation at a constant speed using ServoStar drive. The encoder type, motion profile, and user update rate are the same for Figure 7.12 and Figure 7.13. The receiving electronics, interpolation methods, and interpolation factors are different between Kollmorgen ServoStar and AKD drives.



**Figure 7.13. Position DFT from 20s of rotation at a constant speed using AKD drive. The encoder type, motion profile, and user update rate are the same for Figure 10 and Figure 11. The receiving electronics, interpolation methods, and interpolation factors are different between Kollmorgen ServoStar and AKD drives.**

- III. The noise is dependent on the user update rate
- IV. More harmonics show up at higher user update rate

The same tests were repeated at 2kHz and 16kHz user update rate. The results are illustrated in Figure 7.14 and Figure 7.15. Comparing the data in Figure 7.13 with these two figures reveals that the noise exhibits an aliasing behavior. The Kollmorgen drives are already equipped with antialiasing filters.

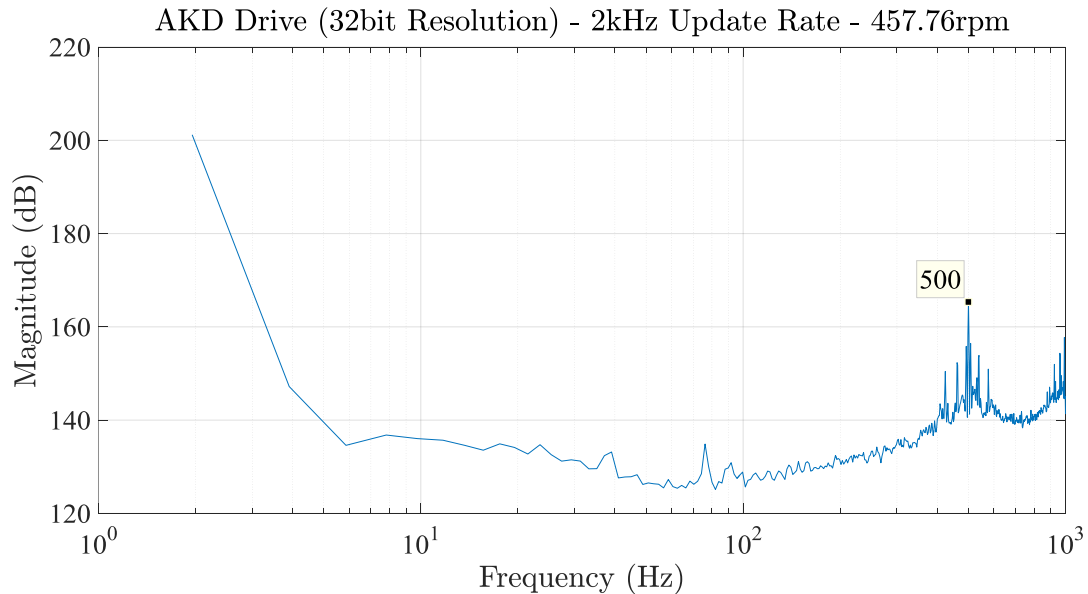


**Figure 7.14. Captured position at 2kHz update rate shows a peak 500Hz. The receiving electronics, encoder, and speed are the same between Figure 7.13, Figure 7.14, and Figure 7.15.**

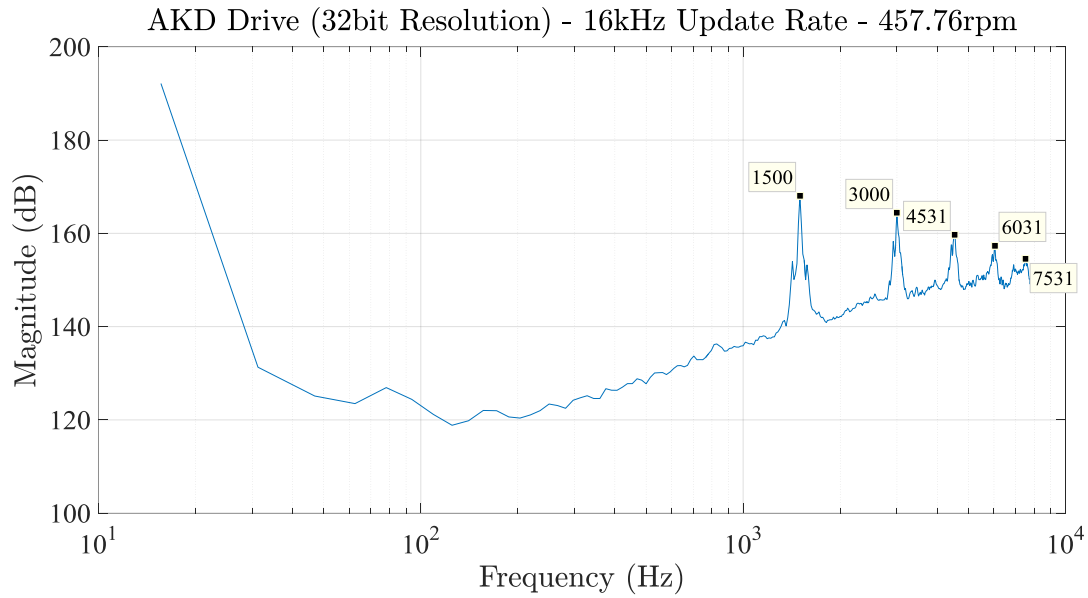


Figure 7.15. Captured position at 16kHz update rate shows multiple harmonics of 1500Hz. The receiving electronics, encoder, and speed are the same between Figure 7.13, Figure 7.14, and Figure 7.15.

V. The noise is highly sensitive to velocity changes

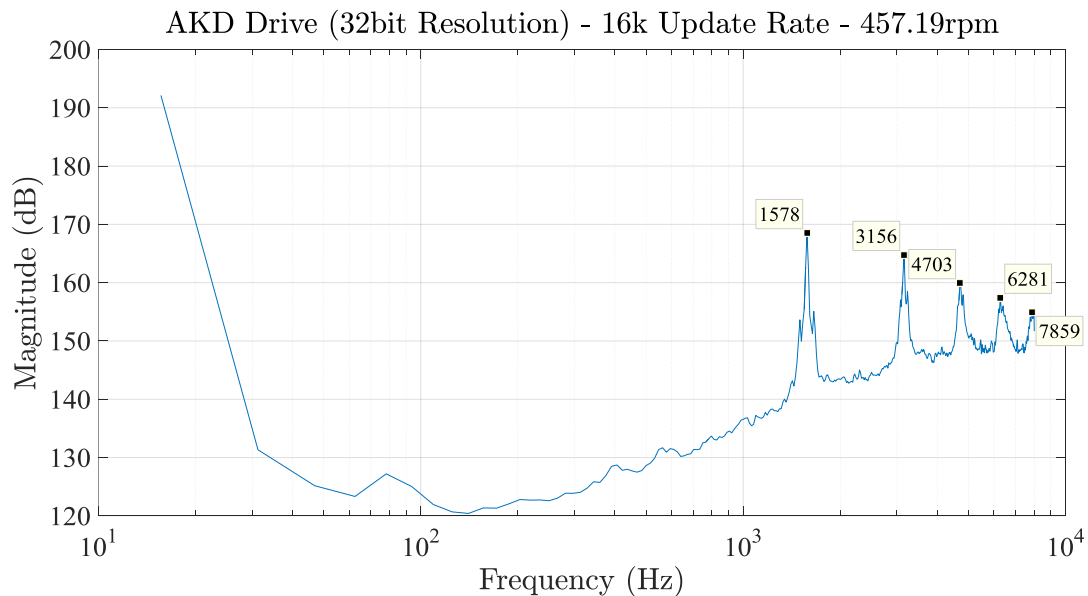


Figure 7.16. The noise is highly dependent on the speed of the shaft. Compare the speed and frequencies of this figure with those of Figure 7.15.

Compare the data in Figure 7.16 for 457.19rpm with Figure 7.15 that is captured at 457.76rpm. At 457.76rpm, the frequency of the encoder sine output is 15625Hz [see Section 7.5.1], which is an order of magnitude higher than the first harmonic shown in the data. If the speed changes to 457.19rpm, the input frequency reduces to 15605Hz, which is the opposite of how the peaks shift

in the experimental data. Both pieces of evidence recommend that the noise is not related to the frequency of the input data being sampled or its harmonics.

Multiple tests also proved that:

- VI. The noise is infinitely repeatable. It is not affected by the motor temperatures or loss of EMI shielding
- VII. Multiple different controllers were designed and tested on the system by the manufacturer control specialists. The noise is independent of the performance or structure of the motion controllers
- VIII. The number of axes in the servo loop may affect the on-time delivery of command and feedback packets. Considering the 48kHz servo update rate of the SynqNet Technology (Kollmorgen, Radford, VA), this is very unlikely. However, experiments with one and eight axes in the loop showed no difference
- IX. Changing the data transmission protocol does not affect the noise. Replacing the communication protocol to serial RS232 at 38400 and 115200 baud rate did not affect the noise

## 7.8 Validating the Quantization Error Estimator

The results presented here are intended for validating the estimator in Section 7.6 against experimental data in Section 7.7. The deterministic quantization error estimator was implemented numerically in MATLAB. For the specific digital servo drive used in the experimental measurements,  $f_{EEO}$  is limited to 2.5MHz. For consistency, both experimental and simulation DFTs are performed using  $2^{11}$  point Hamming window with  $2^{10}$  points overlap. The simulations assume that the actual speed of motions is perfectly constant. Regardless of the performance of the motion controller, there is some error between the commanded and actual velocities. The following results further prove that the quantization error is an artifact of quantization, not actual error. In other words, even if the shaft rotates at perfect speed, the quantization error will be present in the system. Substituting the respective values in equations 61 through 66, the following results are found for AKD drive.

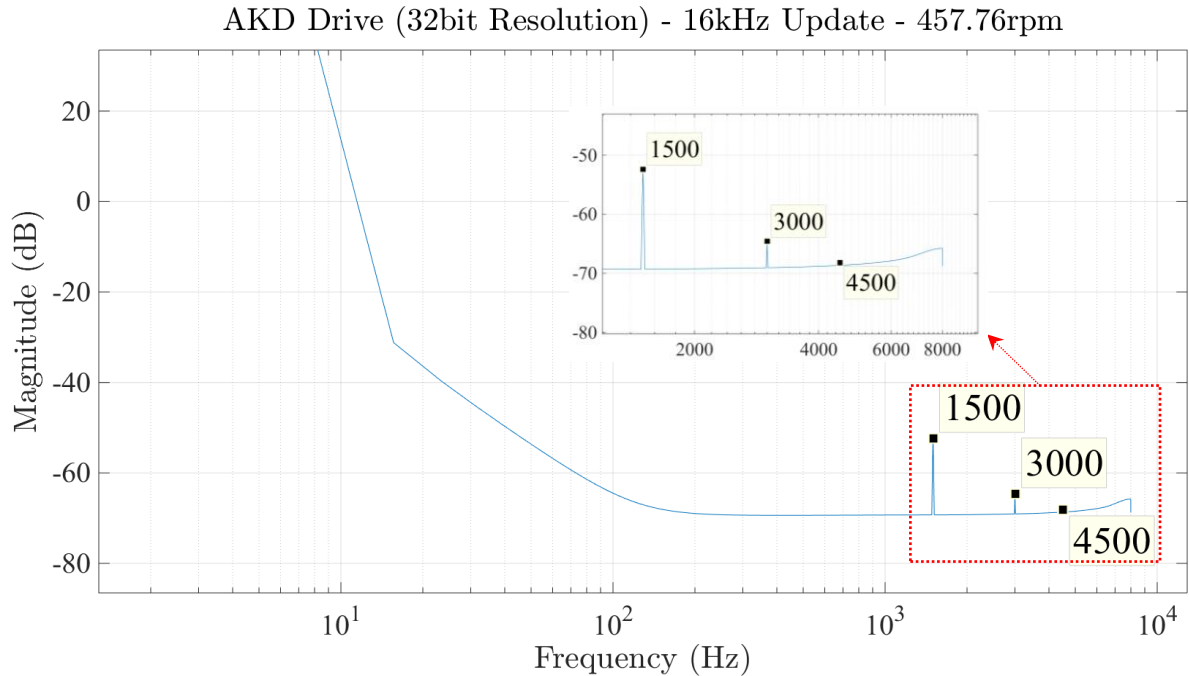


**Figure 7.17. Simulated encoder equivalent output for AKD drives with 16kHz user update rate when the shaft rotates perfectly at 457.76rpm. Compare this figure with Figure 7.15.**

Comparing Figure 7.17 with Figure 7.15 shows a perfect match between the predicted harmonics and the measurements. As mentioned earlier, encoder equivalent output is commonly used in electronic gearing applications. The noise illustrated in Figure 7.17 can significantly reduce the performance of the slave drives. Although the master system is noiseless in reality, the slave systems assume the noisy command signal and try to replicate the noise in the slave systems. Such problem can lead to further unstable conditions if the loop between the master and slave systems is closed by using the motion of slave systems as the feedback of the master. Depending on the servo loop and control architecture, ServoStar drives allow for controlling up to 16 slave amplifiers by the master, via the encoder equivalent output [73].

It was observed in Section 7.7 that the noise is very sensitive to velocity changes. Upon changing the speed to 457.19rpm, the noises shift as shown below:

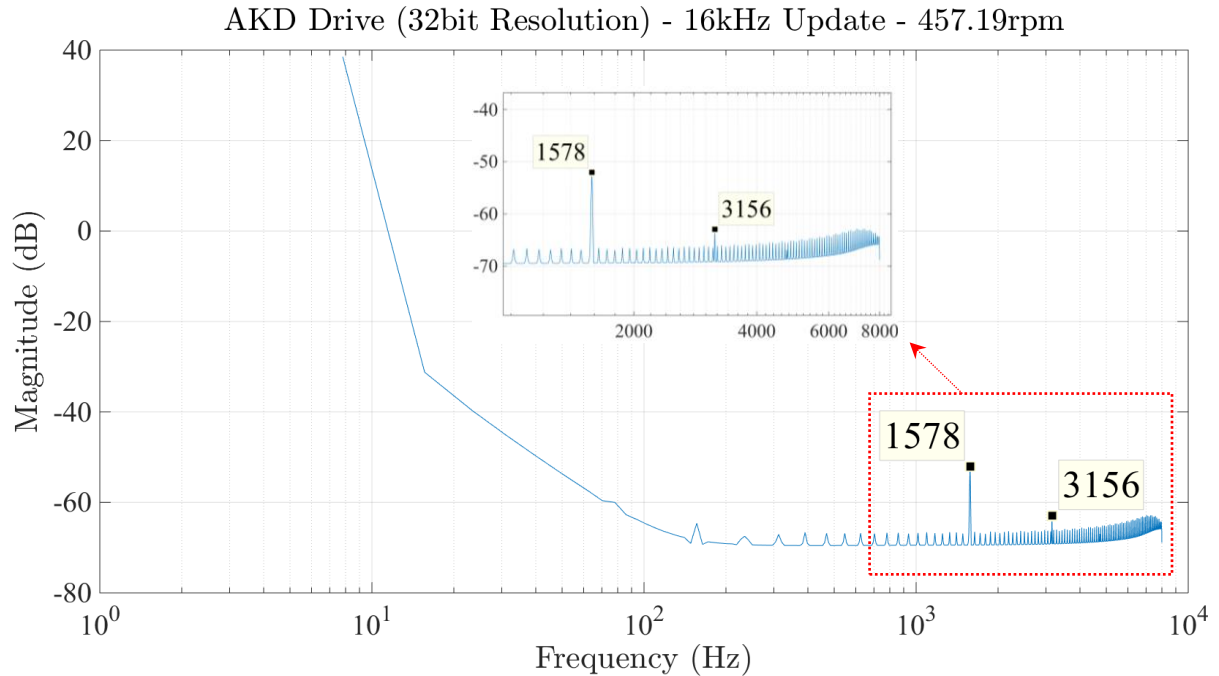


**Figure 7.18. Simulated encoder equivalent output for AKD drives with 16kHz user update rate when the shaft perfectly rotates at 457.19rpm. Compare this figure with Figure 7.16.**

which is in agreement with Figure 7.16. When equation 67 is added to the model for down sampling the encoder equivalent output, the noise peaks will be aliased according to the aliasing formula:

$$f_a = |R \times n - f_s|, \tag{68}$$

where  $f_s$  is the frequency being down sampled,  $f_a$  is the aliased frequency appearing in the measurements, and  $n$  is the closest integer multiple of the sampling rate ( $R$ ) to the signal being aliased ( $f_s$ ). Figure 7.19 and Figure 7.20 verify the capability of the model in predicting the aliasing effect. Figure 7.19 is generated when the user update rate is lowered to 4kHz, and Figure 7.20 is at 2kHz. Compare Figure 7.19 with Figure 7.13, and Figure 7.20 with Figure 7.14.

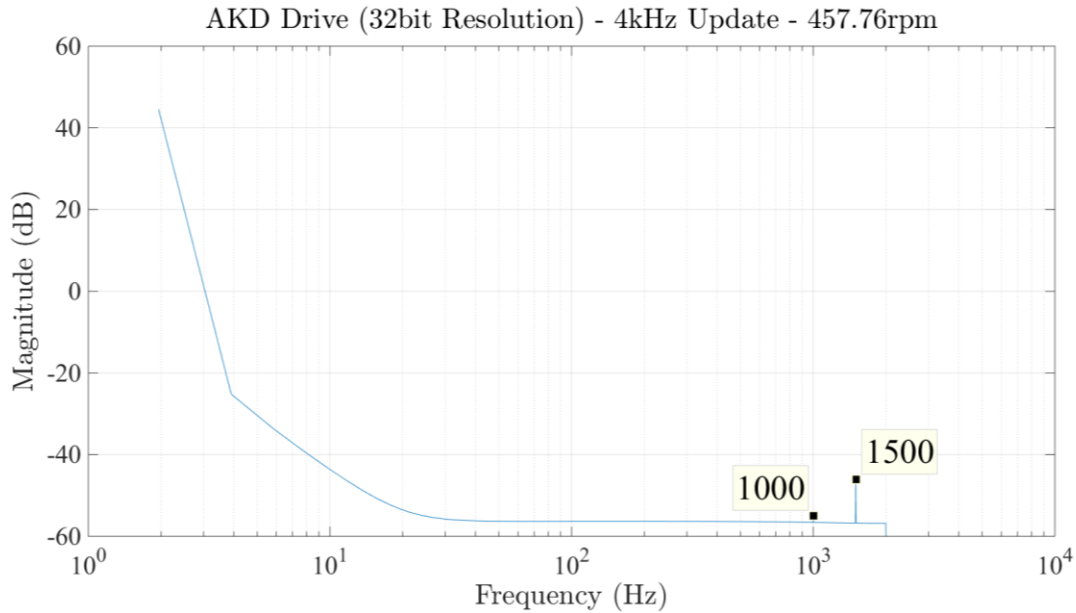


Figure 7.19. Aliased encoder equivalent output for AKD drives with 4kHz user update rate. Compare this figure with Figure 7.13.

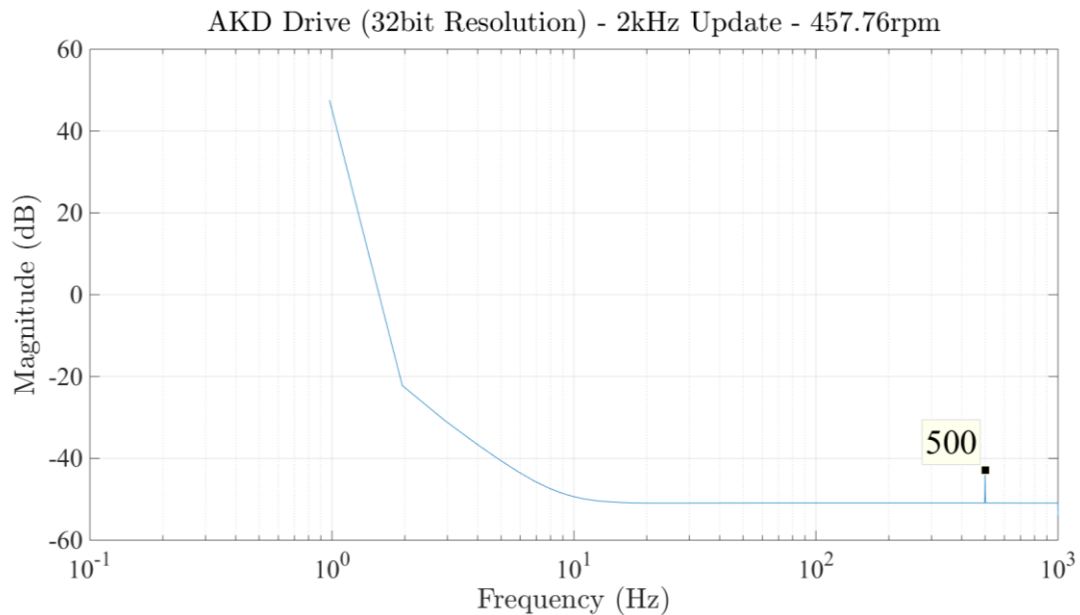


Figure 7.20. Aliased encoder equivalent output for AKD drives with 2kHz user update rate. Compare this figure with Figure 7.14.

## 7.9 Conclusions

Quantization error in encoder equivalent output is different from error caused by discretization, quantization in magnitude, rounding, or hardware related issues. It is caused by a mapping between two quantized domains when transforming the position data from improved encoder data to encoder equivalent output. Any other operation in the modern drives that performs similar transformation

leads to this artificial error. Leaving this error in the output data misleads the user or slave drive in electronic gearing. Such noise can present itself as if it is actually reported by the encoder. The survey on the previously known errors in the encoder output introduced this unknown phenomenon. Experimental identification tests revealed the speed and user update dependency of the noise. A computationally inexpensive model was proposed to model the noise. This model provides the training data for adaptive filters embedded in drive firmware. Various established filtering techniques are available in fields such as telecommunications that can be adapted for this purpose using the proposed model.

## Chapter 8. Component Selection

This section describes the component selection for the systems designed and discussed in previous chapters. For each element, various manufacturers, as well as different product series, were considered. When possible, expert advice was sought from manufacturer application engineers in order to select the most cost effective solution. Seldom, the desired component size is not available or requires a very long lead time. If custom fabrication would result in increased cost or complexity in the system, the next best solution is chosen.

### 8.1 Rotational Servo-Motors

The term "servo motor" does not describe a physical principle such as the terms DC Motor or inductor motor. Moreover, the terms "servo motor" and "servo actuator" do not refer to the same concept, as servo actuator generally refers to brushless direct drive motors. A servo motor is a rotary actuator that allows for precise control of the angular position. It consists of a motor coupled to a sensor for position feedback. The sensor monitors the actual position (e.g. the rotating angle referring to a start position) of the motor axis. This measurement is done by a rotating encoder e.g. resolver, incremental encoder or absolute encoder. A servo amplifier (aka servo drive) then uses the feedback sensor to precisely control the rotary position of the motor.

The electronic regulation compares the signal of this encoder with a given position set point. If a deviation is present, then the motor is turned in that direction, which guarantees a smaller distance to the set point. This leads to the fact that the deviation is reduced. The procedure repeats itself until the current value lies incremental or via approximation within the tolerance limits of the set point. Alternatively, the motor position can be seized digitally and be compared by means of a suitable computer circuit with a set point.

AKM servo motor series offered by Kollmorgen can be used for high dynamic and high precision applications. The motors are high performance and run extremely smooth. They offer multiple connector and feedback options. They conform to UL (508C and 840), CE (2006/42/EC, 2004/108/EC,

and 2006/95/EC), IEC (60204-1), and ISO (12100) standards for maximum safety. Based on the estimated maximum contact forces and moments, AKM84T motors are selected for both wheel and roller drivelines. Figure 8.1 shows a section cut of the AKM84T 3-phase permanent magnet AC synchronous motor and Table 8.1 summarizes the technical data of this motor [68].

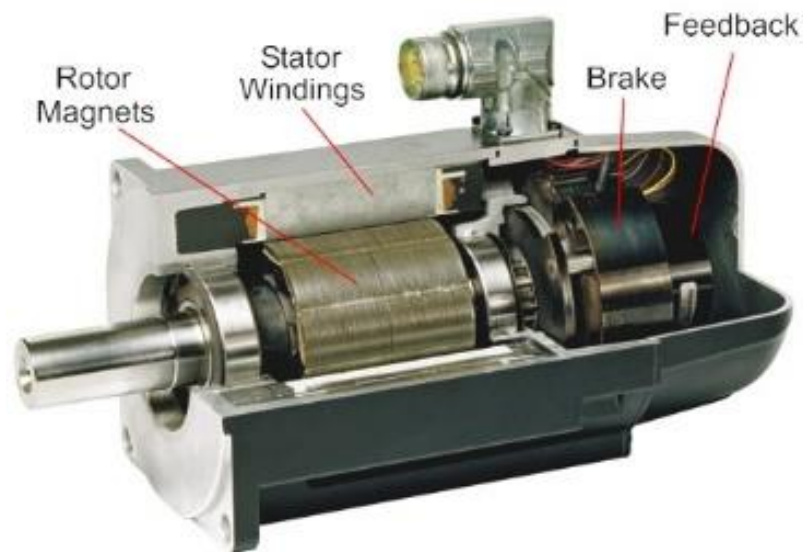


**Figure 8.1. Section cut of the AKM84T 3-phase permanent magnet AC synchronous motor (courtesy of Kollmorgen) [68].**

The AKM motor is equipped with holding brakes to be used in standstill situation (see Section 5.5). These built-in holding brakes without further equipment must not be used to ensure personnel safety. Three major parameters have an influence on the synchronous run of a motor in a servo system: concentricity, cogging, and THD. Additionally, the influence of the feedback system must be observed. Concentricity is a measurement that describes the planeness and alignments of rotor axis to the flange. This is independent of the manufacturing tolerances of the axis, flange, and bearings. It often has two values: N (normal) or R (reduced). For AKM motors, 98% of the production are already R. However, R is also available as an assured option on the product.

Cogging torque designates a phenomenon with electrical motors, which possess permanent magnets in the stator and a slotted anchor from electric sheets or a slotted stand and an anchor with permanent magnets. It is often described as the varying torque behavior caused by changing magnetic flow from rotor to stator. Cogging torque leads to varying torques (jerky run in particular at low speed, bad synchronism). The rotor stops after switching the machine off only to certain positions. Motors with ironless anchor do not possess cogging torque. S772 servo amplifiers have an intelligent function for cogging suppression. For AKM motors nominal cogging value is  $< 2\%$  ( $< \pm 1\%$ ). Motors offered by other manufacturers have typical values of  $< \pm 2\%$  or absolute  $< 4\%$ .

**Table 8.1. Technical data of AKM84T 3-phase permanent magnet AC synchronous motor [68].**

Maximum speed	2500rpm
Rated power (maximum continuous)	19.5kW
Continuous torque (stall)	180Nm
Continuous torque at 60°C (stall)	140Nm
Peak torque	668Nm
Continuous current	67A
Peak current	335A
Number of poles	10
Motor inductance	2.46mH
Rotor inertia	0.0495kg.m <sup>2</sup>
Static friction	2.34Nm
Viscous damping	1.6Nm/krpm
Rated ambient temperature	40°C
Holding brake operating voltage	24 ± 10%
Holding brake torque	150Nm
Holding brake power	49W
Holding brake delay time	300 ∴ 100ms (release ∴ engage)
Holding brake inertia	5.53kg.cm <sup>2</sup>

THD (Total Harmonic Distortion) describes the deviation from theoretic sine wave and the harmonics, caused by unequal resistors and inductivities of the windings and by mechanical tolerances in the production of stator and rotor. For AKM motors, the nominal THD value is < 2%. Motors of other manufacturers have nominal values of > 3%. The THD of the VT Roller Rig power distribution network was found 1.6% (Section 4.3)

#### 8.1.1 Four Quadrant Operation

A servo system capable of controlling velocity and torque in both positive and negative directions is known as having "four-quadrant" operation. Operation in quadrants 1 and 3 is defined as "Motoring", meaning that speed and torque are in the same direction (both positive or both negative). This typically occurs when a system is driving a load and power is being consumed by the motor.

Quadrants 2 and 4 are defined as "generating" (sometimes called regenerating), meaning that speed and torque are in opposite directions (one negative and one positive). Generation occurs when the torque of

the motor is opposing the direction of rotation, and the motor is generating electrical energy. This energy can either be given back to the mains voltage (regenerate energy) or transferred into heat in a regenerative resistor (see Section 8.7) or stored in capacitors (see Section 4.1.5).

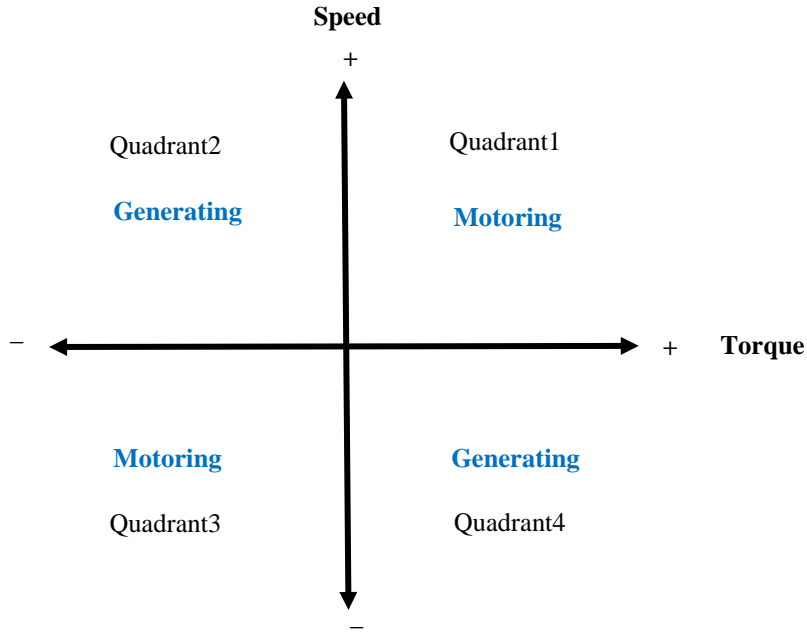


Figure 8.2. Four quadrant diagram for a servo system.

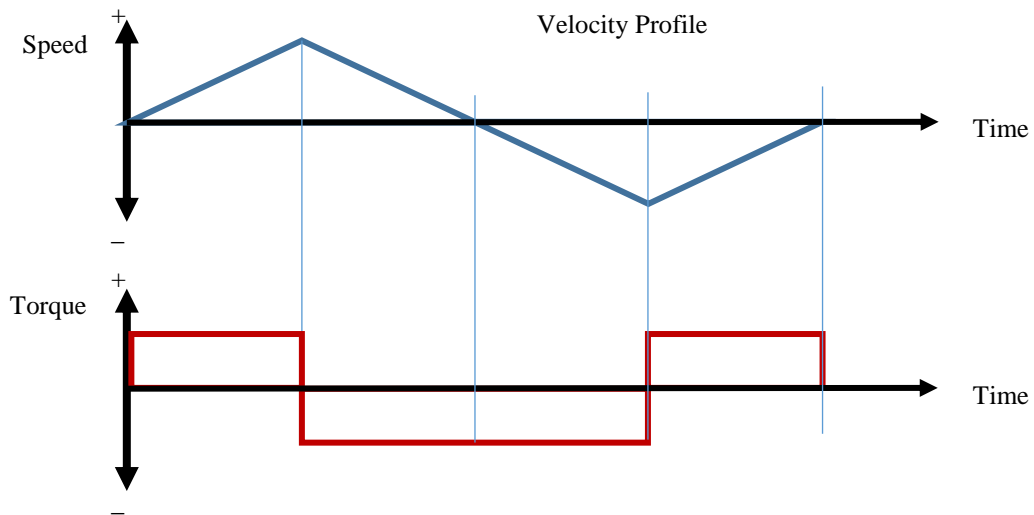


Figure 8.3. A typical motion profile and its relationship to motor torque in a frictionless servo system.

Assuming a frictionless system, the figure above depicts a typical motion profile and its relationship to motor torque. Each segment of the profile can be assigned to a specific quadrant. The first segment shows the motor being accelerated with speed and torque both being positive. Thus, the system is operating in Quadrant 1.

In segment 2, the motor is being decelerated. Speed is still positive. However, torque is negative, which brings the motor to a controlled stop. This is consistent with operation in Quadrant 2.

Segments 3 and 4 exhibit the same properties as segments 1 and 2 with motor rotation being in the opposite (negative) direction, thus placing them in quadrants 3 and 4 respectively.

### 8.1.2 S772 Digital Servo-Amplifier

The S772 digital servo amplifier offered by Kollmorgen drive the AKM84T AC servo motor. This drive conforms to UL (508C and 840), CE (2006/42/EC, 2004/108/EC, and 2006/95/EC), IEC (60204-1), and ISO (12100) standards for providing maximum safety for the user and machinery. It can be operated directly from grounded  $3 \times 480VAC$  mains networks in TN C, TN CS, TN S, TT, or IT architectures. Table 8.2 summarizes the technical data of S772 digital servo amplifier.

**Table 8.2. Technical data of S772 digital servo amplifier [73].**

Rated supply voltage	$3 \times 208V_{-10\%}$ to $3 \times 480V^{+10\%}$ , 50/60Hz
Rated input power for continuous operation	50kVA
Auxiliary DC power supply voltage	24VDC
Rated DC-bus link voltage	290 to 675VDC
Rated output current	72A at $3 \times 480VAC$
Peak output current	140A for 5s
Switching frequency of output stage	8kHz
Thermal dissipation at rated current (without brake dissipation)	1135W at $3 \times 480VAC$
Noise emission	68dB
Control electronics current	2A
Holding brake circuit current	0.15 to 3A

S772 supports EtherCAT, CANopen, and SynqNet bus communication protocols. SynqNet allows for fastest current, speed and position control available in the market that results in higher machine cycle rates (see Chapter 6 for more information on SynqNet Network). The S772 provides two programmable analog inputs, four programmable digital inputs, two programmable digital inputs/outputs (direction selectable). It can output the position as emulation incremental encoder or emulation absolute encoder SSI. As discussed in Section 6.3.4, the analog input on one drive and encoder emulator on the other one can be used for setting up electronic gearing between the wheel and roller drivelines. S772 can read data from a wide range of feedback devices including resolvers, encoders, Hall sensors, and even step

direction interfaces. S772's firmware provides an auto-tuning and cogging suppression feature for easier controller setup. Figure 8.4 shows the S772 servo amplifier. More details on the drive block diagram, connector assignment, and connection diagram are available in Appendix A.



**Figure 8.4.** S772 servo amplifier for driving AMK84T AC servo motors (courtesy of Kollmorgen) [73].

### 8.2 Linear Positioning Servo-Systems

The VT Roller Rig is equipped with positioning mechanisms to replicate real working conditions in railway vehicles. Six linear actuators allow for adjusting the simulated load, angle of attack, rail cant, and lateral displacement at the wheel-rail interface using state-of-the-art motion control technologies. Linear motion can be achieved with different actuation mechanisms including hydraulic, pneumatic, and electric cylinders. Electric cylinders provide precise position control and direct power transmission. Unlike hydraulic and pneumatic systems, electric cylinders do not require pressurized reservoirs, which leads to lower maintenance and easier installation.

The electric cylinders (EC) offered by Kollmorgen are designed for use in a wide variety of industrial, scientific, and commercial applications requiring precise control of linear thrust, speed, or position. They are driven by AKM rotary servo motors, the same motors that drive the wheel and roller drivelines. Therefore, they are highly compatible with the SynqNet command and feedback network. This is very significant since it allows to close the loop between sensors, data acquisition units, and all motors (rotary and linear) using a unified communication protocol. This facilitates data transmission

between these units and eliminates intermittent type conversions, which increases the system clock rate significantly.

The AKM52H servo motor well satisfies the requirements of the VT Roller Rig positioning mechanisms. As part of EC4 linear positioning servo system, the power of AKM52H servo motor is transmitted to a belt/pulley mechanism with a reduction ratio of 2:1. The EC4 unit shown in Figure 8.5 has a 10mm/rev ballscrew mechanism for providing efficient motion conversion. The required stroke length for the AOA, cant angle, and lateral displacement positioning mechanisms is 100mm. The vertical positioning mechanism, however, requires 200mm stroke.

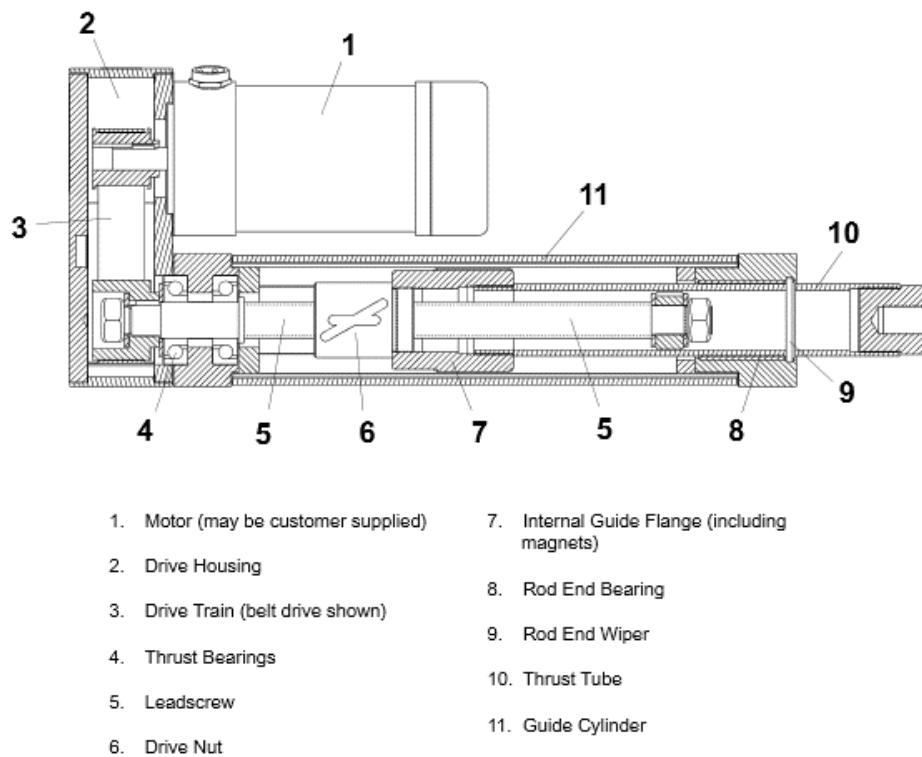


Figure 8.5. Cross-section of an EC4 linear positioning servo system with parallel motor mounting (courtesy of Kollmorgen) [180].

The EC units are equipped with holding brake brakes. This brake option provides a spring-set, electrically-released friction brake mounted to an extension of the leadscrew. It prevents back driving when the unit is at rest, or in the case of power failure. The brake is engaged when power is not applied. Applying power releases the brake, allowing the motion to occur. Similar to other holding brakes, this option is used only for in-position holding, and it should not be used for stopping a moving load.

Although an elastomeric spring inside the cylinder is designed to prevent cylinder jams, position sensors (aka limit switches) are required to prevent such potentially damaging jam conditions. If the

motor is accidentally commanded to move toward a hard-stop, position sensors can signal a stop before a collision occurs. To work properly, position sensors must be positioned inward from the hard-stop, and wired correctly to the motor controller. Using the physical limits of the cylinder (hard stops) will reduce cylinder life and can cause premature component failure. Two hall-effect sensors protect each EC4 linear actuator of the VT Roller Rig, as shown in Figure 8.6. Figure 8.7 shows the wiring diagram of a PSN Hall-effect sensor to a servo amplifier (see Section 8.2.2).



Figure 8.6. Two hall-effect limit switches protect each EC4 linear actuator of the VT Roller Rig against jam conditions (courtesy of Kollmorgen) [180].

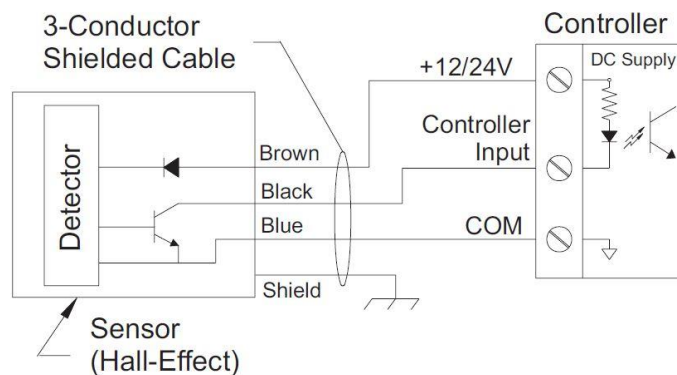


Figure 8.7. Wiring diagram of PSN Hall-effect sensor to the servo amplifier (courtesy of Kollmorgen) [180].

### 8.2.1 Motor Inductance

An important factor in choosing the proper size servo motor for a servo system is the motor inductance. Minimum and maximum permissible motor inductances are given in the technical data of a servo amplifier. Depending on the mains supply voltage, different values are often provided. If motor

inductance is too high, the required motor current cannot be delivered in the requested time. An inductance too low has the result that current is given too fast to the motor.

The minimum load inductance has been researched empirically. For any motor/servo amplifier combination, the goal of motor inductance sizing is that current ripple (rated current and rated voltage at 8kHz) should not exceed 10% of rated current. If the motor inductance is too low, the following setbacks will reduce the performance of the servo system:

- Current ripple and power loss increase
- Motor temperature rises
- Controller performance drops
- Motor trembles or does not run as smoothly as expected
- Motor noise increases
- In extreme cases, servo amplifier generates a fault and disables the output stage (not RTO, see Section 5.3)
- Motor becomes loud

The above symptoms may occur even if the motor had been originally sized properly. They can happen if:

- The operational torque is near the motor torque limit
- Long motor cables (approx. >10m)
- Very smooth running is required for a special test

In such case, the PWM frequency of the servo amplifier should be adjusted. For the S772 servo amplifiers 16kHz is recommended by the manufacturer.

For the maximum motor inductance, the empirical target is delivering the required current within 3 cycles of the current control circuit. The following conditions indicate that the motor inductance is too high:

- Control performance drops
- Current rises slowly, therefore, torque rises slowly
- High-frequency oscillations cannot be controlled

Similar to low inductances, the above symptoms may occur even if the motor has been originally sized properly. They often show up if the highest dynamic capabilities of the motors are required to perform a test (acceleration to target velocity in a few milliseconds)

8.2.2 AKD Digital Servo-Amplifiers

AKD-B00607 digital servo amplifier drives the AKM52H servo motors. It provides a robust and precise servo motion controller for the selected EC4 electric cylinders. This servo amplifier conforms to UL, CE (2004/108/EC, 2006/42/EC, and 2006/95/EC), IEC (60204-1), and ISO (12100) standards for providing maximum safety for the user and machinery. It supports a variety of field bus communication protocols including CANopen, EtherCAT, SynqNet, PROFINET, and Ethernet IP. Table 8.3 summarizes the technical data of AKD-B00607 digital servo amplifier.

**Table 8.3. Technical data of AKD-B00607 servo amplifier [181].**

Rated supply voltage	$3 \times 240 \text{ to } 480\text{VAC} \pm 10\%$ <i>AC with 50Hz to 400Hz <math>\pm 5\%</math> or DC</i>
Rated input current	5.4A
Continuous output current ( $\pm 3\%$ )	6A
Peak output current (for 5 s, $\pm 3\%$ )	18A
Continuous output power	2.5kVA
Peak output power (for 1 s)	7.5kVA
Auxiliary DC power supply voltage	24VDC
Thermal dissipation at rated current	129W
Control electronics current	1 to 2.5A
Switching frequency of output stage	8kHz
Noise emission	43dB

The AKD-B00607 has a built-in advanced dynamic braking circuit similar to what designed for S772 servo amplifiers (Section 8.1.2). When activated, it shorts the motor terminals in phase with the back EMF (q axis) but continues to operate the non-force producing current loop (d-axis) with 0 current. This forces all of the dynamic braking current to be stopping current and ensures the fastest stopping/amp of motor terminal current. This drive also has a 33Ω internal regenerative resistor that dumps the excessive regenerative electrical energy up to 100W continuous power. Unlike the S772 servo amplifiers, no DC-Bus link couples the AKD-B00607’s capacitors (235μF each). Another difference between these devices and S772 series is that they only accept one STO channel and no RTO contact. The Hardware Enable, Holding Brake signals are responded similarly between the two product series.

AKD-B00607 reads data from resolvers, encoders, and step direction interfaces. It provides one programmable analog input, two programmable analog outputs, seven programmable digital inputs, and two programmable digital outputs. For more details about electrical gearing of this servo amplifier see Section 6.3.4 of this document. Figure 8.8 shows the AKD-B00607 servo amplifier. More information on the connector assignments and connection diagram are available in Section B.



**Figure 8.8.** AKD-B00607 servo amplifier driving EC4 linear actuators (courtesy of Kollmorgen) [181].

### 8.3 Isolating Transformer

The S772 and AKD drives can be operated via a 3-phase isolating transformer with Wye-N secondary connection, 480Y/277 secondary voltage, and Delta primary connection. The latter requirement is due to the existing service available at the CVeSS. Moreover, CSA and UL approvals are required, and the transformer should comply with DOE/TP1 and C802.2 efficiency regulations. The HPS Sentinel energy efficient K-factor transformers from Hammond Power Solutions Inc. are designed to tolerate heating due to harmonics associated with non-linear loads. These components have become a popular means of addressing overheating problems where drives, personal computers, electronic ballasts, telecommunication equipment and other similar power electronics are found in high concentration. Bell Electric of Blacksburg helped CVeSS to custom design an isolating transformer from the HPS Sentinel series. Figure 8.9 shows the final component and a representation of the coils inside the housing.



**Figure 8.9. HPS Sentinel isolating transformer.**

The non-linear loads generate harmonic currents that can substantially increase the transformer losses. The K-Factor transformers have a rugged design to prevent overheating, a 200% rated neutral line, and full electrostatic shield. K-factor is defined as the ratio between the additional losses due to harmonics and the eddy current losses at 60Hz. Standard K-factor ratings are 4, 13, and 20. Transformer coils are precision wound with continuous aluminum conductors and are electrically balanced to minimize axial short-circuit forces. The use of duct stick permits the flow of air, thus provides cooling in addition to providing superior radial mechanical strength. Table 8.4 summarizes the technical data of the HPS Sentinel isolating transformer.

**Table 8.4. Technical data of HPS Sentinel isolating transformer.**

Rated power	200kVA
Rated voltage	480/277VAC
Rated Current	241A
Frequency	60Hz
Number of phases	3
Primary connection	Delta
Secondary connection	Wye – N
Temperature rise	150°C
Efficiency regulation	DOE 10 CFR Part 431 and C802.2 – 12
Sound level	–3dBA below NEMA ST
Weight	1350 LBs

### 8.4 3-Phase Power Filters

As discussed in Section 4.1.3, the filtering effect of the mains filters is only assured when the permissible power rating of the mains filters is not exceeded even on peak loading of the servo amplifiers. Assuming coincidence factor of 1 and single axis on each filter,  $P_{Smax}$  is found to be 66.51kVA (38.4kW) for each S772 servo amplifier. Schaffner’s 3-phase FN 258 filters have been known as the industry standard EMC solution for power drive systems. The FN 258-100-35 component well satisfies the requirements of the VT Roller Rig calculated in Chapter 5. Table 8.5 summarizes the technical data of this filter.

**Table 8.5. Technical data of 3-phase Schaffner FN 258-100-35 filters [79].**

Maximum continuous operating voltage	$3 \times 480/277VAC$
Operating frequency	<i>dc to 60Hz</i>
Typical drive power rating	$55kW$
Rated current	$100A$ at $50^{\circ}C$ ( $110A$ at $40^{\circ}C$ )
Overload capability	$4 \times$ rated current at switch on, $1.5 \times$ rated current for 1 minute, once per hour
Leakage current	$25.8mA$
Power loss	$51W$

Figure 8.10 shows the 3-phase FN 258-100-35 filter and its block diagram. Typical filter attenuation of the FN 258 filters is given in Figure 8.11.

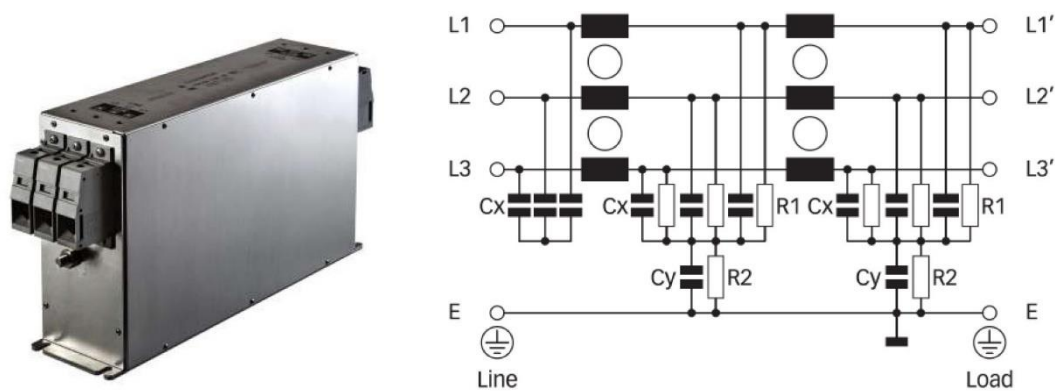


**Figure 8.10. Schaffner FN 258-100-35 filter and its block diagram (courtesy of Schaffner) [79].**

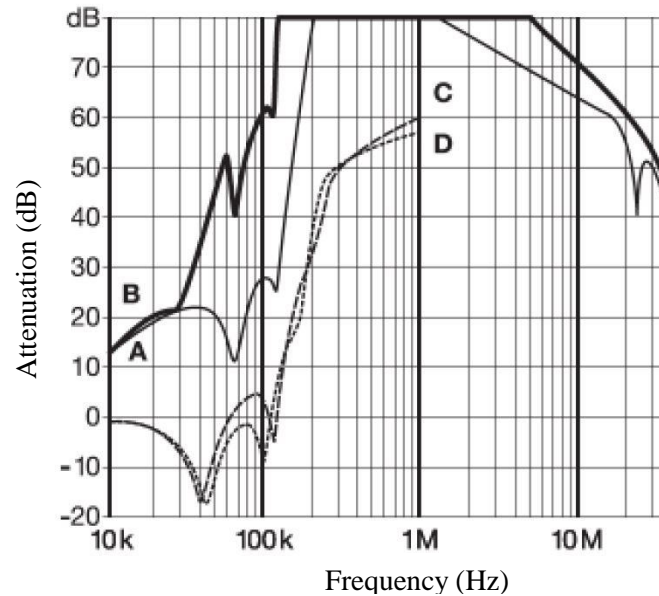


Figure 8.11. Typical filter attenuation of Schaffner FN 258 filters (courtesy of Schaffner) [79].

## 8.5 DC Power System

An uninterruptible auxiliary power system feeds the safety and monitoring circuitry at 24VDC. It is constituted of two parallel DC power systems that each can provide up to 40A rated current (-25°C to 70°C), and up to 215A peak current for 12ms. Each DC power system constitutes of a 3Phase-480AC to 24VDC power supply, a 24VDC to 24VDC electronic switchover unit, and a 38Ah 24VDC battery.

### 8.5.1 Power Supply

Quint-PS/3 AC/24DC/40 power supply units from Phoenix Contact were selected due to a compact size and Selective Fuse Breaking (SFB) technology. With the SFB technology, a current reserve with six times the nominal current for 12ms, is available. With this dynamic power reserve, the faulty current path is disconnected, whereby the load connected in parallel continues to operate without interruption. Therefore, the fault is located, and important system parts continue to operate. Comprehensive diagnostics are provided through constant monitoring of output voltage and current. This preventive function monitors critical operating modes and reports them to the control unit before an error can occur. These units can perform normally even in the event of a permanent phase failure and can handle surge voltages up to 6kV using an integrated gas arrester. Table 8.6 summarizes the most important technical data of the power supply unit. Figure 8.12 and Figure 8.13 show the block diagram and connection of the power supply to different mains networks.

Table 8.6. Technical data of Quint-PS/ 3AC/24DC/40 power supply [182].

Input nominal voltage range	$3 \times 400VAC$ to $500VAC$
Input AC frequency range	45Hz to 65Hz
Nominal output voltage	$24VDC \pm 1\%$
Output current	40A ( $-25^{\circ}C$ to $70^{\circ}C$ ) 45A (with POWER BOOST, $-25^{\circ}C$ to $40^{\circ}C$ continuously) 215A (with SFB technology, 12 ms)
Residual ripple	$< 40mVPP$ (with nominal values)
Peak switching voltages	$< 5mVPP$ (at nominal values, 20 MHz)
Discharge current to PE	$< 3.5mA$

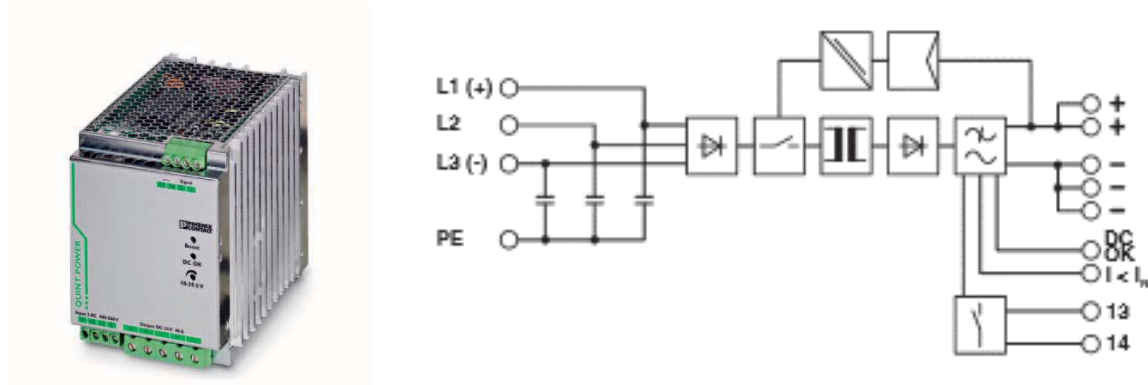


Figure 8.12. Quint-PS/ 3AC/24DC/40 power supply and its block diagram (courtesy of Phoenix Contact) [182].

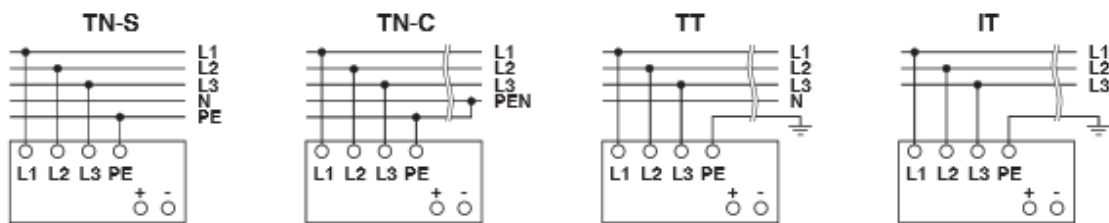


Figure 8.13. Connection of Quint-PS/ 3AC/24DC/40 power supply to different mains networks (courtesy of Phoenix Contact) [182].

### 8.5.2 Electronic Switchover Unit

In the event of mains breakdowns or failures, the electronic switchover unit switches to battery operation without interruption so that loads continue to be consistently supplied. The Quint-UPS/ 24DC/24DC/40 from Phoenix Contact is equipped with IQ technology for maximum system availability. This intelligent battery management technology optimizes and keeps the user informed on

the remaining runtime, the current state of charge, service life and performance of the power storage device. Table 8.7 summarizes the technical data of the Quint-UPS/ 24DC/24DC/40 unit.

Table 8.7. Technical data of Quint-UPS/ 24DC/24DC/40 switchover unit [80].

Input nominal voltage range	18 to 30VDC
Input nominal current	51.9A (maximum) 66mA(no load) 6.9A(charging process)
Nominal output voltage	24VDC (buffered)
Output current	40A (−25°C to 50°C) 45A (Battery operation) In mains mode, output current is limited according to connected upstream power supply unit (see Section 8.5.1)
Output power	960W
Buffer time	1, 2, 3, 5, 10, 15, 20 minute(s) 0.5 minutes default
Power storage charge voltage	24VDC
Power storage charge current	0.2A to 5A

In mains mode (DC input voltage present), the output voltage corresponds to the applied input voltage. In the event of a failure of the voltage supply, switching to battery mode takes place without interruption. The output voltage is not directly dependent on the battery voltage. The IQ technology of this unit detects the battery automatically and optimally adjusts the charging characteristics to ensure fastest possible recharging and maximum availability. Figure 8.14 shows the block diagram of Quint-UPS/ 24DC/24DC/40.

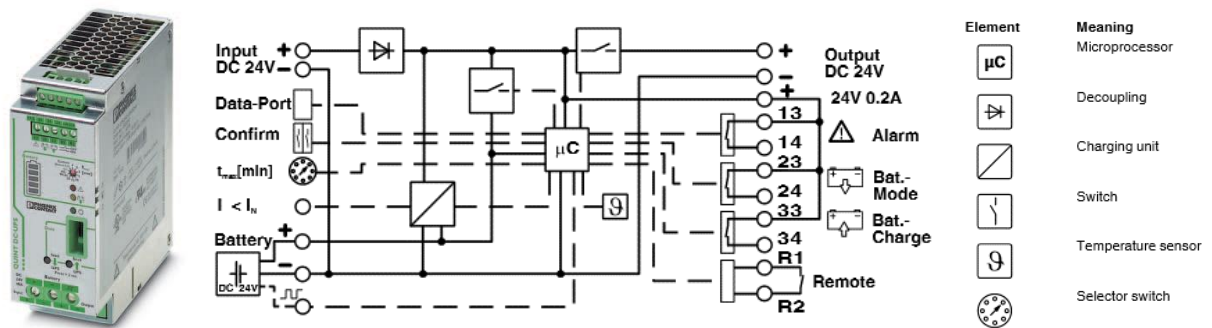


Figure 8.14. Quint-UPS/ 24DC/24DC/40 and its block diagram (courtesy of Phoenix Contact) [80].

### 8.5.3 Power Storage Unit

The power storage unit of the DC power system constitutes of two 12 V battery modules and an electronic monitoring unit. UPS-BAT/VRLA/24DC/38AH power storage units from Phoenix Contact are compatible with IQ technology of Quint-UPS/ 24DC/24DC/40 units. Each power storage unit provides 38 Ah of energy that can feed the VT Roller Rig with 40 A load at 24 VDC load for 35 minutes (72 minutes at 20 A). Figure 8.15 shows the block diagram of the UPS-BAT/VRLA/24DC/38AH power storage unit.

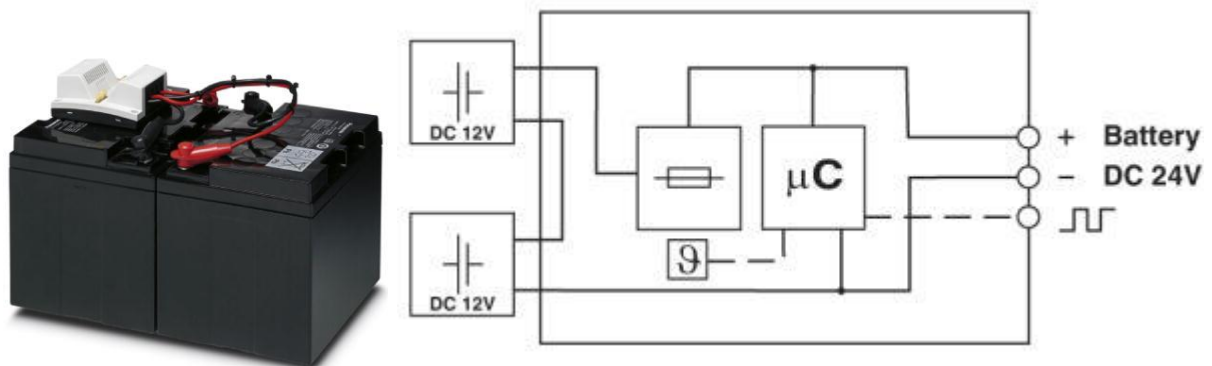


Figure 8.15. UPS-BAT/VRLA/24DC/38AH power storage unit and its block diagram (courtesy of Phoenix Contact) [80].

## 8.6 Relays

All safety relays described below meet the requirements of EN 60947-5-1, EN 60204-1, and VDE 0113-1, and may be used in applications with E-STOP pushbuttons, safety gates, and light beam barriers. Manufacturers provide the UL, TUV, and CCC certifications to ensure proper testing and inspection of each acquired component.

### 8.6.1 Logic ON-OFF Circuit

A 4-pole-double-throw (4PDT) mechanical relay controls the Logic ON-OFF circuit. PR2-R relay from Phoenix Contact is a completely assembled coupling relay for universal use. The coil and contact connections of the relay are located opposite one another and thus meet the requirements of IEC 60664, IEC 62103, and EN 50178. The coil of the PR2-RSC3-LDP-24DC/4X21AU relay has a nominal input voltage of 24VDC with a typical input current of 38mA. Contacts are made of highly durable hard gold-plated AgNi. Contacts can withstand up to 250V AC/DC with limiting continuous current of 5A. Relay contacts can tolerate up to 12A inrush current for 15ms.

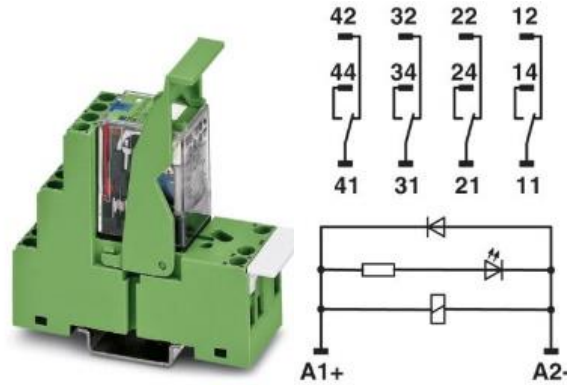


Figure 8.16. PR2-R 4PDT relay and its block diagram for the Logic ON-OFF circuit (courtesy of Phoenix Contact [183]).

### 8.6.2 Emergency Stop Circuit

The emergency stop circuit is constituted of a dual-input solid-state relay with two normally-open contacts and a normally-close contact. This relay is extended with another solid-state relay with eight normally-open contacts and one normally-closed contact. PNOZ S4 safety relays from Pilz are specifically designed for monitoring E-Stop pushbuttons, safety gates, and light beam devices. This device has two 24VDC inputs, three instantaneous NO, one instantaneous NC, and one auxiliary semiconductor outputs. The relay meets the following safety requirements:

- The circuit is equipped with redundant built-in self-monitoring that detects faults in the reset and input circuit, shorts between the input contacts,
- The safety function remains effective in the case of a component failure
- The correct opening and closing of the safety function relays are tested automatically in each on-off cycle
- The unit has an electronic fuse

The relay can be operated in both automatic and manual reset modes. In the automatic mode, the unit is active once the input circuit has been closed. In the manual mode, however, the unit is active once the input circuit is closed and then the reset circuit is closed (while illuminated momentarily pushbutton). Figure 8.17 shows the S4-S11 combination and Figure 8.18 shows the block diagram of both units.



**Figure 8.17.** Connection of PNOZ S4 relay (left) and S11 contact expansion module (right) for emergency stop circuit (courtesy of Pilz Automation Safety) [184,185].

PNOZ S11 expansion unit provides eight instantaneous NO and one auxiliary instantaneous NC contacts. The contact expander module expands the PNOZ S4 circuit. As the output relays are monitored with the S4’s feedback loop, the safety functions on the existing circuit are transferred to the contact expander module. The safety functions remain effective in the case of a component failure.

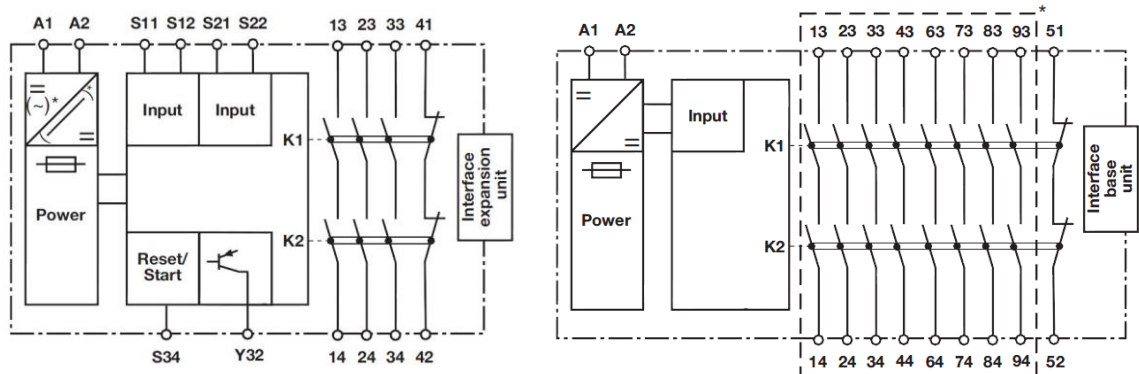


**Figure 8.18.** Block diagrams of PNOZ S4 relay (left) and PNOZ S11 expansion module (right, courtesy of Pilz Automation Safety) [184,185].

### 8.6.3 STO Circuit

The safety switch gears used in this circuit include a programmable solid-state safety relay with two input channels, an extension solid-state relay with 3 normally-open contacts, and another contact expander solid-state relay with 8 normally-open contacts.

PNOZmulti Mini mm0.1p relay is a configurable safety controller that can implement up to three different safety tasks. This device provides twelve digital inputs, eight configurable inputs/outputs, four test pulse outputs, and four semiconductor outputs. The function of the inputs and outputs of the control system depends on the safety circuit created using the PNOZmulti Configurator (Pilz Software). A chip card is used to download the safety circuit to the base unit. The base unit has 2 microcontrollers that monitor each other. They evaluate the input circuits on the base unit and expansion modules and switch the outputs on the base unit and expansion modules accordingly.

Two expansion modules provide enough contacts for the STO circuit. As mentioned in Section 8.6.2 PNOZ S11 provides eight instantaneous NO and one auxiliary instantaneous NC contacts. PNOZ S7.1 adds three instantaneous NO contacts to the circuit. Similar to S11, S7.1's function normally even in the case of a component failure. PNOZ mm0.1p monitors the outputs and transfers the safety functions of the rest of the circuit to the S7.1. Figure 8.19 shows the connection of the three units. Figure 8.20 provides their block diagrams used for wiring and installation.

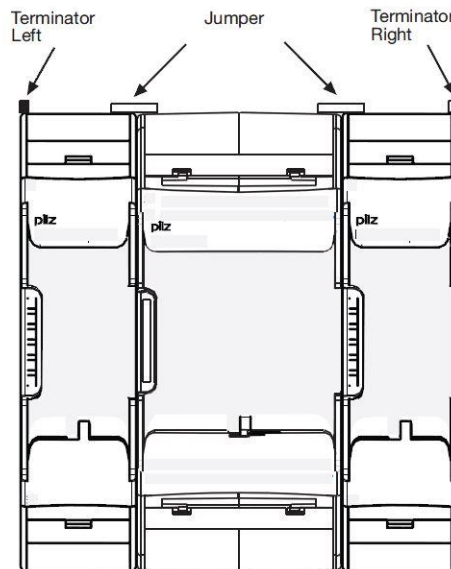


**Figure 8.19. Configuration of PNOZ mm0.1p relay (center), S11 and S7.1 contact expansion modules for STO circuit (courtesy of Pilz Automation Safety) [186].**

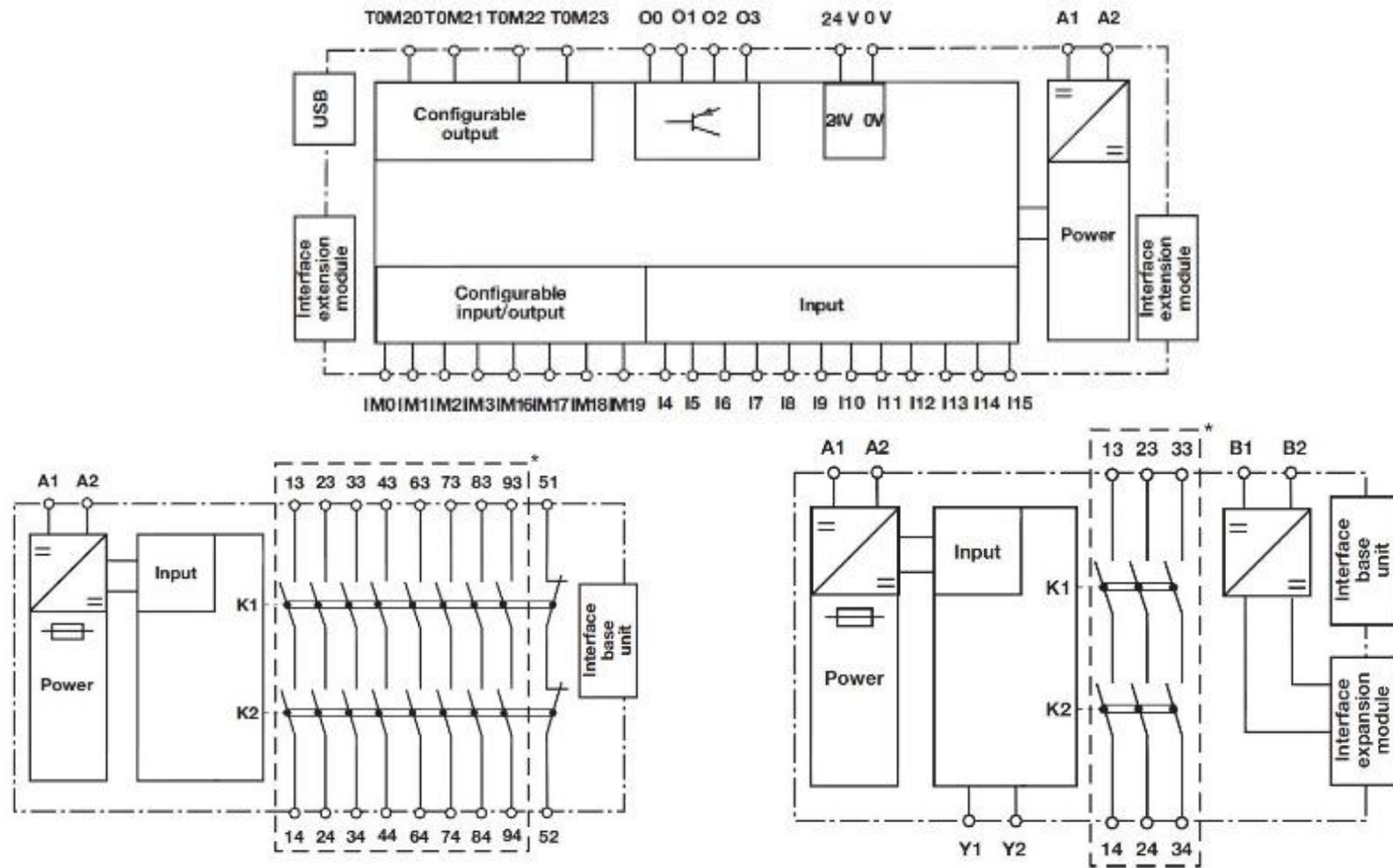
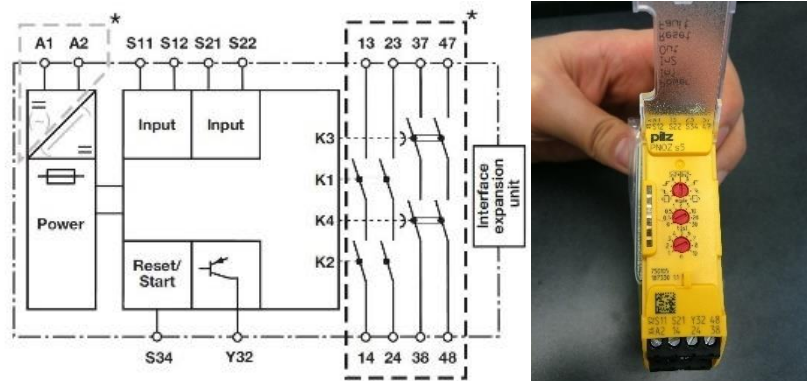


Figure 8.20. Block diagrams of PNOZ mm0.1p relay (top), PNOZ S11 expansion module (left), and PNOZ S7.1 expansion module (right, courtesy of Pilz Automation Safety) [185–187].

### 8.6.4 Motor-Short Dynamic Braking Circuit

The Motor-Short Dynamic Braking circuit is equipped with a time delayed relay that allows for performing Category 1 stops even when the emergency stop switch is depressed. This is possible by giving the servo amplifiers enough time to stop the motors controlled before the Motor-Short Dynamic Brakes kick in. The default setting for the time delay relay is 0ms for providing the highest degree of safety. This setting should only be changed if the user is fully aware of the risks and understands the operational parameters of the servo amplifiers.

This circuit is controlled by a dual-channel time-delayed solid-state relay with UL, CE, and TUV certifications. The PNOZ S5 safety relay from Pilz provides two 24VDC inputs, two instantaneous NO, two time-delayed de-energisation NO, and one auxiliary semiconductor outputs. Operating modes of the relay and delay times can be selected via the rotary switches on the front panel of the unit. The relay is equipped with built-in self-monitoring that automatically tests the correct opening and closing of the safety function relay in each ON-OFF cycle. This allows the safety function to remain effective even in case of a component failure. Figure 8.21 shows the block diagram of the relay and a close view of the adjustable switches.



**Figure 8.21. Block diagram and adjustable switches of the PNOZ S5 relay for Motor-Short Dynamic Braking circuit (courtesy of Pilz Automation Safety) [188].**

The relay can be operated in both automatic and manual reset modes. In the automatic mode, the unit is active once the input circuit has been closed. In the manual mode, however, the unit is active once the input circuit is closed and then the reset circuit is closed (while illuminated momentarily pushbutton).

### 8.6.5 RTO Circuit

The servo amplifiers will open the RTO contacts if a fault is generated. However, an intermittent circuit is required to integrate the VT Roller Rig emergency stop circuit and the two RTO contacts of the servo amplifiers. The output of this circuit would be turned off in case any fault occurs, internally or externally. This signal is a summarized representation of all safety and monitoring systems of the Rig. For the initial tests with the VT Roller Rig, this signal is fed into the shunt tripping circuitry of the I-Line panel (mains 3-phase circuit breakers). PNOZ S3 relay of Pilz meets up with EN ISO 13849-1 requirements. It provides two positive-guided instantaneous NO contacts and an auxiliary semiconductor output. If needs be, the S3 can be expanded with contact expander modules such as S11 or S7.1.

Similar to PNOZ S4 and S5 units, S3 can be operated in both automatic and manual reset modes. The automatic mode only requires closing the input circuit for reactivation. However, the manual mode requires implementation of a redundant reset circuit that should be closed for resetting the relay. Figure 8.22 shows the block diagram and front view of the S3 relay.

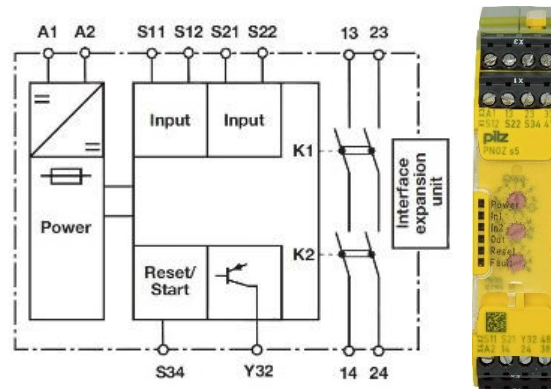


Figure 8.22. Block diagram and front view of the PNOZ S3 relay for the RTO circuit (courtesy of Pilz Automation Safety) [189].

### 8.6.6 Hardware-Enable Circuit

This circuit constitutes of a dual input solid-state relay with two NO contacts, and a solid-state extension relay with eight NO contacts. For consistency between the relay modules, PNOZ S5 and PNOZ S11 were selected for this application. Extensive discussion on these units is available in previous sections of this chapter.

An important factor in selecting the operation mode of the relays is the time behavior of the unit upon opening and closing the input circuits. The time behavior of PNOZ S3, S4, S5, and mm0.1p solid-state relays are almost identical to each other. However, time-delays should be fully understood since they

postpone the activation of important safety features. Figure 8.23 summarizes the time behavior of the VT Roller Rig relays.

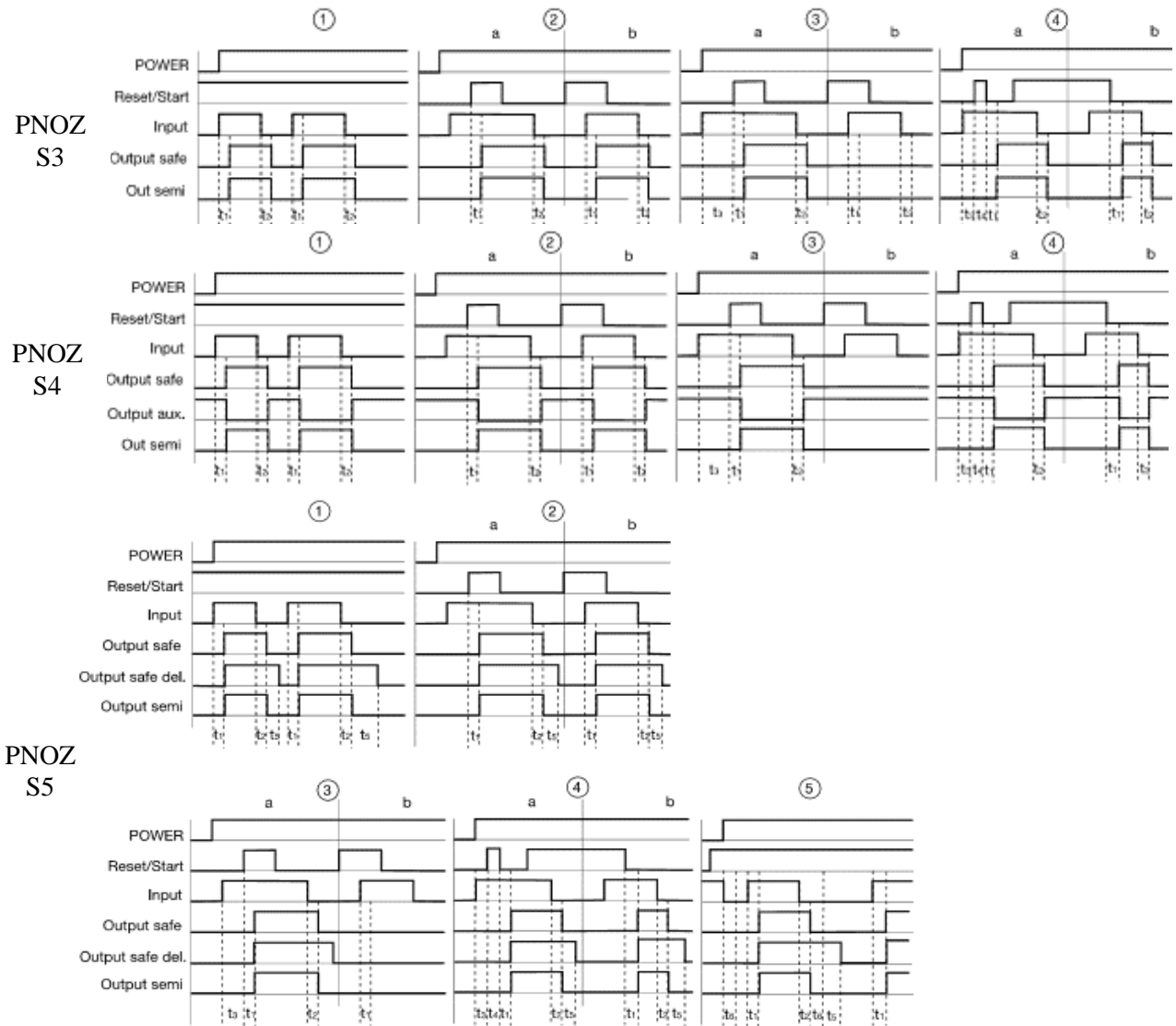


Figure 8.23. Time behavior of PNOZ S3, S4, and S5 solid-state safety relays (courtesy of Pilz Automation Safety) [184,188,189].

**Table 8.8. Keywords used for describing the time behavior of the solid-state safety relays.**

Keyword	Meaning
Power	Supply voltage
Reset/Start	Reset circuit
Input	Input circuits
Output safe	Safety contacts
Output aux	Auxiliary contacts
Output semi	Semiconductor output
1	Automatic reset
2	Manual reset
3	Monitored reset with rising edge
4	Monitored reset with falling edge
5	Reset with start-up test
a	Input circuit closes before reset circuit
b	Reset circuit closes before input circuit
$t_1$	Switch-on delay
$t_2$	Delay-on de-energisation
$t_3$	Waiting period
$t_4$	Waiting period reset circuit was closed
$t_5$	Delay time
$t_6$	Minimum time safety gates open

## 8.7 Regenerative Resistors

Resistor manufacturer recommends up to 130% of the calculated power for maximum product life and failure-free operation. Increasing the power to %160 of rated power of the resistor leads danger of excessive heat and destruction of the resistors. Based on the calculations provided in Section 5.5.1, 6kW rated power per regenerative resistor is used for selecting the proper part. BAS(U) 6000-10 Kollmorgen regenerative resistors are manufactured as plate resistors and have a resistance of 10 $\Omega$ , rated power of 6kW, and maximum power of 9.6kW. This resistor is the biggest regenerative resistors in the series provided by the manufacturer. Figure 8.24 shows the acquired component.



Figure 8.24. BAS(U) 6000-10 Kollmorgen regenerative resistor.

The surface temperature of these resistors can go up to 300K during normal operation. Serious burns can be caused by touching either sides of the heat sinks around the resistor. Figure 8.25 shows the surface temperature of the resistor in dependence of continuous dissipation. Both regenerative resistors of the VT Roller Rig are enclosed within the control cabinet for preventing any unintentional touch. Safety instructions require 1000mm to the nearest component on the back of the resistor, and 300mm on the sides.

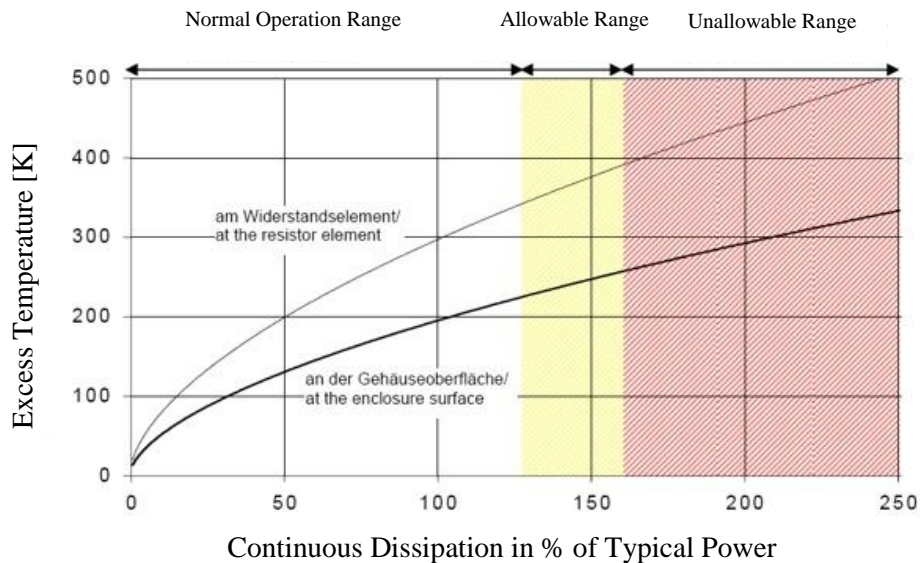


Figure 8.25. Surface temperature of the regenerative resistors relative to continuous dissipation (courtesy of Kollmorgen) [190].

### 8.8 Motor-Short Resistors

Based on the calculations provided in Section 5.5.2 of this document, an  $8.2\Omega$  resistor per phase per servo amplifier can stop the VT Roller Rig from  $\omega_1 = 2000rpm$ , in 1.73s, assuming no

friction in the gearboxes. The peak brake torque required will be 68Nm. In such case, nominal continuous watts on each resistor based on 10x peak to continuous rating will be 505W. Not every desirable size of dynamic resistor is available off the shelf. With the exception of a few, those that are available off the shelf have more than 6 weeks lead time. The main reason for this long lead time is that these components have embedded heat sinks for dissipating the generated heat, and they are only made for specific applications such as VT Roller Rig.

TE Connectivity offers modular Aluminum enclosed resistors for industrial, control, and general-purpose applications. The CJT series of resistors are advantageous to conventional ceramic resistors in terms of oscillation-resistance, safety, and weather proofing. The CJT800 has rated power of 800W in free air. Table 8.9 summarizes the technical data of these resistors and Figure 8.26 shows the actual component.

**Table 8.9. Technical data of CJT800 dynamic resistors [191].**

Resistance	8.2Ω
Rated power in free air	800W
Tolerance	±5%
Composition	<i>Wirewound</i>
Resistor element peak working voltage	1kV

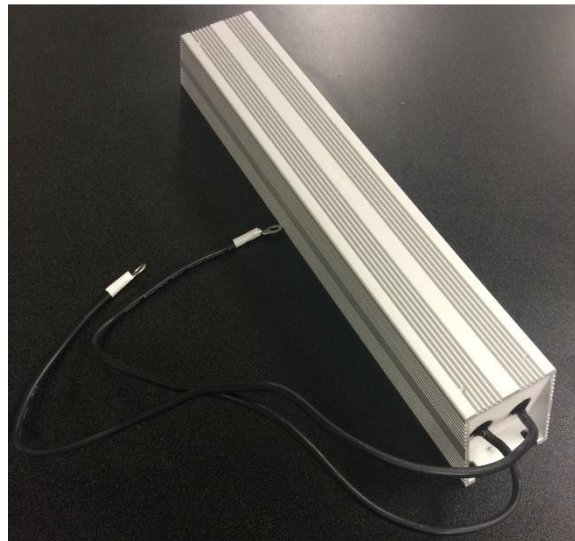


**Figure 8.26. Single CJT800 resistor. Each S772 servo amplifier requires a set of three.**

## 8.9 Contactors

An integral part of the Motor-Short Dynamic Braking circuits are the contactors that are responsible for shorting the motor leads and closing the resistor circuits. Schneider Electric 3-pole-single-throw contactors are chosen to perform this task. The TeSys D (aka Telemecanique) product series have been successfully used for motor control and resistive load applications. The LC1D40ABD component satisfies the power and current requirements calculated for Motor-Short Dynamic Brakes in Section 5.5.2. Table 8.10 summarizes the technical data of the contactor.

**Table 8.10. Technical data of LC1D40ABD 3PST-NO contactor [192].**

Switching power AC3	<i>30hp at 460/480VAC 50/60Hz for 3 – phase motors</i>
Operating voltage	$\leq 690 \text{ VAC } 25 \text{ to } 400\text{Hz}$
Resistive load current	90A
Contact configuration	<i>3PST – NO</i>
Control circuit type	<i>Built – in bidirectional peak limiting diode suppressor</i>
Coil voltage	24VDC
Time constant	34ms

## 8.10 Fuses and Circuit Breakers

Table 8.11 summarizes all the fuses and circuit breakers used in different circuits of the VT Roller Rig. Particular attention should be paid to the standard requirements for each circuit.

**Table 8.11. VT Roller Rig fuses and circuit breakers.**

Circuit	Fuse Type	Component
S772 AC Supply	80A (RK5/cc/J/T), 600VAC 200kA, time delay, UL and CSA approved	Bussmann FRS-R-80 with Eaton RM60100-3CR Block and Eaton CVRI-RH-60100 cover
AKD AC Supply	10A (J), 600VAC 200kA, time delay, UL and CSA approved	Bussmann LPJ-10SPI with Eaton CH30J3I fuse holder
Regenerative Braking	125A, 800VDC UL approved, 14 × 51mm	Bussmann FWP-125A with Eaton BH-133 fuse holder
DC-Bus link	50A, 800VDC UL approved	Bussmann FWP-50A14Fa with Eaton CH142BI finger-safe fuse holder
DC Power Supply	16A (characteristic B), 3 × 480VAC	Phoenix Contact thermomagnetic device circuit breaker - TMC 61C 16A
Holding Brake	8A (characteristic B/C), 24VDC	Phoenix Contact thermomagnetic device circuit breaker – TMC M 08A
STO	6A (characteristic B/C), 24VDC	Phoenix Contact thermomagnetic device circuit breaker - TMC 61C 06A
Hardware Enable	6A (characteristic B/C), 24VDC	Phoenix Contact thermomagnetic device circuit breaker - TMC 61C 06A
Emergency Stop	6A (characteristic B/C), 24VDC	Phoenix Contact thermomagnetic device circuit breaker - TMC 61C 06A
RTO	6A (characteristic B/C), 24VDC	Phoenix Contact thermomagnetic device circuit breaker - TMC 61C 06A
Motor-Short Braking	6A (characteristic B/C), 24VDC	Phoenix Contact thermomagnetic device circuit breaker - TMC 61C 06A

## Chapter 9. Realizable Tests with the Virginia Tech Roller Rig

The wheel-rail contact mechanics and dynamics is one of the most complex aspects of railroading. Although there is a broad, high-level understanding of *what* happens at the wheel-rail interface, much of the science behind *why* it happens is lacking. The Roller Rig that is designed and fabricated by the Virginia Tech's Railway Technologies Laboratory (RTL) is intended to provide a better understanding of the physics of the wheel-rail interface through its unique electro-mechanical configuration and highly precise instrumentation. Some of the studies that are possible with the Roller Rig include:

### 9.1 Precise Measurement of Creep-Creepage Curves

This includes measuring the:

- Influence of angle-of-attack (AoA), rail cant angle, and rail lateral shift
- Velocity-dependent coefficient of friction

The test rig is capable of controlling the differential speed (creepage) at the wheel-rail interface with a high level of precision. Also, a novel force measurement system is configured to accurately read the contact (creep) forces and moments. Therefore, the Rig is capable of conducting precise creepage-creep studies both on straight and curved tracks, for developing new models or improving the existing ones. The contact studies will be generalized to investigate the effect of angle of attack, cant angle, and a lateral shift in creep models. The rig will also shed more light on the spin creepage studies, and creep forces due to spin creepage.

Furthermore, the Rig will allow verifying theories related to velocity-dependent friction coefficient. In particular, the falling friction phenomenon (friction forces reducing at higher speeds) could be investigated extensively. Since both the rotating bodies (wheel and roller) are actively controlled, both positive and negative creepage values could be studied, and the resulting creepage-creep curves could be compared.

## 9.2 Accurate Measurement of Contact Geometry

The test rig can accurately measure the wheel-rail contact geometry to a high degree of precision that surpasses all other rigs that currently exist, worldwide. It is equipped with a state-of-the-art vision system that can provide a precise image of the interface between the wheel and rail. This high-definition imaging system is capable of precisely investigating the contact geometry using advanced image-processing methods and extracting measurements from every frame. Therefore, the area and shape of the contact patch could be recorded at every instant in time. The major and minor axes for the elliptical contact patch can then be measured from the recorded data. This also enables studying the conditions under which double-point contact occurs. Other sensory measurements will be synchronized with the vision data to measure the resulting forces accurately from the single- or double-point contact geometry.

## 9.3 Precise Evaluation of Third Body Layers

Third body layers refer to any material that is placed in between the wheel and rail interface as a third layer to the wheel and rail surface. This includes:

- Friction modifier
- Surface conditioning elements, such as water, oil, sand, leaves, etc.

The test rig can accommodate the equipment necessary for studying the effect of surface condition and friction modifiers. The rig is also capable of studying the characteristics of surface roughness and different interfacial layers at the wheel-rail contact surface, to an accuracy that is unmatched among any other equipment that is currently in existence. Other aspects of the wheel-rail contact dynamics that can be measured precisely include the slope reduction phenomenon in contact curve models and wheel/rail damage due to a contaminant at the interface.

## 9.4 Dynamic Creepage Analysis

The test rig is capable of performing a full range of dynamic creepage studies that will allow the scientists and engineers to get a better understanding of many of the fundamental aspects of the wheel-rail contact physics. The unique design that is used for the Rig enables easily controlling the cant angle, the angle of attack, and lateral displacement, among other critical parameters. A state-of-the-art instrumentation system provides precise measurement of the forces and moments that

occur as a result of the changes. This enables accurately measuring the key aspects of wheel-rail dynamics that have not been studied in the past (due to limitations of the previous roller rigs), such as the time-varying spin creepage (an important factor in the generation of squeal noise) and effect of wheel speed on traction forces.

### 9.5 Wheel-rail Vibration Analysis

The stick-slip dynamics at the wheel-rail interface can result in excessive wheel/rail wear, and noise and vibrations that are difficult to measure in the field. This applies in particular at high AoA, high adhesion, and flanging conditions. The strategic instrumentation of the Rig provides for scientific analysis of this phenomenon to unmatched accuracies, specifically as it relates to:

- Vibration analysis of wheel and rail
- Longitudinal and lateral contact stiffness

Different stick-slip conditions can be emulated for performing lateral, longitudinal, and rotational vibration analyses. The test rig has a provisional design for installing multiple accelerometers for studying wheel-roller vibrations. Modal analysis studies for finding the natural frequencies can also be conducted. The accurate load cell platform of the Rig also allows for precisely measuring the lateral and longitudinal contact stiffness of the wheel.

### 9.6 Wheel-Rail Wear Analysis

Wear is a major source of concern to the U.S. railroads and their suppliers because of its high economic impact and also the effect it has on the efficient operation of rolling stock. Better understanding of

- Rolling contact fatigue (RCF)
- Plastic flow of material under high traction, high loads

will shed light on better understanding the causes and remedies of wear at the wheel-rail interface. The unique design of the Rig and the ability to precisely change the wheel-rail contact conditions enables performing design of experiments that are necessary for better understanding wear in more realistic conditions, as compared with abstract equipment such as four-ball test machines that are often used.

The design of the Rig enables accurately studying the effect of various parameters including loading, adhesion coefficient, the angle of attack, flanging, etc. The results of such studies will lead to better rail safety and also allow the U.S. railroads to optimize their maintenance practices for reducing total life cycle costs. Other wear effects such as rail corrugation and wave-like wear at the top of the rail can also be analyzed regarding their formation mechanisms and influence of the key parameters. Mechanisms by which RCF-induced cracks initiate and grow, which are strongly related to wheel and rail wear, can also be determined by a state-of-the-art vision system that is installed on the Rig. The vision system will also allow for studying other effects, including the plastic flow of material at the contact patch.

### 9.7 Derailment Mechanics

Benefiting from the modern force, torque, acceleration, and displacement sensors, the Virginia Tech's Roller Rig enables investigating the dynamics of the wheel prior, during, and after the derailment. Because it is possible to control the wheel-rail relative motion and constraints in real time, the Rig allows studying:

- Derailment coefficient
- Wheel-climb derailment

Each parameter can be changed precisely and its effect on the forces and moments that cause derailment will be explored. Such design of experiments will allow scientists and practitioners get a better understanding of some of the track and wheel conditions that can result in derailment.

### 9.8 Hardware-in-the-loop (HIL) Operation

One of the unique aspects of the Roller Rig is the ability to perform Hardware-in-the-Loop (HIL) studies. This allows merging the Rig with rail vehicle dynamic simulation models, to bring an unprecedented level of accuracy to the models. HIL allows using the Rig in synchronization with rail vehicle simulation models, such that the output of the Rig becomes the input to the model and, conversely, the output of the model serves as input to the Rig. HIL represents the state of the art in representing complex dynamics, such as wheel-rail interface, in high-fidelity simulation models. This effort will be the first of its kind in rail vehicle dynamics modeling and testing, to the best of our knowledge.

The immediate benefits of HIL are research and engineering development in

- Advanced train control algorithms
- Traction and braking studies

A unified communication protocol between actuators, drives, and data acquisition system eliminates data conversion between these units; hence, facilitating online high-speed measurements and control. The rig will serve as a unique platform for studying advanced train control algorithms, whereby instantaneous measurements from the Rig are fed into the analytical model of the entire train to control the motion of the wheel about the rail in real time. The state-of-the-art measurement and control network used in the Rig makes the sense-to-act process as fast as the sensors' update rate.

## References

- [1] Kumar S, Alzoubi MF, Allsayyed N a. Wheel/rail adhesion wear investigation using a quarter scale laboratory testing facility. Proceedings of the 1996 ASME/IEEE Joint Railroad Conference 1966:247–54. doi:10.1109/RRCON.1996.507984.
- [2] Hosseinipour M, Meymand SZ, Craft MJ, Ahmadian M. Modeling of a roller rig for evaluation of wheel/rail contact mechanics. Proceedings of the 2014 Joint Rail Conference, Colorado Springs, CO, USA JRC2014-3842: 2014.
- [3] Meymand SZ, Hosseinipour M, Ahmadian M. Development of a roller rig for experimental evaluation of contact mechanics for railway vehicles. Proceedings of the 2015 Joint Rail Conference, San Jose, CA: 2015.
- [4] Meymand SZ, Craft MJ. APPLICATION OF ROLLER RIGS FOR STUDYING RAIL VEHICLE. Proceedings of the ASME 2013 Rail Transportation Division Fall Technical Conference, 2013, p. 1–10.
- [5] Iwnicki S. Handbook of railway vehicle dynamics. 2006.
- [6] Jaschinski A. On the application of similarity laws to a scaled railway bogie model. TU Delft, 1990.
- [7] Matsudaira T, Matsui N. Problems on hunting of railway vehicle on test stand. Journal of Engineering for Industry 1969.
- [8] Kim M, Park J, You W. Construction of Active Steering System of the Scaled Railway Vehicle. International Journal of Systems Applications, ... 2008;2:217–26.
- [9] Sweet LM, Karmel a., Fairley SR. Derailment Mechanics and Safety Criteria for Complete Rail Vehicle Trucks. Vehicle System Dynamics 2007;10:203–6. doi:10.1080/00423118108968672.

- [10] Hahn H, Siegl G. Simulation und experimentelle Verifikation des Rad/Schiene-Rollprüfstands. *Ingenieur-Archiv* 1987;57:329–48. doi:10.1007/BF00533946.
- [11] Carling D. Locomotive testing stations. vol. 45. 1972.
- [12] Eadie DT, Elvidge D, Oldknow K, Stock R, Pointner P, Kalousek J, et al. The effects of top of rail friction modifier on wear and rolling contact fatigue: Full-scale rail–wheel test rig evaluation, analysis and modelling. *Wear* 2008;265:1222–30. doi:10.1016/j.wear.2008.02.029.
- [13] Stock R, Eadie DT, Elvidge D, Oldknow K. Influencing rolling contact fatigue through top of rail friction modifier application – A full scale wheel–rail test rig study. *Wear* 2011;271:134–42. doi:10.1016/j.wear.2010.10.006.
- [14] Zhang W, Chen J, Wu X, Jin X. Wheel/rail adhesion and analysis by using full scale roller rig. *Wear* 2002;253:82–8. doi:10.1016/S0043-1648(02)00086-8.
- [15] Miyamoto M. JR rolling stock testing plant capable of testing at a speed of 500 km/h. *Q RTRI* 1991;32:211–2.
- [16] Pfaffl L, Althammer K. Versuchsanlage Rollenprüfstand. *PfafflEisenbahntechnische Rundschau* 1976;25:663–76.
- [17] D. Lubke, M. Mittermaier LP and FZ. Ein Rollenprüfstand zur Erforschung der Rad/Schiene-Technik. *ZEV Glasers Annalen* 1976;100:295–305.
- [18] W. Zhang, H. Dai ZS and JZ. Handbook of railway vehicle dynamics - Chapter 14: Roller Rigs, CRC press, Taylor & Francis Group:Boca Raton, FL; 2006.
- [19] Fries RH. Estimation of transit rail vehicle parameters from roller rig tests. Arizona State University, 1983.
- [20] Cooperrider NK, Law EH, FRIES RH, HAQUE I, Arnold G, Nelson S. TRANSIT CAR DEMONSTRATION TEST PROGRAM ON THE ROLL DYNAMICS UNIT. VOLUME I: STATE-OF-THE-ART-CAR (SOAC) CREEP FORCES AND DYNAMIC RESPONSE ON THE ROLL DYNAMICS UNIT 1982.
- [21] Dukkupati R V. Lateral stability analysis of a railway truck on roller rig. *Mechanism and Machine Theory* 2001;36:189–204. doi:10.1016/S0094-114X(00)00017-3.

- [22] Dukkipati R V. MODELLING AND SIMULATION OF THE HUNTING OF A THREE-PIECE RAILWAY TRUCK ON NRC CURVED TRACK SIMULATOR. THE DYNAMICS OF VEHICLES ON ROADS AND ON TRACKS 1994.
- [23] DUKKIPATI R V. Lateral Stability Simulation of a Rail Truck on Roller Rig. JSME International Journal Series C 2002;45:168–75. doi:10.1299/jsmec.45.168.
- [24] Smith CAM, Dukkipati R V., Canada RL, Laboratory DVD, Laboratory NRCCD of MER. The NRC Curved Track Simulator and Its Potential Use. National Research Council Canada; 1983.
- [25] Jaschinski A, Chollet H, Iwnicki S, Wickens A, Wurzen J. The Application of Roller Rigs to Railway Vehicle Dynamics. Vehicle System Dynamics 1999;31:345–92. doi:10.1076/vesd.31.5.345.8360.
- [26] Allotta B, Conti R, Meli E, Ridolfi A. Modeling and Control of a Full-Scale Roller-Rig for the Analysis of Railway Braking Under Degraded Adhesion Conditions. IEEE Transactions on Control Systems Technology 2015;23:186–96. doi:10.1109/TCST.2014.2320672.
- [27] Jin XS, Zhang WH, Zeng J, Zhou ZR, Liu QY, Wen ZF. Adhesion experiment on a wheel/rail system and its numerical analysis. Proceedings of the Institution of Mechanical Engineers, Part J: Journal of Engineering Tribology 2004;218:293–304. doi:10.1243/1350650041762631.
- [28] Kalousek J. Development of a 1/8 Scale Dual Disc-On-Disc Rail/Wheel Wear Testing Facility. Canadian Metallurgical Quarterly 2013.
- [29] Wheel-Rail Interface Handbook. Elsevier; 2009.
- [30] CHOLLET H. ETUDE EN SIMILITUDE MECANIQUE DES EFFORTS TANGENTS AU CONTACT ROUE-RAIL. 1991.
- [31] Jochim M. Analyse der Dynamik eines Schienenfahrzeuges. TU-Munchen and DLR, 1987.
- [32] Iwnicki S, Shen Z. Collaborative railway roller rig project. Proceedings of SEFI World Conference on Engineering Education, Portsmouth: 1992.

- [33] IWICKI SD, WICKENS AH. Validation of a MATLAB Railway Vehicle Simulation Using a Scale Roller Rig. *Vehicle System Dynamics* 1998;30:257–70. doi:10.1080/00423119808969451.
- [34] Kalivoda J, Bauer P. Roller Rig Implementation of Active Wheelset Steering 2012:1–13.
- [35] Kalivoda J, Bauer P. Scaled Roller Rig Experiments with a Mechatronic Bogie Mechatronic test bogie 2014:1–12.
- [36] Gretschel M, Jaschinski A. Design of an Active Wheelset on a Scaled Roller Rig. *Vehicle System Dynamics* 2004;41:365–81. doi:10.1080/00423110412331300336.
- [37] Rovira A, Roda A, Marshall MB, Brunskill H, Lewis R. Experimental and numerical modelling of wheel–rail contact and wear. *Wear* 2011;271:911–24. doi:10.1016/j.wear.2011.03.024.
- [38] Rovira A, Roda A, Lewis R, Marshall MB. Application of Fastsim with variable coefficient of friction using twin disc experimental measurements. *Wear* 2012;274–275:109–26. doi:10.1016/j.wear.2011.08.019.
- [39] Petersen D, Link R, Fletcher D, Beynon J. Development of a Machine for Closely Controlled Rolling Contact Fatigue and Wear Testing. *Journal of Testing and Evaluation* 2000;28:267. doi:10.1520/JTE12104J.
- [40] Bosso N, Zampieri N. Real-time implementation of a traction control algorithm on a scaled roller rig. *Vehicle System Dynamics* 2013;51:517–41. doi:10.1080/00423114.2012.750001.
- [41] Bosso N, Gugliotta A, Somà A. Dynamic identification of a 1:5 scaled railway bogie on roller rig. *WIT Transactions on the Built Environment*, vol. 88, 2006, p. 829–38. doi:10.2495/CR060811.
- [42] Bosso N, Zampieri N. Experimental and Numerical Simulation of Wheel-Rail Adhesion and Wear Using a Scaled Roller Rig and a Real-Time Contact Code. *Shock and Vibration* 2014;2014:1–14. doi:10.1155/2014/385018.
- [43] Matsumoto A, Sato Y, Ono H, Wang Y, Yamamoto M, Tanimoto M, et al. Creep force characteristics between rail and wheel on scaled model. *Wear* 2002;253:199–203.

doi:10.1016/S0043-1648(02)00100-X.

- [44] Liu QY, Zhang B, Zhou ZR. An experimental study of rail corrugation. *Wear* 2003;255:1121–6. doi:10.1016/S0043-1648(03)00213-8.
- [45] Matsumoto A, Sato Y, Ono H, Tanimoto M, Oka Y, Miyauchi E. Formation mechanism and countermeasures of rail corrugation on curved track. *Wear* 2002;253:178–84. doi:10.1016/S0043-1648(02)00097-2.
- [46] Meli E, Ridolfi A. An innovative wheel–rail contact model for railway vehicles under degraded adhesion conditions. *Multibody System Dynamics* 2013;33:285–313. doi:10.1007/s11044-013-9405-4.
- [47] Meli E, Ridolfi A, Rindi A. An innovative degraded adhesion model for railway vehicles: development and experimental validation. *Meccanica* 2013;49:919–37. doi:10.1007/s11012-013-9839-z.
- [48] Allotta B, Meli E, Ridolfi A, Rindi A. Development of an innovative wheel–rail contact model for the analysis of degraded adhesion in railway systems. *Tribology International* 2014;69:128–40. doi:10.1016/j.triboint.2013.09.013.
- [49] Eom B-G, Kang B-B, Lee HS. A study on running stability assessment methods for 1/5 small scaled bogie of saemaul using small-scaled derailment simulator. *International Journal of Precision Engineering and Manufacturing* 2013;14:589–98. doi:10.1007/s12541-013-0079-x.
- [50] Eom B-G, Kang B-B, Lee H-S. A Running Stability Test of 1/5 Scaled Bogie using Small-Scaled Derailment Simulator. *Journal of the Korean society for railway* 2012;15:9–16. doi:10.7782/JKSR.2012.15.1.009.
- [51] Keylin A. Differences between tangent track and roller rig in terms of normal and tangent contact. Virginia Tech., 2013.
- [52] Meymand SZ. Development of a testing facility for experimental investigation of wheel-rail contact mechanics and dynamics. Virginia Polytechnic and State University, 2015.
- [53] Guan Q, Zeng J, Jin X. An angle of attack-based derailment criterion for wheel flange climbing. *Proceedings of the Institution of Mechanical Engineers, Part F: Journal of Rail*

- and Rapid Transit 2013;228:719–29. doi:10.1177/0954409713490149.
- [54] Elkins J, Wu H. ANGLE OF ATTACK AND DISTANCE-BASED CRITERIA FOR FLANGE CLIMB DERAILMENT. THE DYNAMICS OF VEHICLES ON ROADS AND ON TRACKS - SUPPLEMENT TO VEHICLE SYSTEM DYNAMICS, VOLUME 33. PROCEEDINGS OF THE 16TH IAVSD SYMPOSIUM HELD IN PRETORIA, SOUTH AFRICA, AUGUST 30 - SEPTEMBER 3, 1999, 2000.
- [55] Weinstock HERBERT. Wheel climb derailment criteria for evaluation of rail vehicle safety. Proceedings of the ASME winter annual meeting, 1984.
- [56] Hosseinipour M, Meymand SZ, Ahmadian M. Vibration Analysis for Improving Powertrain Design and Contact Measurements of a Roller Rig. 2015 Joint Rail Conference, ASME; 2015, p. V001T10A002. doi:10.1115/JRC2015-5622.
- [57] Seherr-Thoss H, Schmelz F, Aucktor E. Universal joints and driveshafts. 1998.
- [58] Starbatty F, Richter H. Length-adjustable shaft. US Patent 8,556,733 2013;2.
- [59] Park J-H, Koh H-I, Hur H-M, Kim M-S, You W-H. Design and analysis of an active steering bogie for urban trains. Journal of Mechanical Science and Technology 2010;24:1353–62. doi:10.1007/s12206-010-0341-4.
- [60] Watanabe K, Kawakatsu T, Nakao S. Kinematic and Static Analyses of Tripod Constant Velocity Joints of the Spherical End Spider Type. Journal of Mechanical Design 2005;127:1137. doi:10.1115/1.1909205.
- [61] Baron E. NVH phenomena in constant-velocity joints—a 3-fold approach. I Mech E 1992;C389:51– 60.
- [62] Serveto S, Mariot J-P, Diaby M. Modelling and measuring the axial force generated by tripod joint of automotive drive-shaft. Multibody System Dynamics 2007;19:209–26. doi:10.1007/s11044-007-9091-1.
- [63] Mariot J-P, K’nevez J-Y, Barbedette B. Tripod and Ball Joint Automotive Transmission Kinetostatic Model Including Friction. Multibody System Dynamics 2004;11:127–45.
- [64] Kadota T. Ball fixed type constant velocity joint having low rotational backlash. US Patent 5,855,519 1999.

- [65] Teschl G. Ordinary differential equations and dynamical systems. 2012.
- [66] Campos R, Arciniega G. A limit-cycle solver for nonautonomous dynamical systems. *Revista Mexicana de Física* 2006;9.
- [67] Bose BK. Modern Power Electronic sand AC Drives. N.J.: Prentice-Hall; 2002.
- [68] Kollmorgen Corporation. Kollmorgen AKM Servomotor Selection Guide with AKD Servo Drive Systems 2013:17–54.
- [69] Meirovitch L. Distributed-Parameter Systems: Approximate Methods. Fundamentals of Vibration, New York, NY: McGraw Hill; 2001.
- [70] Chudnovsky, V., D. Kennedy, A. Mukherjee and JW. ModelingFlexible Bodies in SimMechanics. *MATLABDigest* 2006;14.
- [71] Kollmorgen. ServoStar 600 Instructions Manual. 2010.
- [72] International Electrotechnical Commission. IEC 60364. 2005.
- [73] Kollmorgen. Digital Servo Amplifier S748 to S772 Instruction Manual. 2015.
- [74] International Electrotechnical Commission. IEC 61800. 2015.
- [75] Apalachian Power Company. Guide for Electric Service and Meter Installation 2014. [https://www.appalachianpower.com/global/utilities/lib/docs/builders/meter/WV\\_Guide\\_to\\_Electric\\_Service.pdf](https://www.appalachianpower.com/global/utilities/lib/docs/builders/meter/WV_Guide_to_Electric_Service.pdf) (accessed May 17, 2016).
- [76] American Electric Power. Requirements for Connection of New Facilities or Changes to Existing Facilities Connected to the AEP Transmission System 2014. [https://www.aep.com/about/codeofconduct/OASIS/TransmissionStudies/Requirements/AEP\\_Interconnection\\_Requirements\\_Rev1.pdf](https://www.aep.com/about/codeofconduct/OASIS/TransmissionStudies/Requirements/AEP_Interconnection_Requirements_Rev1.pdf) (accessed May 17, 2016).
- [77] Aoyama T, Shibata Y, Kanie T, Noro Y, Takeo T. Adaptive Compensation Method for the Temperature Dependence of RF Transformer Isolation. *Journal of International Council on Electrical Engineering* 2012;2:358–63. doi:10.5370/JICEE.2012.2.4.358.
- [78] Eaton. K-Factor transformers for low voltage electrical harmonics 2016. <http://www.eaton.com/Eaton/ProductsServices/Electrical/ProductsandServices/ElectricalDistribution/Transformers/LowVoltageDry-TypeDistribution/K-Factor/> (accessed May 17,

- 2016).
- [79] Schaffner. 3-Phase Filters FN 258 Book-style EMC/RFI Filter for Inverters and Power Drive Systems. 2016.
- [80] Phoenix Contact. Quint-UPS/24dc/24dc/40. 2011.
- [81] Stephens L. Wiring and Cabling Guideline & Specifications. 2012.
- [82] Caniggia S, Maradei F. SPICE-Like Models for the Analysis of the Conducted and Radiated Immunity of Shielded Cables. IEEE Transactions on Electromagnetic Compatibility 2004;46:606–16. doi:10.1109/TEMC.2004.837841.
- [83] Ott HW. Ground - A Path for Current Flow 1979:167–70.
- [84] Stephens L. Grounding and Shielding Existing Equipment. Kollmorgen White Paper 2012:1–6.
- [85] Pellemounter D. Practical Instructions for Proper Grounding. Advanced Energy Industries, Inc White Paper 2013.
- [86] Rich A. Shielding and Guarding APPLICATION NOTE. Analog Devices 1983;AN-347:1–6.
- [87] González Arteché FJ. EMC: A mapping for the CMS experiment. Oviedo U., 2004.
- [88] Paul CR. The concept of dominant effect in EMC. IEEE Transactions on Electromagnetic Compatibility 1992;34:363–7. doi:10.1109/15.155857.
- [89] Fluke. Fluke 434-II/435-II/437-II Users Manual. 2016.
- [90] Ott HW. Noise reduction techniques in electronic systems. 1988.
- [91] Schlicke HM. Electromagnetic compossibility: applied principles of cost-effective control of electromagnetic interference and hazards. New York : M. Dekker,; 1982.
- [92] Kaiser KL. Electromagnetic Compatibility Handbook. 2004.
- [93] Mardiguan M. Controlling radiated emissions by design. Van Nostrand Reinhold; 1992.
- [94] Kerkman RJ, Skibinski GL, Schlegel DW. AC drives: year 2000 (Y2K) and beyond. APEC '99. Fourteenth Annual Applied Power Electronics Conference and Exposition.

- 1999 Conference Proceedings (Cat. No.99CH36285), IEEE; 1999, p. 28–39 vol.1.  
doi:10.1109/APEC.1999.749486.
- [95] Kerkman RJ. Twenty years of PWM AC drives: when secondary issues become primary concerns. Proceedings of the 1996 IEEE IECON. 22nd International Conference on Industrial Electronics, Control, and Instrumentation, vol. 1, IEEE; 1996, p. LVII–LXIII.  
doi:10.1109/IECON.1996.570890.
- [96] Murai Y, Kubota T, Kawase Y. Leakage current reduction for a high-frequency carrier inverter feeding an induction motor. IEEE Transactions on Industry Applications 1992;28:858–63. doi:10.1109/28.148452.
- [97] Skibinski GL, Kerkman RJ, Schlegel D. EMI Emissions of Modern PWM AC Drives. IEEE Industry Applications Magazine 1999;5:0–10. doi:10.1109/2943.798337.
- [98] Kerkman RJ, Thunes JD, Rowan TM, Schlegel D. A frequency based determination of the transient inductance and rotor resistance for field commissioning purposes. IAS '95. Conference Record of the 1995 IEEE Industry Applications Conference Thirtieth IAS Annual Meeting, vol. 1, IEEE; n.d., p. 359–66. doi:10.1109/IAS.1995.530322.
- [99] Hughes A, Drury B. Electric motors and drives fundamentals, types and applications. Elsevier; 2013.
- [100] Skibinski G, Pankau J, Sladky R, Campbell J. Generation, control and regulation of EMI from AC drives. IAS '97. Conference Record of the 1997 IEEE Industry Applications Conference Thirty-Second IAS Annual Meeting, vol. 2, IEEE; n.d., p. 1571–83.  
doi:10.1109/IAS.1997.629062.
- [101] Ogasawara S, Akagi H. Modeling and damping of high-frequency leakage currents in PWM inverter-fed AC motor drive systems. IEEE Transactions on Industry Applications 1996;32:1105–14. doi:10.1109/28.536872.
- [102] Kistler Holding AG. 3-Component Quartz Force Sensor 9028. 2013.
- [103] Kistler Holding AG. KiTorq Stator 4542A. 2011.
- [104] LAP Laser. LAP Laser Product Overview 2016.
- [105] Kerkman R, Leggate D, Skibinski G. Interaction of drive modulation and cable parameters

- on AC motor transients. IAS '96. Conference Record of the 1996 IEEE Industry Applications Conference Thirty-First IAS Annual Meeting, vol. 1, IEEE; n.d., p. 143–52. doi:10.1109/IAS.1996.557008.
- [106] Vacon. EMC and variable speed drive. Vacon White Paper n.d.
- [107] Schneider Electric. Altivar 212 variable speed drives catalogue 2011.
- [108] Kollmorgen Corporation. AKD, AKD BASIC, and AKD PDMM Installation Manual. 2013.
- [109] Analog Devices I. Shielding and Guarding: How to Exclude Interference-Type Noise Application Note (AN-347) 2014:1–6.
- [110] Commission USFC. Interference handbook. Federal Communications Commission; 1990.
- [111] Licari JJ. Coating Materials for Electronic Applications: Polymers, Processing, Reliability, Testing. William Andrew; 2003.
- [112] Tong XC. Advanced Materials and Design for Electromagnetic Interference Shielding. vol. 19. CRC Press; 2008.
- [113] Monk P. Finite Element Methods for Maxwell's Equations. Clarendon Press; 2003.
- [114] Robinson MP, Benson TM, Christopoulos C, Dawson JF, Ganley MD, Marvin a. C, et al. Analytical formulation for the shielding effectiveness of enclosures with apertures. IEEE Transactions on Electromagnetic Compatibility 1998;40:240–8. doi:10.1109/15.709422.
- [115] Popovic ZPBD. Introductory Electromagnetics. 2000.
- [116] Johnson WC. Transmission lines and networks. McGraw-Hill; 1950.
- [117] Aavid Thermalloy Data Sheet. AavFin Liquid Cold Plates. 2016.
- [118] Kollmorgen. Calculation of Brake Power: Application Note 2015.
- [119] Bross R. Calculation of Deceleration Time and Angular Displacement in a DC Motor with Dynamic Braking, Technical note: TN-33. 2011.
- [120] Matheson M. SynqNet: high performance motion control based on Ethernet. Computing and Control Engineering 2004;15:32–8.

- [121] Cline D, Mitchell JA, Pearce R. Method and system for removing and returning nodes in a synchronous network. US8072999 B1, 2011.
- [122] Wilson D, Boulanger R, Feng X. The NEES geotechnical centrifuge at UC Davis. World Conference on ... 2004.
- [123] Cline D, Mitchell JA, Pearce R. Method and system for scheduling, transporting, and receiving inbound packets efficiently in networks with cyclic packet scheduling. US7969985 B1, 2011.
- [124] Pearce R, Cline D. System for motion control, method of using the system for motion control, and computer-readable instructions for use with the system for motion control. US20020110155A1, 2001.
- [125] Kollmorgen Corporation. QMP SynqNet™ Controller Quick Start Guide. 2012.
- [126] Freescale. QorIQ P2010 and P2020 Processors Brochure. 2016. doi:QP20XXFS REV 4.
- [127] Kollmorgen Corporation. AKD™ SynqNet Communication. 2012.
- [128] Motion Engineering Inc. SQIO Overview 2016.  
<http://support.motioneng.com/Hardware/IO/SQIO/overview.htm> (accessed June 25, 2016).
- [129] Motion Engineering Inc. SynqNet I/O Hardware 2016.  
<http://support.motioneng.com/Hardware/IO/SQIO/default.htm> (accessed June 25, 2016).
- [130] Motion Engineering Inc. MPI Software Guide. 2006.
- [131] Motion Engineering Inc. Motion Console User Guide. 2005.
- [132] Motion Engineering Inc. MPX Quickstart Guide for LabVIEW. 2002.
- [133] Kollmorgen Corporation. Optimize Motion Performance Improve Mechanical Performance, Quickly and Easily with MechaWare™ . 2009.
- [134] Motion Engineering Inc. MechaWare Overview 4.02 (beta) 2016.  
[http://support.motioneng.com/Software-Mechaware\\_04\\_02/default.htm](http://support.motioneng.com/Software-Mechaware_04_02/default.htm) (accessed June 25, 2016).
- [135] Motion Engineering Inc. XMP Seires Quick Start Guide. 2001.

- [136] Motion Engineering Inc. Bode Tool 04.00 2016.  
<http://support.motioneng.com/Utilities/Bode/default.htm> (accessed June 25, 2016).
- [137] Motion Engineering Inc. SynqNet Cable Length 2016.  
[http://support.motioneng.com/Technology/SynqNet/cable\\_length.htm](http://support.motioneng.com/Technology/SynqNet/cable_length.htm) (accessed June 25, 2016).
- [138] Motion Engineering Inc. Should I Use PID or PIV? 2016.  
[http://support.motioneng.com/Downloads-Notes/Tuning/pid\\_or\\_piv.htm](http://support.motioneng.com/Downloads-Notes/Tuning/pid_or_piv.htm) (accessed June 25, 2016).
- [139] Hahn W. Stability of Motion. Berlin, Heidelberg: Springer Berlin Heidelberg; 1967.  
doi:10.1007/978-3-642-50085-5.
- [140] Kaiser D, Compumotor P. Fundamentals of servo motion control. Parker Compumotor 2001.
- [141] Zhou K, Doyle J, Glover K. Robust and optimal control. 1996.
- [142] Motion Engineering Inc. PID Algorithm and D-Rate 2016.  
[http://support.motioneng.com/Downloads-Notes/Tuning/pid\\_drate.htm](http://support.motioneng.com/Downloads-Notes/Tuning/pid_drate.htm) (accessed June 25, 2016).
- [143] Motion Engineering Inc. Scaling PID Tuning Parameters for Different Controller Sample Rates 2016. [http://support.motioneng.com/Downloads-Notes/Tuning/scaling\\_pid\\_param.htm](http://support.motioneng.com/Downloads-Notes/Tuning/scaling_pid_param.htm).
- [144] Kistler Holding AG. Multichannel Charge Amplifier 5070A. 2010.
- [145] Kistler Holding AG. KiTorq Rotor Torque Measuring Unit (Rotor) 4550A. 2012.
- [146] Kistler Holding AG. Torsion Proof Multi-Disk Coupling 2305A. 2012.
- [147] Qi C, Zhao X, Gao F, Ren A, Sun Q. Contact stiffness and damping identification for hardware-in-the-loop contact simulator with measurement delay compensation. *Acta Astronautica* 2016;123:171–80. doi:10.1016/j.actaastro.2016.03.013.
- [148] Bennett WR. Spectra of Quantized Signals. *Bell System Technical Journal* 1948;27:446–72. doi:10.1002/j.1538-7305.1948.tb01340.x.

- [149] Watahiki T, Ishizuka N. Motor control device, image forming apparatus, and motor control method. US20140306635A1, 2014.
- [150] Janosky MS, Lindsay KA. Slow-speed servomechanism. US6037735A, 2000.
- [151] Veale JR. Digital positioning systems having high accuracy. US4429267A, 1981.
- [152] Sakamoto K, Toyozawa Y. Rotor position sensing apparatus for motors. US4623831A, 1986.
- [153] Thanos WN, Peterson BR, Moon WG, Lindsay J, Stone TR. High performance, high capacity micro-winchester disk drive. US5005089A, 1991.
- [154] Wakabashi N, Yoshida S, Inaji T, Onodera H, Yoshiura T, Mitani H. Data transducer position control system for disk storage drive system. US4954905A, 1990.
- [155] Danaher Industrial Controls. Encoder Application Handbook. 2003.
- [156] Dynapar. Encoder Communications Handbook. 2007.
- [157] Cypress Semiconductor Corporation. Quadrature Decoder (QuadDec). 2010.
- [158] Copley Controls. Copley Controls Serial Encoder Guide. 2013.
- [159] Heidenhain. Product Information: ECN 1313, ECN 1325, ERN 1321, ERN 1387. 2015.
- [160] SICK STEGMANN GmbH. Hiperface DLS Manual. 2013.
- [161] SICK STEGMANN GmbH. SICK STEGMANN Encoders Catalog. 2016.
- [162] Heidenhain. Benefits of the EnDat Interface Datasheet. 2016.
- [163] HENGSTLER. BiSS Technical Datasheet Interface. 2016.
- [164] Kollmorgen. SERVOSTAR S- and CD-series Sine Encoder Feedback. vol. 152. 2003.
- [165] Zador PL. Asymptotic Quantization Error of Continuous Signals and the Quantization Dimension. IEEE Transactions on Information Theory 1982;28:139–49.  
doi:10.1109/TIT.1982.1056490.
- [166] Kipnis A, Goldsmith AJ, Eldar YC. Optimal trade-off between sampling rate and quantization precision in Sigma-Delta A/D conversion. 2015 International Conference on

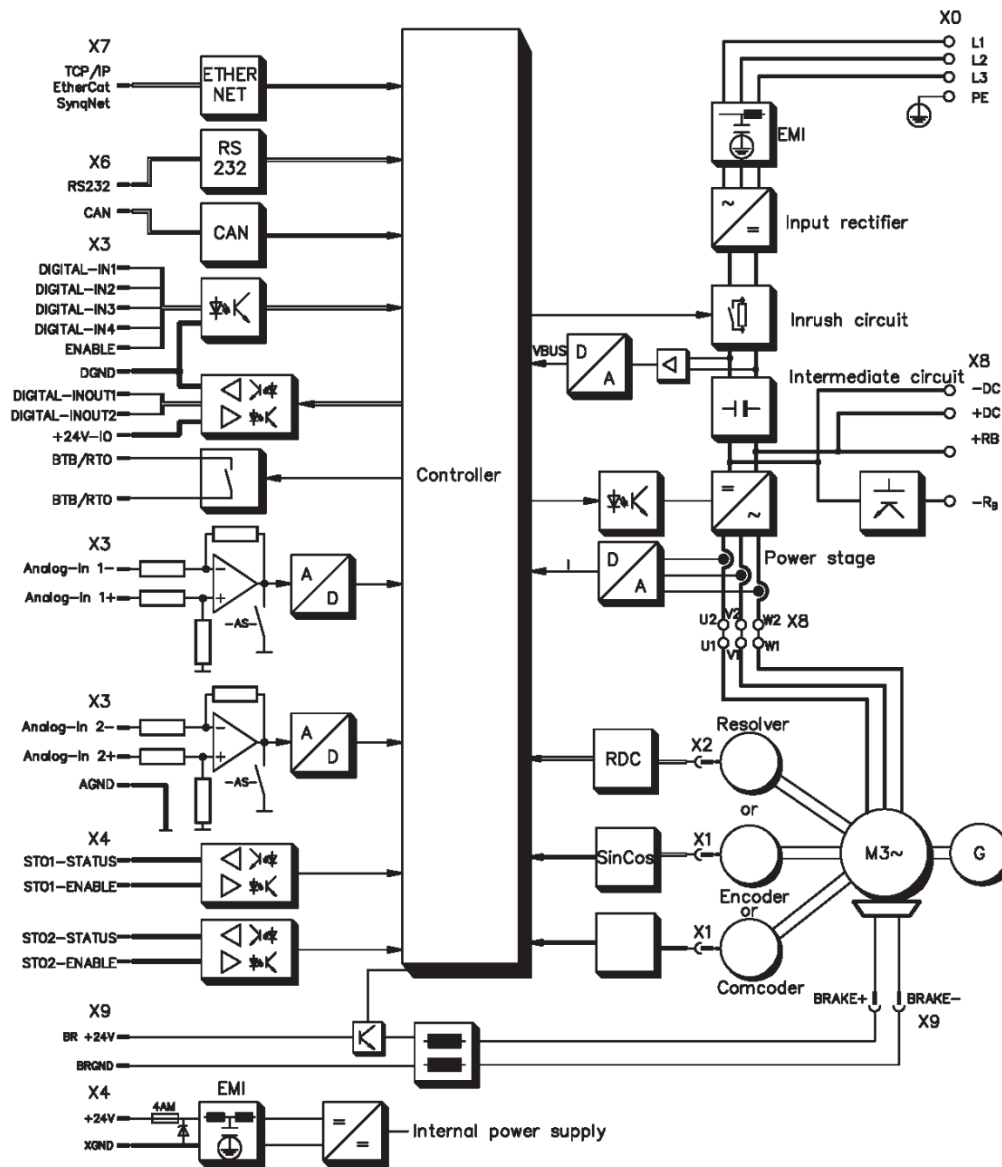
- Sampling Theory and Applications, SampTA 2015 2015:627–31.  
doi:10.1109/SAMPTA.2015.7148967.
- [167] Texas Instruments. Interface to Sin/Cos Encoders With High-Resolution Position Interpolation. 2015.
- [168] Horowitz P, Hill W. The Art of Electronics - 2nd Edition. 1989. doi:10.2277/0521370957.
- [169] Staebler M. TMS320F240 DSP-Solution for High- Resolution Position with Sin/Cos - Encoders. 1998.
- [170] Tan KK, Tang KZ. Adaptive online correction and interpolation of quadrature encoder signals using radial basis functions. IEEE Transactions on Control Systems Technology 2005;13:370–7. doi:10.1109/TCST.2004.841648.
- [171] Heidenhain. Encoder Installation Tolerances. 2016.
- [172] Kim JC, Kim JM, Kim CU, Choi C. Ultra Precise Position Estimation of Servomotor using Analog Quadrature Encoders. Twenty-First Annual IEEE Applied Power Electronics Conference and Exposition, 2006 APEC '06 2006:930–4. doi:10.1109/APEC.2006.1620650.
- [173] Birch KP. Optical fringe subdivision with nanometric accuracy. Precision Engineering 1990;12:195–8. doi:10.1016/0141-6359(90)90060-C.
- [174] Hagiwara N, Suzuki Y, Murase H. A method of improving the resolution and accuracy of rotary encoders using code compensation technique. [1991] Conference Record. IEEE Instrumentation and Measurement Technology Conference, IEEE; 1991, p. 183–4. doi:10.1109/IMTC.1991.161572.
- [175] Madni AM, Jumper M, Malcolm T. An absolute high performance, self calibrating optical rotary positioning system. 2001 IEEE Aerospace Conference Proceedings (Cat. No.01TH8542), vol. 5, IEEE; 2001, p. 2363–73. doi:10.1109/AERO.2001.931195.
- [176] Tan KK, Zhou HX, Lee TH. New interpolation method for quadrature encoder signals. IEEE Transactions on Instrumentation and Measurement 2002;51:1073–9. doi:10.1109/TIM.2002.806028.
- [177] Emura T, Wang L. A high-resolution interpolator for incremental encoders based on the

- quadrature PLL method. IEEE Transactions on Industrial Electronics 2000;47:84–90.  
doi:10.1109/41.824129.
- [178] Kollmorgen. Kollmorgen's New Performance High Resolution Sine Encoder Systems. 2015.
- [179] Heidenhain. Interfaces of HEIDENHAIN Encoders. 2013.
- [180] Kollmorgen Linear Positioners Catalog. 2014.
- [181] Kollmorgen Corporation. AKD™ User Guide. 2013.
- [182] Phoenix Contact. Quint-PS/3ac/24dc/40. 2012.
- [183] PHOENIX CONTACT. Relay Module - PR2-RSC3-LV-120AC/4X21AU - 2834740  
2016. <https://www.phoenixcontact.com/online/portal/us?uri=pxc-oc-itemdetail:pid=2834740> (accessed July 11, 2016).
- [184] Pilz GmbH & Co. KG. PNOZ S4 Operating Manual, 2016.
- [185] Pilz GmbH & Co. KG. PNOZ S11 Operating Manual. 2016.
- [186] Pilz GmbH & Co. KG. PNOZ mm0.1p Operating Manual. 2016.
- [187] Pilz GmbH & Co. KG. PNOZ S7.1 Operating Manual. 2016.
- [188] Pilz GmbH & Co. KG. PNOZ S5 Operating Manual. 2016.
- [189] Pilz GmbH & Co. KG. PNOZ S3 Operating Manual. 2016.
- [190] Kollmorgen. Brake Resistor 2016. <http://www.wiki-kollmorgen.eu/wiki/tiki-index.php?page=Brake+Resistor> (accessed July 11, 2016).
- [191] TE Connectivity. CJT Aluminum Enclosed Resistor Catalogue. 2011.
- [192] Schneider Electric. TeSys IEC Contactors and Overload Relays Catalogue. 2016.

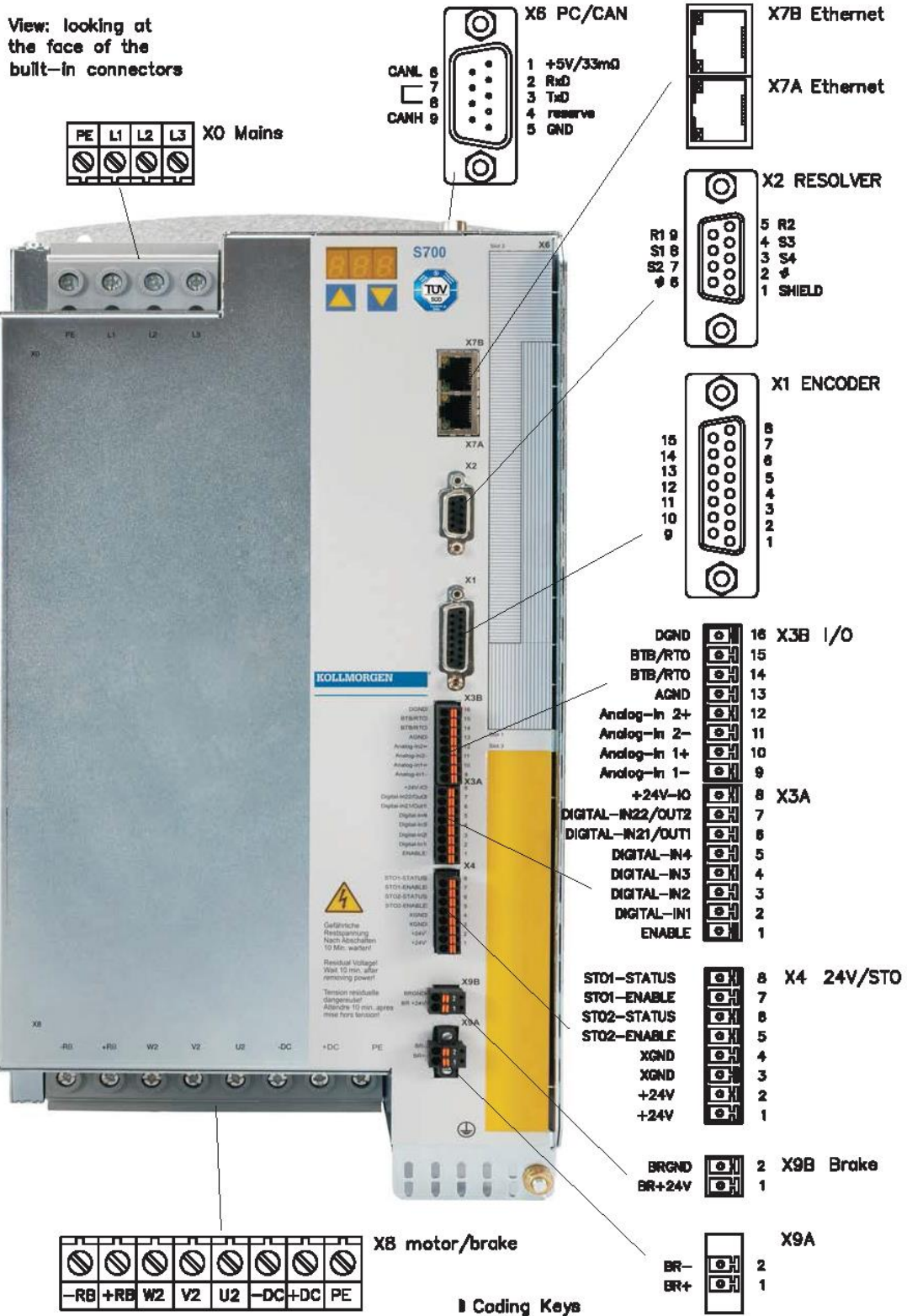
# Appendices

## A. S772 Servo-Amplifier Diagrams

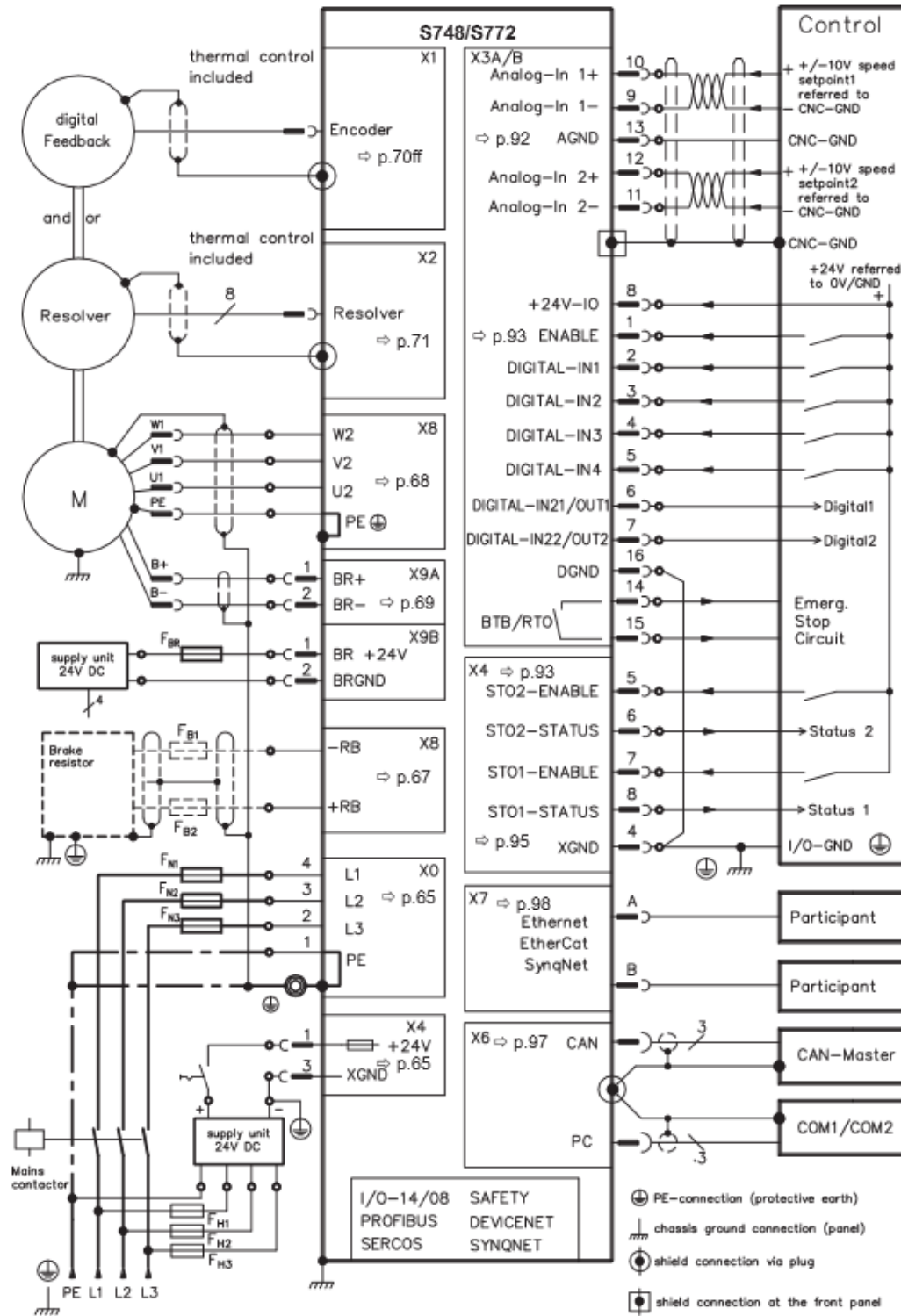
### A.1 Block Diagram



A.2 Connector Assignment

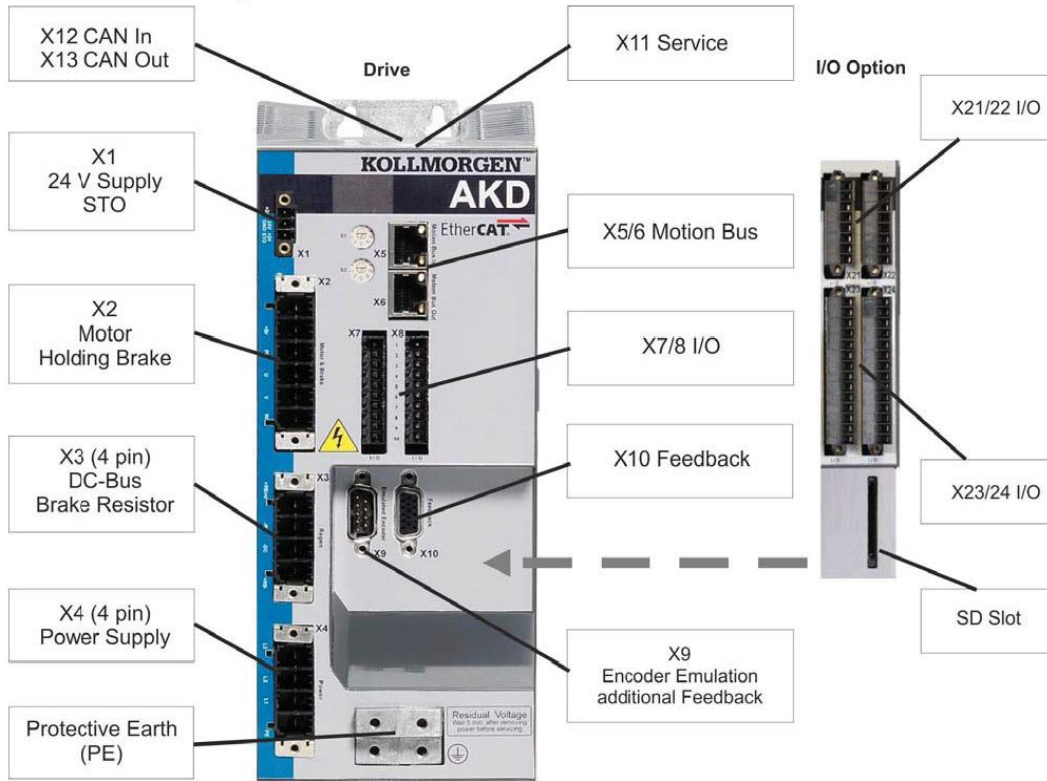


A.3 Connection Diagram



**B. AKD-B00607 Servo-Amplifier Diagrams**

**B.1 Connector Assignment**



B.2 Connection Diagram

